ISBN 978-82-326-4214-4 (printed ver.)
ISBN 978-82-326-4215-1 (electronic ver.)
ISSN 1503-8181

Doctoral theses at NTNU, 2019:309

Marte Kristine Tøgersen

Mineralogical and Textural Characterisation for Increased Iron Oxide Recovery

Exemplified on the Storforshei iron formation

Marte Kristine Tøgersen

Doctoral thesis

Doctoral theses at NTNU, 2019:309

NTNU
Norwegian University of Science and Technology
Thesis for the Degree of
Philosophiae Doctor
Faculty of Engineering
Department of Geoscience and Petroleum

NTNU

NTNU
Norwegian University of
Science and Technology

NTNU
Norwegian University of
Science and Technology

Marte Kristine Tøgersen

Mineralogical and Textural Characterisation for Increased Iron Oxide Recovery

Exemplified on the Storforshei iron formation

Thesis for the Degree of Philosophiae Doctor

Trondheim, October 2019

Norwegian University of Science and Technology
Faculty of Engineering
Department of Geoscience and Petroleum

NTNU
Norwegian University of
Science and Technology

NTNU
Norwegian University of Science and Technology

Thesis for the Degree of Philosophiae Doctor

Faculty of Engineering
Department of Geoscience and Petroleum

ISBN 978-82-326-4214-4 (printed ver.)
ISBN 978-82-326-4215-1 (electronic ver.)
ISSN 1503-8181

Doctoral theses at NTNU, 2019:309

Printed by NTNU Grafisk senter

“There is nothing like looking, if you want to find something. You certainly usually find something, if you look, but it is not always quite the something you were after.”

J.R.R. Tolkien, “The Hobbit”

Acknowledgements

The following work was carried out at the Department of Geoscience and Petroleum at the Norwegian University of Science and Technology. The research was funded by the Research Council of Norway (project no. 232428) and Rana Gruber AS (RG) through the industrial PhD scheme. Thanks very much to production manager Stein Tore Bogen at RG for conceiving this project. I would also like to thank my supervisors Associate professor Kurt Aasly, Associate professor Steinar Ellefmo, and Professor Rolf-Arne Kleiv at the Department of Geoscience and Petroleum (IGP) at the Norwegian University of Science and Technology (NTNU), and to my RG supervisor senior geologist Alexander Kühn for countless productive discussions and help and support throughout the process. Thank you to Rune Johansen who answered all my questions concerning the mineral processing plant at RG, for providing me with the flowsheet, and for advice during the planning and operation of the pilot circuit. Thanks to all the operators at RG, Heia Maskin, and Øijord&Aanes AS that helped with the practical work concerning sampling and moving drill core boxes. A special thanks to the operators from Leonard Nilsen & Sønner (LNS) who showed me an ore they thought were different from the "normal" ore, it was indeed, and ended up being one of the ore types (Granular-Hematite) defined in this PhD. To Ulrik Søvegjarto, the expert on the iron formations in Nordland county, thank you immensely for all the knowledge you have eagerly shared.

Thank you to geologist Marta Lindberg and process engineer Mari Kristin Tro at RG for the good discussions, the pep talks, and all the fun we've had together. I love that you are as interested in Geometallurgy as me! Thank you to the pillars, Perrti Lamberg, Julie Hunt, and Dee Bradshaw inspiring researchers, me included, to become interested in the exiting field of Geometallurgy, and especially to the late Dee Bradshaw for explaining it in such a way that I understood it for the first time! To all my fellow PhD candidates at IGP, thanks for all the talks, coffee breaks, beers, shuffleboards, wine tastings, dinners etc. Thank you to Anette, Marit, Eivind, Mari, Nathan and the rest of the Puffinbiff quiz-team, I really miss our Wednesday quizzes! To Marit and Eivind, thank you so much for letting me stay with you when I visited Trondheim and that you like beer as much as I do. A huge thanks to Nathan and Marit for all the great input and for proof reading at the highest level. Thanks also to my friends in Stavanger and my dear GeoGudruns for always being up for trips and visits when I needed a break, and to my colleagues and friends Elise and Åsa for keeping my spirits up in the last leg!

A very special thanks to Ingjerd Bunkholt, you always have time, you always try to help, and you always have a very good answer. You have helped me more than you know through my PhD work, both through prof reading, discussions, and most of all moral support. Thank you to Laurentius Tijhuis and Morten Raanes for helping me with the XRD and EPMA analyses. A huge thanks to Torill Sørløkk for helping me with everything concerning sample preparation and XRF interpretations, and for always caring, and having time for me. Thank you to all the people who helped me during operation of the pilot circuit: Odd Corneliussen, Erik Larsen, Kristin Aure, Håkon Havskjold, and Przemyslaw Kowalczuk. A huge thank you to Helge Rushfeldt. You made the pilot circuit continuous, and I would be lost without you helping me run it. I learned so much, and most importantly that it is always smart to have a "lazy" engineer on your team, you always see solutions instead of problems.

Thank you to my mom and dad for always inspiring me to go for what I wanted to be, even when you thought I was never going to be done with studying, well now I am (or am I?). You have always pushed me to do my best, and I would not have made it through my PhD, especially this last part, without you backing me every step of the way! You never doubted I could do this. Thank you to my brother Johan for the good discussions and for being as much a nerd as I am. ☺ To my extended family, thank you for all the moral support. I look forward to having more time to spend with you! Look out Dr. Geir Konrad Tøgersen, here comes the next Dr. Tøgersen. Good luck to you soon to be Dr. Jonas Tøgersen Kjellstadli.

Last and most important, thank you to Ida Røisi! You are my geology partner in crime, and my best friend. I don't know how many geological excursions and trips we have been to together, but they were all so much more fun with you. Thank you for all the help, discussions, and pep talks! We did our masters together, and we started our PhD adventure together, and even though we won't finish it together, you are not far behind! To have a best friend and colleague who loves rocks as much as I do makes being a geologist so much more fun (Gold diggers Inc.). I'm certain that neither my master or my PhD would have been as good or even completed without you.

Novel contributions of this work

Some of the results from this research might be of interest for other hematite ore producers.

- The ore types defined based on mineralogical and textural differences, easily distinguishable in the field, and surface hardness measurements enables the use of fast, simple, and inexpensive methods for evaluating production blasts and drill cores
- Ore mineralogy and texture, and surface hardness measurements can be used to evaluate grindability. Fine-grained ore types have higher surface hardness values, and lower grindability, than coarse-grained ore types.
- The hematite liberation and particle sizes affected the efficiency of the wet high intensity magnetic separator, where low hematite liberation and large amount of fines led to poorer separation. The particle textures could be linked to the ore types.
- Calculating the Fe_{tot*} recovery is an underestimation of the real hematite recovery. Determining the Fe_{hem} and Fe_{sil} in crude ore and outputs from the mineral processing plant will provide a more solid prediction of hematite recovery.

Abstract

Process mineralogy is increasingly becoming an important part of quality control in mining operations, and chemical assays are not sufficient for predicting metallurgical performance of complex ore deposits. Knowledge of mineralogical and textural ore properties that affect the mineral processing, may lead to better utilisation of the deposit, and the prediction of recovery becomes more solid.

The Storforshei iron formation (IF) is located in the Dunderlandsdalen valley c. 30 km north-east of Mo i Rana, Nordland county, Norway. The IF consists of highly metamorphosed and deformed hematite-magnetite ore deposits and belongs to the Uppermost Allochthon (UmA) in the Norwegian Caledonides. Rana Gruber (RG) mines deposits in the Storforshei IF, where the main products are hematite concentrates for pellets and sinter production, with magnetite concentrates for pigment production and water purification as a by-product. The main production today is from the Kvannevann deposit, but several other deposits have been in production previously. The deposits in the Storforshei IF show mineralogical and textural differences, and in order to investigate the effects of these differences on the metallurgical performance, a pilot circuit was constructed based on the hematite production line in the full-scale mineral processing plant. The pilot circuit consisted of autogenous milling, wet low intensity magnetic separation (LIMS), and wet high intensity magnetic separation (WHIMS). Three deposits were sampled for testing in the pilot circuit, Kvannevann, Stensundtjern, and Stortjønna. The aim of the pilot circuit was not to fully replicate the full-scale mineral processing plant, but rather to discover differences in the metallurgical performance of the deposits.

Six ore types were defined based on geological mapping and drill core logging from these three deposits, and their surface hardness were measured using Schmidt hammer and Equotip. The ore types are: Granular-Hematite, Specular-Hematite, Hematite-Magnetite, Magnetite-Ore, Mylonitic-Hematite, and Massive-Hematite. Granular-Hematite and Specular-Hematite have relatively coarse-grained hematite with straight grain boundaries, and low surface hardness. The Kvannevann deposit, dominated by these ore types, had high grindability in the AG mill tests, and the mill circuit product had high hematite liberation. As the Kvannevann deposit samples were collected from drift development blasts in the underground mine, they had higher specific charge (Zang, 2016) compared to the Stensundtjern and Stortjønna which were collected from surface and open pit blasts. This and the low surface hardness in the ore types

dominating in the Kvannevann deposit led to a larger amount of microcracks, and a higher grindability as a consequence. The Stensundtjern deposit is also dominated by these ore types, however, has substantial amounts of Hematite-Magnetite and Magnetite-Ore. These ore types have coarse-grained equant-irregular shaped magnetite with irregular grain boundaries, and higher surface hardness than the Granular-Hematite and Specular-Hematite. This together with a lower specific charge during blasting led to less microcracks in the Stensundtjern deposit sample, and likely caused the lower grindability observed for the Stensundtjern deposit sample compared to the Kvannevann deposit sample. The mill circuit product from the Stensundtjern deposit sample had slightly lower hematite liberation than the Kvannevann mill circuit product, which further indicates that there are differences in the ore type distribution between these two deposits.

The Kvannevann deposit sample performed well in the magnetic separation, yielding high Fe_{tot*} grades in the hematite concentrates, and with little loss of hematite to middlings and tailings, and with high hematite liberation in these outputs, further separation on these should recover this hematite. The content of non-economic or gangue minerals are low in the final hematite concentrates.

The Stensundtjern deposit sample preformed similar to the Kvannevann deposit sample in the magnetic separation, however, it had slightly higher content of composite particles. Thus, the loss of hematite to the middlings and tailings also were higher. The higher number of composite particles with hematite is also apparent from the lower hematite liberation in the tailings.

The Mylonitic-Hematite and Massive-Hematite ore types are very fine-grained, where the hematite occurs either disseminated in a matrix of gangue minerals with irregular-to-no visible grain boundaries, or as massive hematite without visible grain boundaries with irregularly folded layers or veins of gangue minerals. These ore types had the highest surface hardness values of all the ore types. The Stortjønna deposit sample had low grindability in the AG milling, and the specific energy consumption was much higher than in Kvannevann and Stensundtjern. This was attributed to the textures and surface hardness values in Mylonitic-Hematite and Massive-Hematite, as breakage of fine-grained rock without grain boundaries requires more energy (Xu et al., 2013), and because the amount of microcracks were, as a consequence of the higher surface hardness and lower specific charge in blasting, lower in the Stortjønna deposit sample compared to the Kvannevann and Stensundtjern deposit samples. The hematite liberation in the Stortjønna mill circuit product was lower than the corresponding

outputs from Stensundtjern and Kvannevann, and the amount of composite particles with hematite was substantial. The particle textures in the Stortjønna mill circuit product corresponds to the textures observed in the Mylonitic-Hematite and Massive-Hematite. The particle distribution in the mill circuit product was broad and there was a notable amount of fines (< 38 µm). This caused challenges in the magnetic separation, as the separation efficiency decreases for fine particles in the WHIMS. Together with the presence of substantial amount of composite particles this led to high loss of hematite to the Stortjønna middlings and tailings. The hematite liberation in these outputs were low, thus, further separation will not improve the hematite recovery as much as it would for the ore types dominating in the Kvannevann- and Stensundtjern deposits.

Minerals containing Fe or Mn, like epidote, biotite/phlogopite, and hornblende, and dolomite were found in middlings and tailings from all the deposits, and as these are returned in the full-scale processing plant, an accumulation of these minerals in the WHIMS circuit might occur, which could lead to them eventually ending up in the final hematite concentrate.

Given that RG produces hematite and magnetite concentrates, the Fe recovery calculations should be based on Fe residing in these minerals, which is equal to the hematite or magnetite recovery, and not the Fe_{tot*} which provides no information of Fe_{hem}, Fe_{mag}, and Fe_{sil}. The relationship between Fe_{tot*}, Fe_{hem}, Fe_{mag}, and Fe_{sil} was investigated on samples from the full-scale mineral processing plant. The mill circuit products and tailings contain more Fe_{sil} than the hematite concentrates, thus, calculating the recovery based on Fe_{hem} or Fe_{mag} rather than on the Fe_{tot*} content led to an increase in recovery for all the hematite concentrates analysed. The importance in these investigations lies in the determination of the amount of Fe_{hem}, Fe_{mag}, and Fe_{sil} in the feed ore, as it provides a more solid prediction of the iron oxide recovery, and a prediction of how much Fe bearing non-economic minerals might end up in the hematite concentrates bringing undesirable elements like Mn, S, and alkalis with them.

By incorporating Equotip measurements in drill core logging, and geological mapping with focus on the ore types defined in this research, RG can easily improve the daily production quality control. However, analyses of modal mineralogy are also recommended, which together with mineral chemistry can be used to determine recoverable Fe located in iron oxides (Fe_{hem} and Fe_{mag}) and the amount of Fe located in non-economic minerals (Fe_{sil}), hence, calculate real iron oxide recovery.

Contributions to papers

All the papers in this thesis were written in collaboration with others. The contributions to the papers are presented in the following.

Paper I: Mineralogy and texture of the Storforshei iron formation, and their effect on grindability

Marte Kristine Tøgersen[1,2], Rolf Arne Kleiv[1], Steinar Ellefmo[1] and Kurt Aasly[1]

[1]*Department of Geoscience and Petroleum, Norwegian University of Science and Technology, Sem Sælandsveg 1, N-7491 Trondheim, Norway*

[2]*Rana Gruber AS, Mjølanveien 29, Gullsmedvik, 8601 Mo i Rana, Norway*

(published in Minerals Engineering, 125, pp. 176-189)

Marte Kristine Tøgersen contributed with the planning, construction, and operation of the pilot circuit. All sampling, sample preparation, and surface hardness measurements were conducted by Marte, in addition to the interpretation and processing of the data and writing the paper.

Rolf Arne Kleiv contributed with input and discussions during planning and construction of the pilot circuit, interpretation of data, especially the milling data. Rolf Arne also contributed to the layout and proofreading the paper.

Steinar Ellefmo contributed to the interpretation of the surface hardness data, processing of drill core data and production of the map, in addition to proofreading, and contributions to the layout of the paper.

Kurt Aasly contributed with input and discussions during the planning and construction of the pilot circuit, interpretation of data, and input on the layout of the paper.

Paper II: The effect of hematite liberation and texture on wet high intensity magnetic separation of a low-grade iron ore

Marte Kristine Tøgersen[1,2] and Kurt Aasly[1]

[1]*Department of Geoscience and Petroleum, Norwegian University of Science and Technology, Sem Sælandsveg 1, N-7491 Trondheim, Norway*

[2]*Rana Gruber AS, Mjølanveien 29, Gullsmedvik, 8601 Mo i Rana, Norway*

(unpublished manuscript)

Marte Kristine Tøgersen contributed with planning, constructing, and operation of the pilot circuit, in addition to all sampling, sample preparation, interpretation and processing of the data, in addition to writing the paper.

Kurt Aasly contributed with input and discussions during the planning and construction of the pilot circuit, in addition to aiding with conducting and interpreting analyses. Kurt also contributed with proofreading, inputs on layout, and general supervision.

Paper III: Fe deportment in non-economic minerals in the Kvannevann iron ore deposit

Marte Kristine Tøgersen[1,2], Steinar Ellefmo[1], Kurt Aasly[1]

[1]*Department of Geoscience and Petroleum, Norwegian University of Science and Technology, Sem Sælandsveg 1, N-7491 Trondheim, Norway*

[2]*Rana Gruber AS, Mjølanveien 29, Gullsmedvik, 8601 Mo i Rana, Norway*

(unpublished manuscript)

Marte Kristine Tøgersen conducted all the analyses and calculations, in addition to interpretations and processing of the results, and writing the paper.

Kurt Aasly contributed to the idea of the paper, and interpretation of the results, especially with regards to the mineralogical- and mineral chemistry analyses, in addition to proofreading and inputs to layout of the paper.

Steinar Ellefmo contributed to the recovery calculations and interpretation of the results, in addition to proofreading and inputs to layout of the paper.

Table of contents

Part 2

Paper I: Mineralogy and texture of the Storforshei iron formation, and their effect on grindability

Paper II: The effect of hematite liberation and texture on wet high intensity magnetic separation of a low-grade iron ore

Paper III: Fe deportment in non-economic minerals in the Kvannevann iron ore deposit

Appendix A: Chemical analyses not presented in the papers

Appendix B: Modal mineralogy of the pilot circuit outputs

Appendix C: Mineral chemistry

Appendix D: Measurements of surface hardness by Schmidt hammer

Appendix E: Collars drill cores measured by Equotip and deposit samples

Appendix F: Drill core sections measured by Equotip

Appendix G: Measurements of surface hardness by Equotip (available in the online version of this thesis at NTNU Open Archive https://ntnuopen.ntnu.no/ntnu-xmlui/ or by requesting the author)

PART 1

1 Introduction

1.1 Project background

As a consequence of the increased industrialisation of underdeveloped countries (Sustainable Development UN, 2018) and the desire for a green shift with renewable energy resources (The Norwegian Government, 2018), metal demand is increasing worldwide (Bradshaw, 2014). Available ore deposits are more complex and have lower grade than previously, thus, in order to create a viable mining operation, it is of increasingly importance to have a better process mineralogical understanding of the ore (Bradshaw, 2014).

Iron ore is used in several applications like water purification, pigment (paint, food), raw material for chemical industries etc. (Rana Gruber, 2019), however, most of the iron ore produced today goes to the steel industry (King, 2019).

The Storforshei iron formation (IF) is located in the Dunderlandsdalen valley in Nordland county, Norway. It is part of the Dunderland formation in the Uppermost Allochthon (UmA) in the Norwegian Caledonides. Dating of surrounding marbles indicates an age of 800-730 Ma (Melezhik et al., 2015), and the iron formation was deposited on a carbonate- siliciclastic-rich shelf at the margins of Laurentia (Grenne et al., 1999) or of an unknown microcontinent in the Iapetus ocean (Melezhik et. al., 2015). There are several hematite-magnetite ore deposits in the Storforshei IF, with mineralogical and textural variations both within each deposit and between them. Rana Gruber AS (RG) is currently the only iron ore producer in Norway and is mining some of the ore deposits in the Storforshei IF. They produce both magnetite- and hematite concentrates, the main product being the hematite concentrates H150 and H400 (average particle size, 150µm and 400µm, respectively). This project was born from a desire to gain more knowledge about how ore variations affect the hematite production. The current daily process control consists mainly of chemical analyses: Fe_{tot*} (total content of Fe measured using titration at RG), S (S_{tot}), MnO, Fe_{mag*} (Fe in magnetic minerals, magnetite and pyrrhotite, as analysed by RG), and alkalis. However, previous experiences have indicated that this is insufficient because mineralogical and textural variations in the ore are neglected (Klomstadlien, 1984). To investigate mineralogical and textural differences in the Storforshei IF a pilot circuit was constructed based on the main operations in the hematite production at RG. Three ore deposits were selected for investigations and sampling in this project, the Kvannevann deposit, currently in production, the Stortjønna deposit, previously in production, and the Stensundtjern deposit which is a new prospect for future production. The Stortjønna

deposit was abandoned after two years due to challenges in processing this ore, especially related to the autogenous milling circuit, and not achieving the expected Fe_{tot*} recovery levels, despite having Fe_{tot*} grades in the feed similar to the Kvannevann deposit (34wt % (NGU, 2017)). Sandvik et al. (2012) investigated these experienced differences in the metallurgical performance related to the autogenous mill circuit, and tested samples from Stortjønna and Kvannevann on a pilot scale mill, which was the same mill as used in the pilot circuit in this research. The samples collected from blasts by Sandvik et al. (2012) were not crushed before being fed to the mill. The Kvannevann feed had a d50 of 50 mm, while the Stortjønna feed had a d50 of 30 mm. The results showed a decrease in mill capacity by 30-40 % when milling the Stortjønna sample compared to the Kvannevann sample, and a finer mill circuit product from Stortjønna than Kvannevann (Sandvik et al., 2012).

These past experiences and tests substantiate the need for a better understanding of the mineralogical and textural variations in the different iron ore deposits in the Storforshei IF. Investigations on which ore properties affect the metallurgical performance provides a more solid foundation for production planning and leads to better utilisation of the deposits (Baum et al., 2004; Hoal, 2008). Several mineralogical studies have been conducted on material from the Storforshei IF (Malvik, 2011). However, these were not directly related to the effect of mineralogical and textural ore properties on the mineral processing. A process mineralogical study of ore deposits in the Storforshei IF of this magnitude has not been conducted before.

1.2 Objectives and scope of work

The main objective of this project was to characterise mineralogical and textural variations in the Kvannevann, Stensundtjern, and Stortjønna deposits, and how these variations affects the mineral processing at RG. The focus was on the hematite production in RG, the magnetite production was not within the scope of this research. Defining ore types based on mineralogical and textural, and surface hardness measurements, and determining how they will behave in the process was an important part of this research. However, the characterisation of the ore types is based on geological mapping and drill core logging of the Kvannevann, Stensundtjern, and Stortjønna deposits only, other ore deposits in the Storforshei IF were not included. To investigate the mineralogical and textural differences in three iron ore deposits and how these differences affected the mineral processing, a pilot circuit was constructed based on the main operations in RG's hematite production: autogenous (AG) milling, wet low intensity magnetic separation (LIMS) and wet high intensity magnetic separation (WHIMS). The aim of the pilot circuit was not to replicate the full-scale processing plant, but rather to discover ore variations

related to metallurgical performance (as used in e.g. Lotter et al., 2011; Bradshaw, 2014) between the three deposits. Another objective was to develop simple inexpensive methods of identifying the mineralogical and textural variations to obtain a better prediction of hematite recovery and Fe grade in the daily production of hematite. The results from this research is a first step towards developing a geometallurgical program (Lamberg, 2011) in RG and provides new insight into process mineralogy in a low-grade metamorphosed hematite-magnetite ore. The methods and to some extent the results from this research should be applicable to other mining operations around the world.

The mineral abbreviations used in this thesis follows Whitney and Evans (2010).

1.3 Research tasks

- Establishing a pilot circuit based on the existing hematite production in RG for testing large ore deposit samples (1-2 tonnes) from the Storforshei IF.
- Define ore types based on geological mapping and drill core logging with emphasis on mineralogical and textural differences and determining the distribution of them in the deposits Kvannevann, Stensundtjern, and Stortjønna.
- Investigate the mineralogical and textural differences in relation to the metallurgical performance of the Kvannevann-, Stensundtjern-, and Stortjønna deposits.
- Determine the relationship between total Fe content (Fe_{tot*}), Fe in iron oxide (Fe_{hem} and Fe_{mag}), and Fe in non-economic minerals (Fe_{sil}), and how the recovery calculations are affected when calculating the recovery based on Fe_{hem} instead of Fe_{tot*}.
- Discover the link between mineralogical and textural variations, and hematite recovery.
- Develop a testing procedure to identify ore types and textural properties that can affect the process by using simple inexpensive methods.

1.4 Organisation of the thesis

This thesis is organised in eight chapters. The first is the introduction, where the background of the project is presented along with the objectives and scope, and more detailed research tasks. The second chapter, which is the background chapter, includes an overview of the definitions, classification and genesis of iron formations, together with an introduction to the Storforshei IF, and the mineral processing plant at RG. A short description of the concept geometallurgy and process mineralogy is also provided in this chapter. In the materials section, of the third chapter or materials and methods, there is a short introduction of the geology of the Kvannevann, Stensundtjern, and Stortjønna deposits, with the locations of the deposit samples,

and the access points of the drill cores measured by Equotip. The sampling procedure used for both the deposit samples and the samples from the pilot circuit are presented, along with the particle size distribution (PSD) of the deposit samples after the primary crushing. In the methods section, a description of the methods used in this research is given. The results chapter is divided into two parts: results from papers, in which the results and key findings from the three papers are presented, and additional results, where results from correlating the XRF and titration methods, testing the reproducibility of the XRF results, and the mass balance of the pilot circuit are presented. The discussion is divided into five sections. The first addresses the first the classification and origin of the Storforshei IF. In the second the effects of ore properties (surface hardness, PSD, ore mineralogy and texture) on comminution are discussed, which also includes an evaluation of the effects of blasting damage on crushing and grinding. The third part of the discussion is focused on the chemical, mineralogical, and textural differences between the deposit samples from Kvannevann, Stensundtjern, and Stortjønna in the WHIMS steps, while the difference between Fe_{tot*} recovery and iron oxide recovery are discussed in the fourth section. The fifth section is a summary of the key findings from the pilot circuit. In the sixth chapter the conclusions of the entire thesis are given, while some recommendations for future work are listed in the seventh chapter, and the reference list comprises the eight chapter of this thesis.

2 Background

2.1 Geological background

2.1.1 Definitions of iron formations

The terms iron formation and ironstone are used interchangeably by different authors. For this thesis Kimberley's (1978, p. 215) definitions of ironstone, iron formation, and chemical sedimentary rock are used.

An ironstone is defined as:

"…chemical sedimentary rock which contains over 15 % Fe."

Iron formation is defined as:

"…a mappable rock unit composed mostly of ironstone, with the uppermost and lowermost beds being ironstone."

A chemical sedimentary rock is defined as:

" ...over 50 % by volume inorganic and/or organic chemical precipitates from a surficial water body and/or diagenetic replacements of those precipitates."

2.1.2 Classification of iron formations

The classification of iron formations is disputed amongst researchers with regards to the basis of classification. In the following a few important classification schemes are presented.

James (1954) uses mineralogy to classify iron formations. There are several valence states where Fe can exist and depending on the chemical composition of the mineral precipitating solution, pH conditions, and Eh (redox potential), different iron minerals will be formed. The minerals formed in IFs, whether primary or secondary, can be used as indicators of the depositional environment, as they record some elements of the chemical origin (James, 1954). James (1954) suggests a facies classification for iron formations based on the iron ores in the Lake Superior district on the border of the US and Canada. He defines four depositional facies for Fe, carbonate, silicate, sulphide, and oxide (Table 1). The four facies indicate different depositional environments: the sulphide facies strongly reducing, the carbonate facies slightly less reducing, the silicate facies with intermediate Eh, varying from mildly reducing to mildly oxidizing, and the oxide facies with intermediate Eh in magnetite-banded deposits, and strongly oxidising in hematite-banded deposits (James, 1954).

Table 1: The table shows James' (1954) four facies for iron formations, with their characteristics. Modified from Ellefmo (2005).

Facies	Characteristics
Oxide facies	Hematite or magnetite, 30-35 % iron, carbonate may be present
Carbonate facies	Inter-banded chert and siderite (iron carbonate) in equal proportions. The siderite lacks oolitic or granular texture
Silicate facies	Generally associated with magnetite, siderite and chert. Primary iron silicates may include greenalite, chamosite (iron-rich chlorite) and glauconite (mica mineral only found in sedimentary rocks), and some minnesotaite and stilpnomelane, ferrous (2+) iron (mostly)
Sulphide facies	Pyritic carbonaceous argillites, formed under anaerobic conditions

Trendall (2002) classified iron formations on the basis of lithology, thus, this classification is purely descriptive. He defined two classes of iron formations, GIF (granular iron formations), and BIF (banded iron formations), with texture as the main difference between the two classes. Trendall (2002) defines an iron formation as a sedimentary rock with ±30 % Fe, and ±50 % SiO_2. Chemical precipitates dominated by these components (Fe and SiO_2), underwent extreme diagenesis and compaction, to form iron formations (Trendall, 2002). Table 2 lists the characteristics of BIF and GIF.

Table 2: Characteristics of BIF and GIF by Trendall (2002). Modified from Ellefmo (2005).

Acronym	Explanation
BIF	• Occurs in greenstone belts sequences of all main old cratons • Mostly tectonically deformed, but do also exist in weakly metamorphosed supracrustal rock sequences • Stratigraphic, sharply bounded units • Distinct mesobanding • No current generated structures • Epiclastic components are almost absent • Uniform chemical composition, but varying mineralogy • Considerable lateral continuity
GIF	• Form sharply bounded units, but relative to BIF they are more interstratified with coarse to medium-grained epiclastic sediments, and partly associated to volcanogenic rocks • Do not have regular mesobanding like BIF. The alternations of iron-rich and silica-rich bands tend to be coarser and less regular. • Current generated structures are common. • The iron-rich bands tend to be granular or oolitic. • Uniform chemical composition. Varying mineralogy. • Not the same lateral continuity as BIF.

Kimberley (1978) discusses the classification of iron formation with regards to paleoenvironment, i.e. the environmental conditions in which the iron formation was deposited. Table 3 lists the different iron formation classes defined in Kimberley (1978).

Table 3: Classification of iron formations based on paleoenvironment (modified after Kimberley, 1978).

Acronym	Full name	General features
SVOP-IF	Shallow-volcanic-platform iron formation	Cherty (Archean and Palaeozoic)
MECS-IF	Metazoan-poor, extensive, chemical-sediment-rich shelf-sea iron formation	Cherty, banded (most abundant Early Proterozoic)
SCOS-IF	Sandy, clayey, and oolitic, shallow island-dotted-sea iron formation	Chert-poor (most abundant Phanerozoic type)
DWAT-IF	Deep-water iron formation	Cherty (mostly Archean)
SOPS-IF	Sandy, oolite-poor, shallow-sea iron formation	Chert-poor, glauconite-rich (only Phanerozoic)
COSP-IF	Coal-swamp iron formation	Chert-poor, non-oolitic (only Phanerozoic)

2.1.3 Genesis of iron formations

Most of the world's IFs were deposited in Precambrian, from 3.8 Ga (Isua, West Greenland, (Klein, 2005))-1.9 Ga. Between 1.9 Ga and 0.8 Ga there was a gap in formation of iron formations. They reappear in the geologic record between 0.8-0.6 Ga (e.g. Hoffman and Schrag, 2002, Klein, 2005).

The genesis of IFs is a debated topic, however, there is a common understanding that they are precipitates, either chemical or biochemical (e.g. Gross, 1983; Kimberley, 1989b; Trendall, 2002). Iron formations represent end-member chemical sediment; however, they can form in a large variety of sedimentary environments. Normally the suite of associated sedimentary rocks reflects the chemical conditions in which the end-member chemical sediment was formed, but such is not the case for most iron formations. The entire spectrum of climatic environments is represented in the rocks associated with for example cherty iron formations: from the late Proterozoic iron formations association with glacial environments, to humid tropical environments associated with early Proterozoic iron formations (Kimberley, 1989b). It is clear, however, that all iron formations have a source from which the Fe came, and that the Fe was in solution, transported and precipitated (e.g. Gross, 1983; Kimberley, 1989b; Klein, 2005). The conditions for mechanical- or chemical liberation of Fe: the source, the degree of precipitation during transportation, and the conditions at the time and place of precipitation determines the primary characteristics of the iron formation (Ellefmo, 2005). These characteristics will later be affected by diagenesis and metamorphism (e.g. Klein, 2005). A genetic classification for iron formations is therefore difficult to determine, since all the factors stated above must be considered (Ellefmo, 2005).

2.1.3.1 Archean to middle Proterozoic iron formations

It is difficult to reconstruct the depositional conditions for most Archean BIFs as the greenstone belts they are part of are highly metamorphosed, deformed, and dismembered. Although for some of the largest BIFs in the world (Transvaal Supergroup, South Africa and Hamersley Range, Western Australia) the reconstruction of the depositional environment has been easier, as deformation and metamorphism are generally lacking (Klein and Gole, 1981; Klein and Beukes, 1989). Microbands and fine laminations are common for most Archean BIFs, which indicates that they were deposited deeper than the modern storm wave base, which is 200 meters (Trendall, 2002). Klein (2005) considers 200 meters as the minimum depth for deposition of the banded iron formations of Archean age. The lack of detrital components in the bulk chemistry of banded iron formations (low content of i.e. Al_2O_3), indicates that the iron formations were deposited beyond the offshore influx of epiclastic material (Trendall, 2002; Klein, 2005). Klein (2005) also emphasises that several of the gel-like Fe-rich precipitates have a delicate nature as an argument for deep depositional basins for the Archean BIFs. The Early Proterozoic iron formations also show well-developed microbands, and in contrast to most Archean BIFs they are well-preserved. Case studies done by Klein and Beukes (1989) and Beukes et.al. (1990) of the Kuruman iron formation in the Transvaal Supergroup in South Africa, which is situated above the Campbellrand carbonate sequence, showed large differences in the water column from which the carbonates and the iron formation were deposited. They proposed a model with a stratified ocean system in Archean-Early Proterozoic, where the carbonates were deposited during a regressive stage, with high organic productivity in the shallow waters, and that the iron formation was deposited in deep waters enriched in FeO and depleted in organic carbon during a transgressive stage. The dissolved FeO was likely supplied by a deep ocean hydrothermal source (Klein and Beukes, 1989; Beukes et al., 1990). The iron formations of middle early Proterozoic are more granular and oolitic than those formed in the Archean-Early Proterozoic, which indicates shallow water deposition, and a breakdown of the stratified ocean system. The hydrothermal influx decreased, and the dissolved Fe was transported to the surface waters. The organic productivity also declined in this period. Iron formations disappear from the geological record at 1.9Ga (Middle Proterozoic). At this point the stratification in the water column was gone: the water was less reducing, and depleted in Fe (Klein, 2005).

2.1.3.2 Neoproterozoic iron formations

Iron formations reappear in the geologic record at about 0.8 Ga (e.g. Klein, 2005). The Neoproterozoic iron formations are very different from the BIFs in that they are associated with

glaciogenic sediments and are dominated by hematite and quartz, as opposed to magnetite which dominates in the older BIFs (Klein and Beukes, 1993). Glaciomarine sediments, dropstones, and faceted pebbles have been found in Neoproterozoic iron formations, leading to the assumption that they are closely associated with the major glacial events of the time (e.g. Hoffman and Schrag, 2002; Klein, 2005; Melezhik et al., 2015). Numerous glacial events occurred between 740 and 582 Ma. These have been grouped together under the term Snowball Earth (Kirschvink, 1992). The Snowball Earth hypothesis is that global glacial events can be affiliated to major climate changes in the Neoproterozoic: a major rise in oxygenation of the ocean and atmosphere, the second of its kind, and the first macroscopic metazoan appearance (Kirschvink, 1992; Hoffman et al., 1998; Hoffman and Li, 2009). Three major glacial events are recognized during the Snowball Earth period, Sturtian (ca. 715-680 Ma), Marinoan (ca. 660-635 Ma), and Ediacarian (ca. 585-582 Ma, Bowring et al., 2003). Most of the Neoproterozoic iron formations are associated with one of these glacial events (Hoffman et al., 2011).

The covering of the oceans with ice sheets lead to stagnation and anoxic conditions, enabling Fe-enrichment of the oceans (Klein, 2005). Klein and Beukes (1992) propose that the source of Fe was either from material dissolved from basin floors or hydrothermal. During interglacial periods with ice sheet withdrawal, leading to quickly rise of ocean-level and direct contact between the oceans and the atmosphere, the ocean circulation was restored, and iron formations were deposited. For precipitation of the precursors to hematite, only small amounts of oxygen were needed (Klein (2005).

2.1.4 The Storforshei iron formation

The Caledonian orogeny in which the Laurentia and Baltica continents collided in Silurian-Devonian time, consists in Norway of a succession of nappe stacks. In all four allochthons (lower, middle, upper and uppermost) were emplaced on top of the Precambrian crystalline basement (Roberts and Gee, 1985). The UmA originated on the Laurentian side of the Iapetus ocean, either on the margin or in association with microcontinents (e.g. Grenne et al., 1999; Roberts et al., 2007). In Nordland the UmA is divided into two terrains: The Helgeland Nappe Complex and the Rødingsfjellet Nappe Complex, while the UmA in the northern part of Nordland and Troms consists of several nappes (Roberts et al., 2007). The Dunderland formation in the Rana area in Norland county, located c. 30 km north-east of Mo i Rana, is part of the Rødingsfjellet Nappe Complex and consists of two stratiform iron formations: Storforshei and Lasken (Søvegjarto et al., 1989). Lasken IF, the lower iron ore horizon of the two, is an apatite-magnetite ore, containing 0.8-1.0 wt % P, with accessory minerals being

carbonates and amphiboles (Bugge, 1948; Roberts et al., 2007). The upper iron ore horizon, Storforshei IF, is a hematite-magnetite ore containing quartz and carbonates. It is currently in production and contains less P than Lasken IF (0.15-0.30 wt % P) (Bugge, 1948). Feldspar, garnet, epidote, biotite, muscovite, chlorite, aegirine-augite and hornblende are among the accessory minerals that can be found in the Storforshei IF (Tøgersen and Aasly, unpublished manuscript). In addition, the Storforshei IF shows banding in several localities (Tøgersen et al., 2018). The host rocks in the Storforshei IF are dominated by marbles and mica schists. Both calcite and dolomite marbles can be found, and in some areas calcareous mica schist is the dominant schist (Bugge, 1948; Søvegjarto et al., 1989; Gjelle et al., 1991). There are also some occurrences of garnet mylonite, meaning a very fine-grained rock consisting mostly of garnet (Søvegjarto, 1972). Melezhik et.al. (2015) dated several carbonate rocks in the Dunderland area and found an age of deposition between 800-730 Ma. There are minor amphibolite intrusions in the area, which are younger than the iron formation (Bugge, 1948; Melezhik et al., 2015). In addition, diamictites associated with glacial events were found in contact with the IF by Melezhik et al. (2015).

The Dunderland formation has undergone at least three stages of deformation, with pre-Caledonian F1 being when the main metamorphism occurred (Søvegjarto, 1990). This has resulted in the Dunderland formation forming a syncline, with a complexly folded rock sequence (Bugge, 1948; Søvegjarto et al., 1989; Gjelle et al. 1991). Søvegjarto (1972) suggests medium metamorphic grade (lower amphibolite facies) for the Dunderland formation. The Storforshei and Lasken IFs can be associated with the Sjåfjell and Håfjellet iron formations in Troms county (Melezhik et al., 2015), which Kimberley (1989b) has classified as a MECS-IF.

Several compilations for comparison of Neoproterozoic iron formations around the world have been made (e.g. Trendall, 2002; Cox et al., 2013). However, they do not include the stratiform iron formations in Norway, as pointed out by Melezhik et al. (2015). The Neoproterozoic iron formations, in the UmA in Norway, are of significant sizes, stretching from Mosjøen in the south to the Tromsø district in the north (approximately 550 km) (Roberts et al., 2007; Melezhik et al., 2015). The Sjåfjell and Håfjellet IFs in the Ofotfjorden area (c. 250 km north of the Dunderlandsdalen valley) are comparable to the IFs in the Dunderland formation both in composition and metamorphic grade. However, the Sjåfjell IF despite having similar composition with the Lasken IF (high-P iron ores), is at a different technostratigraphical level than the Dunderland IFs (Melezhik et al., 2014). The Håfjellet IF has a composition and technostratigraphical level (UmA) comparable to the hematite-magnetite ores in the Storforshei

IF. Sr levels from marbles in the Ofotfjorden area and the Dunderlandsdalen valley show that the Håfjellet IF, the Storforshei IF, and the Lasken IF likely were deposited contemporaneously between 800-730 Ma (Melezhik et al., 2015).

Melezhik et al. (2015) compared other Neoproterozoic IFs in the Caledonide-Appalachian orogen with the Storforshei IF. There are no known Neoproterozoic IFs in the Caledonides in Greenland, Scotland, and Ireland with the exception of magnetite-rich metasediments in the Dalradian Supergroup (Scottish and Irish Caledonides) (Spencer, 1971 as cited in Melezhik et al., 2015). The Chestnut Hill IF, Rapitan Group IF, Tatonduk IF, and Tindir Group IF are in North America, located on the former Laurentian plate's western margin (compiled in Cox et al., 2013). The formation of these four IFs was associated with rifting occurring with the Rodinia breakup. The deposition of the Rapitan Group IF, dominated by hematite and jaspilite (Klein and Beukes, 1993), most likely happened during an interglacial period with transgression and rapid sea-level rise in connection with the Sturtian glacial period in the Neoproterozoic (Halverson et al., 2011). Volcanic activity accompanied the deposition of the four North American IFs (Young et al., 1979; Young, 1982; Gates and Volkert, 2004 as cited in Melezhik et al., 2015; Cox et al., 2013).

The association with mafic lithologies are apparent in, for instance, the basalt clasts in the diamictites in the Rapitan Group IF (Cox et al., 2013). However, there is no evidence of volcanic activity related to the deposition of the Storforshei IF. In addition, the four North American IFs are located on the western part of the Laurentian plate meaning that they were not thrust upon the Baltica plate during the Caledonian orogeny. This suggests that the formation of the Storforshei IF is not related to the North American IFs (Melezhik et al., 2015). Melezhik et al. (2015) argues that the Storforshei and Lasken IFs, and the Håfjellet IF was deposited in association with an unknown microcontinent in the Iapetus ocean, either in a large back arc basin, or at a passive continental margin, on a carbonate-siliciclastic-rich shelf with glacial influence. The accumulation happened far from volcanically active rifting, and as such the Storforshei IF, the Lasken IF, and the Håfjellet IF deviate from other Neoproterozoic IFs (Melezhik et al., 2015).

2.2 The mineral processing plant at RG

The main production at RG is from the Kvannevann deposit, where c. 4 million tonnes crude ore are produced annually. After blasting, the ore is transported by trucks to the primary crushers, a jaw crusher in the underground mine, and a gyratory crusher near the open pit.

Further, the ore is stored in a silo, before being loaded onto trains and transported c. 30 km to the mineral processing plant in Gullsmedvik, Mo i Rana, where the ore again is stored in a large silo. Iron ore from all underground and open pit production faces, are blended in the same silo at the mine, hence, no geographical information about the iron ore exists as it enters the mineral processing plant. The main processing equipment at RG are: AG mills, LIMS, WHIMS, screens and spirals. Figure 1 shows the flowsheet of the hematite production line in the full-scale mineral processing plant at RG. From the silo in Gullsmedvik the ore is transported on one conveyer belt feeding two AG mills. Water is added with the mill feed, creating a pulp thickness of 60 wt % solids. The AG mills are operated in closed circuits with an 800 µm screen. The d_{80} of the mill circuit product is about 210 µm. The first magnetic separator step, LIMS, produces a preliminary magnetite concentrate which goes onward to the magnetite production line (not included in Figure 1). The non-magnetic fraction from the LIMS, passes a 1 mm control screen before it enters the WHIMS. Oversized particles are transported back into the mill, as particles > 1 mm will impede the functioning of the WHIMS.

There are two WHIMS steps, where the first step utilises a higher magnetic field strength than the second step. Each WHIMS produces three outputs: concentrate, middling, and tailing. The middling is washed out of the WHIMS at the edge of the magnetic field. The middlings and tailings from the first WHIMS step at RG are combined, and further treated on spirals, where the hematite concentrate is returned to the main hematite process, one part to LIMS, and the rest to the second step of WHIMS. The hematite concentrates from WHIMS step 1 is sent to WHIMS step 2. The middling from WHIMS step 2 is a circulation load which is returned with the new feed to the WHIMS step 2, while the tailings from WHIMS step 2 are dewatered in a hydro cyclone prior to being sent into the AG mill. The hematite concentrates from WHIMS step 2 is sieved on a 230 µm screen, to prepare the two commercial hematite products, H150 and H400. After screening, the H150 concentrate goes to dewatering and then to storage silos, while the H400 concentrate goes through a cleaning step on spirals, before dewatering and storage. The two hematite concentrates are shipped to sinter and pellet plants worldwide.

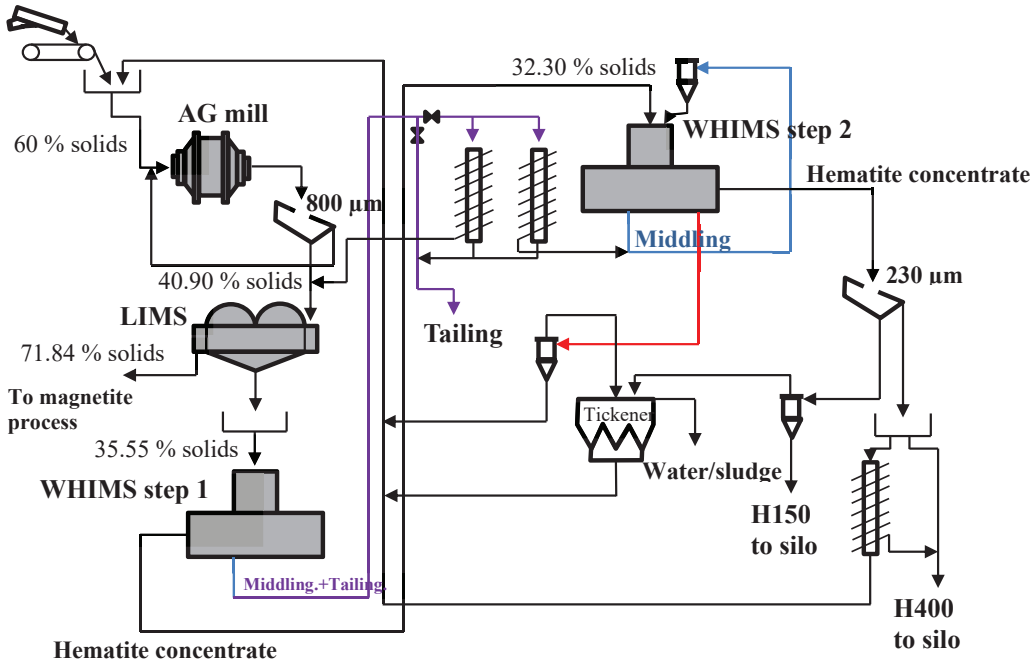

Figure 1: Flowsheet of the hematite production line at RG modified after Rune Johansen (2014).

2.3 Geometallurgy

The term geometallurgy was likely introduced by McQuiston and Bechaud (1968) (as cited in Hoal, 2008), describing the need for knowledge about variations in a deposit, requiring both geological and metallurgical information (Hoal, 2008). After a period where the holistic view of geometallurgy was of less concern during the 20th century, there was a resurgence of geometallurgy at the end of the 20th century (Jackson et al., 2011), with the introduction of courses in geometallurgy and mineral characterisation at major universities in South Africa (Universities of Johannesburg and Cape Town), western Australia, Tasmania, Canada (McGill), and Chile (Universidad Católica), the United States (Colorado School of Mines) (Hoal, 2008). More recently a specialisation in Geometallurgy in the master program Geology at the Norwegian University of Science and Technology was started (Geoforskning, 2018). Due to the low-grade and complexity of available ore deposits and the increasing demand for metals, the field of Geometallurgy has experienced a relatively fast evolution over the last decades (Jackson et al., 2011; Lund, 2013; Bradshaw, 2014). The advancement in analytical techniques and analytical measurements like automated mineralogy enabling fast information about modal mineralogy and mineral liberation has greatly contributed to this development (Gottlieb et al, 2000; Petruk, 2000; Gu, 2003; Moen, 2006; Røisi and Aasly, 2018).

The requirement of collaboration between relevant disciplines is the central theme in the concept of geometallurgy, even though the definitions of the term has a wide range (Jackson et al., 2011). From the narrow view where, similarly to process mineralogy, geological information connected to specific ore types are connected with metallurgical performance, with limited or no spatial characterisation (Helle et al., 2005; Jackson et al., 2011), to the broadest view where the goal is to improve the economic value of a mining operation by combining geology, material characterisation, mineral processing, marketing, and environmental management into a 3D model (Dunham and Vann, 2007; Jackson et al., 2011). The most common definition as stated by Jackson et al. (2011) is where a predictive spatially based geometallurgical model is developed for mineral processing plants by combining chemical, mineralogical, and textural information with metallurgical information of a mineral deposit (Lamberg, 2011). The aim of geometallurgy is to minimise the operational and technical risks and maximise the Net Present Value (NPV) of a mineral deposit (SGS, 2019).

The geometallurgical model requires the development of a geometallurgical program, which consists of several steps of collecting information about the geology, sampling, metallurgical testing, lab testing, defining ore types or geometallurgical domains, and plant simulations among other things (Dobby et al., 2004; Bulled and McInnes, 2005; David, 2007 as cited in Lamberg, 2011). The challenge with the metallurgical testing is that the information collected from a small number of samples and drill cores might be inadequate, as they should represent large tonnage of ore. Hence, the tests should be inexpensive, fast, and preferably fully automated, in order to make it feasible to test larger number of small samples (Lamberg, 2011). Ore types or geometallurgical domains (Lund, 2013) are defined based on ore characteristics known to affect mineral processing, like mineralogy, texture, grain size (Lotter et al., 2011) and surface hardness (Hunt et al., 2013). The most important ore characteristics with regards to metallurgical performance will differ depending on the deposit (Lamberg, 2011), therefore it is important to identify the key performance indicators (KPIs) affecting the metallurgical performance for that specific deposit (Lang et al., 2018a). Lamberg (2011) emphasised the importance of investigating the particles generated during comminution for creating a particle breakage model, and through metallurgical testing create a unit process model which can predict the behaviour of different particles in separation processes. This was proposed as an addition to the geometallurgical program to strengthen the link between geology and metallurgy (Lamberg, 2011).

Geometallurgical work has to a large extent focused on metalliferous ores like porphyry gold deposits in South-America (Leichliter et al., 2011), IOCG deposits (Hunt et al., 2011), uranium deposits (Pownceby et al., 2011, 2014; Bowell et al., 2011), iron oxide Cu-U-Au-Ag deposit in Australia (Ehrig et al., 2012), and porphyry copper-gold-molybdenum deposit in Alaska (Gregory et al., 2013). However, a rising awareness of geometallurgy in academic institutions and the mining industry has led to numerous studies concerning geometallurgy or process mineralogy of ore deposits or industrial mineral operations in Scandinavia (Lund, 2013; Hestnes, 2013; Aasly and Ellefmo, 2014; Bunkholt, 2015; Niiranen, 2015; Lishchuk et al., 2015a, 2015b; Lishchuk et al., 2016, Lishchuk, 2016; Lang et al., 2018a, 2018b; Mena Silva, 2018; Tøgersen et al., 2018). Nevertheless, most of the geometallurgical studies of iron ore operations, are concerned with the high-grade magnetite-apatite ores in Northern Sweden (e.g. Lund, 2013; Lamberg, 2011; Lamberg et al., 2012, 2013; Niiranen, 2015; Lishchuk et al., 2015a, 2015b; Lishchuk et al., 2016; Lishchuk, 2016) and South- Australia (McNab et al., 2009).

2.4 Process mineralogy

Process mineralogy can be an integrated and important part of geometallurgy, and connects mineral characterisation with metallurgical response (Hoal, 2008). The border between the two disciplines are not strict neither technologically nor scientifically, and together with applied mineralogy the definitions of the three disciplines often overlap (Malvik, 2014). Process mineralogy was defined by Henley (1983) and Jones (1987) as cited in Bradshaw (2014), and Petruk (2000) as:

> *"the practical study of minerals associated with the processing of ores, concentrates, and smelter products for the development and optimisation of metallurgical flow sheets"*

However, this definition is restricted to metallic ores only, as are several alternative definitions of process mineralogy. Research by e.g. Watne (2001), Moen (2006), Aasly (2008), Hestnes (2013), Bunkholt (2015), Lang et al. (2018a, 2018b) has shown that process mineralogy is important in industrial mineral operations as well as in metallic ores operations. Malvik (2014) provides a broader definition which applies to all materials from mineral production industry (aggregates, dimension stone, industrial minerals, etc.).

> *"Process mineralogy relates the physical, chemical, mineralogical, and textural properties of the mineral raw materials to their behaviour in the process, to product quality, and the utilisation of the mineral products"*

This definition provides more detail about which type of information should be gathered from the raw material. Process mineralogy has increasingly become more important in mineral processing over the last two decades (Malvik, 2014). As for geometallurgy the increased activity in process mineralogy was enabled by the technological advances in analytical measurements throughout the 1900s. From the early realisation that knowledge of economic geology was important to mining engineers and metallurgist (Irving, 1906 as cited in Bradshaw, 2014), and the developments of methods for testing ore properties like the Bond mill index (Bond, 1952). Up until the early 1980s where Lotter et al. (2011) emphasises (1) the development of automated mineralogy, with Quantitative Evaluation of Scanning Electron Microscopy (QEM*SEM), and Mineral Liberation Analyser (MLA), and (2) the awareness that mineral processing and mineralogy are inevitably linked, as two important breakthroughs in the field of process mineralogy. More extensive reviews of the development and history of process mineralogy can be found in e.g. Baum et al. (2004) and Malvik (2014). A wide variety of analytical methods like Rietveld XRD, surface hardness measurements, SEM, automated mineralogy etc. has enabled a greater understanding of mineralogical and textural differences in a deposit (Hoal, 2008).

Lotter et al. (2011) emphasises the importance of metallurgical test work together with quantitative mineralogical analyses when diagnosing or optimising an existing process or developing a flowsheet for a new process. Investigation of mineralogical characteristics that affect mineral processing parameters can be conducted by sampling areas in a mine known to have different metallurgical performance (Lotter et al., 2011). Pilot circuits are powerful research tools in this respect. While the pilot circuit developed in this research was fixed and investigation of variations in the iron ore was the focus, several other studies use pilot circuits to optimize an existing, or indeed develop a new processing plant (e.g., Miller, 1991; Dandois et. al, 1998; An et al., 2009). Miller (1991) used results from lab work and a pilot plant to design a processing plant for a medium grade iron ore from the Pilbara region in Western Australia. The focus of the development of the processing plant flowsheet was to test different gravity separation equipment on the ore. Initial geological investigations were also included (Miller, 1991). Seppälä et al. (2016) developed a dynamic simulator using the HSC Chemistry® sim (Coleman and Lamberg, 2010) for the mini-pilot plant at Oulu Mining School (OMS). The main operations in the mini pilot plant in OMS are comminution and flotation, with a set-up that can be altered to accommodate different types of sulphide ore. Mineralogical information, process operating parameters and physical ore characteristics are combined by the simulator to provide

better control over the pilot plant (Seppälä et al., 2016). Seppälä et al. (2016) carried out experiments on both open and closed flotation circuits and demonstrated that sulphide ore variations affected grades and recovery from the mini-pilot plant.

Recent research has focused on the practical use of process mineralogy in mining operations through developing easy methods for testing drill cores (e.g. Hunt et al., 2013, Mwanga et al. 2015), or defining ore types or key operation parameters in the raw material related to processing behaviour (e.g. Lund, 2013; Hestnes, 2013; Bunkholt, 2015; Tøgersen et al., 2018). Since analyses of grades might not be sufficient for estimating recovery in complex ores, and with the decreasing of grade in available ores, process mineralogy will become increasingly important in the future (Bradshaw, 2014; Parian et al., 2015).

3 Materials and methods

3.1 Materials

This thesis follows the principles described in Lotter et al. (2018), which defines a sample as a representative part of a lot (area in a deposit or a sampling point in a processing plant), and increments as individually sampled parts of the sample, i.e. when the same sample point in a processing plant is sampled over time, each sampling represents an increment of the sample.

3.1.1 Sampling of deposits in the Storforshei IF

If there are mineralogical and textural differences within and between deposits, as is the case for Storforshei IF, larger samples are needed to obtain representative and reliable results improving the prediction and evaluation of grindability (Van Tonder et al., 2010). A total of four deposit samples from Kvannevann, Stensundtjern, and Stortjønna were collected from blasts near the geographical centre of each of the deposits. The Kvannevann and Stortjønna deposits were selected for sampling based on previous experience where differences in metallurgical performance were observed between the deposits, while the Stensundtjern deposit is a new prospect for future production and was selected with the desire to gain more knowledge about this deposit prior to production. An important consideration in the sampling was to avoid the edges of the deposits, to avoid typical edge lithologies like garnet mylonite (Tøgersen et al., 2018) being overrepresented, and ensure that the sample was representable for the deposit. Figure 2 shows an overview map of Norway where the location of the Dunderlandsdalen valley is marked, while the geology of the Dunderlandsdalen valley is displayed in the geological map in the figure, where the location of the three deposits, Kvannevann, Stensundtjern, and Stortjønna are marked.

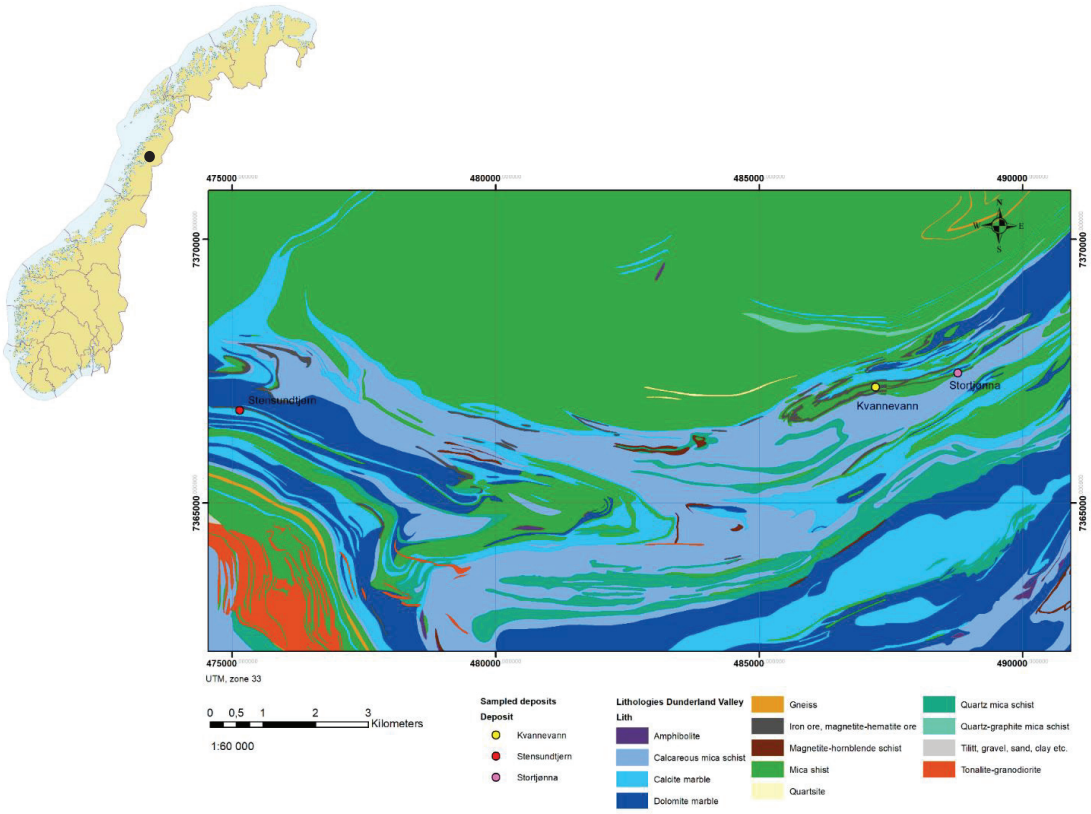

Figure 2: The overview map of Norway (top left corner of the figure) is modified from Geonorge (2019), the black dot indicates the location of the Dunderlandsdalen valley. The geology of the Storforshei area is shown in the geological map (on the right in the figure), which shows the location of the hematite-magnetite iron ores in the Storforshei IF. The geology is compiled from Søvegjarto et al. (1989) and Gjelle et al. (1991). The locations of the three deposit samples are marked.

Two deposit samples were collected from the Kvannevann deposit: Kvannevann 1 was used during the testing and development of the pilot circuit, while Kvannevann 2 was used in the resulting pilot circuit, with the same settings as for the Stortjønna and Stensundtjern deposit samples. Both of the Kvannevann deposit samples were collected from the underground mine at 155 m.a.s.l., where drift development (across the orebody, NNW-SSE) were conducted at the time, and as such the sampling had to be adjusted according to the production plans. The samples were collected from short-hole blasts during drift development. Some considerations could be made concerning the sampling point, for instance areas known to have different composition than the "normal" Kvannevann ore was avoided. Figure 3 shows a geological map of the main part of the Kvannevann deposit with the locations of the deposit samples and the starting point for one of the drill holes in which surface hardness was measured by Equotip. The Kvannevann 1 deposit sample corresponds to the point called 155-33, while the

Kvannevann 2 deposit sample corresponds to the point called 155-49. The first number refers to the level (155 m.a.s.l.) and the second to the drift number (33 and 49).

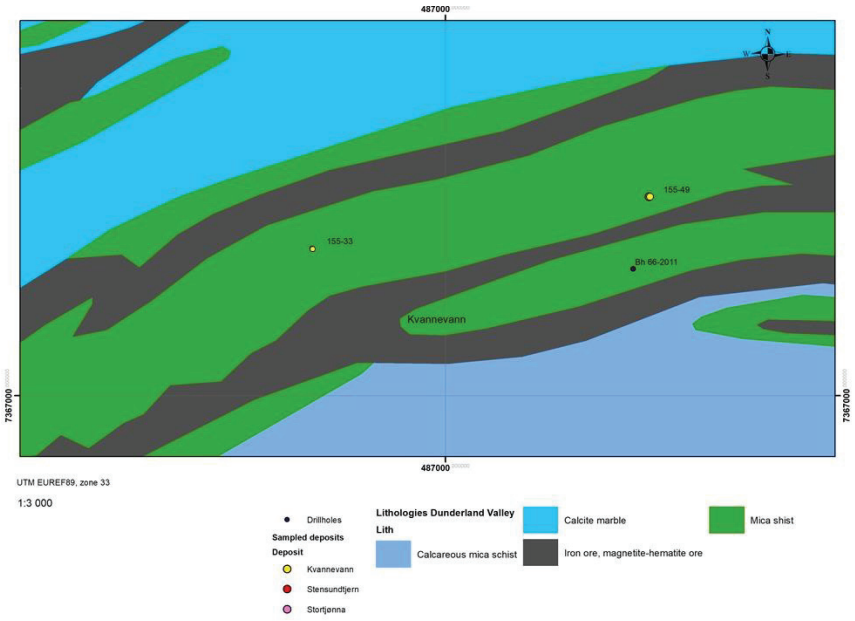

Figure 3: The geology of the Kvannevann deposit area. The geology is compiled from Søvegjarto et al. (1989). The locations of the two deposit samples are marked in yellow, while the access point for one of the drill cores where surface hardness by Equotip were measured is marked in dark blue.

The Stensundtjern deposit sample had to be collected from the surface as the deposit has never been in production. There was only one possible sample location as the deposit is largely covered with vegetation, fortunately is was located in the geographical centre of the ore body, and the edges could be avoided. The Stensundtjern deposit and the surrounding geology is shown in Figure 4. The Stortjønna deposit sample was collected from the old open pit approximately 30-35 meters deeper relative to the surface in the area. The location of the deposit sample, access points to drill cores were surface hardness was measured by Equotip, and the surrounding geology are shown in Figure 5.

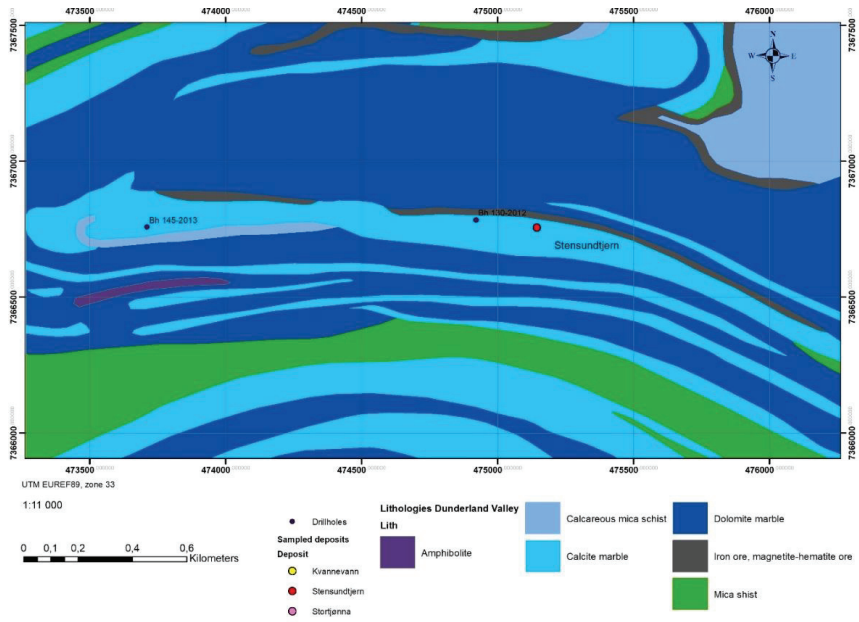

Figure 4: The geology of the Stensundtjern deposit area. The geology is compiled from Søvegjarto et al. (1989). The location of the deposit sample is marked in red, while the access point for the drill cores where surface hardness by Equotip were measured are marked in dark blue.

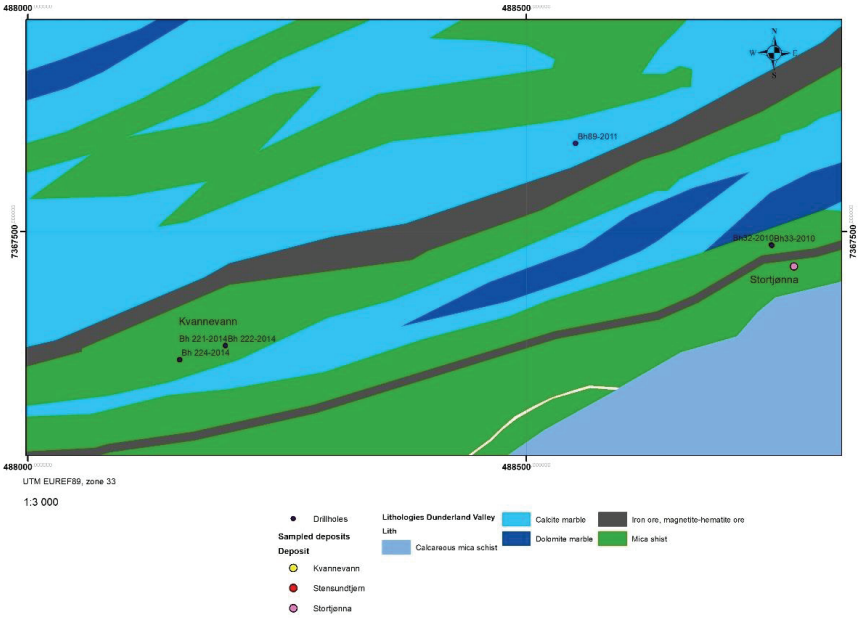

Figure 5: The geology of the Stortjønna deposit area, and part of the Kvannevann deposit area (located west in the map). The geology is compiled from Gjelle et al. (1991). The location of the deposit sample is marked in red, while the access point for the drill cores where surface hardness by Equotip were measured are marked in dark blue (two drill cores in the Stortjønna deposit, and three in the Kvannevann deposit).

In Figure 3-5 the points marking the locations of the deposit samples and access points for the drill cores are not located in the hematite-magnetite ore. This could for the Kvannevann deposit samples (Figure 3), be partly due to them being from the underground mine, although it is not likely that the distance should be as large as it is since the ore body has a steep dip (e.g. Ellefmo, 2005). The Stensundtjern and Stortjønna deposit samples should also be located in the hematite-magnetite ore, as they were collected from the surface. According to the drill core logs, the drilling started in side rock, although for most of the drill cores only the first 5-10 meters consist of side rock. The mismatch between the hematite-magnetite ore and the locations of the deposit samples and access points of the drill cores are likely caused by inaccuracies in the 1:50 000 maps of Søvegjarto et al. (1989) and Gjelle et al. (1991) from which the geological maps in Figure 3-5 is modified. The accuracy of the Garmin GPSMAP 64s used to measure the Stensundtjern and Stortjønna deposit samples is +/- 15 meters 95 % of the time, but in general the accuracy is even higher +/- 5-10 meters (Garmin, 2019). The access points of the drill cores and the deposit samples from Kvannevann were measured with the GPS on the drill rig or a total station, which have the same or higher accuracies than a Garmin GPSMAP 64s.

3.1.2 Sampling from primary crushing of the deposit samples

About 40 tonnes from each of the blasts from the three deposits were collected and crushed on site in a mobile jaw crusher (Figure 6). Samples of 1-2 tonnes were collected into big-bags from the entire width of the discharge from the conveyer belt connected to the mobile jaw crusher, in 3x10 sec intervals (Figure 7), for each of the deposit samples Kvannevann 2, Stensundtjern, and Stortjønna. The Kvannevann 1 sample was crushed in a separate campaign on another mobile jaw crusher and the crushed sample was quartered to collect a representative split for the testing of development of the pilot circuit.

Figure 6: The mobile jaw crusher used to crush the sampled blast from the Kvannevann deposit.

Figure 7: The sampling of the conveyer belt from the mobile jaw crusher by wheel loader with big-bag. Each sample was collected at 3x10 sec intervals. The entire width of the stream was sampled.

The crusher output from the four deposit samples were quartered to c. 100 kg increments for PSD analyses (Figure 8).

Figure 8: The crusher output from Kvannevann 1 deposit sample during the quartering to get a representative split for PSD analysis. This was repeated for the crusher output from the Kvannevann 2, Stensundtjern, and Stortjønna deposit samples.

The PSD of the crusher output for the four deposit samples is shown in Figure 9. The d_{50} of Kvannevann 1, Kvannevann 2, Stensundtjern, and Stortjønna are 7 mm, 10 mm, 38 mm, and 100 mm respectively.

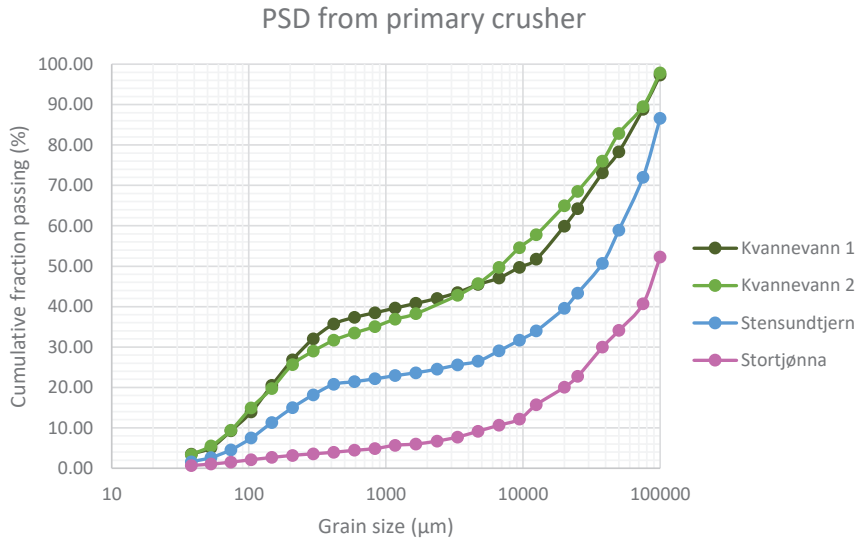

Figure 9: Particle size distribution of the primary crusher outputs for Kvannevann 1, Kvannevann 2, Stensundtjern, and Stortjønna.

3.1.3 Sampling from the pilot circuit and the full-scale processing plant

During operation of the pilot circuit only one output was sampled: the mill circuit product. All the other outputs were collected in their entirety after the operation was completed and split down to suitable size for further analyses. In paper III the mill circuit product, hematite concentrates H150 and H400, and the final tailings were sampled at three different dates in the

full-scale mineral processing plant at RG. The increments were collected from automatic samplers. Further description of sample preparation is given in the papers.

3.2 Methods

This section provides background information of some of the methods used in this research, details about the methods, sample preparation, and equipment used are described in the papers.

3.2.1 Geological mapping and core logging

Geological mapping was conducted with the aim of identifying variations in the iron ore in the three deposits Kvannevann, Stensundtjern, and Stortjønna. Most of the geological mapping was done on the surface, as the operations in the underground mine made it challenging to work there. Thus, only limited mapping was done in the underground mine. The geological maps (Søvegjarto et al., 1989; Gjelle et al., 1991) and ore deposit models accessible at RG were studied in addition to the geological mapping prior to sampling the deposits to ensure that the sampling of the deposits were conducted away from edges of the deposits and would be as representative of the deposits as possible. Core logs and locations were examined prior to selecting the drill cores to measure surface hardness on. The selected drill core sections were logged prior to surface hardness by Equotip being measured. Both to establish the relationship between the ore lithologies defined by RG and the ore types defined in this research, and to ensure that the sections measured were actually the desired ore type to be tested.

3.2.2 Primary crushing

The four deposits samples were crushed on mobile jaw crushers in open circuit. The same mobile jaw crusher with the same settings yielding products < 30 cm, was used for the deposit samples from Kvannevann (Kvannevann 2), Stensundtjern, and Stortjønna. The Kvannevann 1 deposit sample was crushed on another mobile jaw crusher, however, this crusher also yielded a crusher output < 30 cm. Both crushers were set up to produce aggregates.

3.2.3 Development of the pilot circuit

The main objective when designing the pilot circuit was to identify variations in metallurgical performance, related to ore mineralogy and texture, surface hardness, and liberation between the three deposits. Hence, the pilot circuit was fixed, i.e. no process optimisation was attempted. The pilot circuit was constructed to work as a simple, stable, and reproducible process, with the purpose to easily provide outputs displaying the variations between the three different deposits. The circuit was semi-continuous, which ensured less manual material handling, and lower potential for contamination.

3.2.3.1 *The pilot circuit set-up*

The main operations in the hematite production at RG is closed circuit autogenous (AG) milling, with screens, low intensity magnetic separation (LIMS) and two steps of wet high intensity magnetic separation (WHIMS). In the pilot circuit set-up some simplifications were made, as the full-scale mineral processing plant is more complicated than what is feasible for a pilot circuit. For instance, middling and tailing from the two WHIMS-steps are returned in the full-scale mineral processing plant, which was not feasible to include in the pilot circuit as only one pilot WHIMS was available. For practical reasons gravity separation was not a part of the pilot circuit. The hematite concentrates from WHIMS step 2 was initially sieved on a 230 µm Sweco screen, however, this step was abandoned as it does not affect the overall hematite recovery or Fe grade. Figure 10 shows the flowsheet of the constructed pilot circuit.

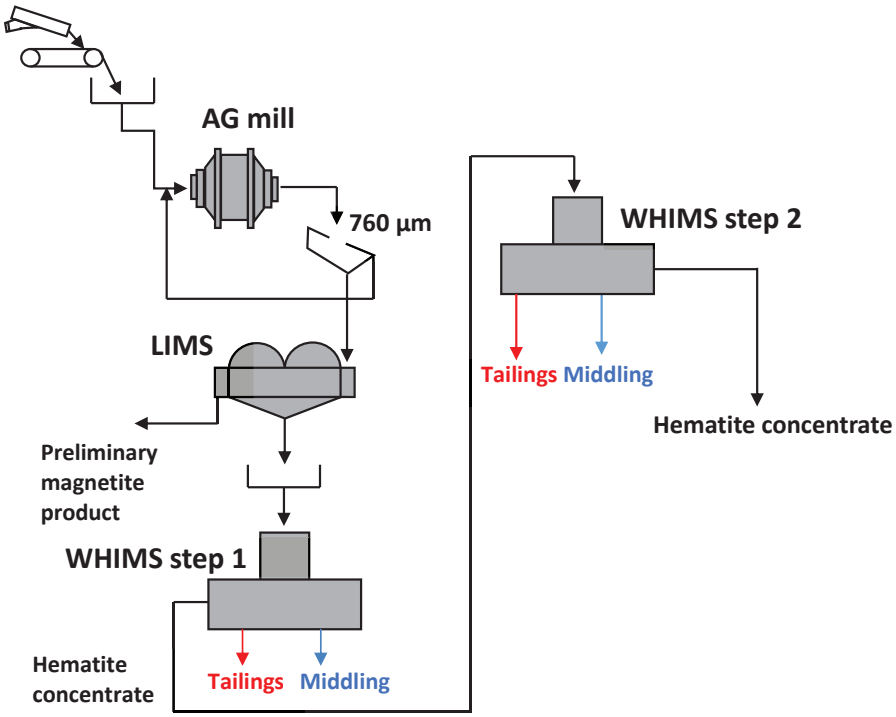

Figure 10: The pilot circuit flowsheet.

3.2.3.2 *Equipment*

The AG mill was 0.8 m long, with an inner diameter of 0.69 m, and a critical speed of 50.5 rpm. Initial settings for the AG mill were based on the mill dimensions and capacity, in addition to experience from previous mill tests performed at NTNU (Sandvik et al., 2012). The AG mill was operated at 36 rpm, 71.2 % of critical speed, and held about 250 kg (solids + water). A

Sweco screen of 760 µm was used in the closed mill circuit. A Sala LIMS single drum separator, with 62 cm drum diameter and 22.8 cm drum width, and a WHIMS Jones P40 (WHIMS) from Coal & Minerals Technology GmbH, Köln, Germany, manufactured in 2013, was used for magnetic separation. In the WHIMS, three outputs were washed out, tailings inside the magnetic field, middling at the edge of the magnetic field, and hematite concentrate outside the magnetic field. Figure 11 shows the AG mill, LIMS and the WHIMS used in the pilot circuit.

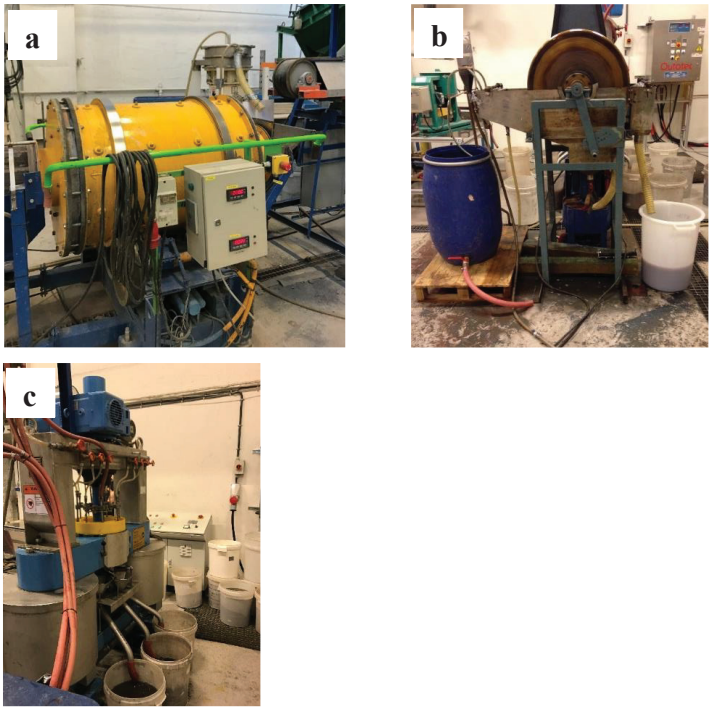

Figure 11: The AG mill (a), LIMS (b) and WHIMS (c) used in the pilot circuit.

3.2.3.3 AG milling

Based on RG's settings in the full-scale mineral processing plant, the pulp thickness in the pilot circuit AG mill was set to 60 wt % solids. During the initial AG mill test with the Kvannevann 1 deposit sample, the solid feed rate was increased from 120 kg/h to 240 kg/h due to rapidly decreasing mill charge with 120 kg/h solid feed rate, and hence, not achieving steady state milling. With 240 kg/h solid feed rate the decrease in mill charge slowed, but the feed material ran out before the mill reached steady state. When milling the Kvannevann 2 deposit sample the solid feed rate was increased to 266 kg/h, and the mill quickly reached steady state. The Stensundtjern- and Stortjønna deposit samples had solid feed rates of 150 kg/h and 100 kg/h,

respectively. The pilot circuit was operated for 3.5 hours with the Kvannevann deposit sample, 3.33 hours for the Stensundtjern deposit sample, and 5.5 hours for the Stortjønna deposit sample.

3.2.3.4 Low intensity magnetic separation

During the initial tests of the pilot circuit, the pump sending material from the LIMS to the WHIMS was identified as a bottle neck. The capacity challenge of the pump was to some degree solved by a frequency converter, which enabled higher speed in the pump, in addition to constructing a splitter that divided the mill circuit product or feed LIMS stream into three equal parts (Figure 12). The splitter enabled reduction of the feed LIMS steam, when needed, to prevent the pump from overflowing. In situations where a reduction in feed LIMS was required, excess material was temporarily stored and sent through the LIMS and WHIMS after the main flow in the pilot circuit was terminated.

Figure 12: The "Mozell"-splitter, constructed on site, was placed on the LIMS feed.

3.2.3.5 Wet high intensity magnetic separation

Material from the full-scale mineral processing plant (feed LIMS) was used for testing of the pilot WHIMS. Based on previous work with iron ore on the pilot WHIMS by Kleiv (2014), the coil current was 0.95 A in the first step and 0.7 A in the second step. In the full-scale mineral processing plant, the magnetic flux density in WHIMS step 2 is adjusted between 0.59 - 0.635 T depending on variations in the material. Thus, it was decided that the material from Kvannevann 2, Stensundtjern, and Stortjønna should be tested at three different coil current settings in the WHIMS step 2. The Fe_{tot*} values of hematite concentrate from WHIMS step 2 at 0.7 A (three increments from the initial testing rounds in the pilot WHIMS), were compared with the Fe_{tot*} values of eight increments from the H150 and H400 concentrates from the full-scale mineral processing plant set at 0.6 T (Table 4).

Table 4: The Fe_{tot*} contents in hematite concentrate from the pilot circuit WHIMS step 2 at 0.7 A, and from the hematite products H150 and H400 in the full-scale mineral processing plant at 0.6 T.

Increments	Average Fe_{tot*} (wt %)
Hematite concentrate WHIMS step 2 pilot circuit (0.7 A)	62.78
H150 and H400	62.96

Based on these results the two other settings for the WHIMS step 2 was set to 0.6 A and 0.8 A. The pilot WHIMS have a current range from 0-10 A. Thus, it was important to ensure that the chosen settings actually gave differences in the magnetic field strength. The magnetic flux density in the pilot WHIMS was measured with a Hirst GM04 Gauss meter. Figure 13 shows the details of the pilot WHIMS. The blue blocks on either side are the magnetic pole pieces. The measurements were taken at feed-, concentrate-, tailings- and middling washing tubes, inside the grooves in the plate boxes (Figure 13).

Figure 13: Details from the pilot WHIMS. The magnetic pole pieces are the blue blocks on either side (a). The measurements, with the Gauss-meter, were conducted inside the grooves at the position of the flushing and feed tubes (b).

The magnetic field was measured for a range of coil currents, from 0.5 A to 0.92 A. The maximum magnetic flux density value for each point was used. The results show a positive correlation between coil current and magnetic flux density (Figure 14). The effect of varying the current on the field measured at the concentrate tube is negligible.

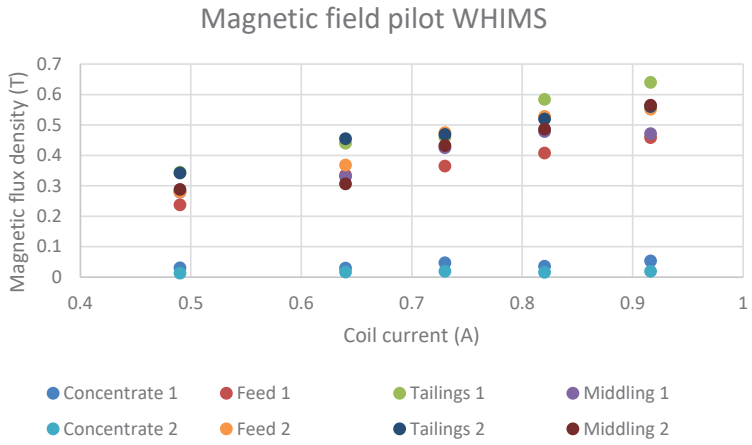

Figure 14: Measurements of magnetic field in the pilot WHIMS.

3.2.4 Chemical analyses

3.2.4.1 X-ray fluorescence

X-ray fluorescence (XRF) is used in various applications from geological and environmental studies, to material science and semiconductor characterisation. The principle is that when a sample is hit by the X-ray radiation an incident photon excites an inner-shell electron, and a fluorescence photon is emitted. Each transition of other-shell electron to fill the vacancy in the inner-shell gives the emitted photon a specific energy. The fluorescence radiation emitted is characteristic for each element enabling identification of the elements in the sample analysed. The intensity of the fluorescence radiation provides the concentration of an element. Usually the quantification in an XRF analysis is based on standards created from samples with similar composition to the sample being analysed (Beckhoff et al., 2009). A Bruker S8 Tiger XRF was used for the analyses conducted in this research, with detection limits down to ppb-level (Bruker, 2009). The non-standard program *Quant Express* was used for the analyses. However, results from testing the same ten samples with both the XRF analysis and the titration method at RG gave a good correlation (described in section 4.3.1). The reproducibility of the XRF analyses and the sample preparation was investigated and are presented in section 4.3.2.

3.2.4.2 Titration analyses at RG

The titration method conducted at RG (as described in their internal procedure) follows the ISO 2597-1: 2006 standard (ISO, 2006) and the ISO 2597-2:2019 (ISO, 2019). The procedure starts with dissolution and boiling of increments in hydrochloric acid, in addition to potassium hydrogen fluoride, creating hydrofluoric acid, which will dissolve the silicates. The remaining

liquid contain ions of Fe^{2+} and Fe^{3+}. To oxidise all Fe to Fe^{3+}, potassium permanganate is added, while tin chloride is used to reduce all Fe^{3+} to Fe^{2+}. In the last stages of the reduction the tin chloride is replaced with titanium chloride. Since the solution containing Fe^{2+} ions are not stable, and some of the Fe^{2+} ions in time will oxidise to Fe^{3+}, perchloric acid is added to slow this process. The titration oxidising Fe^{2+} back to Fe^{3+} is then conducted by adding potassium dichromate. The results are measured against certified standards. Mohassab et al. (2016) tested the titrimetric method described above and found an accuracy of 0.02 %.

3.2.5 X-ray diffraction

X-ray diffraction (XRD) is used to determine a number of chemical and physical characteristic in materials. It is a non-destructive analytical method, which can be applied for analysing crystallographic texture, phase analysis including types and quantities of phases present, macro-stress, macro-strain, electron radial distribution functions, and crystalline size (Will, 2006). The results of electron atoms interacting with X-rays is the X-ray diffraction. If the path rays of two diffracted rays differ by an integral number of wavelengths, the interference between the scattered rays are constructive. This is dependent on the atomic arrangement. Bragg's law describes this selective condition (Equation 1).

$$2d_H \sin\theta_H = n\lambda \qquad \text{Equation 1}$$

The Bragg angle (θ_H) is the angle between incident and reflected beam, λ is the wavelength, d_H is the d-spacing, and H is the Miller indices triplet hkl for each lattice plane. X-rays, synchrotron radiation, and neutrons are the three sources of radiation important for XRD (Will, 2006). In this research the XRD was used for quantitative mineral characterisation, and X-rays was the source of radiation. The Bruker software EVA® was used for the mineral characterisation (Madsen et al., 2001; Scarlett et al., 2001), while the mineral quantification was conducted with Rietveld refinement with the TOPAS software (Rietveld, 1967, 1969; Bruker, 2019). The XRD has a general detection limit of 1 wt % (Madsen et al., 2001; Scarlett et al., 2001; Hestnes et al., 2013).

3.2.6 Scanning electron microscopy

The scanning electron microscopy (SEM) is a powerful instrument used in a range of disciplines within material- and life science (Bogner et al., 2007), and is used for image and analyses of specimens. A Schottky, Thermionic, or field-emission cathode (electron gun) send an electron beam towards an anode. The acceleration of the electrons depends on the voltage difference between the cathode and the anode, the difference range between 0.1 kV and 50 kV. The beam is focused through an electron lens system (Reimer, 2013), and the specimen is scanned along

a parallel line pattern. The impact between the incident electrons and the specimen generates various signals, among others back-scattered electrons (BSE) and X-rays (Bogner et al., 2007). Information on topography, mass thickness, crystallography and the specimen composition may be conveyed by the BSE signal. For a flat specimen without topography, compositional differences in the specimen can be observed as variations in the BSE intensity, which is caused by differences in atomic number in the specimen (Goldstein et al., 2017). The energy of emitted X-rays is characteristic for the element which they were emitted from. The energy dispersive X-ray spectroscopy (EDS) detector measures the energy and the number of X-rays emitted, and provides a qualitative elemental analysis (Bogner et al., 2007). In this research a Hitachi SU-6600 field emission SEM with two Bruker XFlash 5010 EDS was used for point analysis of minerals, and for analysing automated mineralogy together with the NTNU developed prototype software Particle Texture Analyser (PTA) (Moen, 2006). The SEM used has magnification from 10-600,000X, resolution from 1.2 nm at 30 kV to 3 nm at 1kV, and accelerating voltage from 0.5 kV to 30 kV (NTNUa, 2019). The SEM was operated with 20 kV acceleration voltage, 15 mm working distance, and at magnifications between 45X and 500X. The thin sections and polished section analysed was coated with carbon prior to the SEM analyses.

3.2.7 Electron Probe Micro Analyser

The electron probe micro analyser (EPMA) uses the same principles as a SEM. However, the EPMA is equipped with a wave-length-dispersive spectroscopy (WDS) detector, enabling quantitative elemental analyses of particles or minerals as small as 1-2 µm (Goodge, 2018). In this research a JEOL JXA 8500 Hyper probe EPMA, with detectable element range between 4^{Be} and 92^{U}, resolution of 3 nm at 30 kV, and magnification from 40-300,000X (NTNUb, 2019), was used to obtain mineral chemistry for increments collected in the full-scale mineral processing plant. The thin sections analysed in the EPMA was coated with carbon prior to the analyses. The EPMA was operated with an acceleration voltage of 20kV and a working distance of 15 mm.

3.2.8 Surface hardness measurements

The surface hardness was measured by Proseq Type L Original Schmidt hammer on boulders, and by Proseq Type D Equotip 3 on drill cores. The principles of both the Schmidt hammer and Equotip are described in paper I.

4 Results

4.1 Overview of results

The results chapter is divided into two parts: in the first the results and key findings from the papers are presented, while the second part consists of additional results of which not all are presented in the papers.

4.2 Results from papers

4.2.1 Paper I "Mineralogy and texture of the Storforshei iron formation, and their effect on grindability"

Marte Kristine Tøgersen, Rolf Arne Kleiv, Steinar Ellefmo, and Kurt Aasly

(published in Minerals Engineering, 125, pp. 176-189)

In this paper, six ore types with mineralogical and textural differences were defined: Specular-Hematite, Granular-Hematite, Hematite-Magnetite, Magnetite-Ore, Mylonitic-Hematite and Massive-Hematite. The differences between the ore types can clearly be recognised in hand specimens, and even more so under the petrographic microscope.

Specular-Hematite and Granular-Hematite are both banded, with alternating hematite- and quartz rich layers. The layers are folded in Specular-Hematite, while they are more planar in Granular-Hematite. The hematite grains have tabular shapes with straight grain boundaries in both Specular-Hematite and Granular-Hematite. However, the hematite texture in Granular-Hematite is sugar-grained, while it is flaky in Specular-Hematite. The average hematite grain size is 400-500 µm in Specular-Hematite and 200 µm in Granular-Hematite.

Hematite-Magnetite is dominated by hematite occurring either flaky as in Specular-Hematite, or sugar-grained as in Granular-Hematite. In some cases, the Hematite-Magnetite is banded with folded layers. The magnetite content in Hematite-Magnetite ranges from 1-2 % in the Kvannevann specimens, to 9-10 % in the Stensundtjern specimens. The magnetite grains are equant-irregular shaped, have irregular grain boundaries, and have an average grain size of 1 mm. Hematite grains are tabular-shaped, with straight grain boundaries, and an average grain size of 300 µm. Magnetite-Ore is dominated by coarse-grained magnetite with an average grain size of 0.5 cm and contains < 3 % hematite. Similar to the Hematite-Magnetite ore type, the hematite has tabular grain shape with straight grain boundaries, while the magnetite has equant-irregular shape, with irregular grain boundaries.

Mylonitic-Hematite consist of a fine-grained matrix of quartz, hematite, calcite, mica, garnet and epidote, with disseminated grains (10-20 μm) of hematite, quartz and calcite. Fine-grained recrystallised hematite and gangue minerals fills cracks in remnants of larger hematite grains (200-500 μm). The few grain boundaries observed are irregular. Massive-Hematite is another fine-grained ore type, consisting of massive hematite and folded veins of fine-grained gangue consisting of quartz, calcite, garnet, epidote, and mica.

The surface hardness of the ore types was measured using the Schmidt hammer and Equotip, which are simple, fast, and inexpensive methods. Surface hardness by Schmidt hammer was measured on boulders, while surface hardness by Equotip was measured on drill cores. A link between grain size and -boundaries, and surface hardness was determined, where fine-grained ore types with irregular grain boundaries have higher surface hardness values than coarse-grained ore types with straight grain boundaries. The ore types were divided into three groups based on the surface hardness values: low hardness (Specular-Hematite and Granular-Hematite), intermediate hardness (Hematite-Magnetite and Magnetite-Ore), and high hardness (Mylonitic-Hematite and Massive-Hematite). The Granular-Hematite was further divided into two subgroups, as there was a difference in surface hardness by Equotip values in Kvannevann, compared to Granular-Hematite in Stensundtjern and Stortjønna. The difference was attributed the a relatively larger content of quartz in Stensundtjern and Stortjønna, resulting in the subgroups: high quartz Granular-Hematite (Stensundtjern and Stortjønna) and low-quartz Granular-Hematite (Kvannevann).

The relative distribution of the ore types in the Kvannevann, Stensundtjern, and Stortjønna deposits was determined using drill core logs, where the ore lithologies previously logged by RG were compared visually to the ore types defined in this research. The ore lithology categories used by RG are generally broader than that of the ore types defined in this research. For instance, Specular-Hematite and Granular-Hematite is not differentiated in the RG drill core logs, they are grouped together into “Hem_ore”. However, in some cases there is an extra note in the comment sections of the log where the hematite texture is described (specular or granular). In some of the older logs there are only two lithologies: ore and side rock. Thus, newer logs were used to establish the relative distribution of the ore types in the three deposits Kvannevann, Stensundtjern, and Stortjønna. All drill cores where surface hardness by Equotip were measured, were logged with regards to the ore types defined in this research prior to measuring. Specular-Hematite and Granular-Hematite dominate both Kvannevann and Stensundtjern. There are, however, substantial amounts of Hematite-Magnetite, and Magnetite-

Ore in the Stensundtjern deposit compared to the Kvannevann deposit. Mylonitic-Hematite and Massive-Hematite dominate the Stortjønna deposit. Although these two ore types are not found in the drill core logs from Kvannevann or Stensundtjern, observations in the Kvannevann deposit suggests that these ore types are present in some areas.

The results from the AG milling show that the ore types with coarse-grained iron oxides and straight grain boundaries dominating in the Kvannevann deposit have high throughput (266 kg/h) and low specific energy consumption: thus, a high grindability. The fine-grained ore types with irregular-to-no visible grain boundaries dominating in the Stortjønna deposit, had low throughput (100 kg/h) and high specific energy consumption: thus, a low grindability. The ore types dominating in the Stensundtjern deposit have an intermediate grindability compared to Kvannevann and Stortjønna, with a throughput of 150 kg/h and an intermediate energy consumption.

The results presented in paper I show that the most important textural characteristics affecting surface hardness is grain size and -boundaries, and that it is possible to evaluate grindability based on surface hardness measurements and geological mapping for identification of ore types. Including Equotip measurements as part of the drill core logging is a simple and inexpensive method to improve the grindability evaluation.

4.2.2 Paper II " The effect of hematite liberation and texture on wet high intensity magnetic separation of a low-grade iron ore"

Marte Kristine Tøgersen, Kurt Aasly

(unpublished manuscript)

The differences between the Kvannevann, Stensundtjern, and Stortjønna deposits found in paper I were further investigated in this paper, where the chemistry, mineralogy, and hematite liberation in outputs from the pilot circuit were analysed, with emphasis on the separation in the WHIMS. The Fe_{tot*} distribution in the outputs from the pilot circuit for the three deposits indicate that the magnetic separation is affected by other ore parameters besides Fe_{tot*}. The Stortjønna mill circuit product (SØ-PM) have the highest Fe_{tot*} grades of the mill circuit products, and yet the separation does not yield the highest Fe_{tot*} grades in the hematite concentrates. The losses of Fe_{tot*} to middlings and tailings are substantial compared to the corresponding outputs in Kvannevann and Stensundtjern. The highest Fe_{tot*} in hematite concentrates are found in the Stensundtjern deposit sample, which has intermediate Fe_{tot*} values

in the mill circuit product (ST-PM). Lastly, the Kvannevann deposit sample with the lowest Fe_{tot*} grade in the mill circuit product (KV-PM) gives lower hematite concentrate Fe_{tot*} grades at a similar level as the corresponding outputs in Stortjønna, and low loss of Fe_{tot*} to middlings and tailings.

Non-economic minerals containing Fe or Mn, like epidote, biotite/phlogopite, and hornblende, and dolomite, were found in the hematite concentrates from WHIMS step 1, in addition to middlings and tailings from both WHIMS steps. Given that all middlings and tailings from the WHIMS are returned in the full-scale processing plant, there is a possibility that these minerals will accumulate in the WHIMS circuit and end up in the final hematite concentrate.

The KV-PM and ST-PM have relatively coarse-grained tabular liberated hematite, which is consistent with the hematite texture found in paper I in the ore types Specular-Hematite, Granular-Hematite, and Hematite-Magnetite. The higher Fe_{tot*} in the Stensundtjern hematite concentrates compared to the Kvannevann hematite concentrates are likely due to the higher Fe_{tot*} in ST-PM compared to KV-PM. The relatively larger amount of Fe_{tot*} lost to middlings and tailings in Stensundtjern, compared to the corresponding outputs in Kvannevann can likely be attributed the particle textures in the ST-PM where there are more composite particles consisting of two phases: hematite and a non-economic mineral. This suggest a different ore type distribution in the Stensundtjern deposit sample, with a higher content of the Granular-Hematite and Hematite-Magnetite ore types with slightly finer hematite (200-300 µm), than the Specular-Hematite (400-500 µm).

The SØ-PM contains substantial amounts of composite particles: irregular hematite interwoven with non-economic minerals, and hematite as inclusions in non-economic minerals. The hematite textures are very similar to those observed in the Mylonitic-Hematite, with disseminated hematite in a matrix of gangue minerals, and remnants of hematite grains where cracks are filled with gangue minerals. The liberated hematite in the SØ-PM are equant-irregular shaped, which likely have been formed through random breakage of the Massive-Hematite ore type without grain boundaries for breakage to follow.

The hematite liberation in the Stortjønna outputs are lower than in the Kvannevann- and Stensundtjern outputs. For SØ-PM the hematite liberation is 17.8 % and 11 % lower than the KV-PM and ST-PM, respectively. This is caused by the hematite textures in Mylonitic-Hematite and Massive-Hematite. The low hematite liberation together with the large amounts

of fines in SØ-PM (29 % < 38 μm) is the reason for the lower efficiency of the magnetic separation of the Stortjønna deposit sample.

The results indicate that the hematite recovery is largely affected by hematite liberation and particle textures, and less by Fe_{tot*} content.

4.2.3 Paper III "Fe deportment in non-economic minerals in the Kvannevann iron ore deposit "

Marte Kristine Tøgersen, Steinar Ellefmo, Kurt Aasly

(unpublished manuscript)

The present quality control in RG is based mainly on Fe_{tot*} analyses, with MnO, S_{tot}, Fe_{mag*} (magnetic Fe including magnetite but also pyrrhotite), and the content of alkalis as secondary parameters. However, as several non-economic minerals in the ore can accommodate Fe in their crystal lattice, the Fe_{tot*} does not reflect the amount of Fe located in hematite and magnetite. Thus, Fe_{tot*} can be a misleading quality control parameter without complementing mineralogical information. The aim of this paper was to investigate the relationship between Fe_{tot*}, Fe found in non-economic minerals (Fe_{sil}), and Fe located in hematite and magnetite (Fe_{hem} and Fe_{mag}). Furthermore, how the differences in these parameters affect the present Fe recovery based on Fe_{tot*} and the real hematite recovery based on Fe_{hem}.

Sampling from the full-scale mineral processing plant was conducted at three different dates (three increments). In each increment, samples from mill circuit product (MCP), H150, H400, and final tailings (T) were collected. The chemistry, mineralogy, and mineral chemistry were analysed in all twelve samples, to calculate the Fe_{sil}, Fe_{hem}, and Fe_{mag}. At the time of the sampling the Kvannevann deposit was in production, and the mineral chemistry is expected to be the same throughout this deposit. The increments in the three series generally follows the same trend both in chemical composition, and main mineralogy, although the amounts of the elements and minerals vary. The H400 increments contains less non-economic minerals compared with the H150 increments, with the purest hematite concentrates found in series 3. These chemical and mineralogical variations indicate operational differences during processing and/or differences in ore types distribution in the crude ore. Nevertheless, all hematite concentrates have satisfactory Fe_{tot*} grades.

Aegirine-augite, amphibole, ilmenite, epidote, and biotite are the non-economic minerals accommodating the largest amounts of Fe. The Fe_{sil} was calculated based on the mineralogy and the mineral chemistry. The increments show a similar distribution where the mill circuit products and tailings contain around 1 % Fe_{sil}, while the hematite concentrates range from 0.08-0.56 % Fe_{sil}. The exception is the H150 1 sample which has 1.9 % Fe_{sil}, this is largely caused by the ilmenite content accounting for 0.9 % of the Fe_{sil}. Ilmenite was only detected in this increment. Although observations in the microscope suggest that it is present in more increments, the amounts were not large enough to be detected by the XRD with its detection limit of 1 % (Madsen et al., 2001; Scarlett et al., 2001; Hestnes et al., 2013). Epidote and biotite are the largest contributors to the Fe_{sil} in the hematite concentrates, while quartz, dolomite, and muscovite, although containing small amounts of Fe in their crystal lattice, contributes notably to the Fe_{sil} in the MCP and T increments due to the high content of quartz, dolomite, and muscovite in these increments.

When calculating the hematite recovery ($Rec_{realhem}$) as opposed to the Fe_{tot*} recovery ($Rec_{present}$), which is presently calculated at RG, the recovery increased in all the three series. This is likely caused by the relatively higher Fe_{sil} in the MCP increments. The Fe_{tot*} lost to tailings is not large in either of the T increments, however, about 90-93 % of the Fe in the tailings is Fe_{hem}. Although, this hematite might be related to composite particles, which would not be possible to upgrade, observations indicate that there is some liberated hematite in the T increments.

Analysing only the Fe_{tot*} gives no information about the distribution between Fe_{hem} and Fe_{sil}. Even though distinguishing the Fe_{hem} content in hematite concentrates is not crucial, a high Fe_{sil} in a hematite concentrate indicates higher content of non-economic minerals, which can contribute to increased MnO, S_{tot} and/or contents of alkalis. Distinguishing Fe_{hem}, Fe_{mag} and Fe_{sil} is therefore important for drill bits, or crude ore increments, as it provides crucial information about the composition of the ore going into the mineral processing plant. The results from this paper show that by calculating recovery based on Fe_{tot*} instead of Fe_{hem}, RG is underestimating their hematite recovery. Depending on the amount of Fe_{sil} this underestimation can become quite large and may wrongly lead to adjustments in the mineral processing plant.

Analysing the mineral chemistry is time consuming and requires expensive equipment, hence, it is not feasible for the daily production. However, a mineralogical analysis like XRD will be able to identify Fe-bearing non-economic minerals and can together with the findings from this

paper provide a better foundation for prediction of recoverable hematite from the Kvannevann deposit. Modal mineralogy and Fe_{tot*} analyses can also be used to determine the amount of Fe_{hem} lost to tailings. Since the abundance of Fe in non-economic minerals is expected to vary between deposits, the mineral chemistry would have to be analysed before being able to determine Fe_{sil}, Fe_{hem}, and Fe_{mag} in other iron ore deposits in the Storforshei IF.

4.3 Additional results

4.3.1 Correlation between Titration and XRF Bulk chemistry: Titration and XRF results compared

To investigate whether chemical results from the XRF and titration can be compared, ten increments from the WHIMS in the initial testing of the pilot circuit were analysed on the XRF, and another split of the same ten increments were sent to RG's lab for titration. There is a strong correlation between Fe content obtained from titration (Fe_{tot*}) and the Fe content obtained from XRF (Fe_{tot}). The correlation is given by Equation 2 derived from the plot of the XRF and titration results of the ten increments in Microsoft® Office Excel.

$$Fe_{tot*} = 0.9952Fe_{tot} + 0.06 \qquad \text{Equation 2}$$

The correlation has a $R^2 = 0.9996$. Using Equation 2, Fe_{tot} values of outputs from the pilot circuit were recalculated to Fe_{tot*}.

4.3.2 Reproducibility of the XRF results

The reproducibility in the XRF analysis was determined by analysing the same glass fusion discs three times. In Table 5 the average and standard deviation from XRF-analyses of glass fusion discs prepared from the three outputs from Kvannevann WHIMS step 2 at 0.7 A are shown (KVK2 0.7 = hematite concentrate, KVM2 0.7 = middling and KVA2 0.7 = tailings). The standard deviations are generally low for all oxides in all three outputs; however, the totals are high due to uncertainty in the Na_2O values. The first analysis of the hematite concentrate found no Na_2O, while the second and third found 0.82 wt % and 0.77 wt % respectively. This effect is also seen in the middling and tailings analyses, where the average content and standard deviation of Na_2O and totals are higher. Na_2O was found in all three analyses of middling and tailings, however, there was an increase of about 1 % between the first analysis and the other two analyses.

Table 5: Average and standard deviation in the XRF-results from analyses of the glass fusion discs prepared of the outputs from Kvannevann WHIMS step 2 at 0.7 A (abbreviations are explained in section 3.1).

	KVK2 0,7		KVM2 0,7		KVA2 0,7	
	Average (wt %)	StDev	Average (wt %)	StDev	Average (wt %)	StDev
SiO_2	5.09	0.02	25.70	0.30	50.59	0.18
Fe_2O_3	93.17	0.09	54.57	0.30	21.41	0.11
Al_2O_3	1.49	0.05	7.17	0.20	10.21	0.11
CaO	1.04	0.01	5.91	0.03	7.03	0.03
MgO	0.67	0.02	3.44	0.05	4.63	0.05
Na_2O	0.53	0.46	1.48	0.58	2.06	0.42
K_2O	0.18	0.01	0.96	0.03	1.66	0.03
TiO_2	1.40	0.04	0.76	0.01	0.31	0.00
P_2O_5	0.02	0.04	0.16	0.03	0.29	0.01
MnO	0.05	0.003	0.16	0.0001	0.18	0.01
LOI	0.48	0.00	3.28	0.00	4.45	0.00
Total	104.11	0.46	103.61	1.26	102.83	0.44

The reproducibility of the sample preparation was calculated by analysing three increments (splits) from the same sample (KVK2 0.7). The results (Table 6) show very similar results in the three increments, with low standard deviations.

Table 6: XRF-results from three increments of hematite concentrate WHIMS step 2 0.7 A from Kvannevann deposit sample.

	Chemistry (wt %) KVK2 0,7				
	Increment 1	Increment 2	Increment 3	Average	StDev
SiO_2	5.11	5.06	5.14	5.10	0.04
Fe_2O_3	93.22	93.27	92.97	93.15	0.16
Al_2O_3	1.49	1.49	1.50	1.49	0.01
CaO	1.05	1.06	1.08	1.06	0.02
MgO	0.66	0.66	0.64	0.65	0.01
Na_2O	0.00	0.00	0.00	0.00	0.00
K_2O	0.17	0.16	0.16	0.16	0.01
TiO_2	1.36	1.41	1.42	1.40	0.03
P_2O_5	0.00	0.04	0.06	0.03	0.03
MnO	0.05	0.03	0.05	0.04	0.01
LOI	0.48	0.52	0.52	0.51	0.02
Total	103.59	103.69	103.54	103.61	0.08

4.3.3 Mass and Fe_{tot*} distributions in the pilot circuit

The mass and Fe_{tot*} distributions were calculated for the two WHIMS steps in the pilot circuit (Tables 7-9). The feed WHIMS Step 1 is used as the basis for the calculations. The LIMS step was not included as the magnetite concentrate produced is only a preliminary concentrate and would be misleading to include in the Fe_{tot*} recovery. However, there are differences in the amount of preliminary magnetite concentrate produced between the three deposit samples. The

preliminary magnetite concentrate in the Kvannevann deposit sample accounted for 7.3 % of the feed LIMS, while it was 6 % of the feed LIMS in the Stensundtjern deposit sample, and 0.4 % of the feed LIMS for the Stortjønna deposit sample. The feed WHIMS step 1 was 664.51 kg in the Kvannevann deposit sample, 376.15 kg in the Stensundtjern deposit sample, and 326.7 kg in the Stortjønna deposit sample. All Fe_{tot} values are recalculated to Fe_{tot*} using Equation 2. The Fe_{tot*} values in the feed to WHIMS step 1 and 2 were calculated from the outputs in each step. In Stensundtjern and Stortjønna the feed to WHIMS step 2 the calculated Fe_{tot*} values matched the measured Fe_{tot*} values. The calculated Fe_{tot*} and the measured Fe_{tot*} did not match for the Kvannevann feed to WHIMS step 2 (KVK1). This is most likely due to an error in the sample preparation. Hence, the average of the three calculated Fe_{tot*} in the feed to WHIMS step 2 was used for KVK1.

The Kvannevann deposit sample have satisfying Fe_{tot*}- grades and recoveries in the hematite concentrates, and low amounts of Fe_{tot*} lost to middlings and tailings, despite the low calculated Fe_{tot*} in the feed to WHIMS step 1. The mass distribution show that the amount of tailings in WHIMS step 1 is substantial from the Kvannevann deposit sample, however, with a low Fe_{tot*} content. The Stortjønna feed WHIMS step 1 have high calculated Fe_{tot*}, and the Fe_{tot*} grades and -recoveries in the hematite concentrates are satisfactory, however, the loss of Fe_{tot*} to middlings and tailings are substantial. The Fe_{tot*} grades and -recoveries are high in the Stensundtjern hematite concentrates, while there is some loss of Fe_{tot*} to middlings and tailings. The mass distribution show very low amounts of middlings in WHIMS step 2.

Table 7: Overall mass- and Fe_{tot*} distribution over the two WHIMS steps in the pilot circuit for the Kvannevann deposit sample. Abbreviations: Kvannevann = KV, K = hematite concentrate, M = middling, A = tailing, 1 = WHIMS step 1, and 2 = WHIMS step 2.

	Fe_{tot*} (wt %) recalculated by Equation 2	Overall Mass distr. (%)	Overall Fe distr. (%)
	WHIMS step 1		
KVK1	54.61	37.7	82.9
KVM1	14.10	3.5	2.0
KVA1	6.38	58.8	15.1
Calculated Fe_{tot*} conc. in feed step 1 (wt %)	24.8	100	100
	WHIMS step 2 0.6 A		
KVK2 0.6	63.12	30.0	76.1
KVM2 0.6	39.96	1.2	1.9
KVA2 0.6	18.69	6.5	4.9
Calculated Fe_{tot*} conc. in feed step 2 (wt%)	54.68	37.7	82.9
	WHIMS step 2 0.7 A		
KVK2 0.7	62.69	30.7	77.6
KVM2 0.7	36.98	1.3	1.9
KVA2 0.7	14.65	5.7	3.3
Calculated Fe_{tot*} conc. in feed step 2 (wt %)	54.59	37.7	82.9
	WHIMS step 2 0.8 A		
KVK2 0.8	63.30	30.6	78.0
KVM2 0.8	37.51	1.3	2.0
KVA2 0.8	12.21	5.8	2.9
Calculated Fe_{tot*} conc. In feed step 2 (wt %)	54.54	37.7	82.9

Table 8: Overall mass- and Fe_{tot*} distribution over the two WHIMS steps in the pilot circuit for the Stensundtjern deposit sample. Abbreviations: Stensundtjern = ST, K = hematite concentrate, M = middling, A = tailing, 1 = WHIMS step 1, and 2 = WHIMS step 2.

	Fe_{tot*} (wt %) corrected by Equation 2	Overall Mass distr. (%)	Overall Fe distr. (%)
	WHIMS step 1		
STK1	60.29	52.9	89.6
STM1	18.23	4.1	2.1
STA1	6.87	43.0	8.3
Calculated Fe_{tot*} conc. in feed step 1 (wt %)	35.60	100	100
	WHIMS step 2 0.6 A		
STK2 0.6	66.16	45.4	84.4
STM2 0.6	53.12	1.0	1.5
STA2 0.6	20.23	6.5	3.7
Calculated Fe_{tot*} conc. in feed step 2 (wt %)	60.29	52.9	89.6
	WHIMS step 2 0.7 A		
STK2 0.7	65.58	46.0	85.4
STM2 0.7	44.89	0.9	1.2
STA2 0.7	18.05	6.0	3.0
Calculated Fe_{tot*} conc. in feed step 2 (wt %)	59.86	52.9	89.6
	WHIMS step 2 0.8 A		
STK2 0.8	65.65	46.2	85.7
STM2 0.8	41.28	1.0	1.2
STA2 0.8	16.94	5.7	2.7
Calculated Fe_{tot*} conc. in feed step 2 (wt %)	59.95	52.9	89.6

Table 9: Overall mass- and Fe_{tot*} distribution over the two WHIMS steps in the pilot circuit for the Stortjønna deposit sample. Abbreviations: Stortjønna = SØ, K = hematite concentrate, M = middling, A = tailing, 1 = WHIMS step 1, and 2 = WHIMS step 2.

	Fe_{tot*} (wt %) corrected by Equation 2	Overall Mass distr. (%)	Overall Fe distr. (%)
	WHIMS step 1		
SØK1	58.13	55.7	85.1
SØM1	19.02	3.5	1.7
SØA1	12.20	40.8	13.1
Calculated Fe conc. In feed Step 1 (wt %)	38.01	100	100
	WHIMS step 2 0.6 A		
SØK2 0.6	63.00	44.9	74.3
SØM2 0.6	48.78	1.6	2.1
SØA2 0.6	36.82	9.1	8.8
Calculated Fe_{tot*} conc. in feed step 2 (wt %)	58.30	55.7	85.1
	WHIMS step 2 0.7 A		
SØK2 0.7	61.23	47.5	77.9
SØM2 0.7	44.35	1.4	1.6
SØA2 0.7	30.78	6.8	5.6
Calculated Fe_{tot*} conc. in feed step 2 (wt %)	57.08	55.7	85.1
	WHIMS step 2 0.8 A		
SØK2 0.8	62.46	48.3	79.0
SØM2 0.8	41.67	1.3	1.4
SØA2 0.8	30.20	6.1	4.8
Calculated Fe_{tot*} conc. in feed step 2 (wt %)	58.47	55.7	85.1

5 Discussion

5.1 Classification and origin of the Storforshei IF

Kimberley's (1989b) classification scheme for iron formation seems to be the most extensive, as it is based on research on several IFs from all over the world, whilst the other schemes (James, 1954; Trendall, 2002) are based on just a few iron formations. Storforshei IF likely belongs to the MECS-IF type, since it is both compositional and techtonostratigrafically comparable to the Håfjellet IF, classified as MECS-IF by Kimberley (1989b). The dating of carbonate rocks in the Dunderlandsdalen area indicates a Neoproterozoic age (800-730 Ma) of deposition. The lack of evidence of volcanic activity during deposition separates the Storforshei IF (and the Håfjellet IF) from the other Neoproterozoic IFs in the Caledonide-Appalachian orogen (Melezhik et al., 2015). Melezhik et al. (2015) therefore proposes that the Storforshei IF was deposited at the margins of an unknown microcontinent in the Iapetus ocean.

5.2 The effect of ore properties on communition

Six ore types with mineralogical and textural differences were defined in this research: Granular-Hematite and Specular-Hematite with coarse-grained tabular shaped hematite with straight grain boundaries, Hematite-Magnetite and Magnetite-Ore with similar hematite textures as the Specular-Hematite and Granular-Hematite, but with coarse grained, equant-irregular shaped magnetite with irregular grain boundaries, and Mylonitic-Hematite and Massive-Hematite with very fine grained hematite, with irregular-to-no visible grain boundaries. The characterisation was based on geological mapping and drill core logging, and their surface hardness values were measured with Schmidt hammer and Equotip. Results from paper I show that the ore mineralogy and textures together with surface hardness measurements can be used to evaluate grindability, and that the most important textures affecting the surface hardness were the grain size and -boundaries.

The primary crushing of the four deposit samples yielded very different d_{50} in the crusher output, where the two deposit samples from Kvannevann were very fine-grained compared to the Stensundtjern and especially the Stortjønna deposit samples (Figure 9). The similar PSD of the two Kvannevann deposit samples indicates similar primary crushing, even though crushing was carried out in two campaigns on two different mobile crushing units. Both units were originally set up for aggregates. Hence, set up to produce similar top size (< 30 cm) at the same settings. The differences in the PSD in the crusher outputs from Kvannevann, Stensundtjern, and Stortjønna suggests differences in ore quality (mineralogy, textures, etc.) between the

deposits. However, it could also indicate differences in drilling and blasting. The Stortjønna deposit sample dominated by fine-grained high surface hardness ore types, Mylonitic-Hematite and Massive-Hematite, yielded a coarse crusher output, while Kvannevann and Stensundtjern dominated by Specular-Hematite and Granular-Hematite, coarse-grained low surface hardness ore types, yielded finer crusher outputs, especially from the Kvannevann deposit samples. Stensundtjern also contains substantial amounts of intermediate surface hardness ore types, Hematite-Magnetite and Magnetite-Ore, which is likely part of the reason for the coarser crusher output relative to the Kvannevann deposit samples.

When discussing the results from crushing and grinding of the Kvannevann, Stensundtjern, and Stortjønna deposit samples, it is also important to take into account the effects of blasting, as the fragmentation and formation of microcracks during blasting will affect the subsequent crushing and grinding of a material (i.e. Nielsen, 1999a; Nielsen and Malvik, 1999). According to Nielsen and Malvik (1999), blasting should be considered the first step of the comminution process, as it can greatly reduce the costs of crushing and grinding, if more of the size reduction is conducted during blasting. Microcracks are formed throughout the whole rock mass of a blast but are most abundant around the drill holes (Nielsen and Malvik 1999), and large amounts of microcracks and high powder factor in the rock mass will lead to a decrease in the crushing and grinding resistance of the rocks (Nielsen and Malvik, 1999). Even after the primary and secondary crushing a large number of microcracks will be present in each rock fragment, because the microcracks remain small during blasting (Nielsen, 1999b).

The amount of microcracks generated is dependent on the amount of energy (explosives) released in the rock mass (Nielsen, 1999a) and the texture of the rock (Jern, 2002). The Kvannevann deposit samples were collected from blasts in drift development in the underground mine, which generally give 4-5 times higher powder factor (or specific charge (Zang, 2016)) compared with regular stoping (Nielsen and Kristiansen, 1999). It can be assumed that a higher specific charge (amount of explosives per m^2) was used in the blasting of the Kvannevann deposit samples, compared to the surface and open pit blasts of Stensundtjern and Stortjønna, since the Kvannevann deposit samples were from drift development (Zang, 2016). This likely caused the coarser Stensundtjern crusher output, together with the relatively larger amounts of Hematite-Magnetite and Magnetite-Ore, compared to the corresponding output from Kvannevann.

Microcracks forms more easily along straight grain boundaries, than irregular grain boundaries (Jern, 2002), and rock strength decreases with larger grain sizes since the cracks can propagate through a longer path of weakness (Eberhardt et al., 1999). Thus, the relatively large difference in PSD in the crusher outputs between especially the Kvannevann deposit samples and the Stensundtjern and Stortjønna deposit samples is caused by less competence and larger amounts of microcracks in the Kvannevann fragments after blasting, resulting from the higher specific charge and the ore texture in the ore types dominating the Kvannevann deposit. The coarse d_{50} Stortjønna crusher output is the result of the ore textures in the high surface hardness ore types and the lower specific charge, creating less microcracks and higher competence in the fragments.

The PSD of the feed to crushing and grinding is indeed important, but it is highly dependent on the competence of the rocks. As the surface hardness varies with ore texture (Tøgersen et al., 2018), and the amount of microcracks are dependent on ore textures, the surface hardness can be used as a proxy for the resistance too crushing and grinding in the ore types (Jern, 2002). The Kvannevann 1 deposit sample was used only in the initial stage of the pilot circuit development, as such the results from the AG milling of this deposit sample are not comparable to the other deposit samples, and the further discussion will therefore not include the Kvannevann 1 deposit sample.

According to Wills and Finch (2015) the PSD of the feed to an autogenous mill and the PSD of the corresponding mill circuit product is not self-similar, which means that the PSD in the mill circuit product is affected by other factors in addition to the PSD of the feed. The PSD of the mill circuit product is highly dependent on the competence of the fragments in the feed (Wills and Finch, 2015), as such a PSD containing equal amounts of fines and coarse fragments might yield a very fine mill circuit product or a coarse mill circuit product depending on the competence of the larger fragments. The effect of PSD and rock fragment competence is apparent in the results from the AG milling in the pilot circuit in this project. The Kvannevann 2 deposit sample with the finest PSD of the three deposit samples processed through the pilot circuit had high throughput and low energy consumption in the AG mill, hence, high grindability. Part of this is probably due to the amount of fines in the feed, which would not need milling, but rather goes straight through the mill. However, the particles > 760 µm also have a high grindability, i.e. there is no accumulation of mill charge, as apparent from the relatively high throughput, which means that the larger fragments have not been too resistant to the grinding and enabled a good milling of Kvannevann. This is an effect of the microcracks

in the material generated from the underground mining conditions and the ore texture and surface hardness of the ore types in Kvannevann. The Stortjønna deposit sample had 60 % lower throughput compared to the Kvannevann deposit sample, and higher energy consumption, hence, a lower grindability. The feed rate had to be decreased due to accumulation of mill charge. This indicates that the competence of the rocks in the Stortjønna feed is high, caused by less microcraks resulting from the ore texture, high surface hardness, and lower specific charge, leading to abrasion and chipping as the primary crushing mechanism in the AG mill, and creating a mill circuit product with high content of fines. The AG milling of the Stensundtjern deposit sample was, in terms of throughput and specific energy consumption, intermediate compared to the Kvannevann and Stortjønna deposit samples. This is an effect of coarser PSD in the mill feed, but also a higher competence of the fragments compared to the Kvannevann deposit sample. The relatively higher competence is caused by a higher content of the ore types with higher surface hardness, such as Hematite-Magnetite and Magnetite-Ore, and less microcracks (compared with the Kvannevann deposit samples) due to less specific charge in the surface blast of the Stensundtjern deposit sample.

The results from Sandvik et al. (2012) show that even with very similar PSD of the mill feed from Kvannevann and Stortjønna, the results from the AG milling of material was very similar to the results in this research. Sandvik et al. (2012) did not crush the material before AG milling, but rather crushed the largest boulders with a sledge to fit it into the AG mill inlet. Sandvik et al. (2012) found that the capacity of the mill dropped 30-40 % when milling the Stortjønna material compared to the Kvannevann material, which is in the same range as the capacity drop in the AG milling in this project, which was 37 %. The mill power, mill torque and feed rates in this project are also very similar to the ones obtained by Sandvik et al. (2012). If the primary crushing step had been skipped for the Kvannevann 2 deposit sample or if the crushing had been conducted very carefully, the PSD of the Kvannevann mill feed would be more similar to the Stortjønna mill feed. However, the mill feed from Kvannevann would then contain weaker fragments which most likely would be quickly broken apart when entering the mill. Hence, the results from the AG milling would not necessarily be very different from the results obtained in the pilot circuit. Prediction of the results from AG milling is near impossible based solely on the PSD of the feed, as there are as mentioned many other factors affecting the grinding of a material.

5.3 Hematite liberation and textures affecting wet high intensity magnetic separation

The Storforshei IF is a highly metamorphosed, low-grade iron ore, with mineralogical and textural differences between and within its iron ore deposits. Previous research (Klomstadlien, 1984), and the results from this research indicate that the Fe_{tot*} analysis, currently used in the quality control at RG, is not sufficient for detecting these differences. The results from this research show that the constructed pilot circuit can detect variations in metallurgical performance caused by the mineralogical and textural differences between the Kvannevann, Stensundtjern, and Stortjønna deposits. However, the Fe_{tot*} grades in the different coil currents in WHIMS step 2 within a deposit have only small differences, which show no trends. Thus, the small differences observed are likely not significant. Therefore, the results from the different coil currents in WHIMS step 2 will not be discussed in the following, but rather grouped together to describe the differences in the hematite concentrates from WHIMS step 2 between the deposits. The differences between the deposits are likely significant as these are from individual deposits with measurable mineralogical and textural variations.

The Kvannevann mill circuit product (KV-PM) has the lowest Fe_{tot*} content, however, despite this the hematite concentrates have satisfactory Fe_{tot*} grades, and the loss of Fe_{tot*} to middlings and tailings are low. The mass balance show that there are substantial amounts of tailings from WHIMS step 1 in the Kvannevann deposit sample, however, the Fe_{tot*} content is low, suggesting a good separation in the WHIMS. The hematite textures found in Granular-Hematite and Specular-Hematite was recognised in the particles in KV-PM, thus, corroborating the findings from geological mapping and drill cores that the Kvannevann deposit is dominated by Granular-Hematite and Specular-Hematite. The low specific energy consumption in the AG mill may be attributed the hematite textures in Granular-Hematite and Specular-Hematite where breakage could follow the straight grain boundaries of the hematite requiring less energy. Another effect of the coarse-grained hematite textures is the high hematite liberation in KV-PM, and the particle size distribution with small amounts of fines. This suggest that these ore types are favourable for the WHIMS.

The new prospect for production, the Stensundtjern deposit, was like the Kvannevann deposit found to be dominated by Granular-Hematite and Specular-Hematite, however, contains substantial amounts of Hematite-Magnetite and Magnetite-Ore. Hematite-Magnetite and Magnetite-Ore are part of the intermediate surface hardness group, which is likely caused by the magnetite grains that are equant-irregular shaped and have irregular grain boundaries. The

particle textures in the Stensundtjern mill circuit product (ST-PM) with tabular shaped liberated hematite is similar to the particles found in KV-PM, however, there are more composite particles with two phases: hematite and a non-economic mineral. This corroborates a different ore type distribution in the Stensundtjern deposit sample, where Granular-Hematite, Hematite-Magnetite, with an average hematite grain size from 200-300 µm, might be more abundant than the Specular-Hematite with average hematite grain size 400-500 µm. This causes a slightly lower hematite liberation in the ST-PM compared to the KV-PM and might also explain the higher loss of Fe_{tot*} in the Stensundtjern middlings and tailings compared to the corresponding outputs from Kvannevann. The Stensundtjern hematite concentrates from the WHIMS have higher Fe_{tot*} grades than the corresponding outputs in Kvannevann and Stortjønna, this is a result of a higher Fe_{tot*} in the ST-PM, and the relatively high hematite liberation.

The Stortjønna deposit which from previous experience was known to be challenging in the mineral processing plant, proved to be challenging in the pilot circuit as well. The Stortjønna mill circuit product (SØ-PM) had substantially lower hematite liberation compared to the corresponding mill circuit products in Kvannevann and Stensundtjern. Some of the hematite in the SØ-PM were located in composite particles either interwoven with non-economic minerals, or as fine-grained inclusions in non-economic minerals. Both these textures can be linked to the Mylonitic-Hematite where the hematite is disseminated in a fine-grained matrix of gangue minerals, and cracks in the remnants of larger hematite grains are filled with gangue minerals and recrystallised hematite. The liberated hematite particles were irregular shaped, suggesting that they originate from the Massive-Hematite ore types, where there are no visible grain boundaries for breakage to occur along, thereby, creating irregular particles.

The large amount of fines in the SØ-PM have likely affected the separation in the WHIMS, where the separation efficiency decreases for particle sizes < 20 µm according to Shao et al. (1996) and Song et al. (2002). The Fe_{tot*} in the SØ-PM is higher than both KV-PM and ST-PM, and even though the hematite concentrates also have high Fe_{tot*}, the loss of Fe_{tot*} to middlings and tailings are substantial. This is likely caused by the lower hematite liberation in SØ-PM than the KV-PM and ST-PM.

The middlings and tailings from the WHIMS are returned in the full-scale mineral processing plant, and as such high hematite liberation in these outputs, as found in the Kvannevann middlings and tailings will be an advantage for the downstream separation processes. Depending on the Fe_{tot*} amount in these outputs the overall hematite recovery will increase,

however, if the hematite liberation is low, as in the Stortjønna middlings and tailings, these returned outputs might accumulate composite particles with hematite, which could eventually end up in the final hematite concentrate, increasing the hematite recovery, but lowering the Fe_{tot*} grade.

The Fe_{tot*} recoveries were at the same level in the Kvannevann and Stortjønna hematite concentrates, even though the Fe_{tot*} content in SØ-PM is higher than in KV-PM. This suggest that the observed and measured mineralogical and textural properties in the Stortjønna deposit sample leads to more hematite and Fe_{tot*} lost to the middlings and tailings. The highest Fe_{tot*} recovery was found in the Stensundtjern hematite concentrates. Given the similarities in the particle textures in the KV-PM and ST-PM samples the difference in Fe_{tot*} recovery is probably caused by the higher Fe_{tot*} content in ST-PM compared to KV-PM, although the slightly lower hematite liberation in ST-PM leads to increased Fe_{tot*} loss to middlings and tailings.

5.4 Fe_{tot*} recovery vs. iron oxide recovery

The results from the pilot circuit indicate that the mineralogical and textural differences in the ore types highly affects the Fe_{tot*} and iron oxide recovery. However, the recovery calculations based on the Fe_{tot*} contents, does not show the real iron oxide recovery, since Fe_{tot*} does not discriminate between Fe located in iron oxides and non-economic minerals. The hematite recoveries calculated based on Fe_{hem} in increments from the full-scale mineral processing plant were higher compared with the Fe_{tot*} recovery, suggesting that RG is underestimating their hematite recovery. This was caused by the relatively higher Fe_{sil} in the MCP sample. This is an important result as a low Fe_{tot*} recovery might lead to unnecessary adjustments in the full-scale mineral processing plant. The Fe_{tot*} lost to tailings were found to consist of about 90-93 % Fe_{hem}, this is probably due to composite particles with hematite, however, observations suggest that there were liberated hematite in the tailing increments as well. Determining the Fe_{hem}, Fe_{mag}, and Fe_{sil} in especially crude ore and MCP is important as the Fe distribution likely will affect the amount of undesirable elements in the final hematite concentrate (MnO, S_{tot}, and alkalis).

Regardless of whether considering Fe_{tot*} or the hematite recovery, the effect of mineralogical and textural differences in the ore types will still be substantial, where the fine-grained ore types Mylonitic-Hematite and Massive-Hematite will yield lower recoveries than the coarse-grained ore types Granular-Hematite and Specular-Hematite, given the same Fe_{tot*} content in the crude

ore. The high Fe_{tot*} recovery for the Stensundtjern deposit sample indicates that the ore types Hematite-Magnetite and Magnetite-Ore also will yield high hematite recoveries.

The mineral chemistry is not expected to vary to a large extent within a deposit, however, it might vary between them, as such the mineral chemistry results in this research, from the Kvannevann deposit, might not be applicable for the Stortjønna- and Stensundtjern deposits. Therefore, in order to determine Fe_{sil} in these deposits, new analyses of mineral chemistry are needed.

5.5 Summary of key findings

The results from this research show that the ore types dominating the Kvannevann- and Stensundtjern deposits are very suitable for production and should be expected to yield high Fe_{tot*} grades and hematite recoveries. The Stensundtjern deposit might reduce the capacity in the AG mill, depending on the ore type distribution. However, with geological mapping during production, it should be possible to blend areas with higher amounts of the ore types Hematite-Magnetite and Magnetite-Ore, with areas dominated by Granular-Hematite and Specular-Hematite. The ore types Mylonitic-Hematite and Massive-Hematite will cause major capacity issues in the AG mill, with a significant loss of hematite to middlings and tailings from the magnetic separation. Hence, when encountering these ore types in production areas they must be carefully blended into the feed.

The six ore types are easily distinguished in hand specimen and drill cores and can together with surface hardness by Schmidt hammer or Equotip be used in daily quality control during production, or to evaluate whether new areas or deposits are viable for production.

The XRF analysis on the non-standard program *Quant Express* correlated very well with the titration method used at RG. Hence, replacing the titration method with an XRF would be able to produce reliable results even for the increments with high Fe content. The advantage with the XRF is the much higher capacities compared to the titration method. Both the reproducibility of the sample preparation and the XRF analysis were found to have satisfactory reproducibility, with a standard deviation of 0.16 for the Fe values in both XRF and sample preparation.

This research provides new insight into the effect of mineralogical and textural differences on processing highly metamorphosed and deformed hematite-magnetite ores. The characterisation methods can be utilised on especially other iron deposits around the world. Several researchers

have also found links between mineralogy, textures, surface hardness, and comminution behaviour (Kekec et al., 2006; Hunt et al., 2013; Lopera, 2014; Niiranen, 2015). Some of the results from the AG mill might also apply to other deposits, for instance, the particle breakage in fine-grained ore types with irregular to non-visible grain boundaries required more energy, something that was also observed by Xu et al. (2013).

The work conducted in this research can be utilised by RG in the development of a geometallurgical program and ultimately a geometallurgical model for the Storforshei IF. The characterisation of the ore types and the pilot circuit testing is the first and second steps in the geometallurgical program as described by Lamberg (2011).

6 Conclusions

- Six ore types with significant differences in ore mineralogy and texture were defined based on geological mapping and drill core logging.
- The ore mineralogy and textures found in the ore types can be related to surface hardness, where fine-grained ore types with irregular to no visible grain boundaries have higher surface hardness values, than coarse-grained ore types with straight grain boundaries.
- The large difference in the PSD in the crusher outputs for the deposit samples is a result of the differences in ore texture, surface hardness, and specific charge, creating differences in the amounts of microcracks and competence of the fragments.
- Surface hardness can be used as a proxy for determining the amount of microcracks and resulting competence difference in fragments. Where ore types with low surface hardness, resulting from coarse-grained hematite with straight grain boundaries will generate more microcracks during blasting and reduce competence in the fragments, while ore types with high surface hardness, resulting from fine-grained hematite with irregular-to-no visible grain boundaries, will have less microcracks, and higher competence in the fragments. However, the generation of microcracks is also affected by amount of energy released in the rock mass during blasting.
- The most important ore properties affecting the metallurgical performance of the Kvannevann, Stensundtjern, and Stortjønna deposits are grain size and -boundaries, in which the ore types differ substantially.
- The grain size and -boundaries, and the surface hardness values can be used to evaluate grindability. Fine-grained ore types without visible grain boundaries have high surface hardness, and low grindability, while coarse-grained ore types with straight grain boundaries have low surface hardness values, and high grindability.
- The pilot plant testing indicate that it is possible to make satisfying hematite concentrate without the use of return streams in the WHIMS separation. Although, there is a loss of hematite to the middlings and tailings, especially in the Stortjønna deposit sample.
- Hematite liberation is directly affected by grain size and -boundaries in the ore types, where the mill circuit product from fine-grained ore types with no visible grain boundaries have substantially lower liberation, than coarse-grained ore types with straight grain boundaries.

- Non-economic minerals containing Fe or Mn are found especially in hematite concentrates from WHIMS step 1, which indicates that the magnetic susceptibilities in these might be high enough for them the attach to the matrix in the WHIMS, or that they are part of composite particles with hematite.
- Recovery should be calculated based on Fe_{hem} or Fe_{mag} rather than Fe_{tot*}, as the calculation of Fe_{tot*} recovery is an underestimation of the real hematite recovery. Knowledge of the amount of Fe_{sil} will improve the prediction of how much undesirable elements might end up in the final hematite concentrate.

The results from this research show a potential for a more solid quality control in the daily production at RG. The definition of ore types and pilot circuit testing is the first steps towards the development of a geometallurgical program for the Storforshei IF. Ore types in blasts, new areas, new deposits, and drill cores can be identified using simple, non-expensive methods like geological mapping, and surface harness measurements by Schmidt hammer and Equotip. The drill core logging program should include characterisation of ore types, and surface hardness by Equotip.

When entering a new area of a deposit or a new deposit the following characterisation should be conducted:

- Geological mapping with focus on ore type
- Surface hardness measurements
- Assessment of the ore type distribution
- Chemical and mineralogical investigations using XRF and XRD, for determination of recoverable hematite

Following these steps and using the results from the work presented here, RG can predict how the ore will behave in the processing plant, and the hematite recovery and Fe grade. This research provides new insights into the effects of processing a highly metamorphosed and complex low-grade hematite-magnetite iron ore. The methods used can also be utilised on other deposits, as characterisation of the effect of mineralogical and textures variation on metallurgical performance is increasingly becoming important as deposits available are more complex and have lower grades.

7 Recommendations for future work

- To further improve the daily quality control in the production RG should consider acquiring on-site XRF and XRD, which can be specially accommodated the ore through development of standards in the methods, yielding reliable results, and which have high capacities for analysing increments from both drill bits, and process outputs.
- Ore types in blasts, new areas/deposits and drill cores can be identified using simple, non-expensive methods like geological mapping, and surface hardness measurements. Therefore, the drill core logging program should include characterisation of ore types and measurements of surface hardness by Equotip, while the daily production in the mine should include geological mapping of blast with regards to identification of ore types and determination of the distribution of them.
- A more thorough geological mapping determining the distribution of the ore types should be conducted
- Increments from the same deposit sample should be processed in the pilot circuit to test whether the differences in Fe_{tot*} grades and -recoveries from WHIMS step 2 are significant. Increased intervals between coil currents should also be considered.

8 References

Aasly, K. (2008) *Properties and behaviour of quartz for the silicon process*. PhD thesis, Norwegian university of Science and Technology, Trondheim, 236 p.

Aasly, K. and Ellefmo, S. (2014) 'Geometallurgy applied to industrial minerals operations', *Mineralproduksjon*, 5, pp. A21-A34. Available at: http://mineralproduksjon.no/publikasjoner/volum-5-2014/ [Accessed 04.08.2019]

An, J.W., Jung, B.H., Lee, Y.H., Tran, T., Kim, S.J., Kim, M.J. (2009) 'Production of high purity molybdenum compounds from a Cu-Mo acid-washed liquor using solvent extraction. Part 2: Pilot and plant operations', *Minerals Engineering*, 20, pp. 1026-1031.

Baum, W., Lotter, N.O., Whittaker, P.J. (2004) 'Process mineralogy – a new generation for ore characterization and plant optimization', *SME Annual Meeting Feb. 23-25*, Denver, Colorado.

Beckhoff, B., Gottwald, A., Klein, R., Krumrey, M., Müller, R., Richter, M. and Ulm, G. (2009) 'A quarter-century of metrology using synchrotron radiation by PTB in Berlin', *physica status solidi (b)*, 246(7), pp. 1415-1434.

Beukes, N. J., Klein, C., Kaufman, A. J., and Hayes, J. M. (1990) ,Carbonate petrography, kerogen distribution, and carbon and oxygen isotope variations in an early Proterozoic transition from limestone to iron-formation deposition, Transvaal Supergroup, South Africa', *Economic geology and the bulletin of the Society of Economic Geologists*, 85(4), pp. 663-690.

Bradshaw, D.J. (2014) 'The role of 'process mineralogy' in improving the process performance of complex sulphide ores', *IMPC 2014 Santiago Chile*, keynote paper 932.

Bogner, A., Jouneau, P. H., Thollet, G., Basset, D., and Gauthier, C. (2007) 'A history of scanning electron microscopy developments: towards "wet-STEM" imaging', *Micron*, 38(4), pp. 390-401.

Bond, F.C. (1952) 'The Third Theory of Comminution', *Transactions AIME Mining Engineering*, 193, pp. 484-494.

Bowell, R. J., Grogan, J., Hutton-Ashkenny, M., Brough, C., Penman, K., and Sapsford, D. J. (2011) 'Geometallurgy of uranium deposits', *Minerals Engineering*, 24 (12), pp. 1305-1313.

Bowring, S., Myrow, P., Landing, E., Ramezani, J., and Grotzinger, J. (2003) 'Geochronological constraints on terminal Neoproterozoic events and the rise of Metazoan', *EGS-AGUEUG Joint Assembly*.

Bruker (2009) *S8 Tiger* [online]. Available at: *fn-iq.com/wp-content/uploads/2014/03/BrukerAXS.pdf* (Accessed: 07.08.2019)

Bruker (2019) *TOPAS Rietveld analysis software* [online]. Available at: https://www.bruker.com/products/x-ray-diffraction-and-elemental-analysis/x-ray-diffraction/xrd-software/topas/rietveld-analysis-software.html (Accessed: 06.01.2019)

Bugge J.A.W. (1948) 'Rana Gruber: Geologisk beskrivelse av jernmalmfeltene i Dunderlandsdalen', *Norges Geologiske Undersøkelse*, No. 171, pp. 1-149.

Bunkholt, I. (2015) *The implications of sulphides in GCC feed and the potential for their removal during alkaline amine flotation*. PhD Thesis, Norwegian University of Science and Technology, Trondheim, 194 p.

Coleman, R. and Lamberg, P. (2010) 'Flotation circuit optimisation using modelling and simulation software', *Outotec Australia's quarterly e-newsletter*, 26 (August), pp. 1-4.

Cox, G. M., Halverson, G. P., Minarik, W. G., Le Heron, D. P., Macdonald, F. A., Bellefroid, E. J., and Strauss, J. V. (2013) 'Neoproterozoic iron formation: an evaluation of its temporal, environmental and tectonic significance', *Chemical Geology 362*, pp. 232-249.

Dandois, P., Cáceres, G., Joly, P. and Frenay, J. (1998) 'Development of a pilot plant using clean technology for the recovery of gold from small scale mines', *Minerals Engineering*, 11 (5), pp. 453-455.

Dunham, S., and Vann, J. (2007, June) 'Geometallurgy, geostatistics and project value—does your block model tell you what you need to know', *Proceedings of the Project Evaluation Conference, Melbourne, Australia*, pp. 19-20.

Eberhart E, Stimpson B., and Stead D. (1999) 'Effects of Grain size on the initiation and propagation thresholds of stress-induced brittle fractures', *Rock Mech. & Rock Eng.*, 32 (2), pp.81-99.

Ehrig, K., McPhie, J., and Kamenetsky, V. S. (2012) 'Geology and mineralogical zonation of the Olympic Dam iron oxide Cu-U-Au-Ag deposit, South Australia', *Society of Economic Geologists, Inc.*, Special publication 16, pp. 237-267.

Ellefmo, S. (2005) *A probabilistic approach to the value chain of underground iron ore mining*. PhD Thesis, Norwegian University of Science and Technology, Trondheim, 273 p.

Garmin (2019) *GPS nøyaktighet* [online]. Available at: https://support.garmin.com/nb-NO/?faq=aZc8RezeAb9LjCDpJplTY7 (Accessed: 05.08.2019)

Geonorge (2019) *Norge, illustrasjonskart* [online]. Available at: https://kartkatalog.geonorge.no/metadata/kartverket/norge-illustrasjonskart/a374f867-60c0-4524-9eda-b15ab4d12858 (Accessed: 28.07.2019)

Geoforskning (2018) *Vil utdanne geometallurger* [online]. Available at: http://www.geoforskning.no/nyheter/bergverk/1746-vil-utdanne-geometallurger (Accessed: 26.01.2019)

Gjelle, S., Søvegjarto, U., Tveiten, B. (1991) *Dunderlandsdalen 2027 I*, berggrunnsgeologisk kart 1: 50,000. Norges geologiske undersøkelse, Trondheim.

Goldstein, J. I., Newbury, D. E., Michael, J. R., Ritchie, N. W., Scott, J. H. J., and Joy, D. C. (2017) *Scanning electron microscopy and X-ray microanalysis*. 4th edition, Springer.

Goodge, J. (2018) *Electron probe micro-analyser* [online]. Available at: https://serc.carleton.edu/research_education/geochemsheets/techniques/EPMA.html (Accessed: 03.02.2019)

Gottlieb, P., Wilkie, G., Sutherland, D., Ho-Tun, E., Suthers, S., Perera, K., Jenkins, B., Spencer, S., Butcher, A. and Rayner, J. (2000) 'Using Quantitative Electron Microscopy for Process Mineral Applications', *JOM Journals of Metals*, 52 (4), pp. 24-25.

Gregory, M. J., Lang, J. R., Gilbert, S., and Hoal, K. O. (2013) 'Geometallurgy of the Pebble porphyry copper-gold-molybdenum deposit, Alaska: Implications for gold distribution and paragenesis', *Economic Geology*, 108(3), pp. 463-482.

Grenne, T., Ihlen, P.M., Vokes, F.M. (1999) 'Scandinavian Caledonide Metallogeny in a plate tectonic perspective', *Mineralium Deposita*, 34 (5-6), pp. 422–471.

Gross, G. A. (1983) 'Tectonic systems and the deposition of iron-formation', *Precambrian Research*, 20(2-4), pp. 171-187.

Gu, Y. (2003) 'Automated Scanning Electron Microscope Based Mineral Liberation analysis', *Journal of Minerals & Materials Characterization & Engineering*, 2, pp. 33-41.

Halverson, G. P., Poitrasson, F., Hoffman, P. F., Nédélec, A., Montel, J. M., and Kirby, J. (2011) 'Fe isotope and trace element geochemistry of the Neoproterozoic syn-glacial Rapitan iron formation', *Earth and Planetary Science Letters*, 309 (1-2), pp. 100-112.

Helle, S., Kelm, U., Barrientos, A., Rivas, P., and Reghezza, A. (2005) 'Improvement of mineralogical and chemical characterization to predict the acid leaching of geometallurgical units from Mina Sur, Chuquicamata, Chile', *Minerals Engineering*, 18(13-14), pp. 1334-1336.

Hestnes, K. (2013) *Development of process mineralogy for optimization and increased value of the mineral production in Sibelco Nordic*. PhD Thesis, Norwegian University of Science and Technology, Trondheim.

Hestnes, K.H., Aasly, K., Sandøy, R. and Sørensen, B.E. (2013) 'Occurrence of iron in industrial granitic pegmatite', *Minerals Engineering*, *52*, pp.21-30.

Hoal, K. O. (2008) 'Getting the geo into geomet', *SEG Newsletter, Society of Economic Geologists,* 73 (April), pp. 11-15.

Hoffman, P. F., Kaufman, A. J., Halverson, G. P., and Schrag, D. P. (1998) 'A Neoproterozoic snowball earth', *Science*, 281(5381), pp. 1342-1346.

Hoffman, P. F., and Schrag, D. P. (2002) 'The snowball Earth hypothesis: testing the limits of global change', *Terra nova*, 14(3), pp. 129-155.

Hoffman, P. F., and Li, Z. X. (2009) 'A palaeogeographic context for Neoproterozoic glaciation. Palaeogeography, Palaeoclimatology', *Palaeoecology*, 277(3-4), pp. 158 172.

Hoffman, P. F., Macdonald, F. A., and Halverson, G. P. (2011) 'Chemical sediments associated with Neoproterozoic glaciation: iron formation, cap carbonate, barite and phosphorite', *Geological Society London, Memoirs*, 36(1), pp. 67-80.

Hunt, J., Berry, R., and Bradshaw, D. (2011) 'Characterising chalcopyrite liberation and flotation potential: Examples from an IOCG deposit', *Minerals Engineering*, 24(12), pp. 1271-1276.

Hunt, J., Kojovic, T., Berry, R. (2013) 'Estimating Comminution Indices from Ore Mineralogy, Chemistry and Drill Core Logging', *The Second AUSIMM International Geometallurgy Conference (GeoMet)*, Brisbane, Qld, 1, pp.173-176.

Jackson, J., McFarlane, A. J., and Olson Hoal, K. (2011, January) 'Geometallurgy-back to the future: Scoping and communicating geomet programs', *GeoMet 2011-1st AusIMM International Geometallurgy Conference 2011*, Australasian Institute of Mining and Metallurgy, pp. 125-131.

James, H.L. (1954) 'Sedimentary facies of iron-formation', *Economic Geology*, 49, pp. 235-293.

Jern, M. (2002) 'Micro- and Macro Crack Growth as a Result of Blasting', *Proc. of the 7'" international symposium on rock fragmentation by blasting, Beijing, China. Metallurgical Industry Press,* pp 155-161.

Johansen, R. (2014) 'Flowsheet with process and chemical data', *Internal report, Rana Gruber AS.*

Kekec, B., Unal, M., Sensogut, C. (2006) 'Effect of the textural properties of rocks on their crushing and grinding features', *Journal of University of Science and Technology Beijing, Mineral, Metall, Material*, 13 (5), pp. 385–392.

Kimberley, M.M. (1978) 'Paleoenvironmental Classification of Iron Formations', *Economic Geology*, 73, pp. 215-229.

Kimberley, M.M. (1989b) 'Exhalative Origins of Iron Formations', *Ore Geology Reviews*, 5, pp. 13-145.

King, H.M. (2019) *Iron ore* [online]. Available at: https://geology.com/rocks/iron-ore.shtml (Accessed: 20.01.2019)

Kirschvink, J.L. (1992) 'Late Proterozoic low-latitude global glaciation: The Snowball Earth', In J.W. Schopf and C. Klein (eds.) *The Proterozoic Biosphere: a multi-disciplinary study*. New York: Cambridge University Press, pp. 51-52.

Klein, C., and Gole, M. J. (1981) 'Mineralogy and petrology of parts of the Marra Mamba iron formation, Hamersley Basin, Western Australia', *American Mineralogist*, 66(5 6), pp. 507-525.

Klein, C., and Beukes, N. J. (1989) 'Geochemistry and sedimentology of a facies transition from limestone to iron-formation deposition in the early Proterozoic Transvaal Supergroup, South Africa', *Economic Geology*, 84(7), pp.1733-1774.

Klein, C. and Beukes, N.J. (1992) 'Proterozoic iron-formations', *Developments in Precambrian Geology*, 10, pp. 383-418.

Klein, C., and Beukes, N. J. (1993) 'Sedimentology and geochemistry of the glaciogenic late Proterozoic Rapitan iron-formation in Canada', *Economic Geology*, 88(3), pp. 542-565.

Klein, C. (2005) 'Some Precambrian banded iron-formations (BIFs) from around the world: Their age, geologic setting, mineralogy, metamorphism, geochemistry, and origin', *American Mineralogist*, 90, pp. 1473-1499.

Kleiv, R.A. (2014) 'Vurdering av oppredningsløsninger for produksjon av konsentrat til masovn og DR-pellets ved Rana Gruber – Sluttrapport fra DP3 i RaNaGass prosjektet', *Internal report, Norwegian University of Science and Technology.*

Klomstadlien, (1984) **'**Silikat bundet jern i råmalm, konsentrat og avgang, Rana Gruber AS', Internal report, Norsk Jernverk.

Lamberg, P. (2011) 'Particles-the bridge between geology and metallurgy', *Proceedings Conference in mineral engineering*, Luleå, pp. 1-16.

Lamberg, P., and Lund, C. (2012) 'Taking Liberation Information into a Geometallurgical Model: Case Study Malmberget, Northern Sweden', *Proceedings Process Mineralogy '12 Conference*.

Lamberg, P., Rosenkranz, J., Wanhainen, C., Lund, C., Minz, F. E., Mwanga, A., and Parian, M. (2013) 'Building a geometallurgical model in iron ores using a mineralogical approach with liberation data', *The Second AUSIMM International Geometallurgy Conference*, Brisbane, Qld, 30, pp. 317-324.

Lang, A.M., Aasly, K., Ellefmo, S.L. (2018a) 'Mineral characterization as a tool in the implementation of geometallurgy into industrial mineral mining', *Minerals Engineering*, 116, pp. 114-122.

Lang, A., Ellefmo, S., Aasly, K. (2018b) 'Geometallurgical Flowsheet as a Tool for Designing and Communicating Geometallurgical Programs', *Minerals* 8 (9), p. 372.

Leichliter, S., Hunt, J., Berry, R., Keeney, L., Montoya, P. A., Chamberlain, V., and Jahoda, R. (2011) 'Development of a predictive geometallurgical recovery model for the La Colosa, Porphyry Gold Deposit, Colombia', *Proceedings from the 1st AusIMM international geometallurgy conference*, The Australasian Institute of Mining and Metallurgy, Melbourne, pp. 85-92.

Lotter, N.O., Kormos, L.J., Oliveira, J., Fragomeni, D., Whiteman, E. (2011) 'Modern Process Mineralogy: Two case studies', *Minerals Engineering*, 24, pp. 638-650.

Lotter, N.O., Evans, C.L., Engström, K. (2018) 'Sampling – A key tool in modern process mineralogy', *Minerals Engineering*, 116, pp. 196-202.

Lopera, P.A.M. (2014) *Geometallurgical mapping and mine modelling – comminution studies: La Colosa Case Study*. AMIRA P843A Research Master Thesis. University of Tasmania,75p. Available at: https://oatd.org/oatd/record?record=oai%5C%3Aeprints.utas.edu.au%5C%3A18741 (Accessed: 04.08.2019)

Lishchuk, V., Koch, P. H., Lund, C., and Lamberg, P. (2015a) 'The geometallurgical framework: Malmberget and Mikheevskoye case studies', *Mining Science*, 22, Special Issue 2, pp. 57-66.

Lishchuk, V., Lamberg, P., and Lund, C. (2015b) 'Classification of geometallurgical programs based on approach and purpose', *13th Biennial SGA Meeting, Mineral Resources in a Sustainable World*, Nancy, 4, pp.1431-1434.

Lishchuk, V., Lamberg, P., and Lund, C. (2016) 'Evaluation of sampling in geometallurgical programs through synthetic deposit model', *XXVIII International Mineral Processing Congress*, Québec City, 11.-15. September 2016.

Lishchuk, V. (2016) *Geometallurgical programs–critical evaluation of applied methods and techniques*, PhD Thesis, Luleå University of Technology.

Lund, C. (2013) *Mineralogical, Chemical and Textural Characterisation of the Malmberget Iron Ore Deposit for a Geometallurgical Model*, PhD Thesis, Luleå University of Technology, 190 p.

Nielsen, K. (1999a) 'Economic effects of blasting on the crushing and grinding of ores', *Fragblast 1999*, Johannesburg, South African Institute of Mining and Metallurgy, pp. 251-256.

Nielsen, K. (1999b) 'The Economic Consequences of Drill Hole Deviation in Crushed Aggregate Production', *Proc. Explo-99 Conference Kalgoorlie*, pp. 9-13.

Nielsen, K. and Malvik, T. (1999) 'Grindability enhancement by blast-induced microcraks', *Powder Technology 105*, pp. 52-56.

Nielsen, K. and Kristiansen, J. (1999) 'Can blasting enhance the grindability of ores?', *Transactions of the Institution of Mining and Metallurgy*, Section A, 104, pp. A144-A148.

Madsen, I.C., Scarlett, N.V.Y., Cranwick, L.M.D., Lwin, T. (2001) 'Outcomes of the international union of crystallography commission on powder diffraction round robin on quantitative phase analysis: samples 1a to 1h', *Journal of Applied Crystallography*, 34, pp. 409–426.

Malvik, T. (2011) 'Sammendrag av prosjekter innenfor temaet prosessmineralogi utført for Rana Gruber ved NTNU/SINTEF i tiden 1990-2011', *Internal report, Norwegian University of Science and Technology*, M-TMA 2011:18, 23p.

Malvik, T. (2014) 'History and growth of modern process mineralogy', *Mineralproduksjon*, 5, pp. A1-A19, Available at: http://mineralproduksjon.no/publikasjoner/volum-5-2014/ (Accessed: 04.08.2019)

McNab, B., Jankovic, A., David, D., and Payne, P. (2009) 'Processing of magnetite iron ores comparing grinding options', *Proceedings of Iron Ore 2009 Conference*, Perth, Australia, pp. 27-29.

Melezhik, V.A., Kuznetsov, A.B., Pokrovsky, B.G., Solli, A., Gorokhov, I.M., Fallick, A.E.,Lindahl, I., Konstantinova, G.V., Melnikov, N.N. (2014) 'Chemostratigraphic insight into deposition of the Melkedalen Marble formation, Narvik Nappe Complex, North-Central Norwegian Caledonides', *Norwegian Journal of Geology*, 94 (1), pp. 35-52.

Melezhik, V.A., Ihlen, P.M., Kuznestov, A.B., Gjelle, S., Solli, A., Gorokhov, I.M., Fallick, A.E., Sandstad, J.S., Bjerkgård, T. (2015) 'Pre-Sturtian (800–730 Ma) depositional age of carbonates in sedimentary sequences hosting stratiform iron ores in the Uppermost Allochthon of the Norwegian Caledonides: A chemostratigraphic approach', *Precambrian Research*, 261, pp. 272−299.

Mena Silva, C., Sørensen, B., Aasly, K., and Ellefmo, S. (2018) 'Geometallurgical Approach to the Element-to-Mineral Conversion for the Nabbaren Nepheline Syenite Deposit', *Minerals*, 8(8), p. 325.

Miller, D.J. (1991) 'Design and operating experience with the Goldsworthy mining limited BATAC jig and spiral separator iron ore beneficiation plant', *Minerals Engineering*, 4 (3-4), pp. 411-435.

Moen, K. (2006) *Quantitative measurements of mineral microstructure*, PhD Thesis, Norwegian University of Science and Technology, Trondheim, 194 p.

Mohassab, Y., Elzohiery, M., Chen, F., & Sohn, H. Y. (2016) 'Determination of total iron content in iron ore and DRI: titrimetric method versus ICP-OES analysis'. In Allanore A., Barlett, L., Wang, C., Zhang, L. and Lee, J. (eds.) *EPD Congress 2016*, Cham: Springer, pp. 125-133.

Mwanga, A., Lamberg, P., Rosenkranz, J. (2015) 'Comminution test method using small drill core samples', *Minerals Engineering*, 72, pp. 129-139.

Niiranen, K. (2015) *Characterization of the Kiirunavaara iron ore deposit for mineral processing with a focus on the high silica ore type B2*, PhD Thesis, Montanuniversität Leoben, 133 p.

NGU (2017) *Database Norwegian Ores* [online]. Available at: http://geo.ngu.no/kart/mineralressurser_mobil/ (Accessed: 12.03.2018)

NTNUa (2019) *Overview for Hitachi Analytical Variable Pressure SU6600 SEM* [online]. Available at: https://www.material.ntnu.no/lab/material/equipment/HitachiFEG.jpg (Accessed: 07.08.2019)

NTNUb (2019) *JEOL JXA-8500F Electron Probe Micro Analyzer (EPMA)* [online]. Available at: https://www.material.ntnu.no/lab/material/equipment.html (Accessed: 07.08.2019)

Parian, M., Lamberg, P., Möckel, R., Rosenkranz, J. (2015) 'Analysis of mineral grades for geometallurgy: Combined element-to-mineral conversion and quantitative X-ray diffraction', *Minerals Engineering*, 82, pp. 25-35.

Petruk, W. (2000) *Applied Mineralogy in the Mining*. 1st edition. Amsterdam: Elsevier.

Pownceby, M. I., Aral, H., and Hackl, R. (2011) 'Geometallurgy and processing of Australia's uranium deposits', *Proceedings ALTA Uranium*, ALTA Metallurgical Services, Perth, Australia, pp. 1-18.

Pownceby, M. I., and Johnson, C. (2014) 'Geometallurgy of Australian uranium deposits', *Ore Geology Reviews*, 56, pp. 25-44.

Rana Gruber (2019) *Products* [online]. Available at: http://ranagruber.no/index.php?id=33&L=-1%27 (Accessed: 20.01.2019)

Reimer, L. (2013) *Scanning electron microscopy: physics of image formation and microanalysis*, Vol. 45, Springer.

Rietveld, H.M. (1967) 'Line profiles of neutron powder-diffraction peaks for structure refinement', *Acta Crystallographica*, 22, pp. 151–152.

Rietveld, H.M. (1969) 'A profile refinement method for nuclear and magnetic structures', *Journal of Applied Crystallography*, 2, pp. 65–71.

Roberts, D., Gee, D.G. (1985) 'An introduction to the structure of the Scandinavian Caledonides', In Gee, D.G. and Sturt, B.A. (eds.) *The Caledonide Orogen – Scandinavia and Related Areas*. Chichester: John Wiley & Sons, pp. 55−68.

Roberts, D., Nordgulen, Ø. and Melezhik, V. (2007) 'The Uppermost Allochthon in the Scandinavian Caledonides: From a Laurentian ancestry through Taconian orogeny to Scandian crustal growth on Baltica', *The Geological Society of America Memoir,* 200, pp. 357-377.

Røisi, I. and Aasly, K. (2018) 'The effect of graphite filler in sample preparation for automated mineralogy– a preliminary study', *Mineralproduksjon*, 8, A1-A23. Available at: http://mineralproduksjon.no/publikasjoner/volum-8-2018/ (Accessed: 04.08.2019)

Sandvik, K.L., Rein, A., Corneliussen, O., Kleiv, R.A., Larsen E. (2012) 'Autogenmaling av jernmalm fra Kvannevann og Stortjønna', *Internal report, Norwegian University of Science and Technology*, M-RAK 2012:11.

Scarlett, N.V.Y., Madsen, I.C., Cranswick, L.M.D., Lwin, T., Groleau, E., Stephenson, G., Aylmore, M., Agron-Olshina, N. (2001) 'Outcomes of the international union of crystallography commission on powder diffraction round robin on quantitative phase analysis: samples 2, 3, 4, synthetic bauxite, natural granodiorite and pharmaceuticals', *Journal of Applied Crystallography*, 35, pp. 383–400.

SGS (2019) *Geometallurgy* [online]. Available at: https://www.sgs.com/en/mining/exploration-services/geometallurgy (Accessed: 07.08.2019)

Shao, Y., Veasy, T.J. and Rowson, N.A. (1996) 'Wet high intensity magnetic separation of iron minerals', *Magnetic and Electrical Separation*, 8, pp. 41-51.

Song, S., Lu, S., Lopez-Valdivieso, A. (2002) 'Magnetic separation of hematite and limonite fines as hydrophobic flocs from iron ores', *Minerals Engineering*, 15, pp. 415-422.

ISO (2006) *Iron ores — Determination of total iron content — Part 1: Titrimetric method after tin(II) chloride reduction* [online]. Available at: https://www.iso.org/standard/39725.html (Accessed: 08.08.2019)

ISO (2019) *Iron ores — Determination of total iron content — Part 2: Titrimetric method after titanium(III) chloride reduction* [online]. Available at: https://www.iso.org/standard/74312.html (Accessed: 08.08.2019)

Sustainable Development UN (2018) *Sustainable Development Goal 9* [online]. Available at: https://sustainabledevelopment.un.org/sdg9 (Accessed: 19.12.2018)

Søvegjarto, U. (1972) *Berggrunnsgeologiske undersøkelser i Dunderlandsdalen, Nordland*. Post graduate thesis, University of Oslo, 139p.

Søvegjarto, U., Marker, M., Graversen, O., Gjelle, S. (1989) *Storforshei 2027 IV*, berggrunnsgeologisk kart 1: 50,000. Norges geologiske undersøkelse, Trondheim.

Søvegjarto, U. (1990) 'Jernmalmer i Rana', In Rui, I.J. (eds). *Deformasjon og remobilisering av malmer*. Internal technical report no. 76, BVLI-prosjekt, pp. 154-176.

Seppälä, P., Sorsa, A., Paavola, M., Ruuska, J., Remes, A., Kumar, H., Lamberg, P., Leiviska, K. (2016) 'Development and calibration of a dynamic flotation circuit model', *Minerals Engineering*, 96-97, pp. 168-176.

The Norwegian Government (2018) 'Green shift – climate and environmentally friendly restructuring', Available at: https://www.regjeringen.no/en/topics/climate-andenvironment/climate/innsiktsartikler-klima/green-shift/id2076832/ (Accessed: 19.12.2018)

Trendall, A.F. (2002) 'The significance of iron-formation in the Precambrian Stratigraphic record', In Altermann, W. and Corcoran, P.L. (eds.) *Precambrian Sedimentary Environments: A modern Approach to Ancient Depositional Systems*. Special publication number 33, International Association of Sedimentologists. Cornwall: Blackwell Science, pp. 33-66.

Tøgersen, M.K., Ellefmo, S., Kleiv, R.A., Aasly, K. (2018) 'Mineralogy and texture of the Storforshei iron formation, and their effects on grindability', *Minerals Engineering*, 125, pp. 176-189.

Tøgersen, M.K., Aasly, K. (unpublished manuscript) 'The effect of hematite separation and texture on wet high intensity magnetic separation of a low-grade iron ore'.

Van Tonder, E., Deglon, D.A., Napier-Munn, T.J. (2010) 'The effect of ore blends on the mineral processing of platinum ores', *Minerals Engineering*, 23 (8), pp. 621−626.

Watne, T. A. K. (2001) *Geological Variations in Marble Deposits-Implications for the Mining of Raw Material for Ground Calcium Carbonate Slurry Products*. PhD Thesis, Norwegian university of Science and Technology, Trondheim.

Will, G. (2006) *Powder diffraction: The Rietveld Method and the Two Stage Method to Determine and Refine Crystal Structures from Powder Diffraction Data*. Berlin Heidelberg: Springer, pp. 41-64.

Wills, B. A., and Finch, J. (2015) *Wills' mineral processing technology: an introduction to the practical aspects of ore treatment and mineral recovery*. 8th edition. Butterworth-Heinemann, Elsevier.

Whitney, D.L., Evans, B.W. (2010) 'Abbreviations for names of rock-forming minerals', *American Mineralogist*, 95, pp. 185−187.

Xu, W., Dhawan, N., Lin, C.-L., Miller, J.D. (2013) ‘Further study of grain boundary fracture in the breakage of single multiphase particles using X-ray microtomography procedures’, *Minerals Engineering*, 46−47, pp. 89−94.

Zang, Z-X. (2016) *Rock Fracture and Blasting: Theory and Applications*. Butterworth-Heinemann

PART 2

Paper I

Mineralogy and texture of the Storforshei iron formation, and their effect on grindability

Marte Kristine Tøgersen[1,2], Rolf Arne Kleiv[1], Steinar Ellefmo[1] and Kurt Aasly[1]

[1]*Department of Geoscience and Petroleum, Norwegian University of Science and Technology, Sem Sælandsveg 1, N-7491 Trondheim, Norway*

[2]*Rana Gruber AS, Mjølanveien 29, Gullsmedvik, 8601 Mo i Rana, Norway*

(published in Minerals Engineering, 125, pp. 176-189)

Additional note: There is a typo on page 178 and 183. The d_{50} of the Kvannevann mill feed is 7 mm, not 70 mm as is written.

Minerals Engineering 125 (2018) 176–189

Contents lists available at ScienceDirect

Minerals Engineering

journal homepage: www.elsevier.com/locate/mineng

Mineralogy and texture of the Storforshei iron formation, and their effect on grindability

Marte Kristine Tøgersen[a,b,*], Rolf Arne Kleiv[a], Steinar Ellefmo[a], Kurt Aasly[a]

[a] Department of Geoscience and Petroleum, Norwegian University of Science and Technology, Sem Sælandsveg 1, N-7491 Trondheim, Norway
[b] Rana Gruber AS, Mjølanveien 29, Gullsmedvik, 8601 Mo i Rana, Norway

ARTICLE INFO

Keywords:
Storforshei iron formation
Surface hardness
Texture
Ore mineralogy
Grindability

ABSTRACT

Investigating how ore mineralogy and texture affect the recovery from the processing plant is important for any mining operation. The results will assist in production planning and optimising the utilisation of a deposit. Easily available validated tests are desirable and useful.

The Storforshei iron formation (IF) consists of several iron oxide deposits with mineralogical and textural differences. Although the Fe grades of the ores are similar, mineralogical and textural characteristics of the deposits affect the individual recoveries from the magnetic separation. For this paper three of the ore deposits were sampled, and important mineralogical and textural properties were investigated and tested. The investigations included geological mapping and optical microscopy, and the test work involved surface hardness measurements by Schmidt hammer and Equotip, and autogenous milling tests (i.e., grindability). The aim of the study was to investigate whether ore mineralogy and textures can be correlated to surface hardness measurements, and whether these three parameters can be used to evaluate grindability. The ores were classified into six ore types based on mineralogy and textures. The results show that the ore mineralogy and texture influence the surface hardness. Fine-grained ore types with irregular-to-no visible grain boundaries have higher surface hardness than coarser-grained ore types with straight grain boundaries. Furthermore, surface hardness measurements and grindability evaluations (using throughput (kg/h) and specific energy consumption (kWh/tonne)) of samples from three of the iron oxide deposits indicate that grindability decreases with increasing surface hardness. The relationship found between the parameters ore mineralogy, texture, surface hardness, and grindability suggests that geological mapping and surface hardness measurements can be used to evaluate grindability, and thus assess ore processing performance.

1. Introduction

Rana Gruber AS (RG AS) currently mines iron ore from underground and open pit operations in the Dunderlandsdalen valley, about 30 km north east of Mo i Rana, Nordland County, Norway. Four million tonnes of iron ore are mined from the Kvannevann deposit annually, and the main products are hematite and magnetite concentrates. There are 13 ore deposits in the Storforshei IF, with varying mineralogical and textural properties leading to variable recovery. The mineral processing at RG AS includes autogenous (AG) milling, wet low-intensity magnetic separation (LIMS) followed by wet high-intensity magnetic separation (WHIMS). The AG mills are in closed circuit, with 800 μm screens. The d_{80} of the mill circuit product is 210 μm.

The Kvannevann- and Stortjønna iron ores have a total Fe content of 34 wt% (NGU, 2017). The Stortjønna open pit was abandoned in 2013 after 2 years in production because recoveries did not reach expected levels, indicating that other properties than grade affect recovery. Samples were collected from the Kvannevann and Stortjønna deposits. Additionally, the Stensundtjern deposit, a possible upcoming mining target in the Storforshei IF, was included in this study.

The aim of the research presented in this paper was to investigate the effect of ore mineralogy, texture, and surface hardness on the ore grindability and on the particle size distribution of the mill circuit products. The throughput (kg/h) and specific energy consumption (kWh/tonne) in the AG mill were used to determine grindability.

The classification of ore types is based on mineralogical and textural characteristics of the iron ores. Contrary to previous work (e.g., Lopera, 2014; Mwanga et al., 2015), the classification is performed before surface hardness measurements and grindability testing. This approach is similar to the work of Voordouw et al. (2010) where platinum mineral assemblages were grouped based on ore mineralogy and trace elements. Lund (2013) defined preliminary geometallurgical ore types

* Corresponding author at: Department of Geoscience and Petroleum, Norwegian University of Science and Technology, Sem Sælands vei 1, N-7491 Trondheim, Norway.
E-mail address: marte.togersen@ntnu.no (M.K. Tøgersen).

https://doi.org/10.1016/j.mineng.2018.06.009
Received 30 April 2017; Received in revised form 12 May 2018; Accepted 6 June 2018

first according to mineralogy and geochemistry, and later included ore texture. Others like Lopera (2014) and Niiranen (2015) used surface hardness and mill tests to divide ores into different comminution domains.

The main objective of the present study was to provide increased predictability in the processing of highly metamorphosed iron ores. If surface hardness can be used to evaluate grindability, the iron ores can be tested by easy, fast and non-destructive methods prior to mineral processing.

The main research questions were:

- Is it possible to correlate ore mineralogy and texture with surface hardness?
- How is grindability affected by ore mineralogy and textures?
- Can surface hardness be used to evaluate grindability?

2. Background

2.1. Geological setting

The Storforshei IF is a metasedimentary iron formation and part of the Dunderland formation, located in the Uppermost Allochthon in the Norwegian Caledonides (Sovegjarto, 1972; Grenne et al., 1999). The IF belongs to a series of iron formations located between the city of Mosjøen (lat. 65°20′) in the south to the city of Tromsø in the north (lat. 69°40′), a distance of 550 km (Melezhik et al., 2015). The Storforshei IF is the only iron formation currently mined in Norway, and the main economic minerals according to NGU (2017) are hematite (40%) and magnetite (5%). The Neoproterozoic host rocks are mainly marbles and mica schists (Bugge, 1948; Sovegjarto, 1972). The sedimentary precursor of the IF was deposited on a carbonate-silica-rich shelf which was located either near a microcontinent or on the margin of Laurentia (e.g., Grenne et al., 1999; Melezhik et al., 2015). After deposition, the iron formation was subjected to several deformation phases, dominated by the Caledonian orogeny where Laurentia and Baltica collided (Sovegjarto, 1972; Roberts and Gee, 1985). The Storforshei IF was subjected to amphibolite facies metamorphism and is intensely banded reflecting mineralogy and textures (Sovegjarto, 1972; Ellefmo, 2005). The geology of the relevant area is shown in Fig. 1. The locations of the sampled deposits; Kvannevann, Stortjønna and Stensundtjern are highlighted on the map. Stensundtjern is a separate ore horizon located to the west in the Dunderlandsdalen valley. Kvannevann and Stortjønna belong to the same ore horizon. Kvannevann is larger than Stensundtjern, while Stortjønna is notably smaller than the other two deposits.

2.2. Previous relevant geometallurgical research

Lund (2013) quantified mineral processing properties of apatite-magnetite ores and developed a geometallurgical program for the Malmberget iron ore (Sweden), which enabled improved production and resource utilisation (Lund, 2013) based on a comprehensive characterisation and analyses of the iron ores. However, no surface hardness measurements or grindability tests were reported. Niiranen (2015) performed comminution tests on three apatite-magnetite ore types from the Kiirunavaara iron ore. The ore types were defined by their SiO_2 and P contents. After comminution, one ore type was divided into two subgroups, and a link between mineralogy and grindability was established. Available literature (i.e., Lund, 2013; Niiranen, 2015) focuses mainly on high-grade magnetite dominant ores; hence the present study contributes to increased knowledge on the processing behaviour of low-grade hematite ores.

The Schmidt hammer method is widely used in concrete and rock characterisation (e.g., Deere and Miller, 1966; Szilágyi and Borosnyói, 2009). Viles et al. (2011) used the Schmidt hammer and Equotip methods on dimension stone and demonstrated difficulties in comparing the two methods. Mining related research has focused on developing simple procedures to categorise ore types to predict comminution behaviour (e.g., Hunt et al., 2013; Lopera, 2014). Rock mechanical tests such as the JK Tech drop weight test (Napier-Munn et al., 1996), the JK Rotary Breakage Test (Shi et al., 2009), the SMC test (Morrell, 2004), and standard Bond grindability test (Bond, 1952) require at least 10 kg of material. The amount of material required for the procedures may, according to Mwanga et al. (2015), be an issue for greenfield exploration activities. Hence, Mwanga et al. (2015) developed the geometallurgical comminution test (GCT) as an approach to achieve representative results for test batches of 220 g material. The GCT is a small-scale comminution test which makes use of a lab-scale jaw crusher, a screen, and a small laboratory tumbling mill. Mwanga et al. (2015) argued that the GCT is a cost and time-efficient test that provides substantial data from limited sample sizes.

Ores are additive if the grindability of an ore blend is the same as the weighted average grindability of the ore types in the blend (e.g., Van Tonder et al. 2010 and the references therein). To evaluate grindability of an ore with notable internal variability in mineralogy and texture, larger homogenised test batches are needed to get representative and reliable results. Van Tonder et al. (2010) investigated mineral processing of platinum ores and the effect of ore blending in Rustenburg, South Africa. The ore blend consisted of four rather homogenous different ore types with a high inter-ore-type variability. They found through lab-scale tests that blends of ore types with varying metallurgical properties displayed non-additive characteristics. Larger test batches will therefore improve the prediction capabilities of the production-scale non-additive grindability.

Understanding the effect of mineralogy, geochemistry, lithology, and alteration on the comminution processes are valuable for processing any ore. Hunt et al. (2013) successfully modelled comminution parameters using information obtained from drill core logs, together with measured comminution data collected on site. The drill core log information included lithology and alteration type, as well as mineralogy and chemistry data. Hunt et al. (2013) included Semi-Autogenous Grinding Power Index (SPI), Bond Work Index (BWI), and Julius Kruttschnitt Mineral Research Centre (JKMRC) drop weight test (A*b) as parameters to characterise the comminution behaviour. These indices and tests were selected because they can be conducted at low cost and on drill core samples. Hunt et al. (2013) stressed the need to classify sample sets based on alteration type and lithology to identify correlations between mineralogy or chemistry and grindability. Lopera (2014) used surface hardness data together with mineralogy, chemistry, and a range of comminution tests to define comminution domains. Surface hardness measurements were collected from drill cores and hand specimens representing different lithologies. Surface hardness values varied between lithologies and were low in tectonically-induced weakness zones. Within each lithology variability was low (Lopera, 2014). Kekec et al. (2006) investigated the effect of rock textures on comminution. The investigations were based on experiments on different types of rock (granite, marble, travertine, and andesite). They observed that rocks of similar origin show differences in the crushing and grindability behaviour caused by the differences in rock texture. Xu et al. (2013) found that the specific energy required for breakage of a copper ore increases with decreasing particle size, and that grain boundary fractures require relatively low specific energy. By characterising the geochemistry, mineralogy, and grindability of the cemented layer, Philander and Rozendaal (2011) improved the mill design to accommodate a complex calcium-magnesium-rich cemented layer, part of the clastic Cainozoic ore-bearing sequence in the Namakwa Sands heavy mineral deposit (Brand-se-Baai, South Africa), previously not viable for production.

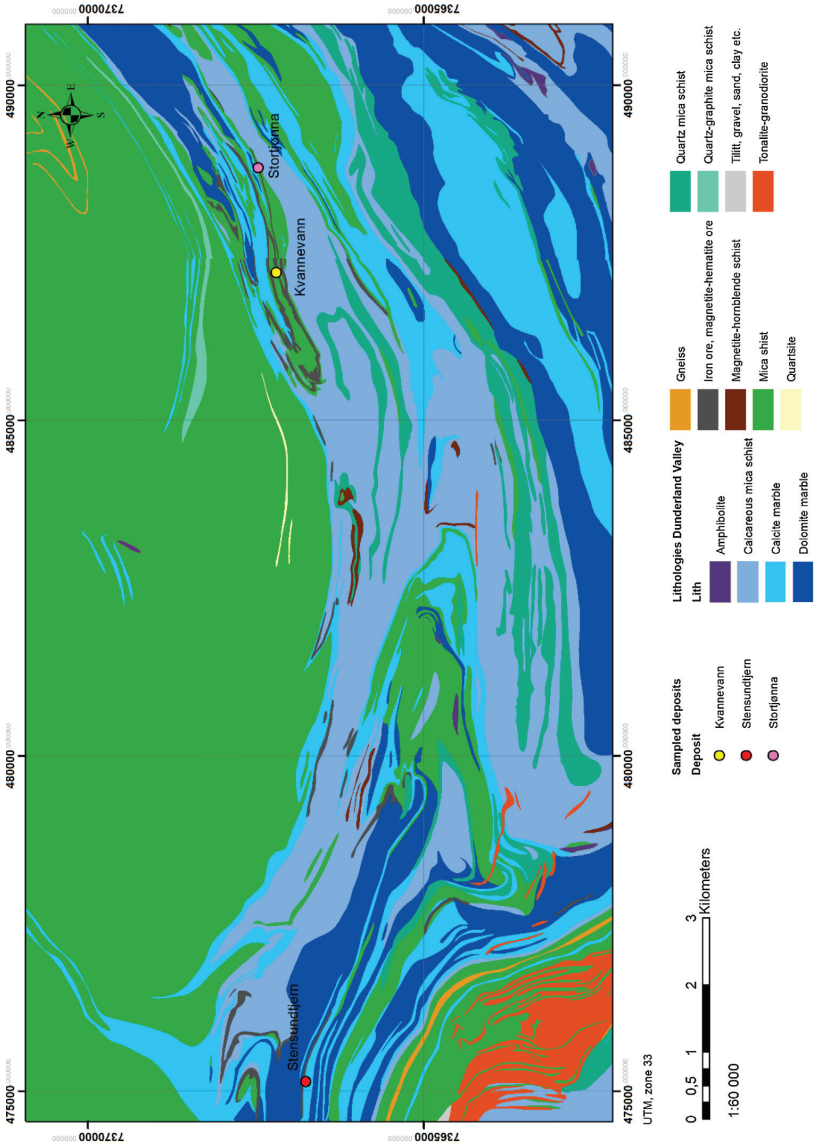

Fig. 1. Geology of the Storforshei area, showing the location of the magnetite-hematite iron ores in Storforshei iron formation. The geology is compiled from Sovegjarto et al. (1989) and Gjelle et al. (1991).

3. Materials and methods

3.1. Materials

The Kvannevann-, Stortjønna-, and Stensundtjern iron ore deposits found in the Storforshei IF were sampled for pilot scale testing. One truck-load (40 tonnes) from blasts in the geographical centre (Fig. 1) of each deposit was crushed with a mobile jaw crusher. The sampling point was at the end of the associated conveyer belt. The entire width of the material stream was collected into a big bag. Representative samples from the conveyer belt were obtained by collecting several increments at regular intervals during crushing (3 × 10 s per big bag). A total of 2 tonnes, in two big bags, were sampled from the conveyer belt for each deposit. D_{50} of the Kvannevann, Stensundtjern, and Stortjønna crusher products were 70 mm, 38 mm, and 100 mm, respectively, while the top size was 300 mm in all three products. In the lab, one subsample for particle size distribution analysis was split from each 2-tonne sample by quartering. Hand specimens (5–10 kg) displaying mineralogical and textural variations were sampled from the three deposits. Polished thin sections were made from 20 of the selected hand specimens, at the Department of Geoscience and Petroleum. Also, split drill cores (42 mm diameter) were made available by RG AS for surface hardness tests.

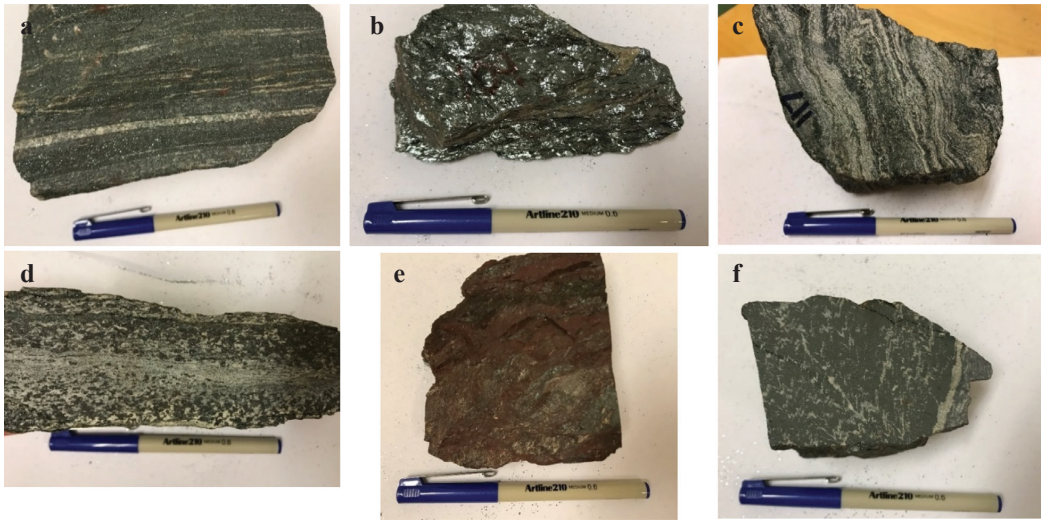

Fig. 2. (a) Granular-Hematite, (b) Specular-Hematite, (c) Hematite-Magnetite, (d) Magnetite-Ore, (e) Mylonitic-Hematite, and (f) Massive-Hematite. (The scale is 13.5 cm).

3.2. Methods

3.2.1. Microscopy

A Nikon Eclipse E600 petrographic light microscope with Diagnostic Instruments Inc. Spot IN320 colour digital camera was used to document and identify mineralogy and textures. A Hitachi SU-6600 low vacuum field emission scanning electron microscope (SEM) with two Bruker XFlash 5010 energy-dispersive X-ray spectroscopy (EDS) detectors, was used for collecting x-ray analyses of minerals, with a 30 s counting time per point. The SEM was run at 20 kV and 0.49 nA beam current.

3.2.2. Surface hardness measurements

A *Proseq Type L Original Schmidt hammer* (Schmidt hammer) was used to measure surface hardness of boulders, and a *Proseq Type D Equotip 3* (Equotip) instrument was used on drill cores. Both instruments measure the rebound energy after delivering a given impact energy to the sample. The Schmidt hammer has an impact energy of 0.735 N m and measuring range from 10 to 70 N/mm^2 compressive hardness (Proseq, 2016). The Equotip instrument delivers an impact energy of 11 N mm to the samples, and it can measure a maximum sample hardness of 890 HLD. The Leeb Hardness (HL) is calculated from the rebound velocity v_r and the impact velocity v_i ratio. The "D" in HLD reflects the type of Equotip used (Proseq, 2016).

The Schmidt hammer measurements were conducted on non-weathered surfaces of roughly 0.5 m^3 boulders obtained from blasts. Twenty measurements were conducted both parallel and perpendicular to the foliation. For boulders with no foliation, 20 measurements were collected from only one surface. Following the standard of the International Society for Rock Mechanics (1978), the 10 lowest values were discarded from each dataset of 20 measurements.

The selection of drill cores for Equotip measurement was based on the drill core logs and their locations in the iron formation. Based on procedures defined by Lopera (2014) and local lithological variations, measurements were taken every 3 cm along the core. All measurements under 100 HLD were discarded (only 5 out of 5689 measurements). The low HLD values are assumed to be incorrect measurements because of temporarily inaccuracies in the execution of the measuring procedures.

A total of 5689 points on drill cores were measured using the Equotip, while 34 boulders were measured using the Schmidt hammer. All ore types were measured by the Equotip, while all but the ore types Hematite-Magnetite and Magnetite-Ore (Section 4.1) were measured by Schmidt hammer. The reason for not measuring these two ore types with Schmidt hammer was lack of suitable specimens.

3.2.3. Pilot-scale autogenous (AG) milling

Wet closed-circuit pilot-scale milling of the Kvannevann, Stensundtjern, and Stortjønna samples were performed using an AG mill (inner dimensions: Ø 0.69 m × L 0.80 m) and a 0.760 mm Sweco screen. The initial charge settings for the mill circuit were derived from previous lab work conducted on the Storforshei iron ores (Sandvik et al., 2012). The initial charge was set to 250 kg, and the mill was run at 36 rpm (i.e., 71.3% of critical speed). During operation, the mill was fed with a series of discrete solid batches and a continuous addition of water corresponding to a pulp thickness of 60 wt% solids. The feed rate was manually adjusted to obtain a stable mill charge. For Kvannevann, torque, power, mill charge, and water feed rate were recorded automatically every second, whereas manual logging at 2-minute intervals was used when processing the Stensundtjern and Stortjønna samples. The mill feed and the mill circuit product were sampled for all three deposits.

4. Results

4.1. Ore types and mineral textures

4.1.1. Granular-Hematite

The Granular-Hematite ore type demonstrates a sugar-grained hematite texture, supported by more competent mm-sized quartz layers (Fig. 2a). By measuring the longest axis in thin sections, the average grain size of hematite was estimated to 200 μm. Granular-Hematite is characterised on the microscale by a random orientation of hematite grains within the layers. The hematite is equigranular, with tabular shape, and has straight grain boundaries. Disseminated hematite grains (≈10 μm) occur in the quartz-rich layers. Some grains of carbonate minerals are present (Fig. 3a).

4.1.2. Specular-Hematite

Deer et al. (1992) define specular hematite or specularite as "crystalline material with metallic lustre." Specular-Hematite has a

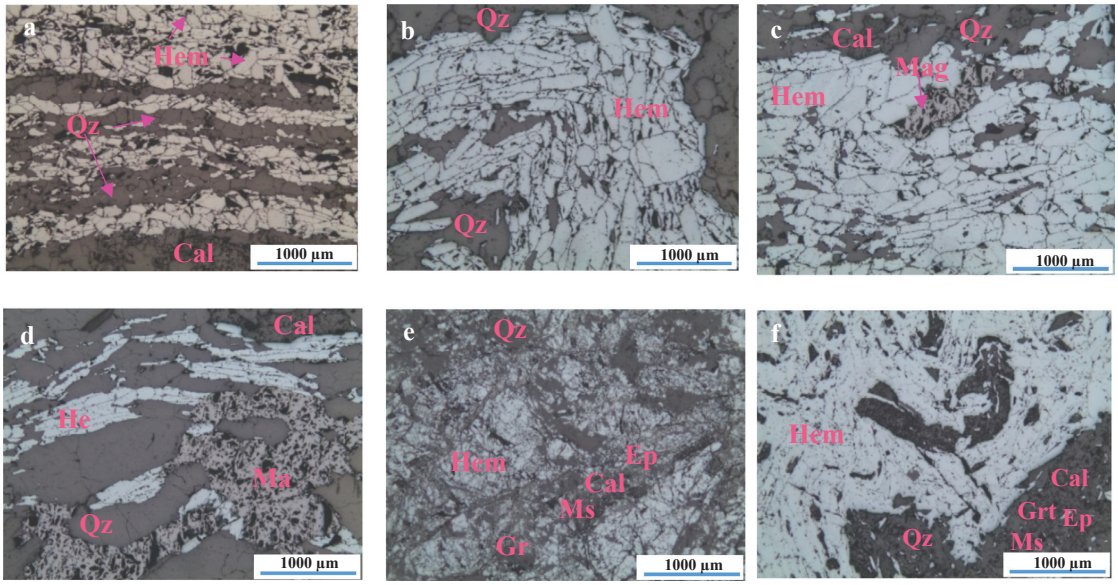

Fig. 3. Reflected light photomicrographs showing typical hematite texture in the different ore types. (a) Granular-Hematite, (b) Specular-Hematite, (c) Hematite-Magnetite, (d) Magnetite-Ore, (e) Mylonitic-Hematite, and (f) Massive-Hematite. Mineral abbreviations after Whitney and Evans (2010).

characteristic flaky appearance in hand specimen (Fig. 2b), and is frequently banded, with alternating mm-sized layers of quartz or carbonates and hematite. The layers are usually folded (Fig. 3b). Under the microscope, Specular-Hematite is similar to the Granular-Hematite, demonstrating equigranular textures and straight grain boundaries. However, Specular-Hematite is distinguished by the overall grain size, averaging between 400 and 500 µm. Hematite grains are tabular, elongated, and oriented parallel to the layering (Fig. 3b).

4.1.3. Hematite-Magnetite

The Hematite-Magnetite ore type is dominated by hematite and shows magnetite content typically in the range of 1–2% in Kvannevann and 9–10% in specimens from Stensundtjern. The texture of the hematite in hand specimens varies between sugar-grained and flaky. It can also be banded, with quartz and/or calcite layers in-between hematite/magnetite layers (Fig. 2c) and is typically folded similarly to the Specular-Hematite. The average hematite grain size is 300 µm with typical shape preferred orientation (SPO), whereas the grain size of magnetite is typically 1 mm (Fig. 3c), without any visible SPO. Grain boundaries are straight within the hematite layers, and towards the quartz-calcite layers. Magnetite grain boundaries are typically irregular. The grain shape of iron oxides differs, with the magnetite having an equant-irregular shape, while the hematite is tabular (Fig. 3c).

4.1.4. Magnetite-Ore

The Magnetite-Ore type is coarse-grained (average grain size 0.5 cm) (Figs. 2d and 3d), and consists mainly of magnetite, with minor quartz, calcite, and small amounts of hematite (< 3%). The magnetite grains are typically equant to irregular, while the hematite is tabular. The grain boundaries are straight to irregular.

4.1.5. Mylonitic-Hematite

Mylonitic-Hematite is, in hand specimen, characterised by a distinct red colour (Fig. 2e). Hematite, quartz, and calcite grains (10–20 µm) are disseminated in a fine-grained matrix of gangue minerals, where individual minerals are difficult to distinguish. However, quartz, hematite, calcite, epidote, mica, and garnet were identified by SEM-EDS analyses. Some remnants of hematite grains (200–500 µm) can be found, with cracks filled with fine-grained recrystallised hematite, and gangue minerals (Fig. 3e). The few observed grain boundaries are irregular. The term Mylonitic-Hematite refers to the presence of textures related to tectonic activity.

4.1.6. Massive-Hematite

The Massive-Hematite ore type is a fine-grained hematite ore, with massive hematite and irregularly folded layers or veins of fine-grained gangue (Fig. 2f). Individual hematite grains are not easily distinguished, but grain boundaries between gangue and hematite appear to be irregular (Fig. 3f). SEM-EDS show that the gangue mainly consist of quartz, calcite, garnet, epidote, and mica.

4.2. Distribution of lithologies

The lithologies defining the Storforshei IF iron ores were previously established during drill core logging by RG AS. For the present study, the lithologies were re-defined to comprise the six ore types defined in this paper and hence, improve the link between ore lithology and grindability. However, by using the original lithology descriptions, some correlations can be made (Table 1).

Fig. 4 shows the relative distribution of the original ore lithologies, as well as the most important host rocks in the three deposits. The relative distribution is based on the length of intersection in drill holes. Ore lithologies that could not be linked to a specific ore type were

Table 1
Lithologies logged by RG AS, and their possible corresponding ore types.

Lithologies logged by RG AS	Ore types
Hematite ore (grained or specular annotation are often used in the comments)	Granular-Hematite, Specular-Hematite, can also include Massive-Hematite and Mylonitic-Hematite
Magnetite-hematite ore	Hematite-Magnetite
Magnetite ore	Magnetite-Ore
Hematite mylonite	Mylonitic-Hematite

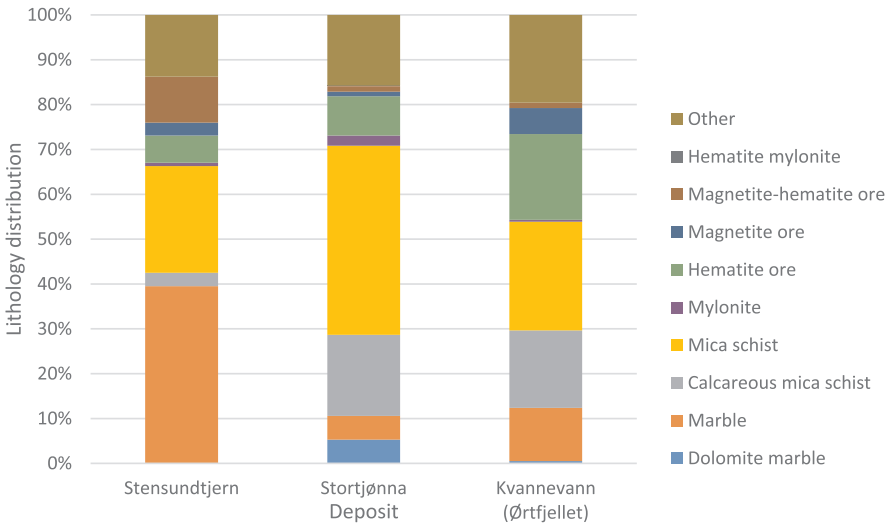

Fig. 4. Lithological composition of the three deposits.

combined in one group (Other). The Kvannevann data in Fig. 4 represents a larger area (Ørtfjellet) and contain data from some small ore deposits in addition to the Kvannevann deposit. Small variations are known in the ores of the Ørtfjellet area, but to the best knowledge of the authors, Fig. 4 is a good representation of the lithologies observed in the Kvannevann deposit.

The most frequent ore type in Kvannevann is the Hematite ore, followed by the group "Other". Additionally, Kvannevann contains significant amounts of magnetite ore with minor magnetite-hematite ore. Stortjønna also contains magnetite ore. The hematite mylonite is found in minor content in Stortjønna, however, based on recent field observations it also occurs in the Ørtfjellet area. Stensundtjern contains hematite ore, but is dominated by magnetite-hematite ore and has substantial amounts of magnetite ore. The main host rocks are calcareous mica schist, mica schist, and marbles. Mylonite is predominantly found in Stortjønna but occur in all three deposits. Mylonite is used as a collective term for very fine-grained rocks that are found in veins at the ore-host rock contact. They are dominated by garnet, with varying contents of quartz, manganocalcite, and epidote.

4.3. Surface hardness results

Minitab®17 (Minitab Inc., 2017) was used to prepare and analyse cumulative distribution plots for the surface hardness data. The data have been examined graphically and summary statistics calculated to identify differences between deposits and ore types. Schmidt hammer and Equotip measurements were not conducted on the same specimen; hence, they cannot be plotted in a scatter plot to investigate correlations. The results can, however, be used to compare the surface hardness of the different ore types.

4.3.1. Surface hardness by Schmidt hammer

Summary statistics from the Schmidt hammer measurements by Schmidt hammer of samples from Kvannevann, Stensundtjern, and Stortjønna are listed in Table 2. The lowest average surface hardness measured are in Specular-Hematite from Kvannevann and Stensundtjern, and Granular-Hematite from Kvannevann. Mylonitic-Hematite in Stortjønna has the highest surface hardness measured by Schmidt hammer. The surface hardness values in Kvannevann have a higher range than the surface hardness values in Stensundtjern, which is also reflected in the lower standard deviation in the surface hardness values in Stensundtjern. The maximum values for Massive-Hematite and Mylonitic-Hematite in Stortjønna are higher than the maximum values for Granular-Hematite and Specular-Hematite in Kvannevann and Stensundtjern, while the minima are similar for the four ore types.

Table 2
Summary statistics of Schmidt hammer measurements of Kvannevann, Stensundtjern, and Stortjønna. n.a. = not available.

Schmidt hammer measurement (N/mm^2)				
	Granular-Hematite	Specular-Hematite	Mylonitic-Hematite	Massive-Hematite
Mean				
Kvannevann	38	33	n.a.	n.a.
Stensundtjern	47	35	n.a.	n.a.
Stortjønna	n.a.	n.a.	52	45
Standard deviation				
Kvannevann	8.4	8.1	n.a.	n.a.
Stensundtjern	4.7	4.9	n.a.	n.a.
Stortjønna	n.a.	n.a.	9.9	8
Max				
Kvannevann	56	52	n.a.	n.a.
Stensundtjern	56	47	n.a.	n.a.
Stortjønna	n.a.	n.a.	75	65
Min				
Kvannevann	22	17	n.a.	n.a.
Stensundtjern	38	27	n.a.	n.a.
Stortjønna	n.a.	n.a.	34	29
Number of observations				
Kvannevann	160	260	n.a.	n.a.
Stensundtjern	40	60	n.a.	n.a.
Stortjønna	n.a.	n.a.	60	80

The differences in surface hardness values by Schmidt hammer are illustrated with cumulative distribution plots (Fig. 5). An apparent difference in surface hardness can be seen, with Stortjønna having a mean of 48 N/mm^2, Stensundtjern with a mean value of 40 N/mm^2, and Kvannevann with a mean value of 35 N/mm^2.

Fig. 6 illustrates surface hardness for the different ore types. Mylonitic-Hematite shows the highest surface hardness values, with P_{80} at 60 N/mm^2, while Massive-Hematite samples from Stortjønna and

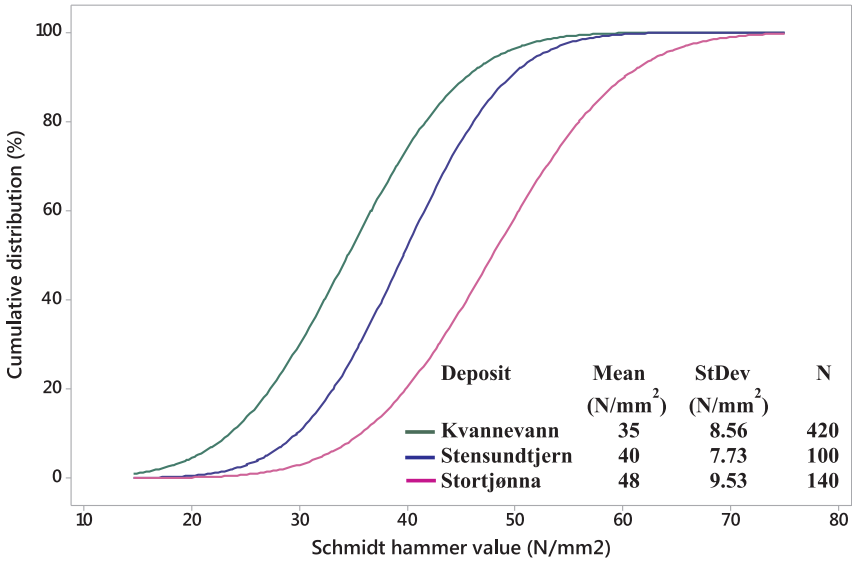

Fig. 5. Cumulative distribution of surface hardness values by Schmidt hammer for each deposit irrespective of ore type.

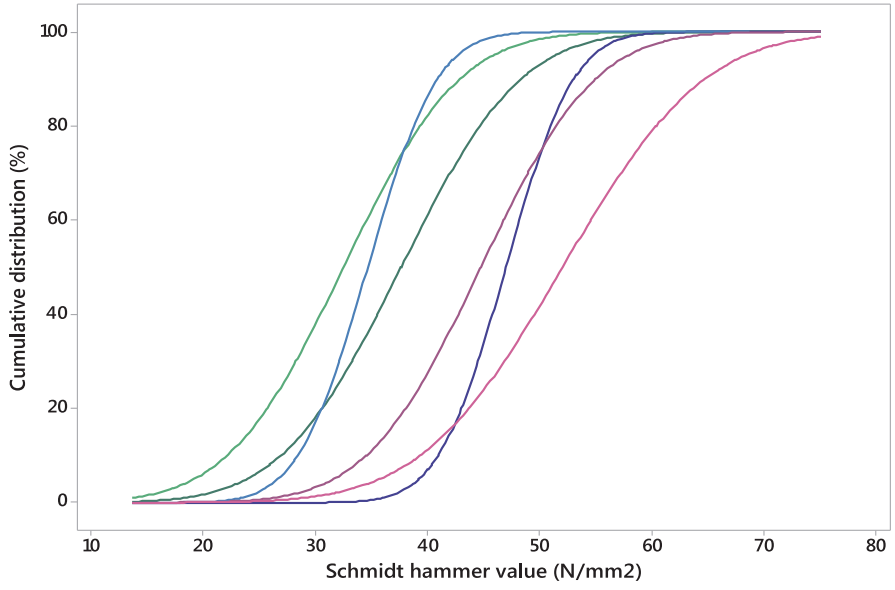

Deposit	Ore type	Mean (N/mm²)	StDev (N/mm²)	N
Kvannevann	Granular-Hematite	38	8.35	160
Kvannevann	Specular-Hematite	33	8.10	260
Stensundtjern	Granular-Hematite	47	4.72	40
Stensundtjern	Specular-Hematite	35	4.86	60
Stortjønna	Massive-Hematite	45	7.97	80
Stortjønna	Mylonitic-Hematite	52	9.91	60

Fig. 6. Cumulative distribution of surface hardness values by Schmidt hammer in the ore types in the three deposits.

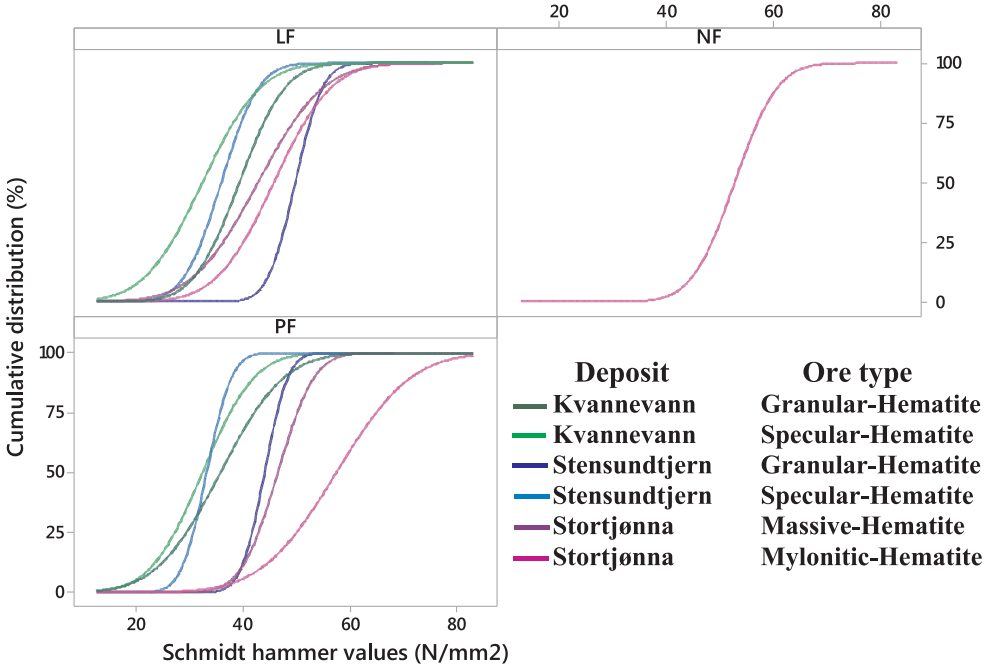

Fig. 7. The cumulative distribution of surface hardness by Schmidt hammer for the ore types, divided into measurements collected perpendicular to the foliation (PF), parallel to the foliation (LF) and without any foliation (NF).

Granular-Hematite from Stensundtjern have the second highest values, with P_{80} at 52 N/mm^2 and 51 N/mm^2, respectively. For Kvannevann Granular-Hematite P_{80} is 44 N/mm^2. Specular-Hematite from Kvannevann and Stensundtjern have the lowest surface hardness values by Schmidt hammer with a P_{80} at 38 N/mm^2 and 39 N/mm^2, respectively.

In Fig. 7, the surface hardness values by Schmidt hammer are displayed according to ore type, the presence or absence of foliation, and the measurement direction. Most of the ore types are banded, and measurements have been collected both parallel and perpendicular to the foliation (LF and PF respectively). Some samples of Mylonitic-Hematite showed no foliation (NF). Surface hardness of Granular-Hematite and Specular-Hematite show a deposit-dependent variation and have highest values both for LF and PF in Stensundtjern. For Mylonitic-Hematite, PF-values are higher (P_{80} of 66 N/mm^2) than the LF-values (P_{80} of 53 N/mm^2). For Mylonitic-Hematite (NF) have a P_{80} of 57 N/mm^2 (Fig. 7).

4.3.2. Surface hardness by Equotip

Summary statistics for Equotip measurements according to ore type and deposit are reported in Table 3. Mylonitic-Hematite in Stortjønna returned the highest average surface hardness (711 HLD), while Granular-Hematite and Specular-Hematite in Kvannevann returned the lowest surface hardness (533 HLD and 575 HLD respectively). The maximum and minimum surface hardness values appear to be random for all ore types in the three deposits. The maximum surface hardness values for ore types in Stortjønna are at the higher end of the scale, while all ore types in Kvannevann have minimum surface hardness under 200 HLD. The standard deviation is high for all ore types in the three deposits, especially for Granular-Hematite, Mylonitic-Hematite, and Massive-Hematite in Stortjønna. Mylonitic-Hematite and Massive-Hematite were not found in the core logs from Kvannevann and Stensundtjern.

Fig. 8 shows the cumulative distribution of surface hardness values using Equotip for all deposits. Stortjønna has the highest values, with a P_{80} of 762 HLD, followed by Stensundtjern and Kvannevann, with P_{80} of 731 HLD and 672 HLD, respectively. The average surface hardness in Stortjønna is 650 HLD, whereas it is 635 HLD in Stensundtjern, and 571 HLD in Kvannevann. The number of measurements (N) in each deposit varies (Fig. 8).

The surface hardness values by Equotip for the ore types and their cumulative distribution are shown in Fig. 9. Average surface hardness varies between 711 HLD for Mylonitic-Hematite and 576 HLD for Specular-Hematite.

The surface hardness measurements of the ore types in the three deposits using the Equotip are compared in Fig. 10. Specular-Hematite, Hematite-Magnetite, and Magnetite-Ore types display similar surface hardness values by Equotip in the three deposits. The Granular-Hematite from Kvannevann have lower surface hardness by Equotip than Granular-Hematite from Stensundtjern and Stortjønna. This is also apparent from Table 3.

4.4. Pilot-scale AG milling

To obtain a stable circuit, the solid feed rate had to be adjusted for each deposit sample. The final steady-state solid feed rates, the resulting mill torque, and mill power are summarised in Table 4. Figs. 11–13 show the data recorded during the experiments.

4.5. Particle size distribution

Samples collected from both the mill feed and the mill circuit product were sieved on a rot-tap sieve shaker using the W.S. Tyler sieves series. Fig. 14 presents the particle size distribution (PSD) for the mill feed of all three deposit samples. The d_{50} values were found to be 70 mm, 38 mm, and 100 mm for Kvannevann, Stensundtjern, and Stortjønna, respectively.

Table 3
Summary statistics for the Equotip measurements divided into ore types and deposits. n.a. = not available.

Equotip measurements (HLD)						
	Granular-Hematite	Specular-Hematite	Hematite-Magnetite	Magnetite-Ore	Mylonitic-Hematite	Massive-Hematite
Mean						
Kvannevann	533	575	619	668	n.a.	n.a.
Stensundtjern	651	595	645	649	n.a.	n.a.
Stortjønna	649	626	633	669	711	648
Standard deviation						
Kvannevann	115.4	118	110.4	110.3	n.a.	n.a.
Stensundtjern	115.2	114.5	103.2	122.8	n.a.	n.a.
Stortjønna	133.8	121.2	113.9	104.3	136.5	137.7
Max						
Kvannevann	832	878	807	874	n.a.	n.a.
Stensundtjern	844	834	814	860	n.a.	n.a.
Stortjønna	865	852	875	864	896	864
Min						
Kvannevann	106	128	129	195	n.a.	n.a.
Stensundtjern	236	250	363	155	n.a.	n.a.
Stortjønna	167	154	183	251	378	126
Number of observations						
Kvannevann	1153	1852	390	195	n.a.	n.a.
Stensundtjern	697	471	269	286	n.a.	n.a.
Stortjønna	237	90	58	120	39	440

Fig. 15 shows the particle size distribution of the mill circuit products from Kvannevann, Stensundtjern, and Stortjønna. The Stortjønna mill circuit product has a $d_{80} \approx 147$ μm and is thus the finest product. The Kvannevann mill circuit product also has relatively fine material with $d_{80} \approx 170$ μm. The Stensundtjern mill circuit product shows a coarser particle size distribution compared with the other two with $d_{80} \approx 280$ μm. Stortjønna contains substantial amounts of fines (< 38 μm) compared to Kvannevann and Stensundtjern.

5. Discussion

5.1. The relationship between ore mineralogy, texture, and surface hardness

The defined ore types show significant differences in ore mineralogy and textures. The most pronounced characteristics can be summarised as:

Granular-Hematite and Specular-Hematite are mainly similar, although some differences in hematite grain shapes are seen in hand specimen (Fig. 2). Hematite is mostly banded and relatively coarse-grained (200–500 μm), with small hematite grains (≈10 μm) disseminated in bands dominated by quartz or carbonates.

Hematite-Magnetite and Magnetite-Ore have a coarse-grained

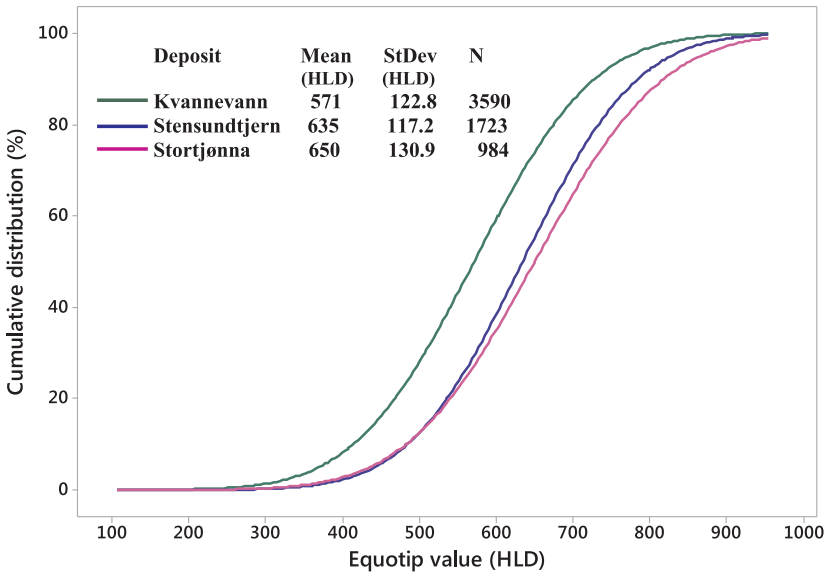

Fig. 8. Cumulative distribution of surface hardness values by Equotip in Kvannevann, Stensundtjern, and Stortjønna.

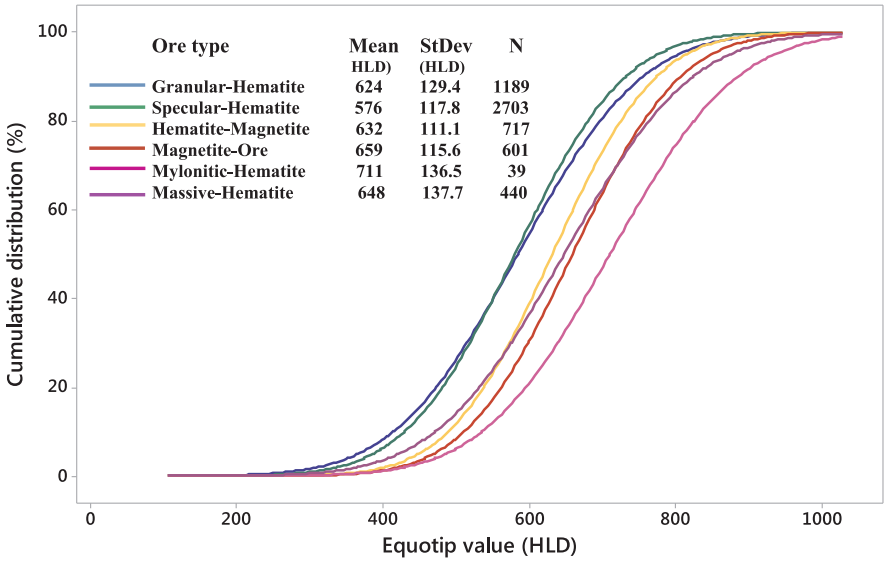

Fig. 9. The cumulative distribution of surface hardness values by Equotip for the ore types regardless of the deposits.

texture, especially the magnetite grains, which range from 1 to 5 mm (Fig. 3c and d) (the coarsest magnetite is found in Magnetite-Ore). Hematite and magnetite have straight and irregular grain boundaries, respectively. Hematite-Magnetite and Magnetite-Ore are mainly distinguished by the high hematite content in Hematite-Magnetite.

Mylonitic-Hematite typically contains fine-grained hematite, disseminated in a fine-grained matrix of gangue minerals. There are also relics of coarse-grained hematite in the matrix.

Massive-Hematite is dominated by fine-grained hematite, without clearly distinguishable grain boundaries, with veins consisting of a

Table 4
Solid feed rate, mill torque, and mill power during steady-state milling of the Kvannevann, Stensundtjern, and Stortjønna ores.

	Time (hh:mm)	Solid feed rate (kg/h)	Mill torque (kN)	Mill power (kW)
Kvannevann	01.30–03.00	266	530.5	2.2
Stensundtjern	01:00–03:00	150	367.5	1.6
Stortjønna	02:30–04:30	100	522.6	2.2

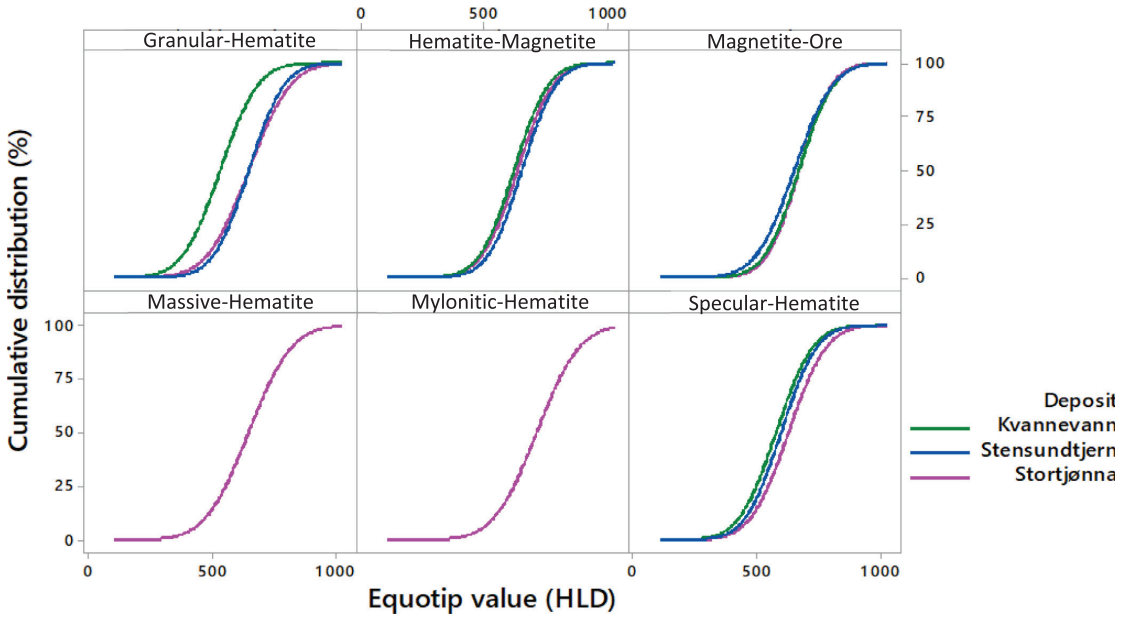

Fig. 10. Surface hardness values by Equotip for ore types in the three deposits.

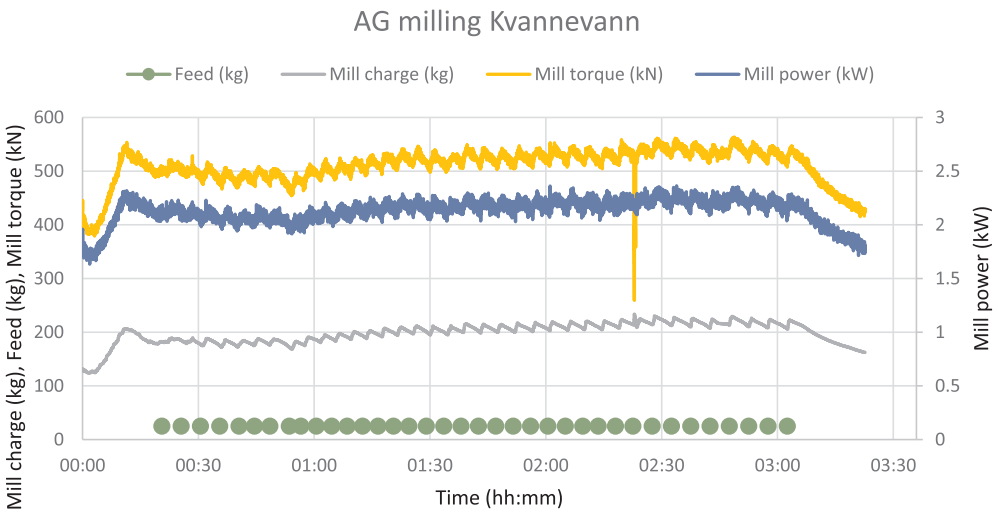

Fig. 11. Kvannevann milling results.

matrix of fine-grained minerals, mainly quartz, mica, feldspar, epidote, and garnet. Grain boundaries between hematite and gangue appear to be irregular.

Quantified by the Equotip, the Granular-Hematite in Kvannevann exhibits lower surface hardness values than Granular-Hematite in Stensundtjern and Stortjønna (Fig. 10). While exhibiting similar textures, varying amounts of gangue affect the surface hardness. The increased surface hardness is caused by a high quartz content in Granular-Hematite. Hence, the ore type can be divided into two subgroups: high-quartz Granular-Hematite found in Stensundtjern and Stortjønna, and low-quartz Granular-Hematite found in Kvannevann. The slightly lower surface hardness of Specular-Hematite compared with Granular-Hematite is related to the flaky hematite textures in Specular-Hematite, resulting in less competent hematite bands. Table 5 shows surface hardness measurements by Equotip and important textural properties of the six ore types.

The Hematite-Magnetite and Magnetite-Ore have higher surface hardness values by Equotip than Granular-Hematite and Specular-Hematite, although all four have approximately the same hematite grain sizes. Possible explanations for high values are irregular grain boundaries of the equant-irregular magnetite grains, or the higher contents of magnetite in the Hematite-Magnetite and the Magnetite-Ore. The high surface hardness by Equotip in Mylonitic-Hematite and Massive-Hematite can be explained by the fine-grained texture, and irregular to no visible grain boundaries. Based on the ore mineralogy, textures, and surface hardness values presented in the results, the ore types can be divided into three groups (Table 6).

The surface hardness measurements by Schmidt hammer confirm the same trend as the surface hardness values by Equotip, with the lowest surface hardness values obtained for Specular-Hematite and Granular-Hematite whereas Mylonitic-Hematite and Massive-Hematite have the highest surface hardness (Table 2). The standard deviation of the surface hardness values by Schmidt hammer in Stensundtjern is lower than for the same ore types in Kvannevann, indicating more

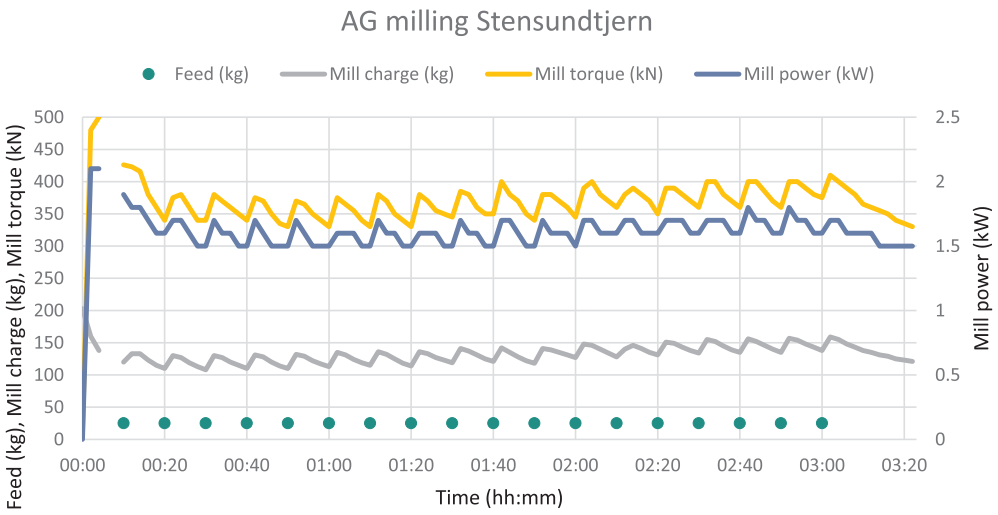

Fig. 12. Stensundtjern milling results.

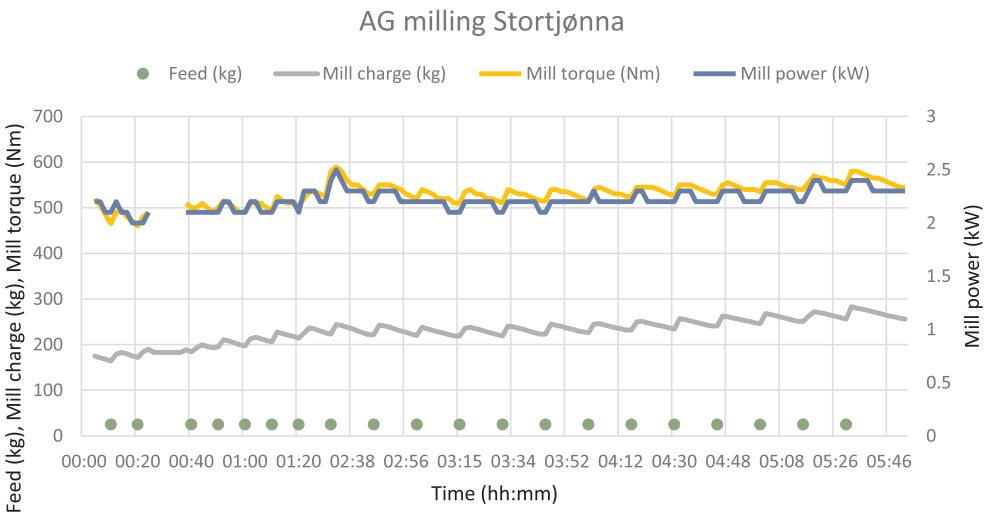

Fig. 13. Stortjønna milling results.

homogeneous ore types in Stensundtjern (Table 2). The measurement direction relative to foliation has only a minor effect on surface hardness for the banded ore types Granular-Hematite, Specular-Hematite, and Massive-Hematite (Fig. 7). Due to lack of suitable specimens for surface hardness measurements, Hematite-Magnetite and Magnetite-Ore have not been tested with the Schmidt hammer and the total number of specimens tested was limited. Hence, the following discussion will focus on the surface hardness values by Equotip.

5.2. The effect of ore mineralogy and textures on grindability

Unlike Mwanga et al. (2015) who focused on mill tests on small (220 g) relatively homogeneous ore types or units, the mill testing presented in this paper was carried out on a larger scale (1–2 tonnes) to represent the mineralogical and textural variability between the three deposits. Xu et al. (2013) postulated that ore with straight grain boundaries and coarse grains will break more easily, and that low specific energy is sufficient for grain boundary fractures to occur. This agrees with the results of the present study. The Kvannevann sample, dominated by coarse-grained hematite, required a solid feed rate of 266 kg/h for the mill to reach steady state (Fig. 11). This is almost three times the corresponding rate for the Stortjønna sample, dominated by fine-grained hematite, where the solid feed rate was 100 kg/h. Mill power and torque were approximately the same for the Stortjønna- and the Kvannevann sample, indicating lower grindability for the Stortjønna sample given the lower solid feed rate. The Stensundtjern sample achieved steady-state with a solid feed rate of 150 kg/h. Hence, the grindability was lower than for the Kvannevann sample. This is probably partly related to a finer-grained mill feed for the Kvannevann sample than the Stensundtjern sample (Fig. 14), making the Kvannevann sample easier to grind. Another factor affecting the grindability is the relatively high content of Hematite-Magnetite at Stensundtjern, where the magnetite has irregular grain boundaries.

The Stortjønna mill feed was coarser than the Kvannevann- and

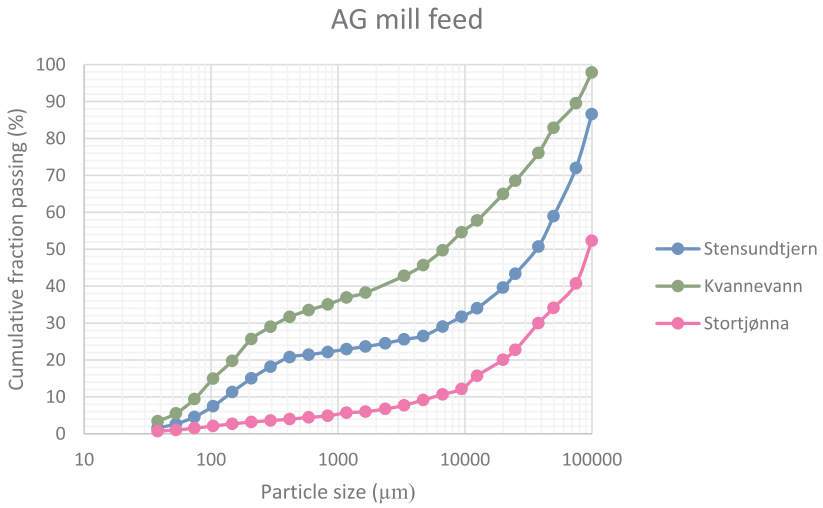

Fig. 14. Particle size distribution of the mill feed.

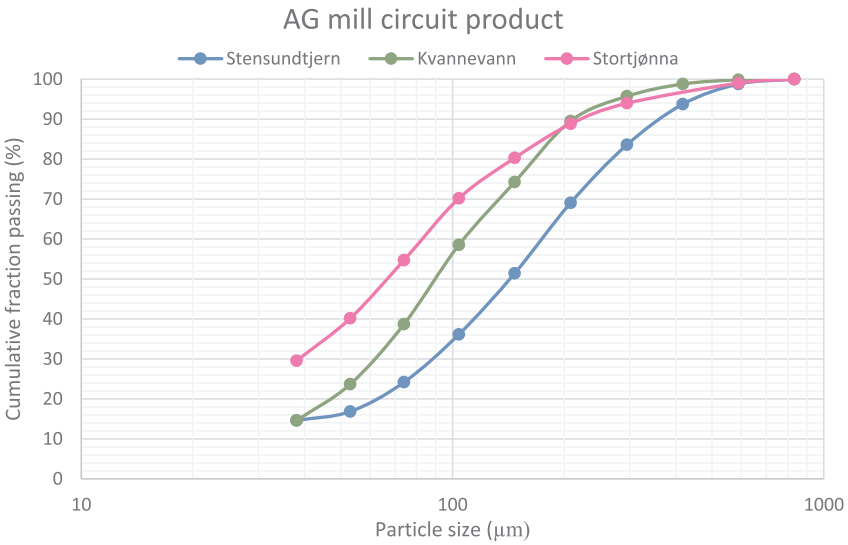

Fig. 15. The particle size distributions of the Kvannevann, Stensundtjern, and Stortjønna mill circuit products.

Table 5
Surface hardness by Equotip and textural properties of ore minerals in the six ore types.

Ore type	Average surface hardness by Equotip (HLD)	Average grain size	Grain shape	Grain boundaries
Granular-Hematite	624	hematite: 200 μm	hematite: tabular	Straight
Specular-Hematite	576	hematite: 400–500 μm	hematite: tabular	Straight
Hematite-Magnetite	632	hematite: 300 μm magnetite: 1 mm	hematite: tabular magnetite: equant-irregular	Straight to irregular
Magnetite-Ore	659	magnetite: 0.5 cm	magnetite: equant-irregular hematite: tabular	Straight to irregular
Mylonitic-Hematite	711	Disseminated hematite: 10–20 μm	hematite: irregular	Irregular to not visible
Massive-Hematite	648	Single grains are difficult to identify	Grain shapes are difficult to identify	Boundary between massive hematite and gangue: irregular

Table 6
Ore types divided into three groups based on surface hardness measurements.

Surface hardness group	Ore type
Low hardness	Granular-Hematite and Specular-Hematite
Intermediate hardness	Hematite-Magnetite and Magnetite-Ore
High hardness	Mylonitic-Hematite and Massive-Hematite

Stensundtjern mill feeds, while the mill circuit product was finer-grained compared to the corresponding samples from Kvannevann and Stensundtjern. A coarse feed also suggests a lower grindability in Stortjønna, with a longer residence time in the mill, creating a fine-grained mill circuit product. Stensundtjern has an intermediate feed size but produces the coarsest mill circuit product. The mill tests compared to mineralogical and textural characteristics indicate that grain size and shape, combined with the structure of grain boundaries, influence grindability. These results confirm the work by Kekec et al. (2006), Mwanga et al. (2015), and Xu et al. (2013).

5.3. Using surface hardness to evaluate grindability

The weighted average surface hardness by Equotip was calculated from the distribution of lithologies in the deposits (Fig. 4). Based on geological mapping, the ore logged as Hematite ore in Stensundtjern and Kvannevann was assumed to consist of Granular-Hematite and Specular-Hematite, while Hematite ore in Stortjønna was assumed to consist of Mylonitic-Hematite and Massive-Hematite. Thus, the surface hardness of the ore types can be related to the performance in the mill tests. Table 7 shows the relationship between arithmetic- and weighted average surface hardness by Equotip (HLD), arithmetic average surface hardness by Schmidt hammer (N/mm^2), throughput, and specific energy consumption during milling in the three deposits.

Kvannevann has the lowest surface hardness values, high throughput, and relatively low specific energy consumption, indicating high grindability. Stortjønna has the highest surface hardness, low throughput, and substantially higher specific energy consumption, indicating low grindability. Stensundtjern has intermediate surface hardness, a lower throughput, and slightly higher specific energy consumption than Kvannevann, hence, intermediate grindability. This suggests that it should be possible to use simple surface hardness measurements to evaluate grindability. The available sample material will determine whether Equotip or Schmidt hammer is the best surface hardness method in a mining operation. Equotip cannot be used on irregular surfaces and hence, is best suited for use on drill cores. The Schmidt hammer, on the other hand, is better suited for large-sized boulders. For statistical and efficiency reasons the Equotip is the preferred method, and drill cores are often readily available at most mine sites.

Table 7
Relationship between average surface hardness, throughput, and specific energy consumption during steady state milling for the three deposits.

	Surface hardness			Mill performance	
Deposits	Weighted average (HLD)	Arithmetic average (HLD)	Arithmetic average (N/mm^2)	Throughput (kg/h)	Specific energy consumption (kWh/tonne)
Kvannevann	574	571	35	266	8.27
Stensundtjern	640	635	40	150	10.7
Stortjønna	674	650	48	100	22.0

6. Conclusion

The presented research shows that the grindability of the different ores is affected by ore mineralogy and texture in addition to Fe grade. This corresponds well with on-site experiences. The six ore types defined can be placed into three groups based on their surface hardness values (Table 6).

The main textural characteristics influencing surface hardness are grain size and grain boundaries, as fine-grained ore types with irregular-to-no visible grain boundaries show the highest surface hardness. Whether ore mineralogy (magnetite content) influences surface hardness is difficult to determine and needs further investigation. Ore types with coarse-grained iron oxides and straight grain boundaries have higher throughput and lower specific energy consumption, thus a higher grindability, than fine-grained ore types with irregular-to-no visible grain boundaries. The results of this research show how surface hardness measurements combined with characterisation of ore mineralogy and textures can be used to evaluate grindability. To further investigate the relationship between ore mineralogy and texture, and grindability, automated mineralogy should be performed on the mill circuit products. Results from such analyses may also be used to predict the material's performance in the magnetic separation, which is the next step in the processing of this iron ore, and ultimately the recovery of iron. Identifying key ore characteristics, and knowledge of how they affect mineral processing can lead to better production control and utilisation of ore bodies. The choice of surface hardness measurement method strongly depends on the available sample material. In general surface hardness measurements on drill cores using the Equotip is more efficient and provides more results in a shorter time, than the measurements using Schmidt hammer on larger specimens. The disadvantage with the Equotip is that a flat sample surface is required. However, as most mine sites have available drill cores from drill campaigns, drill core availability is rarely an issue.

Acknowledgements

This research is funded by the Research Council of Norway (project no. 232428) and RG AS through the industrial PhD scheme. Thanks also to senior geologist Alexander Kühn and geologist Marta Lindberg at RG AS for helping with sampling strategies and being good discussion partners. Thanks to workers in RG AS, Leonard Nilsen og Sønner (LNS), Heia Maskin and Øijord&Aanes AS for helping with the practical work concerning sampling; blasting, loading, transporting, crushing, and splitting. A huge thanks goes to Helge Rushfeldt, Torkjell Breivik, and Kristin Bergseth Aure at IGP, NTNU for help with planning and running the pilot circuit. Finally, many thanks to Ingjerd Bunkholt, Nathan Church and Ida Røisi for proofreading my manuscript.

References

Bond, F.C., 1952. The Third Theory of Comminution. Transactions AIME Mining Engineering, 485 p.
Bugge J.A.W., 1948. Rana Gruber: Geologisk beskrivelse av jernmalmfeltene i Dunderlandsdalen. Norges Geologiske Undersøkelse No. 171.
Deer, W.A., Howie, R.A., Zussman, J., 1992. An Introduction to the Rock Forming Minerals, second ed. Pearson Education Limited, 685 p.
Deere, D.U., Miller, R.P., 1966. Engineering Classification and Index Properties for Intact Rock. Technical Report no. AFWL-TR-65-116, University of Illinois. 300 p.
Ellefmo, S., 2005. A Probabilistic Approach to the Value Chain of Underground Iron Ore Mining Doctoral Thesis. NTNU, Trondheim, pp. 205.
Gjelle, S., Søvegjarto, U., Tveiten, B., 1991. Dunderlandsdalen 2027 I, berggrunnsgeologisk kart 1: 50,000. Norges geologiske undersøkelse.
Grenne, T., Ihlen, P.M., Vokes, F.M., 1999. Scandinavian Caledonide Metallogeny in a plate tectonic perspective. Mineralium Deposita 34, 422–471.
Hunt, J., Kojovic, T., Berry, R., 2013. Estimating Comminution Indices from Ore Mineralogy, Chemistry and Drill Core Logging, The Second AUSIMM International Geometallurgy Conference, Brisbane, QLD.
International Society for Rock Mechanics, 1978. Commission on Standardization of Laboratory and Field Tests. Int. J. Rocks Mech. Min. Sci. Geomech. Abstr. vol. 15, pp. 89–97.
Kekec, B., Unal, M., Sensogut, C., 2006. Effect of the textural properties of rocks on their crushing and grinding features. J. Univ. Sci. Technol. Beijing Mineral Metall. Mater. 13 (5), 385–392.
Lopera, P.A.M., 2014. Geometallurgical mapping and mine modelling – comminution studies: La Colosa Case Study. AMIRA P843A Research Master Thesis. University of Tasmania, 75 p. < https://oatd.org/oatd/record?record=oai%5C%3Aeprints.utas.edu.au%5C%3A18741 > .
Lund, C., 2013. Mineralogical, Chemical and Textural Characterisation of the Malmberget Iron Ore Deposit for a Geometallurgical Model. Doctoral Thesis, LTU, Luleå, 190 p.
Melezhik, V.A., Ihlen, P.M., Kuznestov, A.B., Gjelle, S., Solli, A., Gorokhov, I.M., Fallick, A.E., Sandstad, J.S., Bjerkgård, T., 2015. Pre-Sturtian (800–730 Ma) depositional age of carbonates in sedimentary sequences hosting stratiform iron ores in the Uppermost Allochthon of the Norwegian Caledonides: A chemostratigraphic approach. Precambrian Res. 261, 272–299.
Minitab Inc., 2017. Minitab Home Page, Minitab Incorporated. Available from: http://www.minitab.com/en-us/ [11.09.2017].
Morrell, S., 2004. Predicting the specific energy of autogenous and semi-autogenous mills from small diameter drill core samples. Miner Eng. 17, 447–451.
Mwanga, A., Lamberg, P., Rosenkranz, J., 2015. Comminution test method using small drill core samples. Miner. Eng. 72, 129–139.
Napier-Munn, T.J., Morrell, S., Morrison, R.D., Kojovic, T., 1996. Mineral Comminution Circuits: Their Operation and Optimalisation. Julius Kruttschnitt Mineral Research Centre, Australia.
NGU, 2017. Transcript from Database Norwegian Ores. http://geo.ngu.no/kart/mineralressurser_mobil/ [12.03.2018].
Niiranen, K., 2015. Characterization of the Kiirunavaara iron ore deposit for mineral processing with a focus on the high silica ore type B2. Diss., Leoben, Montanuniversität, Lehrstuhl für Aufbereitung und Veredlung.
Philander, C., Rozendaal, A., 2011. The contributions of geometallurgy to the recovery of lithified heavy mineral resources at the Namakwa Sands mine, West Coast of South Africa. Miner. Eng. 24, 1357–1364.
Proseq, 2016. Operating instructions, Original Schmidt. Avaliable from: http://www.proceq.com/en/site/downloads/Original%20Schmidt.html [02.11.2016] Operating Instructions Equotip 3. Available from: http://www.proceq.com/site/downloads/Equotip%203.html [03.11.2016].
Roberts, D., Gee, D.G., 1985. An introduction to the structure of the Scandinavian Caledonides. In: Gee, D.G., Sturt, B.A. (Eds.), The Caledonide Orogen – Scandinavia and Related Areas. John Wiley & Sons, Chichester, pp. 55–68.
Sandvik, K.L., Rein, A., Corneliussen, O., Kleiv, R.A., Larsen E., 2012. Autogenmaling av jernmalm fra Kvannevann og Stortjønna. M-RAK 2012:11, NTNU.
Shi, F., Kojovic, T., Larbi-Bram, S., Manlapig, E., 2009. Development of a rapid particle breakage characterisation device – the JKRBT. Miner. Eng. 22 (7–8), 602–612.
Szilágyi, K., Borosnyói, A., 2009. 50 years of experience with the Schmidt rebound hammer. Concrete Struct. 10, 46–56.
Sovegjarto, U., 1972. Berggrunnsgeologiske undersøkelser i Dunderlandsdalen, Nordland. Post graduate thesis. University of Oslo, 139p.
Søvegjarto, U., Marker, M., Graversen, O., Gjelle, S., 1989. Storforshei 2027 IV, berggrunnsgeologisk kart 1: 50,000. Norges geologiske undersøkelse.
Van Tonder, E., Deglon, D.A., Napier-Munn, T.J., 2010. The effect of ore blends on the mineral processing of platinum ores. Miner. Eng. 23 (8), 621–626.
Viles, H., Goudie, A., Grab, S., Lalley, J., 2011. The use of Schmidt hammer and Equotip for rock hardness assessment in geomorphology and heritage science: a comparative analysis. Earth Surf. Process. Landforms 36, 320–333.
Voordouw, R.J., Gutzmer, J., Beukes, N.J., 2010. Zoning of platinum group mineral assemblages in the UG2 chromitite determined through in situ SEM-EDS-based image analysis. Mineralium Deposita 45 (2), 147–159.
Whitney, D.L., Evans, B.W., 2010. Abbreviations for names of rock-forming minerals. Am. Mineralogist 95, 185–187.
Xu, W., Dhawan, N., Lin, C.-L., Miller, J.D., 2013. Further study of grain boundary fracture in the breakage of single multiphase particles using X-ray microtomography procedures. Miner. Eng. 46–47, 89–94.

Paper II

The effect of hematite liberation and texture on wet high intensity magnetic separation of a low-grade iron ore

Marte Kristine Tøgersen[1,2] and Kurt Aasly[1]

[1]*Department of Geology and Mineral Resources Engineering, Norwegian University of Science and Technology, Sem Sælandsveg 1, N-7491 Trondheim, Norway*

[2]*Rana Gruber AS, Mjølanveien 29, Gullsmedvik, 8601 Mo i Rana, Norway*

(unpublished manuscript)

The effect of hematite liberation and texture on wet high intensity magnetic separation of a low-grade iron ore

Marte Kristine Tøgersen[1,2] and Kurt Aasly[1]

[1]*Department of Geology and Mineral Resources Engineering, Norwegian University of Science and Technology, Sem Sælandsveg 1, N-7491 Trondheim, Norway*

[2]*Rana Gruber AS, Mjølanveien 29, Gullsmedvik, 8601 Mo i Rana, Norway*

Abstract

Magnetic separation processes are highly dependent on mineral liberation and mineral content. Iron oxides are not the only minerals with magnetic susceptibility. Minerals containing paramagnetic elements (Fe, Mn, Ti, Cr etc.) may be susceptible enough to attach to the wet high intensity magnet and go into the concentrate. The Storforshei iron formation (IF) in the uppermost allochthon of the north-central Norwegian Caledonides, consists of several hematite-magnetite iron ore deposits with mineralogical and textural differences. Previous experience indicates that Fe_{tot*} is not sufficient for predicting metallurgical performance of the iron ores, thus, a pilot circuit was constructed to discover the effects of mineralogical and textural differences on the metallurgical performance in three iron ore deposits from the Storforshei IF. The focus of this study was the wet high intensity magnetic separation (WHIMS) in the pilot circuit, which were operated as a two-step separation. The results show that the hematite liberation affect the efficiency in the magnetic separation and is dependent on the ore type distribution in the feed to the pilot circuit. The particle textures in the mill circuit products could be linked with previously defined ore types in the Kvannevann, Stensundtjern, and Stortjønna deposits. The Kvannevann and Stensundtjern mill circuit products have high hematite liberation, with coarse grained tabular shaped hematite similar to the Granular-Hematite, Specular-Hematite, and Hematite-Magnetite ore types. The Stortjønna mill circuit product on the other hand have lower hematite liberation, caused by composite particles consisting of non-economic minerals and hematite, which are similar to the hematite textures found in the Mylonitic-Hematite and Massive-Hematite. This together with a larger amount of fines in the mill circuit product leads to a poorer magnetic separation of the Stortjønna deposit sample, where the loss of hematite to middlings and tailings is higher than the corresponding outputs in Kvannevann and Stensundtjern. There are slightly more composite particles in the Stensundtjern mill circuit product, which is probably caused by a different ore type distribution and causes slightly more hematite lost to middlings and tailings compared to the corresponding

outputs in the Kvannevann deposit sample. The most important Fe bearing gangue minerals in the three deposits are epidote, biotite, and hornblende, while dolomite is the most important Mn bearing mineral. These minerals report to middlings and tailings, which are returned in the full-scale processing plant. Hence, there is a possibility that these will accumulate in the WHIMS circuit and ultimately end up in the final hematite concentrate.

Key words: Storforshei iron formation, hematite-magnetite ore, wet high intensity magnetic separation, hematite liberation, hematite texture

1 Introduction

The six ore types defined from the Kvannevann, Stensundtjern, and Stortjønna deposits showed different metallurgical performance in the mill circuit caused by mineralogical and textural variations between the ore types (Tøgersen et al., 2018). These differences likely affect which particles are produced in the mill circuit, which may in turn affect the magnetic separation depending on hematite liberation, particle size distribution, and mineralogy. Lamberg (2011) emphasises the importance of particle characterisation to better understand which particles form during comminution and how they will behave in separation processes.

The Kvannevann ore deposit, part of the Storforshei iron formation (IF), is currently being mined by Rana Gruber AS (RG). Situated in the Dunderlandsdalen valley approximately 30 km north-east of the city Mo I Rana, Nordland county, Norway, the Storforshei IF consist of several hematite-magnetite ores with internal variations and variations between deposits with respect to mineralogical and textural properties. RG's main product are two hematite concentrates, H150 and H400 (with d_{50} of approximately 150 µm and 400 µm, respectively). Magnetite concentrates are also produced as by-products; however, these are not within the scope of this paper. The main operations in the hematite production consist of autogenous (AG) milling, low intensity magnetic separation (LIMS), wet high intensity magnetic separation (WHIMS) and gravity separation (spirals). The production quality control is mainly based on chemical analyses: Fe_{tot*} (total Fe by titration method in RG), Fe_{mag*} (Fe in magnetic minerals, magnetite and pyrrhotite, as analysed by RG), MnO S_{tot} and the amount of alkali elements in the feed ore, concentrates, and tailings. However, production experience at RG and results from tests conducted by Tøgersen et al. (2018), suggest that using only chemical analyses are insufficient when predicting hematite recovery, Fe_{tot*}, and the behaviour of the ore in the mineral processing plant. Previous research indicates that hematite recovery and Fe_{tot*} is affected by other ore

parameters besides Fe_{tot*} in the feed (Klomstadlien, 1984). A pilot circuit was designed in order to investigate mineralogical and textural effects on the results from mineral processing. Three iron ore deposits from the Storforshei IF were tested: Kvannevann, Stortjønna, and Stensundtjern. The Stortjønna ore deposit had been mined previously, however, later abandoned due to challenges during mineral processing which were seen as lower hematite recovery than expected (calculated as Fe_{tot*} recovery). The Stortjønna and Kvannevann deposits have similar Fe_{tot*} values of approximately 34 wt % (NGU, 2017). The Kvannevann deposit does not cause significant challenges in the mineral processing plant, and the hematite recovery and Fe_{tot*} grade in the hematite concentrate are as expected. The Stensundtjern deposit is a prospect for future production. Hence, it was desirable to include this deposit for assessment of mineralogy and texture, and metallurgical performance of this ore.

Six ore types with differences in mineralogy and texture were identified by Tøgersen et al. (2018) based on geological mapping and drill core logs from the Kvannevann-, Stortjønna-, and Stensundtjern deposits. Tøgersen et al. (2018) found that the Stortjønna deposit is dominated by the fine-grained ore types Mylonitic-Hematite and Massive-Hematite. These ore types showed higher surface hardness values and had lower grindability, compared to the coarser-grained ore types Granular-Hematite and Specular-Hematite dominating in Kvannevann (Tøgersen et al., 2018). The Stensundtjern deposit is dominated by the same ore types as Kvannevann, however, also contains a substantial amount of ore types with magnetite (Hematite-Magnetite and Magnetite-Ore), giving the Stensundtjern deposit intermediate surface hardness values and grindability compared to the Kvannevann and Stortjønna deposits (Tøgersen et al., 2018).

While the mineralogical and textural differences between the three deposits found in Tøgersen et al. (2018) were related to the AG milling, the aim of this paper is to investigate the effects of ore properties on the mineral separation at RG, especially in the WHIMS steps as the focus of the presented work is on the hematite production at RG. Bulk chemistry, mineralogy, hematite liberation, and particle textures in outputs from the pilot circuit will be analysed. The main objective is to identify significant differences between the three deposits. The pilot circuit WHIMS was operated with the same operational settings for the three deposits. Hence, differences observed are mainly related to differences in ore properties. Investigating the hematite particle textures, including composite particles provides important links to the efficiency of the magnetic separation, and may further explain the final Fe_{tot*} and Fe_{tot*} recovery in the concentrates.

The main objectives for the presented research are to:

- Characterise mineralogical and chemical differences between the Kvannevann, Stensundtjern, and Stortjønna outputs from the pilot circuit
- Examine the particles produced in the AG mill with focus on differences in the feed to the magnetic separation in the three deposits
- Evaluate the effect of hematite liberation, particle sizes and -textures, and mineral associations on the WHIMS separation
- Evaluate the distribution of hematite in the magnetic separation in terms of how much is lost to middlings and tailings for each of the deposits

Understanding which ore properties affect the WHIMS will provide a more solid foundation for daily production planning. Knowledge of how the easily identifiable ore types behave in the process can be used to evaluate blast blending in the mine, and thus lead to better utilisation of the iron ore deposits.

2 Background

2.1 Geological setting and RG hematite production line

The hematite-magnetite iron ores of the Storforshei iron formation belongs to the Dunderland formation, in the mid-central Caledonides of Norway. It is part of the Rødingsfjellet Nappe Complex, which constitutes part of the uppermost allochthon in the Norwegian Caledonides (Roberts et al., 2007). Iron formations in the uppermost allochthon of Norway stretches over approximately 500 km, from Mosjøen in the south to Tromsø in the north. Melezhik et al. (2015) found that a passive continental margin of a microcontinent in the Iapetus ocean is most likely where the iron formations accumulated. Dating of marble host rocks in the Rana area returned ages of late Sturtian (800-730 Ma) (Melezhik et al., 2015). Four different folding faces has inflicted the Storforshei iron formation. These different folding events have led to mineralogical and textural variations between and within iron ore deposits in the Storforshei iron formation (Søvegjarto, 1972; Ellefmo, 2005; Melezhik et al. 2015). Based on these variations, six ore types were defined by Tøgersen et al. (2018); Granular-Hematite, Specular-Hematite, Hematite-Magnetite, Magnetite-Ore, Mylonitic-Hematite and Massive-Hematite (Tøgersen et al., 2018). The ore types differ mainly in the iron oxide textures. Granular- and Specular-Hematite consist of relatively coarse tabular hematite grains (200-500 µm) with straight grain boundaries, where the hematite in Granular-Hematite has a sugar-grained texture, while the hematite in Specular-Hematite is flaky. Hematite-Magnetite has a similar hematite texture to

both Granular- and Specular-Hematite, however, also consist of equant-irregular magnetite with irregular grain boundaries. Magnetite-Ore is dominated by coarse-grained (0.5 cm) equant-irregular magnetite, with irregular grain boundaries, and only minor amounts of hematite (< 3 %). Mylonitic-Hematite consists of disseminated hematite, quartz, and calcite (10-20 µm) in a fine-grained matrix of gangue minerals. Massive-Hematite is also a fine-grained ore type, where the hematite is massive without distinguishable individual grains, and cut by folded veins of gangue minerals (Tøgersen et al., 2018).

The flowsheet for the RG hematite production line is shown in Figure 1. The process is relatively simple, with AG milling, LIMS, two steps of WHIMS, and some spirals. However, there are a number of returns present, which complicates the process.

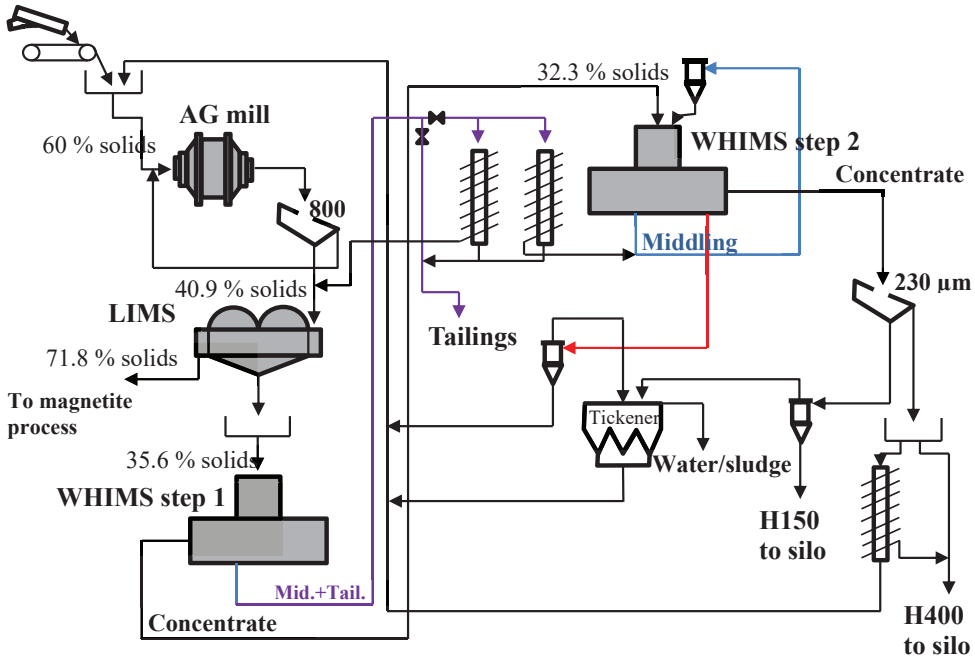

Figure 1: Flowsheet showing the hematite production line in RG (Johansen, 2014).

2.2 Magnetic separation of hematite ores

Rosenblum and Brownfield (1999) measured the magnetic susceptibility on several paramagnetic minerals using a Frantz Isodynamic Magnetic Separator (Model L-1). Their approach was a more practical one, as the magnetic susceptibility was measured in ampere needed to separate the minerals (from 0.01 -1.70 A on the magnetic separator), and not the actual centimetre-gram-second units used for magnetic susceptibility internationally (Rosenblum and Brownfield, 1999). The focus was on why there is a difference in susceptibility

in minerals of similar composition. The size range of the samples were 125-150 µm, where there were few or no mineral inclusions in 90-95 % of the grains. The results showed that the magnetic susceptibility can be altered by some metal substitutions in the mineral lattices. For instance, in carbonates and olivine where Ca (only in carbonates) and Mg can be substituted by Fe, making mineral variations containing more Fe more magnetic than mineral variations containing less Fe. Mn also gave this effect in carbonates and olivine (Rosenblum and Brownfield, 1999). Table 1 lists the magnetic susceptibilities measured by (Rosenblum and Brownfield, 1999) for relevant minerals found in the Storforshei IF. Minerals with lower ampere values have higher magnetic susceptibility and vice versa. It should be noted that the measurements are conducted on dry liberated mineral samples, thus it is not directly comparable to wet magnetic separation of complex mineralogy. However, the measurements show the relative relationship between the minerals.

Table 1: Magnetic susceptibilities of minerals found in Storforshei IF. Modified after Rosenblum and Brownfield (1999). dc = depends on chemical composition.

Mineral	Total range (A)	Best range (A)
Albite	> 1.70	> 1.70
Biotite - Phlogopite	0.20 - 1.20	0.30 - 0.80 dc
Calcite	> 1.70	> 1.70
Chlorite	0.10 - 0.90	0.20 - 0.50
Clinozoisite	0.30 - 1.30	0.50 - 1.00 dc
Diopside	0.30 - 0.80	0.40 - 0.60
Dolomite	> 1.70	> 1.70
Epidote	0.30 - 1.00	0.40 - 0.70
Hematite	0.025 - 0.50	0.10 - 0.30
Hornblende	0.10 - 0.90	0.30 - 0.60
Magnetite	< 0.01 - 0.05	0.01
Muscovite	0.30 - 1.40	0.70 - 1.30 dc
Quartz	> 1.70	> 1.70
Siderite	0.10 - 0.50	0.20 - 0.30
Titanite	0.70 - > 1.70	0.80 - > 1.70 dc

There is limited research available on wet high intensity magnetic separation on hematite ores. Most available literature concerning processing of iron ores are focused on magnetite-apatite

ores, in which flotation is the main separation method (i.e. Lund, 2013; Niiranen, 2015). Other studies have focused on dry high intensity magnetic separation using rare earth roll magnetic separator and induced roll magnetic separator on a low-grade hematite ore (Triphaty et al., 2014, 2017). Both these studies focused on the effects of process parameters like magnetic field intensity and rotor speed on the efficiency of the separation of coarse feeds (d_{50} between 600µm and 1.5 mm) (Triphaty et al., 2014, 2017). Since the aim of the pilot circuit used in the presented research was not to optimise the WHIMS, but rather to investigate the effect of ore properties on the magnetic separation, and given the finer particle size distribution, the work of Triphaty et al. (2014, 2017) is not relevant for this paper.

The WHIMS can accommodate lower particle sizes than dry magnetic separators (Wills et al., 2015). Wills et al. (2015) gives a general size range requirement for feed to wet high intensity magnetic separators from 1 µm - 300 µm. However, stating that the material should be as coarse as possible to achieve maximum separation efficiency. The manufacturer of the WHIMS Jones P40 separator, MBE Coal & Minerals Technology Gmbh, lists only the maximum top size of the feed < 2 mm (mbe-cmt.com, 2018). Shao et al. (1996) tested four different Fe minerals on a wet high intensity magnetic separator to determine if and how magnetic susceptibility and particle size affected the separation. The tests included goethite, limonite, and two variations of hematite, the latter differing in magnetic susceptibility. The results showed that particle size influenced the magnetic separation of the hematite with the highest magnetic susceptibility. Particles < 23 µm returned poor recovery and should be pre-treated in e.g. a flocculation process before entering the WHIMS (Shao et al., 1996). Further, Shao et al. (1996) states that iron ore particle sizes < 20 µm is in practice unsuitable for WHIMS separation. In the tests conducted by Shao et al. (1996) pure mineral samples were used. However, in a real situation the iron ore feed to the WHIMS includes gangue minerals that have a negative effect on the collision between the matrix surface and the iron oxide minerals. Song et al. (2002) states like Shao et al. (1996) that a lower size limit of the WHIMS as 10-20 µm is used. However, Song et al. (2002) emphasises that the lower size limit depends on parameters such as field intensity, field gradient, and the modal mineralogy in the feed to the separator. Song et al. (2002) tested Floc Magnetic Separation (FMS) on fine-grained hematite and limonite ore in order to investigate whether the FMS could act as a substitute for high gradient- or high intensity magnetic separators. After grinding, the hematite ore had a d_{50} of 4.1 µm, while the limonite ore had a d_{50} of 7.3 µm. The principle of FMS is that the ore slurry from wet grinding is treated to form

hydrophobic flocs of iron minerals before magnetic separation. The results from the FMS showed an improvement on hematite and limonite recovery (Song et al., 2002).

3 Materials and methods

3.1 Materials

The three iron ore deposits, Kvannevann, Stensundtjern and Stortjønna, were sampled from blasts in the geographical centre of the deposits, with the purpose of being processed in a pilot circuit, hence large samples were needed (Tøgersen et al., 2018). The Kvannevann deposit sample was collected from level 155 m.a.s.l. from the underground mine, while the Stortjønna and Stensundtjern were collected at suitable surface locations at the geographical centre of the deposits approximately. Sampling from each of the three deposits resulted in approximately 40 tonnes of material (Tøgersen et al., 2018) that were crushed in a mobile jaw crusher. A wheel loader with a big-bag attached was used for collecting representative samples covering the entire width of the material steam at the end of the conveyer belt. During crushing several increments were collected at regular intervals (3 x 10 sec per big-bag). Two big-bags with a total of 2 tonnes were collected from each deposit and sent to the lab and the pilot circuit (Tøgersen et al., 2018). Before the material entered the pilot circuit, 100 kg were split out for particle size distribution analyses of the mill feed, where the d_{50} for the Kvannevann, Stensundtjern, and Stortjønna mill feeds were 7 mm, 38 mm, and 100 mm, respectively (Figure 6). The remaining ore were fed manually into the AG mill. The mill circuit product was sampled during operation, whilst the entirety of the outputs from the magnetic separation were dried and split down to suitable sizes. This research follows the sample and increment definitions described in Lotter et al. (2018). However, since the pilot circuit were operated only once per deposit sample, sample is equal to increment in this paper.

3.2 Pilot circuit

The circuit consisted of an autogenous mill (length 0.8 m, inner diameter 0.69 m), with an 800 µm Sweco screen, a low intensity magnetic separator (LIMS), and two steps of wet high intensity magnetic separator (WHIMS Jones P40). In the first step the WHIMS was operated with a coil current at 0.95 A, while in the second step, operated at three different coil currents; 0,6 A, 0,7 A and 0,8 A. The choice of coil currents was based on the operating settings of the full-scale mineral processing plant, and previous work on iron ore from the Storforshei IF (Kleiv, 2014). The WHIMS was operated with the same rotational speed (rpm), pulp density (% solids), feed rate (t/h), and magnetic field intensities (T) for all three deposits. Contrary to the mineral processing plant at RG, the same WHIMS was used for both WHIMS steps. Hence,

the WHIMS was not run continuous and return streams were not included. This paper will mainly focus on the WHIMS step 1, as this is the main hematite separation, whereas WHIMS step 2 is to be considered a cleaning step of the preliminary hematite concentrate produced in WHIMS step 1.

3.3 Methods

3.3.1 Sample preparation

All outputs to be analysed by X-ray fluorescence and X-ray diffraction were split down to c. 40 g and milled for 4 minutes at 750 rpm in a Siebtechnik TS 250 vibrating-disc mill with agate chamber. The target particle size was 40 µm.

3.3.2 X-ray fluorescence

For chemical analyses the Bruker S8 Tiger X-Ray Fluorescence (XRF) instrument was used. The outputs from the pilot circuit were prepared as glass fusion discs in steps. First igniting about 2.5 g of the sampled material at 1000°C (loss on ignition, LOI) for 2 hours. Secondly 0.5 g of the ignited sample was mixed with 5.0 g of flux (66 % Lithium tetraborate/ 34 % Lithium metaborate) and finally, 60 µl of LiI (Lithium iodide) was added before the sample were fused and moulded as a disc. The analyses were calculated with the non-standard program *Quant Express*. Ten increments collected from the initial testing of the WHIMS were analysed on both the XRF with *Quant Express* and with wet chemical titration method at RG (Tøgersen et al., unpublished manuscript). Four concentrate increments, three middling increments, and three tailing increments were analysed. The increments were milled according to the description in section 3.3.1 and split on a rotary splitter, one part was sent to RG for titration analyses, while the other was prepared as a glass fusion disc and analysed by the XRF (Tøgersen et al., unpublished manuscript). Comparing the Fe content obtained by *Quant Express* (Fe_{tot}) with the Fe content from the wet chemical titration method at RG (Fe_{tot*}), a strong correlation was found as shown in Equation 1. The equation was calculated, from the linear relationship between the Fe analysed by XRF and the Fe analysed by titration, in Microsoft® Office Excel (Tøgersen et al., unpublished manuscript).

$$Fe_{tot*} = 0.9952Fe_{tot} + 0.06 \qquad \text{Equation 1}$$

All values were normalised to 100 % to enable better comparison between the three deposits, and all Fe_{tot} values were recalculated to Fe_{tot*}.

3.3.3 X-ray diffraction

A Bruker D8 Advanced X-Ray diffraction (XRD) with Rietveld refinement was used to analyse bulk mineralogy. The outputs with a target size 40 µm, was further micronised to c. 10 µm was

conducted on 2 g of the sample, with 10 ml ethanol on a McCrone micronising mill with agate grinding material.

3.3.4 Automated mineralogy

A Hitachi SU-6600 field emission scanning electron microscope was used to analyse the mill circuit product, and hematite concentrate, middling and tailings from WHIMS step 1 and 2. Automated mineralogy was analysed using SEM-EDS together with the Particle Texture Analyser (PTA) software. The SEM was operated with 20 kV accelerating voltage, 0.49 nA beam current, 15 mm working distance, and at 75x magnification. The PTA is a NTNU developed prototype software (Moen, 2006), developed further to use Bruker Quantax Espirit, and imports Bruker Feature database via DLL file. In Bruker feature, the SEM is set up to perform centroid analyses of grains, where the centre point of each grain is analysed for 1 second. In the PTA software, grain-based data from Bruker Espirit is reclassified to particle-based data. This allows the PTA software to calculate important particle properties, such as mineral content, mineral liberation, mineral associations, etc. Boundary particles are not part of the classification as fields are not merged.

The analyses do not differentiate between hematite and magnetite; thus, the hematite identified is actually hematite + magnetite. Although, for simplicity, hematite will be used as a collective term when discussing the results from the automated mineralogy. The samples analysed with the SEM-EDS and PTA, were prepared as polished sections following Røisi and Aasly (2018) with about 2.5 g sample, and 0.20 g fine-grained (< 20 µm) ultra-pure graphite. Graphite is used to separate particles, and prevent segregation, although Røisi and Aasly (2018) found little effect on the latter. To prevent the effect of segregation on the results, the polished section was cut vertically after being prepared as a normal polished section, and the resulting 4 vertical sections were then remoulded. The size fraction 104 – 147 µm of the mill circuit products, hematite concentrates, middlings, and tailings from WHIMS step 1 and 2 were chosen for automated mineralogy. Unfortunately, there is no polished section of hematite concentrate WHIMS step 1 from Stensundtjern, due to lack of material.

4 Results

4.1 Bulk chemistry

Tables 2-4 show the bulk chemical analyses of different mineral processing streams (outputs) from the Kvannevann-, Stensundtjern-, and Stortjønna deposits. The Fe_{tot*} distribution in the outputs from the Kvannevann deposit show that in spite of a relatively low Fe_{tot*} in the mill circuit product, the Fe_{tot*} in the hematite concentrates from WHIMS step 2 are high, while there are relatively small amounts of Fe_{tot*} lost to middlings and tailings. This is especially applicable in the middlings and tailing from WHIMS step 1. The highest Fe_{tot*} content in the Kvannevann deposit outputs is found in the preliminary magnetite concentrate. The Fe_{tot*} distribution in the Stensundtjern show high Fe_{tot*} contents in the concentrates (both magnetite and hematite), however, some of the Fe_{tot*} is lost to middlings and tailings especially in WHIMS step 2. The Stortjønna mill circuit product have a high Fe_{tot*}, however, the loss of Fe_{tot*} to the middlings and tailings from WHIMS step 2 is substantial, which is reflected by slightly lower Fe_{tot*} contents in the concentrates (both magnetite and hematite). Figure 2 show that Fe_2O_3 has negative correlations with most of the other oxides, with the exception of TiO_2 where the correlation is positive, and MnO where the correlation is positive with low Fe_2O_3 contents, and negative with high Fe_2O_3 contents.

Table 2: Bulk chemical analyses by XRF of the Kvannevann outputs (normalised values, wt %). Fe_{tot*} calculated from Equation 1 are also included. Abbreviations: KV = Kvannevann, PM = mill circuit product, Mag = preliminary magnetite concentrate, K = hematite concentrate, M = middling, A= tailing, 1 = WHIMS step 1, 2 = WHIMS step 2, and 0.6, 0.7, 0.8 = ampere settings in WHIMS step 2.

	Bulk chemistry Kvannevann (wt %)												
Outputs	SiO_2	Fe_2O_3	Fe_{tot*}	Al_2O_3	CaO	MgO	Na_2O	K_2O	TiO_2	P_2O_5	MnO	LOI	Total
KV-PM	43.27	37.87	26.42	6.92	3.61	2.39	1.63	1.10	0.51	0.35	0.10	2.24	100.00
KV-Mag	7.07	92.01	64.11	1.35	0.61	0.53	0.30	0.20	0.14	0.00	0.18	-2.39	100.00
KVK1	17.17	71.51	49.84	3.47	2.38	1.54	0.60	0.51	1.15	0.14	0.07	1.45	100.00
KVM1	50.89	20.16	14.10	10.10	6.42	4.09	1.75	1.46	0.31	0.40	0.16	4.26	100.00
KVA1	64.65	9.08	6.38	9.88	4.77	3.41	2.42	1.65	0.14	0.49	0.11	3.39	100.00
KVK2 0.6	4.90	90.59	63.12	1.10	0.90	0.56	0.00	0.13	1.38	0.00	0.00	0.43	100.00
KVK2 0.7	4.93	89.98	62.69	1.44	1.01	0.63	0.00	0.16	1.32	0.00	0.05	0.48	100.00
KVK2 0.8	4.25	90.85	63.30	1.32	0.96	0.62	0.00	0.13	1.36	0.00	0.05	0.45	100.00
KVM2 0.6	22.96	57.33	39.96	6.16	5.08	2.94	0.68	0.82	0.83	0.16	0.15	2.88	100.00
KVM2 0.7	24.80	53.04	36.98	6.97	5.81	3.31	0.80	0.91	0.74	0.19	0.16	3.28	100.00
KVM2 0.8	23.89	53.81	37.51	7.00	5.96	3.34	0.73	0.79	0.78	0.17	0.17	3.35	100.00
KVA2 0.6	44.64	26.76	18.69	9.34	6.87	4.42	1.46	1.43	0.37	0.27	0.18	4.26	100.00
KVA2 0.7	49.32	20.95	14.65	9.96	6.83	4.57	1.54	1.62	0.30	0.28	0.19	4.45	100.00
KVA2 0.8	53.28	17.46	12.21	9.88	6.50	4.49	1.66	1.55	0.26	0.37	0.17	4.39	100.00

Table 3: Bulk chemical analyses by XRF of Stensundtjern outputs (normalised values, wt %). Fe_{tot*} calculated from Equation 1 are also included. Abbreviations: ST = Stensundtjern, PM = mill circuit product, Mag = preliminary magnetite concentrate, K = hematite concentrate, M = middling, A= tailing, 1 = WHIMS step 1, 2 = WHIMS step 2, and 0.6, 0.7, 0.8 = ampere settings in WHIMS step 2.

	Bulk chemistry Stensundtjern (wt %)												
Outputs	SiO_2	Fe_2O_3	Fe_{tot*}	Al_2O_3	CaO	MgO	Na_2O	K_2O	TiO_2	P_2O_5	MnO	LOI	Total
ST-PM	39.25	42.33	29.52	5.04	4.03	2.47	1.46	0.91	0.32	0.63	0.24	3.32	100.00
ST-Mag	5.12	95.02	66.20	0.81	0.55	0.40	0.00	0.13	0.07	0.07	0.27	-2.43	100.00
STK1	7.44	86.53	60.29	1.62	1.68	0.74	0.00	0.19	0.52	0.01	0.11	1.17	100.00
STM1	46.98	26.11	18.23	6.90	6.94	3.84	1.14	1.28	0.19	0.59	0.36	5.66	100.00
STA1	66.22	9.78	6.87	6.71	5.60	3.27	1.37	1.37	0.09	0.86	0.25	4.48	100.00
STK2 0.6	2.77	94.95	66.16	0.73	0.46	0.21	0.00	0.04	0.50	0.00	0.04	0.29	100.00
STK2 0.7	3.02	94.13	65.58	1.00	0.59	0.38	0.00	0.00	0.58	0.00	0.00	0.30	100.00
STK2 0.8	2.86	94.22	65.65	0.89	0.69	0.27	0.00	0.03	0.56	0.00	0.06	0.41	100.00
STM2 0.6	11.78	76.23	53.12	3.22	3.59	1.47	0.23	0.36	0.41	0.11	0.23	2.39	100.00
STM2 0.7	17.11	64.41	44.89	4.88	5.65	2.36	0.31	0.53	0.36	0.12	0.33	3.93	100.00
STM2 0.8	19.55	59.22	41.28	5.41	6.47	2.81	0.41	0.66	0.33	0.16	0.38	4.59	100.00
STA2 0.6	40.82	28.97	20.23	7.81	8.80	4.22	0.70	1.09	0.24	0.35	0.50	6.51	100.00
STA 2 0.7	42.19	25.85	18.05	8.08	8.83	4.51	1.32	1.12	0.25	0.58	0.48	6.80	100.00
STA2 0.8	44.82	24.26	16.94	7.75	8.63	4.39	0.95	1.31	0.18	0.43	0.48	6.80	100.00

Table 4: Bulk chemical analyses by XRF of Stortjønna material streams (normalised values, wt %). Fe_{tot*} calculated from Equation 1 are also included. Abbreviations: SØ = Stortjønna, PM = mill circuit product, Mag = preliminary magnetite concentrate, K = hematite concentrate, M = middling, A = tailing, 1 = WHIMS step 1, 2 = WHIMS step 2, and 0.6, 0.7, 0.8 = ampere settings in WHIMS step 2.

	Bulk chemistry Stortjønna (wt %)												
Outputs	SiO_2	Fe_2O_3	Fe_{tot*}	Al_2O_3	CaO	MgO	Na_2O	K_2O	TiO_2	P_2O_5	MnO	LOI	Total
SØ PM	31.78	49.57	34.56	5.55	4.03	1.75	1.11	1.25	0.41	0.72	0.38	3.46	100.00
SØ Mag	21.24	66.65	46.46	4.33	2.87	1.09	0.35	0.98	0.34	0.46	0.41	1.27	100.00
SØK1	9.47	83.42	58.13	2.08	1.63	0.69	0.00	0.34	0.59	0.21	0.34	1.24	100.00
SØM1	45.92	27.24	19.02	8.07	6.38	2.61	0.67	1.80	0.31	0.95	0.59	5.46	100.00
SØA1	57.58	17.45	12.20	7.89	5.76	2.15	0.85	1.91	0.22	0.84	0.40	4.94	100.00
SØK2 0.6	5.32	90.42	63.00	1.20	0.85	0.42	0.00	0.17	0.60	0.17	0.23	0.62	100.00
SØK 2 0.7	6.27	87.88	61.23	1.63	1.03	0.53	0.56	0.24	0.61	0.31	0.25	0.69	100.00
SØK2 0.8	5.80	89.65	62.46	1.24	0.99	0.42	0.00	0.19	0.61	0.13	0.27	0.70	100.00
SØM2 0.6	17.09	69.99	48.78	3.89	3.16	1.28	0.00	0.64	0.49	0.37	0.67	2.41	100.00
SØM2 0.7	20.85	63.63	44.35	4.52	3.91	1.48	0.29	0.73	0.45	0.40	0.72	3.02	100.00
SØM2 0.8	22.86	59.78	41.67	5.01	4.36	1.77	0.40	0.80	0.43	0.40	0.76	3.42	100.00
SØA2 0.6	27.83	52.81	36.82	5.44	4.91	1.95	0.44	1.02	0.43	0.48	0.79	3.90	100.00
SØA 2 0.7	33.08	44.14	30.78	6.77	5.59	2.33	0.68	1.14	0.41	0.63	0.75	4.48	100.00
SØA2 0.8	33.73	43.30	30.20	6.66	5.83	2.27	0.54	1.24	0.39	0.57	0.75	4.72	100.00

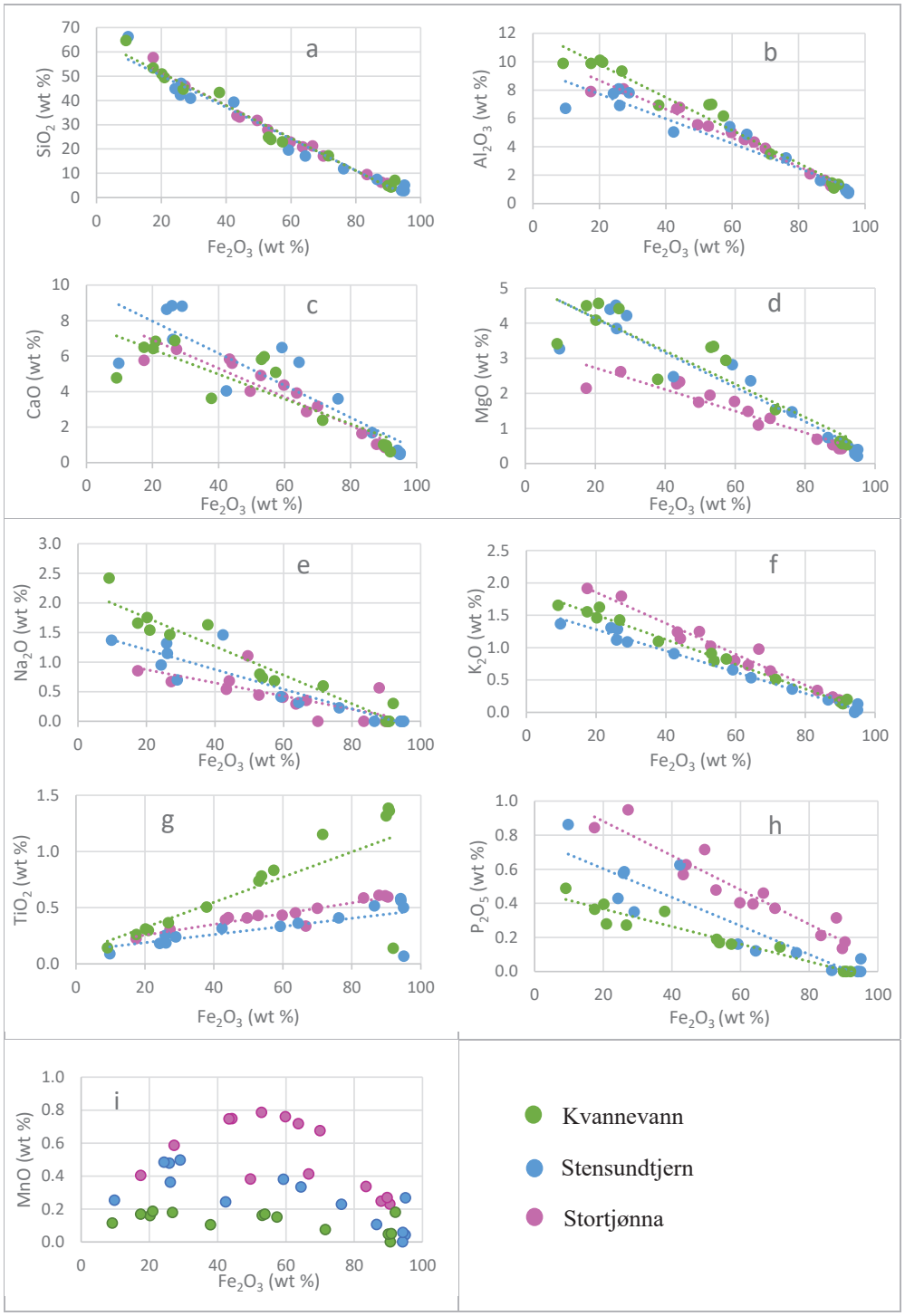

Figure 2: The correlations between Fe_2O_3 and (a) SiO_2, (b)Al_2O_3, (c) CaO, (d) MgO, (e) Na_2O, (f) K_2O, (g) TiO_2, (h) P_2O_5, (i) MnO.

4.2 Modal mineralogy

Figure 3-5 show the bulk mineralogy analysed by XRD in the Kvannevann-, Stensundtjern- and Stortjønna outputs from the pilot circuit. The colour scheme is modified after Butcher and Haberlah (2015). The most important non-economic minerals in the Kvannevann outputs are quartz, albite, epidote, hornblende, biotite, muscovite, and dolomite, with small amounts of chlorite. Few of the non-economic minerals end up in the KV-Mag output (quartz, albite, and small amounts of biotite and muscovite), which means that most of them continues to the hematite separation process. The hematite content in KV-PM is quite low (20.1 %). The KVK2 outputs have high hematite contents, with only small amounts of non-economic minerals (7.8 - 13.5 wt %). KV-Mag contains 79.1 wt % magnetite, and 4.4 wt % hematite. The KVM1 and KVA1 have low hematite contents, while it is higher in KVM2 and KVA2 (Figure 3). Siderite was found in KV-PM, KV-Mag, and the tailings from WHIMS step 2. The contents are all below 0.1 %, thus, they are too small to show in Figure 3.

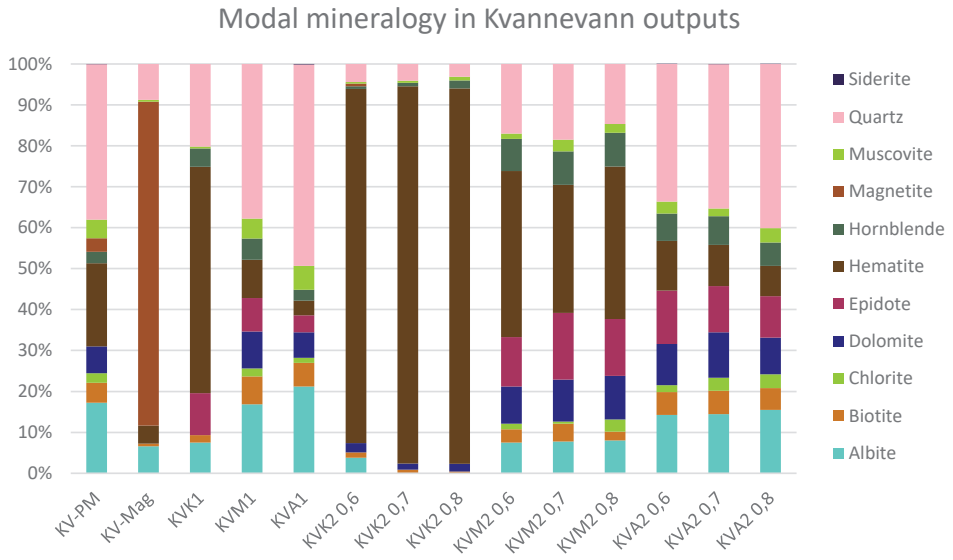

Figure 3: Modal mineralogy (analysed by XRD) in the Kvannevann outputs from the pilot circuit. The values are normalised to 100 %. Colours modified after Butcher and Haberlah (2015).

Despite the low hematite content in ST-PM (15.1 wt %), the hematite content in ST-Mag, STK1 and STK2 are high. The main non-economic minerals in the Stensundtjern outputs from the pilot circuit are quartz, epidote, dolomite, albite, phlogopite, with small amounts of biotite, muscovite, and hornblende. ST-Mag contains 84.5 wt % magnetite and 5.3 wt % hematite, with quartz, clinozoisite, and biotite as the only non-economic minerals. The STK from both

WHIMS steps have high hematite contents, with relatively low hematite content in STM1 and STA1, and STA2, and somewhat higher hematite content in STM2.

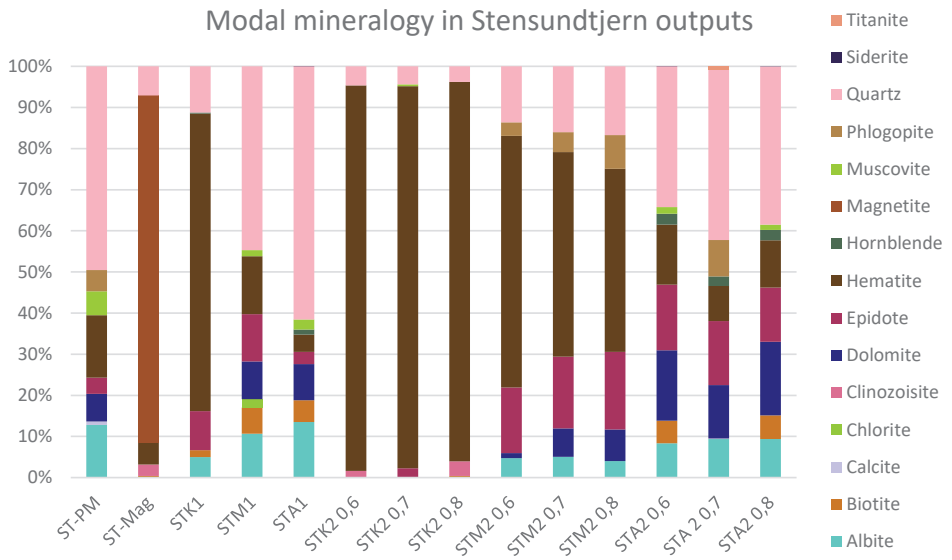

Figure 4: Modal mineralogy (analysed by XRD) in the Stensundtjern outputs from the pilot circuit. The values are normalised to 100 %. Colours modified after Butcher and Haberlah (2015).

The most important non-economic minerals in the Stortjønna outputs are quartz and muscovite, which occurs in all outputs. Epidote occurs in the SØ-PM, SØM1, SØA1, and SØM2 outputs, while clinozoisite occurs in SØA2. The SØ-Mag output contains 31.4 wt % magnetite and 28.8 wt % hematite. The SØK1 output contains 79.9 wt % hematite, with only quartz, muscovite, dolomite and albite as the non-economic minerals, while the SØK2 outputs have even higher hematite contents and less non-economic minerals. However, there is a quite substantial amount of hematite in SØM2 and SØA2.

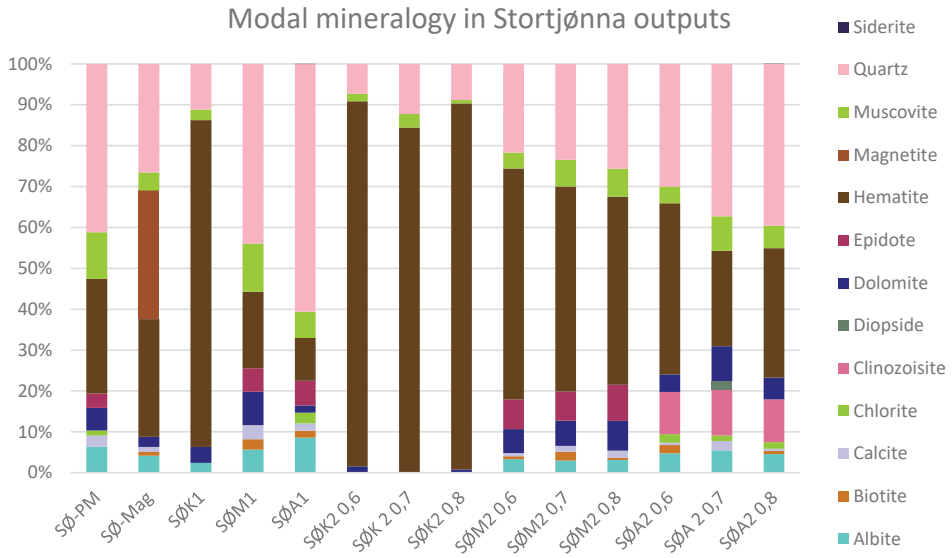

Figure 5: Modal mineralogy (analysed by XRD) in the Stortjønna outputs from the pilot circuit (analysed by XRD). The values are normalised to 100 %. Colours modified after Butcher and Haberlah (2015)

4.3 Particle size distribution

The particle size distribution (PSD) for AG mill feed, mill circuit products, hematite concentrates, and tailings WHIMS step 2 in Kvannevann, Stensundtjern, and Stortjønna are shown in Figure 6. The d_{50} values in the Kvannevann, Stensundtjern, and Stortjønna AG mill feed are 7 mm, 38 mm, and 100 mm, the mill circuit products are c. 90 µm, 147 µm, and 70 µm, in the hematite concentrates c. 80 µm, 170 µm, and 80 µm, and in the tailings c. 100 µm, 130 µm, and 75 µm, respectively. There are substantial amounts of fines (29 % < 38 µm in SØ-PM) in the Stortjønna outputs: 29 % < 38 µm in SØ-PM, 16 % < 38 µm in SØK1, and 25 % < 38 µm in SØA1, and the PSD for both the mill feed and the three outputs from Stortjønna are broad.

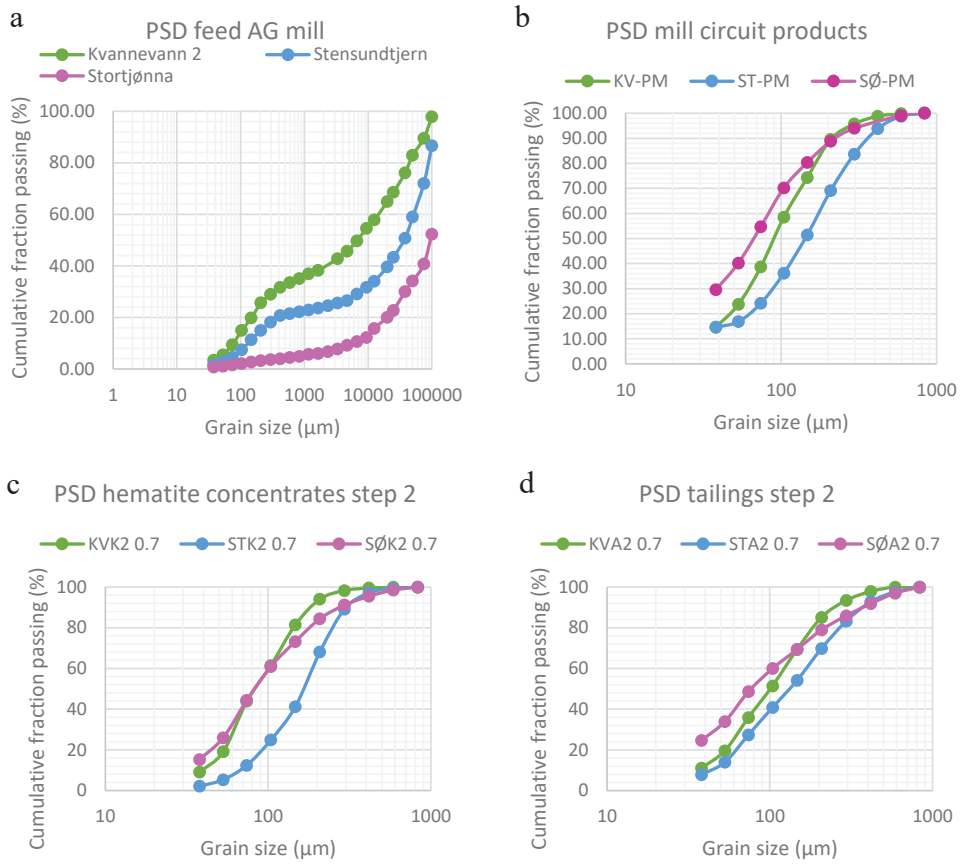

Figure 6: Particle size distribution for (a) the AG mill feed, (b) the mill circuit products (PM), (c) hematite concentrates (K), and (d) tailings (A) from WHIMS step 2 for Kvannevann (KV), Stensundtjern (ST), and Stortjønna (SØ).

4.4 Hematite liberation

Figure 7-9 show the hematite liberation of selected outputs from Kvannevann, Stensundtjern and Stortjønna. The Stensundtjern outputs have high hematite liberation, although the liberation is slightly lower in the tailings. The hematite liberation in the Stortjønna outputs are relatively low, especially in the middling and tailings, the exception is in the hematite concentrate from WHIMS step 1 where the liberation is quite high. The hematite liberation is high in all Kvannevann outputs.

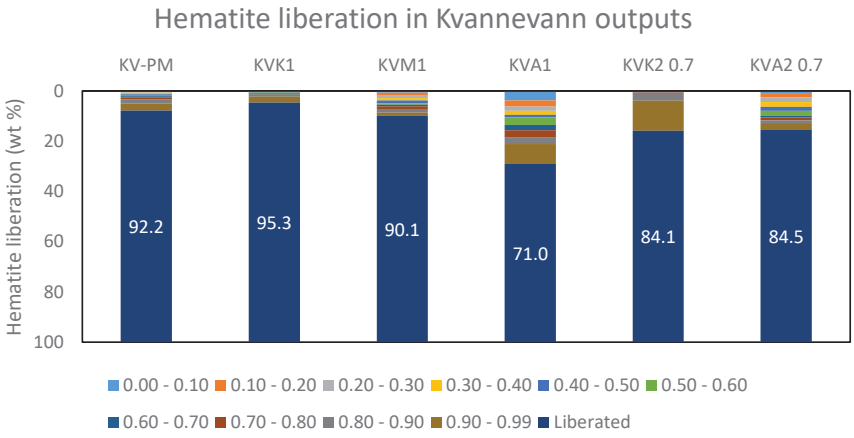

Figure 7: Hematite liberation in outputs in the 104-147 µm fraction from the Kvannevann deposit sample.

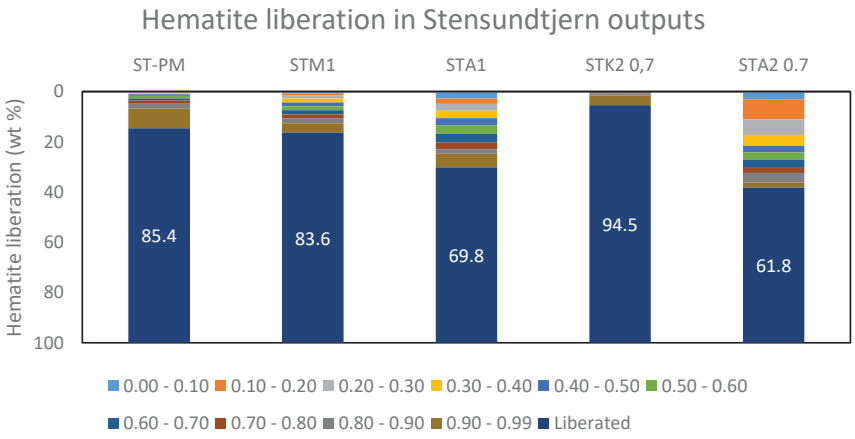

Figure 8: Hematite liberation in outputs, in the 104-147 µm fraction, from the Stensundtjern deposit sample.

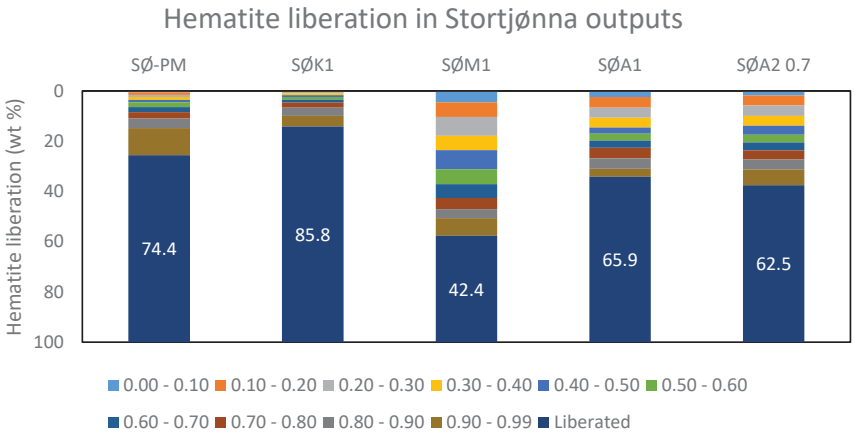

Figure 9: Hematite liberation in outputs in the 104-147 µm fraction from the Stortjønna deposit sample.

4.5 Particle textures and mineral associations

Figure 10 depicts the typical particle texture found in KV-PM, ST-PM, and SØ-PM. The hematite particles in KV-PM and ST-PM are relatively coarse, largely liberated and equigranular, with tabular shapes. In KV-PM there are only a few particles of non-economic minerals with small hematite inclusions (Figure 10a). In ST-PM there are some composite particles consisting of two phases; hematite and a non-economic mineral with straight grain boundaries between the phases, and some non-economic minerals with hematite inclusions (Figure 10b). The liberated hematite particles in SØ-PM have equant-irregular shapes and are in some instances very fine-grained. However, a notable amount of the hematite is located in composite particles. Some of these particles consists of mainly hematite with some non-economic minerals, where the hematite and non-economic minerals are intergrown. Other composite particles in SØ-PM consist of non-economic minerals with small hematite inclusions (Figure 10c).

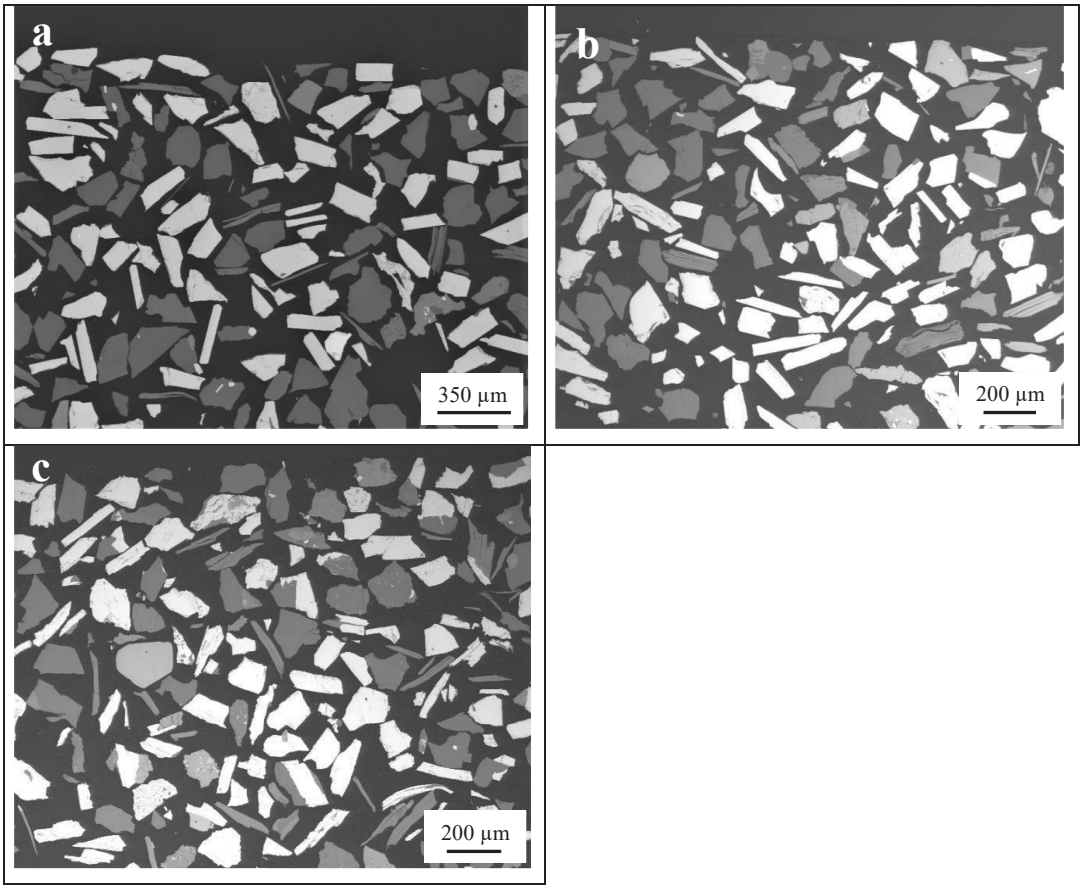

Figure 10: Backscatter electron image from (a) the KV-PM output, (b) the ST-PM output, and (c) the SØ-PM output.

Hematite associations in the outputs from WHIMS step 1 are shown in Figure 11. A number of associations were discovered in the PTA processing, however, associations with contents < 1 % were grouped together in "Other hematite associations". The most common association is hematite and quartz, followed by hematite and biotite. The KVK1 output has high hematite liberation and contains small amounts of composite particles with hematite. The tailings from all three deposit samples have relatively high content of composite particles. The Stortjønna outputs have high content of composite particles, especially hematite and quartz, hematite and biotite, and other hematite associations. The Stensundtjern middling and tailing are dominated by the association's hematite and quartz, hematite and biotite, and other hematite associations.

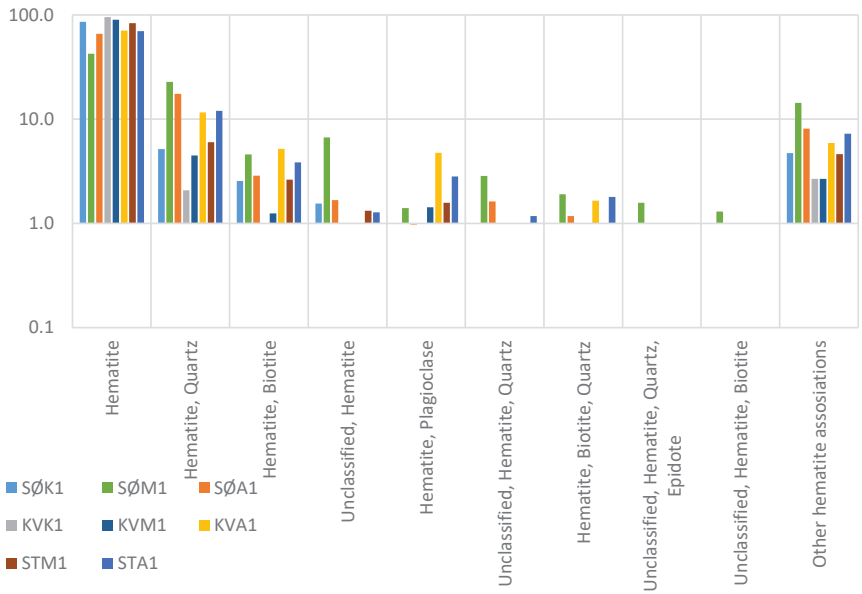

Figure 11: Hematite associations in the outputs from WHIMS step 1.

5 Discussion

The WHIMS was operated with identical settings (pulp density, rotational speed, feed rate, coil currents) in the pilot circuit for the three deposit samples, as such the experienced differences can be attributed to mineralogical and textural variations between the three deposit samples.

Most of the oxides has a negative correlation with Fe_2O_3, with the exception of TiO_2 which has a positive correlation related to ilmenite lamellas in hematite, and MnO which show negative correlation with Fe_2O_3 contents < 50 wt %, and positive correlation with Fe_2O_3 contents > 50 wt %. This is especially apparent in the Stortjønna outputs from the pilot circuit and might be due to the relatively lower content of dolomite in the magnetite and hematite concentrates.

The Fe_{tot*} content in the mill circuit products from the three deposits varies, however, it seems to be of minor consequence for the efficiency of magnetic separation. The Kvannevann mill circuit product (KV-PM) have the lowest Fe_{tot*} content of the mill circuit products. The Kvannevann hematite concentrate from step 1 has lower Fe_{tot*}grade than the corresponding outputs from Stensundtjern and Stortjønna, probably caused by the lower Fe_{tot*} in KV-PM. However, the amount of Fe_{tot*} lost to middlings and tailings is low, and the Fe_{tot*} grades in the hematite concentrates from WHIMS step 2 are satisfying, suggesting a good magnetic separation for the Kvannevann material. The Stortjønna mill circuit product (SØ-PM) with the highest Fe_{tot*} of the mill circuit products, has slightly lower Fe_{tot*} in the hematite concentrates

from step 2 than the corresponding outputs in Kvannevann, and a substantially larger loss of Fe_{tot*} to middlings and tailings (from both WHIMS steps) than the corresponding outputs from Kvannevann and Stensundtjern, suggesting less efficient magnetic separation. The Stensundtjern mill circuit product (ST-PM) have intermediate Fe_{tot*} content, and although the loss of Fe_{tot*} to middlings and tailings are slightly higher than in Kvannevann, the hematite concentrates from both WHIMs steps in Stensundtjern have the highest Fe_{tot*} grades. The fact that the SØ-PM output has the highest Fe_{tot*} content of the three deposits, but a poor separation further corroborates that other ore parameters besides chemistry affects the magnetic separation.

There are generally more non-economic minerals in hematite concentrates from WHIMS step 1 than the concentrates from WHIMS step 2, which is to be expected as the coil current are higher in step 1 and also considering that the WHIMS are operated in a series, therefore less non-economic minerals are present in the feed to WHIMS step 2.

Epidote, biotite, and hornblende are the most important Fe bearing minerals, while dolomite is the most important Mn bearing minerals in the three deposits. There are substantial amounts of these minerals in the middlings and tailings and considering that these outputs are returned in the full-scale mineral processing plant, there is a possibility that these minerals are accumulated in the WHIMS circuit, thus ultimately ending up in the final hematite concentrate.

The PSD of the Stortjønna mill feed and mill circuit product suggests that abrasion and chipping rather than impact was the main method of breakage for the Stortjønna material, caused by a high competence in the fragments, the coarse PSD in the feed, and the large amount of fines in the mill circuit product. The high competence of the fragments led to a low throughput, high specific energy consumption, and longer residence time in the mill compared to the Kvannevann and Stensundtjern AG milling (Tøgersen et al., 2018). The Stortjønna outputs has a substantially larger fines content (< 38 μm) than the corresponding outputs in Kvannevann and Stensundtjern, which in accordance with the findings in Shao et al. (1996) and Song et al. (2002) might have contributed to the less efficient magnetic separation of the Stortjønna deposit sample. The Kvannevann mill feed has a notably finer PSD than the corresponding feeds from Stensundtjern and Stortjønna, which enabled a high throughput and low specific energy consumption in the AG mill (Tøgersen et al., 2018), indicating less competent fragments in this material, which is likely an effect of the low surface hardness of the ore types dominating in the Kvannevann deposit sample, Specular-Hematite and Granular-Hematite, and the effects of the blasting and primary crushing. However, the PSD of the mill circuit product is intermediate compared to the corresponding mill circuit products in Stensundtjern and Stortjønna, suggesting

that the milling managed to create an acceptable product in spite of the very fine PSD of the mill feed. The PSD of the Stensundtjern mill feed is intermediate, while the mill circuit product is the coarsest of the three mill circuit products. The throughput and the specific energy consumption was intermediate compared to the Kvannevann and Stortjønna AG milling (Tøgersen et al., 2018), which could be an effect of the coarser PSD in the feed. However, it could also be caused by the substantial amount of ore types with higher surface hardness, Hematite-Magnetite and Magnetite-Ore, compared to the Kvannevann deposit sample, resulting in higher competence fragments in the Stensundtjern mill feed compared to the Kvannevann mill feed.

Since the hematite liberation analyses were performed on the particle size range between 104-147 µm and considering the mean particle size of 150 and 400 µm in the two hematite concentrates in the full-scale production, it was expected that the current analyses would indicate high degree of hematite liberation. However, this was not the case for all the deposit samples.

The observed textures in the ore types defined by (Tøgersen et al., 2018) can be recognised in the mill circuit products from the three deposit samples. The hematite particles in KV-PM and ST-PM are to a large extent liberated, coarse, and have tabular shapes. These textures are also observed in the Granular-Hematite and Specular-Hematite (Tøgersen et al., 2018). Although ST-PM have more composite particles compared to KV-PM, these particles are often binary particles with straight grain boundaries between the hematite and the non-economic mineral. The higher content of composite particles with hematite in ST-PM suggests that the Stensundtjern deposit sample had more Granular-Hematite or Hematite-Magnetite where the hematite grain sizes (200 and 300 µm) are lower than in Specular-Hematite (400-500 µm). This might also have contributed to the lower hematite liberation in the Stensundtjern outputs, and larger loss of Fe_{tot*} and hematite to the middlings and tailings.

The Mylonitic-Hematite consists of hematite disseminated in a fine-grained matrix of gangue minerals, with some remnants of larger hematite grains where the cracks are filled with gangue minerals (Tøgersen et al., 2018). These hematite textures are very similar to the ones observed in SØ-PM, with a relatively high content of composite particles where hematite and non-economic minerals are intergrown or consist of non-economic minerals with very fine-grained hematite inclusions. The equant-irregular shapes of liberated hematite in the SØ-PM might be caused by random breakage of the ore type Massive-Hematite where there are no visible grain boundaries for the breakage to follow (Tøgersen et al., 2018). The lower hematite liberation in

the Stortjønna outputs is likely a consequence of the hematite textures in the Mylonitic-Hematite and Massive-Hematite ore types.

The relatively large amount of hematite in the Stortjønna middlings and tailings can be attributed the low hematite liberation and the hematite textures in the ore types dominating the Stortjønna deposit. Between 40-60 % of the hematite in the Stortjønna middlings and tailings are liberated, while the corresponding outputs in Kvannevann and Stensundtjern has even higher hematite liberation (60-80 %). Since these middlings and tailings are returned in the full-scale processing plant, a higher hematite liberation will be beneficial for further separation. One reason for the liberated hematite particles entering the tailings might be caused by non-economic minerals affecting the collision between hematite particles and the matrix in the WHIMS as described by Shao et al. (1996).

The results from this paper corroborates the findings in Tøgersen et al. (2018) where the hematite liberation was expected to be low in the Stortjønna outputs from the pilot circuit based on the textural composition of the ore types dominating in this deposit. Even though the Stortjønna deposit sample produces satisfying Fe_{tot*} grades in the hematite concentrates, the loss of Fe_{tot*} lost to middling and tailings is substantial, thus, it is suggested that the ore types Mylonitic-Hematite and Massive-Hematite is carefully blended into the feed to the full-scale mineral processing plant.

6 Conclusion

- The Fe_{tot*} in the feed is not suitable for predicting the Fe_{tot*} grade and -recovery from the WHIMS, as it neglects mineralogical and textural variations. This is apparent from the Kvannevann deposit sample which has the lowest Fe_{tot*} grade in the feed and still yields hematite concentrates with satisfying Fe_{tot*} grades. The loss of hematite to middlings and tailings are lower than for the Stensundtjern and Stortjønna deposit samples.
- The particle textures in the Kvannevann and Stensundtjern mill circuit products suggest that these deposit samples are dominated by the ore types Granular-Hematite, Specular-Hematite, and Hematite-Magnetite. Although, more composite particles in the Stensundtjern mill circuit product suggest that the ore type distribution differs.

- The differences in the mill feed and mill circuit product PSDs from Kvannevann, Stensundtjern, and Stortjønna indicate that differences in surface hardness and effects of blasting probably affected the competence of the fragments. Hence, the throughput.
- The hematite liberation of the Stortjønna outputs are lower than for the Kvannevann- and Stensundtjern outputs. This is probably caused by the fine-grained hematite textures in the ore types dominating Stortjønna, Mylonitic-Hematite and Massive-Hematite.
- A large amount of hematite is lost to the Stortjønna middlings and tailings, which is also a result of the particle texture, and non-economic particles partly obstructing the collision between hematite particles and the WHIMS matrix.
- The poor magnetic separation (large hematite losses) in Stortjønna might also be affected by the relatively large fines content (29 % < 38 μm) in the feed to the magnetic separation.
- Some of the minerals containing Fe (epidote, biotite/phlogopite, hornblende) as well as minerals containing Mn (dolomite) report to the middlings and tailings which are returned to the full-scale processing plant, this might lead to an accumulation of these minerals in the WHIMS circuit, where they eventually might end up in the hematite concentrate.

7 Acknowledgements

This research is funded by the Research Council of Norway (project no. 232428) and RG through the industrial PhD scheme. Thank you to senior geologist Alexander Kühn and geologist Marta Lindberg at RG for helping with sampling strategies and being good discussion partners. Thanks to workers in RG, Leonard Nilsen og Sønner (LNS), Heia Maskin and Øijord&Aanes AS for helping with the practical work concerning sampling; blasting, loading, transporting, crushing, and splitting. Finally, huge thanks to Helge Rushfeldt, Torkjell Breivik, and Kristin Bergseth Aure at IGB, NTNU for help with planning and running the pilot circuit, and Helge Rushfeldt for numerous productive discussions about everything concerning the pilot circuit.

8 References

Butcher, A.R., Haberlah, D. (2015) *A short history of automated mineralogy colours*, [Online] Available at: http://automatedmineralogy.blogspot.com/2015/08/the-story-behind-colour-scheme-used-in.html (Accessed: 22.07.2019)

Ellefmo, S. (2005) *A probabilistic approach to the value chain of underground iron ore mining*. PhD Thesis, Norwegian University of Science and Technology, Trondheim, 273 p.

Johansen, R. (2014) 'Flowsheet with process and chemical data', *Internal report, Rana Gruber AS.*

Lamberg, P. (2011) 'Particles-the bridge between geology and metallurgy', *Proceedings Conference in mineral engineering*, Luleå, pp. 1-16.

Lotter, N.O., Evans, C.L., Engström, K. (2018) 'Sampling – A key tool in modern process mineralogy', *Minerals Engineering*, 116, pp. 196-202.

Lund, C. (2013) *Mineralogical, Chemical and Textural Characterisation of the Malmberget Iron Ore Deposit for a Geometallurgical Model*, PhD Thesis, Luleå University of Technology, 190 p.

Kleiv, R.A. (2014) 'Vurdering av oppredningsløsninger for produksjon av konsentrat til masovn og DR-pellets ved Rana Gruber – Sluttrapport fra DP3 i RaNaGass prosjektet', *Internal report, Norwegian University of Science and Technology.*

Klomstadlien, (1984) 'Silikatbundet jern i råmalm, konsentrat og avgang, Rana Gruber AS', Internal report, Norsk Jernverk.

Moen, K. (2006) *Quantitative measurements of mineral microstructure*, PhD Thesis, Norwegian University of Science and Technology, Trondheim.

MBE Coal Minerals Technology Gmbh (2018) [online]. Available at: https://www.mbe-cmt.com/index.php?id=52 (Accessed: 14.12.2018)

Melezhik, V.A., Ihlen, P.M., Kuznestov, A.B., Gjelle, S., Solli, A., Gorokhov, I.M., Fallick, A.E., Sandstad, J.S., Bjerkgård, T. (2015) 'Pre-Sturtian (800–730 Ma) depositional age of carbonates in sedimentary sequences hosting stratiform iron ores in the Uppermost Allochthon of the Norwegian Caledonides: A chemostratigraphic approach', *Precambrian Research*, 261, pp. 272−299.

NGU (2017) *Database Norwegian Ores*. Available at: http://geo.ngu.no/kart/mineralressurser_mobil/ (Accessed: 12.03.2018)

Niiranen, K. (2015) *Characterization of the Kiirunavaara iron ore deposit for mineral processing with a focus on the high silica ore type B2*. PhD Thesis, Montanuniversität Leoben, 133 p.

Roberts, D., Nordgulen, Ø. and Melezhik, V. (2007) 'The Uppermost Allochthon in the Scandinavian Caledonides: From a Laurentian ancestry through Taconian orogeny to Scandian crustal growth on Baltica', *The Geological Society of America Memoir,* 200, pp. 357-377.

Rosenblum, S. and Brownfield, I.K. (1999) 'Magnetic Susceptibilities of Minerals', *U.S. Geological Survey*, Open-File Report 99-0529.

Røisi, I. and Aasly, K. (2018) 'The effect of graphite filler in sample preparation for automated mineralogy– a preliminary study', *Mineralproduksjon*, 8, A1-A23. Available at: http://mineralproduksjon.no/publikasjoner/volum-8-2018/ (Accessed: 04.08.2019)

Shao, Y., Veasy, T.J. and Rowson, N.A. (1996) 'Wet high intensity magnetic separation of iron minerals', *Magnetic and Electrical Separation*, 8, pp. 41-51.

Song, S., Lu, S., Lopez-Valdivieso, A. (2002) 'Magnetic separation of hematite and limonite fines as hydrophobic flocs from iron ores', *Minerals Engineering*, 15, pp. 415–422.

Søvegjarto, U. (1972) *Berggrunnsgeologiske undersøkelser i Dunderlandsdalen, Nordland*. Post graduate thesis, University of Oslo, 139p.

Triphaty, S.K., Banerjee, P.K., Suresh, N. (2014) 'Separation analysis of dry high intensity induced roll magnetic separator for concentration of hematite fines', *Powder Technology*, 264, pp. 527-535.

Triphaty, S.K., Singh, V., Murthy, Y.R., Banerjee, P.K., Suresh, N. (2017) 'Influence of process parameters of dry high intensity magnetic separators of separation of hematite', *International Journal of Mineral Processing*, 160, pp. 16-31.

Tøgersen, M. K., Kleiv, R. A., Ellefmo, S., & Aasly, K. (2018) 'Mineralogy and texture of the Storforshei iron formation, and their effect on grindability', *Minerals Engineering*, 125, pp. 176-189.

Tøgersen, M.K., Kleiv, R.A., Ellefmo, S., and Aasly, K. (unpublished manuscript) 'Development of a pilot circuit for identifying variations in metallurgical performance for iron ore from Storforshei iron formation'.

Wills, B. A., & Finch, J. (2015) Wills' mineral processing technology: an introduction to the practical aspects of ore treatment and mineral recovery, 8th edition, Butterworth Heinemann, Elsevier.

Paper III

Fe deportment in non-economic minerals in the Kvannevann iron ore deposit

Marte Kristine Tøgersen[1,2], Steinar Ellefmo[1], Kurt Aasly[1]

[1]*Department of Geoscience and Petroleum, Norwegian University of Science and Technology, Sem Sælandsveg 1, N-7491 Trondheim, Norway*

[2]*Rana Gruber AS, Mjølanveien 29, Gullsmedvik, 8601 Mo i Rana, Norway*

(unpublished manuscript)

Fe deportment in non-economic minerals in the Kvannevann iron ore deposit

Marte Kristine Tøgersen[1,2], Steinar Ellefmo[1], Kurt Aasly[1]

[1]*Department of Geoscience and Petroleum, Norwegian University of Science and Technology, Sem Sælandsveg 1, N-7491 Trondheim, Norway*

[2]*Rana Gruber AS, Mjølanveien 29, Gullsmedvik, 8601 Mo i Rana, Norway*

Abstract

A typical iron ore sample from the Storforshei iron formation (IF) contains the iron oxides, hematite and magnetite, plus several non-economic silicates and carbonates. Phosphates and sulphides may also be present. Several of these non-economic minerals contain Fe, thus an analysis of total iron content (Fe_{tot}) in the crude ore does not give information about recoverable Fe from iron oxides (Fe_{hem} and Fe_{mag}). In the daily production the Fe_{tot}, S, MnO, magnetic Fe (Fe_{mag*}) and alkalis (Na, K) are the quality control parameters, the most important of these being the Fe_{tot}. Rana Gruber (RG) mines mainly from the Kvannevann deposit and calculates the Fe recovery based on Fe_{tot} analyses from the feed and the hematite concentrate. There are mineralogical and textural variations between and within an ore deposit depending on the ore type distribution. An analysis of Fe_{tot} neglects these variations, which are found to affect the metallurgical performance of the ore deposits. To investigate the mineral deportment in the hematite process, the chemistry, mineralogy, and mineral chemistry in samples of mill circuit product (MCP), two final hematite concentrates (H150 and H400) and final tailing (T) from the mineral processing plant at RG were analysed. Three increments were collected at three different dates of the four samples. The four increments collected on a date represents a series. The results show that there are slight differences in chemistry and mineralogy between the three series, suggesting a different ore type distribution in the crude ore and/or operational differences on the days the increments in the series were produced. The non-economic minerals with the highest Fe contribution are ilmenite, aegirine-augite, amphibole, epidote and biotite. The mineralogy and mineral chemistry were used to calculate Fe from non-economic minerals, which were higher in the mill circuit products and tailings (around 1 %), and lower in the hematite concentrates (0.08-0.56 %, with one exception: H150 1 at 1.9 %). When calculating Fe recovery based on Fe_{hem} (hematite recovery), as opposed to calculating Fe recovery from Fe_{tot}, there was a notable increase. This effect is caused by the relatively higher amount of Fe_{sil}

(Fe in non-economic minerals) in the MCP increments. The Fe_{tot*} lost to tailings are mostly located in hematite, whether this hematite is liberated or not is a question for further study, however, observations in the optical microscope indicates some liberated hematite which could potentially be recovered. Calculating the real hematite recovery will provide RG with increased quality control of their hematite process, and possibly prevent unnecessary adjustment in the mineral processing plant, which might occur when calculating the Fe_{tot*} recovery, since this can be much lower than the real hematite recovery, depending on the Fe_{sil}.

Key words: Kvannevann deposit, hematite recovery, Fe in non-economic minerals, recoverable Fe, recovery calculations

1 Introduction

In an iron ore deposit Fe is mainly related to hematite and magnetite. However, Fe also resides in non-economic minerals such as hornblende, biotite, epidote, and pyroxene, pyrite and pyrrhotite, dolomite and ankerite. Therefore, the analyses of the total content of Fe in the ore (Fe_{tot}) may deviate from the Fe related to the hematite and magnetite in the ore and thus provide an inaccurate prediction of the expected Fe recovery.

The Storforshei iron formation (IF) is located 30 km north east from Mo i Rana, Nordland county, Norway, in the Dunderlandsdalen valley. The Kvannevann iron ore deposit, one of several iron ore deposits in the Storforshei IF (e.g. Tøgersen et al., 2018), is currently being mined by Rana Gruber AS (RG AS). The annual iron ore production is about four million tonnes. Typical iron oxide content in the ore is distributed between hematite (40 mass %) and magnetite (5 mass %) (NGU, 2017). The ore deposits show mineralogical and textural variations both within and between deposit (-s). The most critical parameter for daily quality control for the production of hematite concentrates is the Fe_{tot} in the crude ore. The Fe recovery is calculated from the Fe_{tot} in the ore and Fe_{tot} in the hematite and magnetite concentrates. However, the recovery of hematite is most important in this process as hematite is the economic mineral. Calculating the recovery based on Fe_{hem} will correspond to the hematite recovery (Wills et al., 2015). Other quality control parameters are Fe_{mag*} (Fe in magnetic minerals, mainly magnetite, but also pyrrhotite) MnO (mainly found in garnet, carbonates and hematite), alkalis (feldspar, pyroxene, amphibole, mica), and S_{tot} (total content of S, mainly found in iron sulphides).

Raw materials classified as separate ore types, and raw materials originating from various deposits in the Storforshei IF behave differently in the processing plant, thus giving products of different qualities (Tøgersen et al., 2018).

The previously mined Stortjønna deposit, had Fe_{tot} of typically 34 mass %, similar to the Kvannevann deposit being mined now (NGU, 2017). However, the Stortjønna operation was abandoned after two years due to challenges in ore processing, thus not obtaining the expected Fe recovery levels.

Klomstadlien (1984) investigated the Fe contribution from silicates in the Kvannevann deposit and suggested that the recovery of Fe is highly affected by the content of silicates hosting Fe. Furthermore, the wet chemical Fe_{tot} analysis (titration) was found to be insufficient in predicting the recovery, since the method does not distinguish between Fe from non-economic minerals and Fe from iron oxides. The most important silicates contributing to Fe_{tot} were identified as hornblende and biotite (Klomstadlien, 1984).

These experiences indicate the need for additional analyses in the daily production, as the Fe_{tot} analysis will misrepresent the recoverable Fe or Fe in iron oxides (Fe_{hem} + Fe_{mag}).

Fe_{sil} (Fe in non-economic minerals) is used as a collective term for Fe from non-economic minerals, including silicates, carbonates and sulphides. Fe_{tot} consist of Fe from the iron oxides and non-economic minerals containing Fe, as shown in Equation 1.

$$Fe_{tot} = Fe_{hem} + Fe_{mag} + Fe_{sil} \quad \text{Equation 1}$$

The general formula for recovery from Wills et al., (2015) is given in Equation 2, where M_{conc} and M_{feed} are the mass of the concentrate and feed respectively, while g_{conc} and g_{feed} are the grades of the concentrate and feed respectively.

$$Rec = ((M_{conc}g_{conc})/(M_{feed}g_{feed}))*100 \quad \text{Equation 2}$$

Presently the recovery at RG AS is calculated based on the Fe_{tot} as shown in equation 3.

$$Rec_{present} = ((M_{conc}Fe_{totconc})/(M_{feed}Fe_{totfeed}))*100 \quad \text{Equation 3}$$

$Rec_{present}$ is the Fe recovery based on Fetot in the concentrate and feed ($Fe_{totconc}$ and $Fe_{totfeed}$). The calculation of oxide recovery should rather be based on the Fe residing in the iron oxides (Fe_{hem} + Fe_{mag}) as shown in equation 4, where Rec_{real} is the actual Fe recovery from the iron oxides (hematite + magnetite); $Fe_{hemconc}$ + $Fe_{magconc}$ and $Fe_{hemconc}$+ $Fe_{magconc}$ points to Fe from iron oxides in the concentrate and feed respectively.

$$Rec_{real} = (((M_{conc}(Fe_{hemconc}+Fe_{magconc}))/((M_{feed}(Fe_{hemfeed}+Fe_{magfeed})))*100 \quad \text{Equation 4}$$

Equation 4 can be divided into recovery of hematite and recovery of magnetite, as shown in Equation 5 and 6 respectively.

$$Rec_{realhem} = (((M_{conc}(Fe_{hemconc}))/((M_{feed}(Fe_{hemfeed})))*100 \quad \text{Equation 5}$$

$$Rec_{realmag} = (((M_{conc}(Fe_{magconc}))/((M_{feed}(Fe_{magfeed})))*100 \quad \text{Equation 6}$$

This paper presents a characterisation of Fe deportment in non-economic minerals in the Kvannevann iron ore deposit. Twelve increments from the RG processing plant have been analysed with respect to bulk chemistry, modal mineralogy and mineral chemistry. The main objective is to increase knowledge of implications from modal mineralogy and Fe deportment on recovery estimations. This will contribute to an improved prediction on recoverable Fe (Fe_{hem}+ Fe_{mag}). To achieve this objective the following research tasks have been defined:

- Element and mineral deportment analyses in the feed, hematite concentrates, and the tailing
- Determining the corresponding difference between Fe_{tot} and Fe_{hem}+ Fe_{mag}.
- Estimate and present the effect of the above on recovery estimates and the Fe lost to tailing

The conclusions in this paper are made assuming that mineral chemistry will not differ within the deposit. The mineralogy and chemistry are however expected to vary, due to the presence of several ore types in the same deposit (Tøgersen et al., 2018). X-Ray Fluorescence (XRF) and

X-Ray Diffraction (XRD) data will be combined with mineral chemistry data for relevant silicates, carbonates and iron oxides, to investigate Fe deportment in the increments.

The same procedure can later be used for other ore deposits of interest in the Storforshei IF, or indeed other ore deposits experiencing similar challenges. Hestnes et al. (2013) presented a similar study of granitic pegmatites. Fe deportment to economic and gangue was defined, using EPMA and analyses of backscatter electron images. The results showed potential for reducing Fe_2O_3 in microcline products, thus enabling an improved process and product quality (Hestnes et al., 2013).

2 Background

2.1 Geological setting

The Storforshei IF is part of the Dunderland Formation in the Uppermost Allochthon of the North-Central Norwegian Caledonides. It is a stratiform hematite-magnetite iron ore, with mica schist, calcareous mica schist, and dolomite and calcite marbles as the dominating host rocks (Bugge, 1948; Søvegjarto, 1972; Melezhik et al., 2015). The Dunderland formation forms a syncline, which is the result of at least three different deformation stages, with the main metamorphism occurring during the pre-Caledonian F1 (Søvegjarto, 1990). The iron formation is tilted and dips 20 degrees west (U. Søvegjarto, personal communication 2016). In the hanging wall of the Kvannevann deposit, there is a very fine-grained rock containing garnet, named garnet mylonite (Søvegjarto, 1972). In the eastern end of the Kvannevann deposit and towards the Stortjønna deposit, the iron ore becomes more folded, and some of the garnet mylonite is folded into the iron ore. Six ore types were identified by Tøgersen et al. (2018): Granular-Hematite, Specular-Hematite, Hematite-Magnetite, Magnetite-Ore, Mylonitic-Hematite and Massive-Hematite. The distribution of the ore types in the Kvannevann-, Stensundtjern-, and Stortjønna deposits was determined based on drill core logs, and geological mapping. The Kvannevann deposit is dominated by two ore types, Granular-Hematite and Specular-Hematite (Tøgersen et al., 2018). Both are banded ore types, with hematite and quartz in alternating layers. The hematite is relatively coarse-grained, approximately 200 µm in Granular-Hematite and 400-500 µm in Specular-Hematite. There is also lower content of Magnetite-Ore and Hematite-Magnetite.

2.2 The mineral processing plant at RG

After blasting, the ore goes through a primary jaw crusher, before being transported by train to the mineral processing plant for autogenous (AG) milling and mineral separation. A simplified flowsheet of the hematite production line is shown in Figure 1. The mineral separation of the

ore entails two different types of magnetic separation, low intensity magnetic separator (LIMS) for enrichment of magnetite, two steps of wet high intensity magnetic separator (WHIMS) for removal of silicates and upgrading of the hematite concentrate. A set of spirals are used to collect hematite from middling and tailing, and as a cleaner for one of the hematite concentrates. Particularly in the WHIMS steps some non-economic minerals have been known to follow hematite into the concentrate.

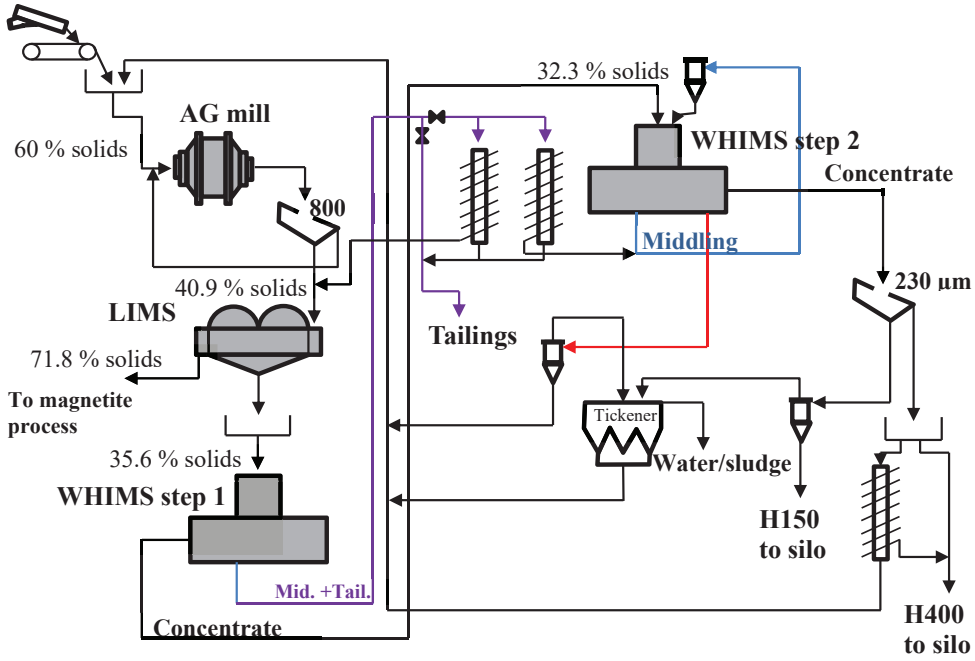

Figure 1: Flowsheet of the hematite production line at RG, modified after Rune Johansen (2014). Abbreviations; Mid = middling, Tail = tailings, concentrate = hematite concentrate.

3 Materials and methods

3.1 Materials

Four different product steams were sampled from the full-scale mineral processing plant; the mill circuit product, the two hematite concentrates, H150 and H400, and the main tailings. Three increments were collected from each of the four samples at three different dates. The increments from one date represents a series, with each series consisting of four increments. Each sample represents a lot (the area of the Kvannevann deposits which was produced at the dates). The increments in a sample represents the different steps in the processing of the lot. This follows the principles described by Lotter et al. (2018).

Sampling was carried out using automatic samplers, which collected the entire width of the product streams to ensure representative increments. Table 1 gives an overview of the increments, and the date they were collected. The *mill circuit product* (MCP) was collected from the product stream after the AG mill circuit. *H150* and *H400* are hematite concentrates, the numbers 150 and 400 reflects their average particle size (µm). *Tailing* (T) are collected from the final tailings before the tailings pond.

Table 1: Overview of the increments collected from the mineral processing plant at RG.

Collection date				
16.08.2013 (series 1)	MCP-1	H150-1	H400-1	T-1
20.08.2013 (series 2)	MCP-2	H150-2	H400-2	T-2
23.08.2013 (series 3)	MCP-3	H150-3	H400-3	T-3

3.2 Methods

3.2.1 Microscopy

Grain mounts of bulk material for all increments in Table were prepared as polished thin sections and analysed in a Leica DM2500P microscope (magnification from 25-500x).

3.2.2 X-Ray Fluorescence (XRF)

The chemistry was analysed using a Bruker S8 Tiger X-ray fluorescence (XRF). Bulk material from each increment were milled to about 40-50 µm using a vibratory disc mill. All increments were milled with stainless steel, except H150-3, H400-3, and T-3 where tungsten carbide was used as milling media. To calculate the loss on ignition (LOI) 2.5 grams of each increment was heated at 1000°C for two hours before the increments were weighed again. The samples were prepared as glass fusion discs by using 0.5 grams of the heated increment and 5 grams of flux (66 % Lithium tetraborate and 34 % Lithium metaborate), adding 60 µL of LiI (Lithium iodide) before melting. The non-standard program *Quant Express* was used. The XRF Fe data correlated very well to Fe data obtained from the titration method used by RG AS, when ten samples were analysed using both methods (Tøgersen et al., unpublished manuscript). The correlation executed in Microsoft® Office Excel, based on the linear relationship between the ten analyses of Fe by titration and the ten analyses by XRF, gave the following equation from which the Fe by titration (Fe_{tot*}) can be calculated from Fe by XRF (Fe_{tot}) (Tøgersen et al., unpublished manuscript).

$$Fe_{tot*} = 0.9952Fe_{tot} + 0.06 \qquad \text{Equation 7}$$

3.2.3 X-Ray Diffraction (XRD)

The mineralogy was analysed by X-ray diffraction (XRD), on a Bruker D8 Advanced, with a Cu-anode. Mineral identification was conducted using Bruker's EVA® software (Madsen et al., 2001; Scarlett et al., 2001), while the minerals were quantified by Rietveld refinement using the TOPAS software (Rietveld, 1967, 1969; Bruker, 2019). About 2 g of the increments already milled on the vibratory disc mill were micronised with 10 ml ethanol in a McCrone micronizing mill to about 10 µm, before drying and pressing powdered pills. The general detection limit for the XRD is 1 mass % (Madsen et al., 2001; Scarlett et al., 2001; Hestnes et al., 2013).

3.2.4 Electron Probe Micro Analyser (EPMA)

A JEOL JXA 8500 Hyper probe Electron Probe Micro Analyser (EPMA) was used to analyse the mineral chemistry. 261 points/particles were analysed on 9 thin sections. The variation in the mineral chemistry is assumed to be very low, as all increments are from the same deposit. The analyses of all increments entailed the following element list: Si, Fe, Al, Ca, Na, K, Ti, Mn, Mg, Cu, S, and V. One increment (MCP-1) was analysed two times, and while having the same list of main elements, there was a slightly different list of trace elements the second time (Cu, S and V were not analysed, while P and Cl were). The content of Fe was given as FeO in the EPMA results. These FeO results were recalculated to Fe_2O_3 to enable comparison of the results to the other quantification methods. The content of CO_2 in carbonates were also calculated. Mineral structural formulas were calculated from the EPMA data, following stoichiometric principles described in Deer et al. (1992). Four sulphides were analysed with totals between 150-200 %, thus these were not included in this paper. Analyses with low totals that did not correspond to any mineral were disregarded, as they are most likely edge analyses or affected by inclusions in particles, 12 of the 261 points were disregarded due to these effects.

4 Results

4.1 Bulk chemistry

Table 2 lists the bulk chemical analyses of the increments in series 1, 2 and 3. The chemical composition of the increments generally follows the same trend in the three series, with the exception of Cr_2O_3 and NiO contents that are absent in some products in series 1 and 3. MnO is found in all increments, ranging from 0.55 - 1.08 mass %. The content of K_2O are low in the hematite concentrates, while Na_2O is absent in these increments.

Table 2: Bulk chemical composition obtained by XRF analyses of the increments (values are normalised to 100 %).

	Chemistry (mass %)															
Increments	SiO_2	Fe_2O_3	Fe_{tot}	Al_2O_3	CaO	MgO	Na_2O	K_2O	TiO_2	P_2O_5	MnO	Cr_2O_3	NiO	WO_3	LOI	Total
MCP-1	40.83	36.98	25.86	5.76	4.85	2.15	1.24	1.26	0.34	0.48	0.93	0.11	0.49	0.00	4.58	100.00
MCP-2	37.71	42.17	29.49	5.27	4.60	1.94	1.14	1.03	0.36	0.41	0.78	0.08	0.33	0.00	4.17	100.00
MCP-3	40.75	39.27	27.46	4.90	4.55	1.92	1.05	0.90	0.32	0.40	0.69	0.20	0.87	0.00	4.18	100.00
H150-1	3.96	89.94	62.90	1.49	1.35	0.41	0.00	0.09	0.64	0.00	1.08	0.00	0.00	0.00	1.04	100.00
H150-2	3.36	91.39	63.92	1.29	1.05	0.33	0.00	0.08	0.67	0.00	0.80	0.09	0.36	0.00	0.59	100.00
H150-3	2.94	91.48	63.98	1.44	1.28	0.41	0.00	0.09	0.52	0.05	0.59	0.00	0.00	0.07	1.14	100.00
H400-1	3.36	91.66	64.11	1.09	1.08	0.41	0.00	0.08	0.47	0.00	0.63	0.09	0.34	0.00	0.78	100.00
H400-2	3.76	90.84	63.53	1.19	1.07	0.40	0.00	0.08	0.53	0.00	0.71	0.14	0.59	0.00	0.68	100.00
H400-3	3.56	90.86	63.55	1.19	1.46	0.50	0.00	0.11	0.38	0.00	0.55	0.00	0.00	0.08	1.31	100.00
T-1	56.2	17.14	11.99	6.91	6.09	2.54	1.59	1.41	0.23	0.66	0.75	0.13	0.62	0.00	5.72	100.00
T-2	55.77	16.44	11.50	7.18	6.27	2.65	1.60	1.54	0.25	0.63	0.74	0.17	0.84	0.00	5.93	100.00
T-3	59.73	13.92	9.74	6.09	6.57	2.73	1.44	1.32	0.20	0.74	0.64	0.00	0.00	0.22	6.40	100.00

Figure 2 show the distribution of Fe_{tot*} in the increments from the three series. There are some differences in the Fe_{tot*} content in the MCP and T increments in the three series, while the hematite concentrates are quite similar. The largest difference is found in series 1, where H150-1 has the lowest Fe_{tot*} content of all the concentrates, while H400-1 has the highest.

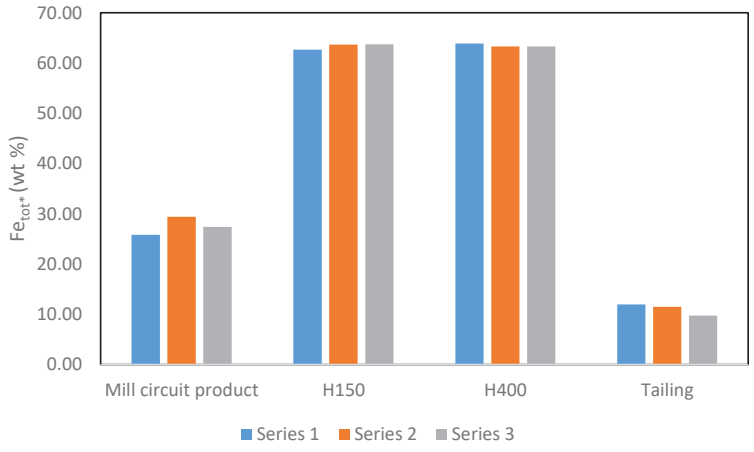

Figure 2: The distribution of Fe_{tot*} (mass %) in the increments from the three series.

4.2 Mineralogy

Quartz, feldspar, epidote, biotite, garnet and carbonates were identified in the optical microscope as the main non-economic minerals in the increments. The observations also

indicate a high degree of hematite liberation, although there are a few occurrences of multiphase particles with both fine-grained hematite and non-economic minerals (Figure 3). In addition to iron oxides, the hematite concentrates contain some liberated silicates and carbonates (Figure 4). Silicates and carbonates (yellow/brown-green transparent) are fine-grained compared to the hematite (grey).

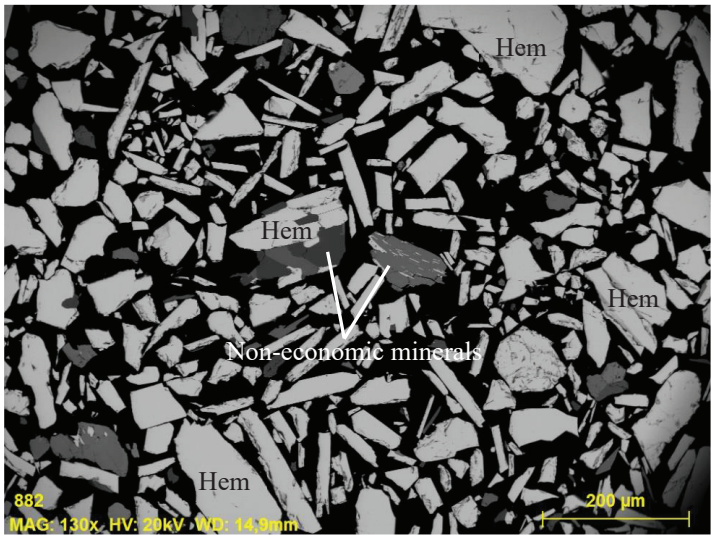

Figure 3: Backscatter electron image from H400-2. Two multiphase particles containing hematite, one with fine-grained hematite, are located in the centre of the picture and marked with "non-economic minerals".

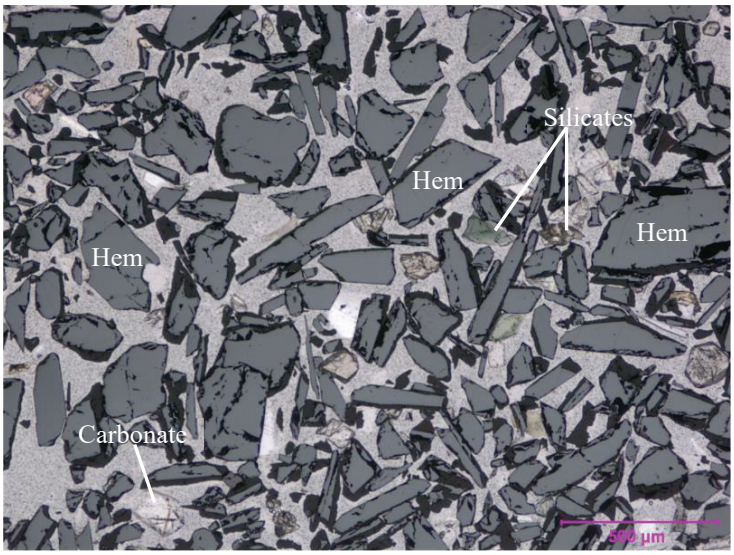

Figure 4: A section of the increment H150-3 under reflected light. The figure shows the presence of silicates and carbonates (light yellow-brown-green, transparent). The Hematite (grey) is liberated.

The results from the XRD analyses of the three series are shown in Table 3. The three series contain more or less the same minerals; however, the amounts of each mineral vary. The hematite content differs between H150 and H400, with higher content in H400 series 1 and 2, while the opposite is the situation in series 3.

Table 3: Modal mineralogy (obtained from XRD) of the increments in the three series (values are normalised to 100 %). Mineral abbreviations after Whitney and Evans (2010).

	Mineralogy (mass %)																	
Increments	Qz	Hem	Ms	Dol	Cal	Ep	Ab	Bt	Mc	Sps	Alm	Di	Mag	Ilm	Amp	Chl	Sd	Total
MCP-1	41.5	26.1	2.6	7.8	2.5	1.9	12.3	2.7	0.7	1.9	n.d.	n.d.	n.d.	n.d.	n.d.	n.d.	n.d.	100.0
MCP-2	45.4	27.2	1.7	4.7	1.5	2.2	11.0	3.0	1.0	n.d.	2.3	n.d.	n.d.	n.d.	n.d.	n.d.	n.d.	100.0
MCP-3	43.4	30.9	2.3	7.9	0.6	2.5	9.6	2.6	n.d.	n.d.	0.2	n.d.	n.d.	n.d.	n.d.	n.d.	n.d.	100.0
H150-1	3.0	78.9	1.4	2.1	0.5	4.0	n.d.	0.6	n.d.	4.4	n.d.	2.8	n.d.	2.4	n.d.	n.d.	n.d.	100.0
H150-2	1.9	88.4	0.4	1.4	n.d.	3.2	n.d.	1.4	n.d.	3.2	n.d.	n.d.	0.2	n.d.	n.d.	n.d.	n.d.	100.0
H150-3	2.1	95.7	n.d.	n.d.	n.d.	1.1	n.d.	0.4	n.d.	n.d.	0.8	n.d.	n.d.	n.d.	n.d.	n.d.	n.d.	100.0
H400-1	2.4	92.0	0.3	n.d.	n.d.	3.4	0.9	n.d.	n.d.	1.0	n.d.	n.d.	n.d.	n.d.	n.d.	n.d.	n.d.	100.0
H400-2	3.0	94.3	n.d.	n.d.	n.d.	0.3	n.d.	n.d.	n.d.	2.4	n.d.	n.d.	n.d.	n.d.	n.d.	n.d.	n.d.	100.0
H400-3	3.5	94.0	n.d.	n.d.	n.d.	1.1	n.d.	0.6	n.d.	n.d.	0.8	n.d.	n.d.	n.d.	n.d.	n.d.	n.d.	100.0
T-1	58.2	11.2	1.7	7.3	1.9	1.8	14.5	2.4	0.7	0.4	n.d.	n.d.	n.d.	n.d.	n.d.	n.d.	n.d.	100.0
T-2	49.5	13.1	3.5	9.4	3.4	2.1	12.8	4.1	2.0	n.d.	0.2	n.d.	n.d.	n.d.	n.d.	n.d.	n.d.	100.0
T-3	56.5	8.9	3.0	10.3	3.2	1.3	11.1	2.2	1.9	n.d.	0.2	n.d.	n.d.	n.d.	0.7	0.6	0.04	100.0

All the increments in all three series contain garnet, either as spessartine or almandine. The amount varies, with the highest contents in series 1, and the lowest in series 3. Spessartine found in series 1 and 2, is enriched in the H150 concentrate. Epidote is also found in all increments, with the lowest amount in series 3 (total for the four increments). T-3 is the only increment that contains small amounts of amphibole, chlorite, and siderite. The carbonates are mainly present in mill circuit products and tailings; however, some amounts are found in H150-1 and -2. The XRD classifies the micas as biotite and muscovite. Magnetite is only found in increment H150-2, with just 0.2 mass %. Diopside and ilmenite were found only in increment H150-1, with 2.8 mass % and 2.4 mass % respectively. The feldspars found by the XRD are albite and microcline, and they are only present in mill circuit product and tailings, apart from 0.9 mass % albite in H400-1. Ilmenite is only found in H150-1, and was observed in the microscope as liberated particles, with titano-hematite lamellas.

4.3 Mineral chemistry

Table 4 show the mineral chemistry of all minerals analysed by the EPMA.

Table 4: Mineral chemistry of the production increments from EPMA. The numbers in the parenthesis behind the minerals reflect the number of grains analysed. All minerals are normalised to 100 %, except the carbonates where the percentage missing from 100 is assumed to represent CO_2. n.a. = not analysed.

Mineral	Statistics	Oxides (mass %)														
		SiO_2	Fe_2O_3	Al_2O_3	CaO	Na_2O	K_2O	MgO	TiO_2	P_2O_5	MnO	CuO	Cl	SO_3	V_2O_3	Total
Magnetite (2)	Average	0.01	99.57	0.11	0.00	0.01	0.01	0.02	0.003	n.a.	0.23	0.01	n.a.	0.004	0.03	100.00
	StDev	0.02	0.02	0.06	0.00	0.02	0.01	0.01	0.004		0.05	0.02		0.01	0.03	
Hematite (23)	Average	0.06	98.45	0.28	0.01	0.04	0.003	0.01	1.01	0.01	0.06	0.02	0.01	0.03	0.02	100.03
	StDev	0.09	1.35	0.16	0.05	0.15	0.01	0.02	1.38	0.01	0.08	0.02	0.01	0.07	0.02	
Ilmenite (2)	Average	0.01	53.65	0.0005	0	0.01	0.004	0.28	44.59	n.a.	0.92	0.03	n.a.	0	0.50	100.00
	StDev	0.02	3.88	0.001	0	0.004	0.01	0.02	3.73		0.07	0.04		0	0.003	
Aegirine-augite (13)	Average	53.56	18.50	2.04	8.14	8.24	0.01	6.25	0.10	n.a.	3.11	0.03	n.a.	0.02	0.01	100.00
	StDev	0.25	1.47	0.32	1.01	0.62	0.02	0.85	0.05		0.77	0.03		0.02	0.02	
Epidote (33)	Average	39.17	14.26	23.40	22.51	0.01	0.004	0.05	0.02	0.004	0.54	0.01	0.002	0.01	0.01	100.00
	StDev	0.24	1.16	0.85	0.44	0.02	0.01	0.03	0.03	0.01	0.31	0.03	0.01	0.02	0.01	
Piemontite (2)	Average	39.13	10.87	21.34	21.61	0.01	0.03	0.05	0.03	n.a.	6.88	0.02	n.a.	0.03	0.01	100.00
	StDev	0.49	1.69	0.65	0.44	0.01	0.01	0.004	0.01		1.05	0.02		0.04	0.01	
Garnet-1 (16)	Average	37.98	2.24	19.55	4.74	0.05	0.01	0.72	0.17	n.a.	34.51	0.02	0.02	0.01	0.01	100.02
	StDev	0.30	0.59	0.38	0.85	0.06	0.01	0.19	0.08		0.98	0.03	0.00	0.01	0.01	
Garnet-2 (12)	Average	38.02	8.70	19.64	4.05	0.04	0.01	1.59	0.26	n.a.	27.64	0.03	n.a.	0.02	0.01	100.00
	StDev	0.45	1.98	0.20	0.45	0.02	0.01	0.45	0.58		2.66	0.03		0.02	0.01	
Garnet-3 (9)	Average	37.89	4.42	18.57	5.53	0.02	0.02	1.09	0.186	n.a.	32.24	0.02	0.01	0.01	0.02	100.04
	StDev	0.28	0.62	0.96	1.18	0.03	0.06	0.56	0.15		2.13	0.02	0.01	0.02	0.02	
Amphibole (5)	Average	46.14	15.22	12.24	10.13	2.40	0.49	12.44	0.19	n.a.	0.69	0.02	n.a.	0.01	0.01	100.00
	StDev	1.63	1.97	1.00	0.90	0.28	0.30	1.69	0.33		0.41	0.03		0.03	0.01	
Biotite (25)	Average	40.59	14.26	17.40	0.02	0.17	9.50	16.86	0.85	0.01	0.30	0.01	0.005	0.03	0.02	100.02
	StDev	0.90	3.03	0.42	0.03	0.07	0.46	2.61	0.69	0.01	0.18	0.02	0.01	0.02	0.02	
Muscovite (15)	Average	50.97	6.29	29.64	0.07	0.59	9.04	2.67	0.52	0.02	0.06	0.02	0.01	0.18	0.04	100.11
	StDev	0.88	0.98	1.59	0.20	0.26	1.04	0.51	0.35	0.01	0.06	0.03	0.01	0.32	0.04	
Quartz (36)	Average	99.41	0.36	0.05	0.04	0.01	0.01	0.01	0.01	0.02	0.06	0.01	0.01	0.03	0.004	100.04
	StDev	0.61	0.44	0.11	0.12	0.03	0.02	0.01	0.02	0.02	0.21	0.03	0.01	0.06	0.01	
Albite (7)	Average	68.43	0.34	19.10	0.15	11.64	0.10	0.01	0.15	0.001	0.07	0.01	0.00	0.01	0.01	100.02
	StDev	0.54	0.19	0.59	0.19	0.26	0.03	0.01	0.34	0.002	0.12	0.0001	0.01	0.01	0.01	
Oligoclase (8)	Average	64.49	0.31	21.98	3.28	9.71	0.16	0.03	0.01	0.01	0.01	0.02	0.001	0.005	0.01	100.02
	StDev	1.23	0.29	0.67	1.00	0.58	0.29	0.06	0.02	0.01	0.01	0.02	0.002	0.004	0.01	
Calcite (5)	Average	0.00	0.75	0.03	52.46	0.00	0.01	0.01	0.03	n.a.	0.12	0.01	n.a.	0.01	0.01	53.44
	StDev	0.00	1.42	0.05	0.68	0.00	0.01	0.01	0.05		0.04	0.02		0.01	0.01	
Dolomite-1 (3)	Average	0.06	0.60	0.08	30.74	0.03	0.003	3.47	0.004	n.a.	20.92	0.005	n.a.	0.00	0.00	55.91
	StDev	0.11	0.45	0.10	2.45	0.03	0.01	0.81	0.01		1.41	0.01		0.00	0.00	
Dolomite-2 (2)	Average	0.00	0.79	0.02	36.81	0.02	0.01	5.63	0.02	0.01	13.99	n.a.	0.01	n.a.	n.a.	57.30
	StDev	0.00	0.35	0.02	2.35	0.01	0.01	0.42	0.02	0.01	1.00		0.01			
Dolomite-3 (2)	Average	0.00	2.49	0.00	28.61	0.003	0.002	11.35	0.00	n.a.	14.62	0.02	n.a.	0.00	0.002	57.10
	StDev	0.00	1.06	0.00	0.50	0.004	0.002	1.42	0.00		4.81	0.02		0.00	0.002	
Dolomite-4 (1)		0.00	1.10	0.00	32.65	0.01	0	22.65	0.05	0.00	1.15	n.a.	0.01	n.a.	n.a.	57.63
Ankerite-1 (11)	Average	0.004	9.26	0.01	30.49	0.01	0.002	15.91	0.002	0.001	2.45	0.02	0.001	0.01	0.005	58.18
	StDev	0.01	2.85	0.01	1.15	0.01	0.002	1.34	0.004	0.002	1.13	0.04	0.001	0.02	0.01	
Ankerite-2 (8)	Average	0.00	2.50	0.01	55.20	0.02	0.01	2.88	0.02	0.02	2.54	0.02	0.01	0.03	0.01	63.27
	StDev	0.00	0.60	0.01	3.94	0.02	0.01	0.84	0.03	0.02	2.03	0.03	0.004	0.02	0.02	
Ankerite-3 (5)	Average	0.00	5.97	0.01	30.65	0.02	0.00	14.48	0.01	0.02	6.79	0.02	0.01	0.01	0.01	58.00
	StDev	0.00	1.49	0.01	1.52	0.019	0.01	0.45	0.02	0.03	1.36	0.02	0.001	0.01	0.02	

Three variations of garnet were identified, all belonging to the almandine-spessartine series with varying contributions from the endmembers. Based on the mineral formula calculated stoichiometrically, garnet-1 consists of $Sps_{78.8}Alm_{4.5}Prp_{2.8}$ and 13.6 % from the andradite-grossular series, garnet-2 consists of $Sps_{63.7}$ $Alm_{17.8}$ $Prp_{6.4}$ and 11.8 % from the andradite-grossular series, and garnet-3 consists of $Sps_{70.7}Alm_{8.6}Prp_{4.2}$ and 15.3 % from the andradite-grossular series.

Table 5 show the calculated structural mineral formulas of all minerals identified in the EPMA analyses. For some mineral groups, variations or different species were found, these have separate mineral formulas. Deer et al. (1992) defines ankerite as minerals with Mg/Fe ≤ 4:1, and dolomite as minerals with Mg/Fe > 4:1.

Table 5: The calculated mineral structural formulas from the EPMA-data. Calculated following the principles in Deer et al. (1992).

Mineral	Mineral structural formula
Magnetite	$Fe_{3.97}O_4$
Hematite	$Fe_{1.96}O_3$
Ilmenite	$Fe_{0.94}Ti_{0.78}O_3$
Aegirine-augite	$(Ca, Na)_{0.97}(Mg, Fe, Al)_{1.002}Si_{2.09}O_6$
Epidote	$Ca_{1.94}Al_2O.\ (Al, Fe)_{1.09}OH[Si_{2.16}O_7]\ [SiO_4]$
Piemontite	$Ca_{1.89}(Mn, Fe, Al)_{3.19}O.OH[Si_{2.19}O_7]\ [SiO_4]$
Garnet-1 ($sp_{78.82}$, $alm_{4.49}$, $py_{2.83}$) ($gro+and+uv_{13.64}$)	$(Mg, Fe, Mn, Ca)_{6.01}(Al, Ti)_{3.76}\ Si_{6.16}O_{24}$
Garnet-2 ($sp_{63.70}$, $alm_{17.82}$, $py_{6.39}$) ($gro+and+uv_{11.77}$)	$(Mg, Fe, Mn, Ca)_{5.95}(Al, Ti)_{3.79}\ Si_{6.17}O_{24}$
Garnet-3 ($sp_{70.70}$, $alm_{8.55}$, $py_{4.20}$) ($gro+and+uv_{15.33}$)	$(Mg, Fe, Mn, Ca)_{6.20}(Al, Ti)_{3.57}\ Si_{6.15}O_{24}$
Hornblende/Amphibole	$(Ca, Na)_{2.35}(Fe, Mg, Mn, Al)_{5.82}Si_{6.99}Al_{1.01}O_{22}(OH)_2$
Phlogopite-Biotite	$(K, Ca, Na)_{1.76}(Mg, Fe, Mn, Al)_{5.74}(Si, Al)_8O_{22}$
Muscovite	$(K, Ca, Na)_{1.79}(Fe, Al, Mg)_{5.31}Si_{7.16}Al_{0.84}O_{20}(OH)_4$
Quartz	$Si_{1.00}O_2$
Albite	$Na_{0.99}Al_{0.99}Si_{3.01}O_8$
Oligoclase	$(Ca, Na)_{0.99}Al_{1.14}Si_{2.85}O_8$
Calcite	$Ca_{0.91}CO_3$
Dolomite-1 (Kutnohorite)	$Ca_{1.12}(Mn, Mg)_{0.78}\ (CO_3)_2$
Dolomite-2 (Kutnohorite)	$Ca_{1.96}(Mn, Mg)_{1.01}\ (CO_3)_2$
Dolomite-3 (Kutnohorite)	$Ca_{1.48}(Mg, Mn)_{1.42}\ (CO_3)_2$
Dolomite-4	$Ca_{1.48}Mg_{1.43}\ (CO_3)_2$
Ankerite-1	$Ca_{1.08}(Mg, Fe, Mn)_{1.08}\ (CO_3)_2$
Ankerite-2	$Ca_{2.10}(Mg, Mn, Fe)_{0.3}\ (CO_3)_2$
Ankerite-3	$Ca_{1.09}(Mg, Mn, Fe)_{1.05}\ (CO_3)_2$

4.4 Fe deportment

The non-economic minerals accommodating the largest amount of Fe_2O_3 are ilmenite, aegirine-augite, amphibole, epidote and biotite, with 53.65 mass %, 18.5 mass %, 15.22 mass %, 14.26 %, and 14.25 mass %, respectively (Table 4). Four dolomites and three ankerites were identified from the EPMA analyses. Dolomite-3 has the highest Fe_2O_3 content of the dolomites with 2.49 mass %. The ankerites contain more Fe_2O_3 compared to the dolomites, with 2.50-9.26 mass %.

Fe_{sil} is calculated for all increments based on XRD- and EPMA results (Table 6). Dolomite-3 from EPMA, with the highest Fe_2O_3 content, was used for calculation of Fe contribution from dolomites. Garnet-1 was used to calculate the Fe contribution from the spessartine, while garnet-2 was used to calculate the Fe contribution from almandine given that these variations of garnet have the highest contents of spessartine and almandine respectively. The largest variation in Fe_{sil} is found in the H150 concentrates, where it varies between 0.20-1.90 %. For the mill circuit products and tailings, the Fe_{sil} is around 1 %, while the H400 concentrates vary between 0.08-0.38 %.

Table 6: Calculation of Fe_{sil} in the increments, based on mineral chemistry and XRD results. n.d. = not detected. A = Fe in mineral (from EPMA), B= Mineral in increment (from XRD), and C = Fe contribution in increment.

		Minerals (mass %)													Fe_{sil} (p.p.)
		Quartz	Albite	Feldspar	Muscovite	Calcite	Dolomite	Epidote	Spessartine	Almandine	Biotite	Diopside	Ilmenite	Amphibole	
	A	0.25	0.23	0.21	4.40	0.52	1.74	9.97	1.57		9.97				
MCP-1	B	41.5	12.3	0.7	2.6	2.5	7.8	1.9	1.9	n.d.	2.7	n.d.	n.d.	n.d.	
	C	0.1	0.03	0.001	0.11	0.01	0.14	0.19	0.03		0.27				0.89
	A	0.25	0.23	0.21	4.40	0.52	1.74	9.97		6.09	9.97				
MCP-2	B	45.4	11	1	1.7	1.5	4.7	2.2	n.d.	2.3	3	n.d.	n.d.	n.d.	
	C	0.11	0.03	0.002	0.07	0.01	0.08	0.22		0.14	0.3				0.97
	A	0.25	0.23		4.40	0.52	1.74	9.97		6.09	9.97				
MCP-3	B	43.4	9.6	n.d.	2.3	0.6	7.9	2.5	n.d.	0.2	2.6	n.d.	n.d.	n.d.	
	C	0.11	0.02		0.1	0.003	0.14	0.25		0.01	0.26				0.89
	A	0.25			4.40	0.52	1.74	9.97	1.57		9.97	12.94	37.53		
H150-1	B	3	n.d.	n.d.	1.4	0.5	2.1	4	4.4	n.d.	0.6	2.8	2.4	n.d.	
	C	0.01			0.06	0.003	0.04	0.4	0.07		0.06	0.36	0.9		1.90
	A	0.25			4.40		1.74	9.97	1.74		9.97				
H150-2	B	1.9	n.d.	n.d.	0.4	n.d.	1.4	3.2	3.2	n.d.	1.4	n.d.	n.d.	n.d.	
	C	0.005			0.018		0.024	0.319	0.056		0.14				0.56
	A	0.25						9.97		6.09	9.97				
H150-3	B	2.1	n.d.	n.d.	n.d.	n.d.	n.d.	1.1	n.d.	0.8	0.4	n.d.	n.d.	n.d.	
	C	0.01						0.11		0.05	0.04				0.20
	A	0.25	0.23		4.40			9.97	1.57						
H400-1	B	2.4	0.9	n.d.	0.3	n.d.	n.d.	3.4	1	n.d.	n.d.	n.d.	n.d.	n.d.	
	C	0.01	0.002		0.01			0.34	0.02						0.38
	A	0.25						9.97	1.74						
H400-2	B	3	n.d.	n.d.	n.d.	n.d.	n.d.	0.3	2.4	n.d.	n.d.	n.d.	n.d.	n.d.	
	C	0.01						0.03	0.04						0.08
	A	0.25						9.97		6.09	9.97				
H400-3	B	3.5	n.d.	n.d.	n.d.	n.d.	n.d.	1.1	n.d.	0.8	0.6	n.d.	n.d.	n.d.	
	C	0.01						0.11		0.05	0.06				0.23
	A	0.25	0.23	0.21	4.40	0.52	1.74	9.97	1.57		9.97				
T-1	B	58.2	14.5	0.7	1.7	1.9	7.3	1.8	0.4	n.d.	2.4	n.d.	n.d.	n.d.	
	C	0.15	0.03	0.001	0.07	0.01	0.13	0.18	0.01		0.24				0.82
	A	0.25	0.23	0.21	4.40	0.52	1.74	9.97		6.09	9.97				
T-2	B	49.5	12.8	2	3.5	3.4	9.4	2.1	n.d.	0.2	4.1	n.d.	n.d.	n.d.	
	C	0.12	0.03	0.004	0.15	0.02	0.16	0.21		0.01	0.41				1.12
	A	0.25	0.23	0.21	4.40	0.52	1.74	9.97		6.09	9.97			10.65	
T-3	B	56.5	11.1	1.9	3	3.2	10.3	1.3	n.d.	0.2	2.2	n.d.	n.d.	0.7	
	C	0.14	0.03	0.004	0.13	0.02	0.18	0.13		0.01	0.22			0.07	0.94

4.5 Calculations of recovery ($Rec_{present}$ and $Rec_{realhem}$)

The distribution of Fe in the twelve increments are shown in Table 7. The Fe_{tot*} is calculated by Equation 7. From the results in Table 2 and Table 6, and with Fe_{tot*} as the basis, Fe_{hem} and Fe_{mag} was calculated using Equation 1. The XRD detected magnetite only in H150-2. Thus, Fe_{mag} could be calculated for this increment only.

Table 7: The relationship between Fe_{tot}, Fe_{tot*}, Fe_{sil}, Fe_{hem} and Fe_{mag} in the increments.

Increments	Fe_{tot}	Fe_{tot*}	Fe_{sil}	Fe_{hem}	Fe_{mag}
MCP-1	25.86	25.8	0.89	24.91	-
MCP-2	29.49	29.41	0.97	28.45	-
MCP-3	27.46	27.39	0.89	26.5	-
H150-1	62.9	62.66	1.9	60.76	-
H150-2	63.92	63.68	0.56	63	0.11
H150-3	63.98	63.73	0.2	63.53	-
H400-1	64.11	63.86	0.38	63.49	-
H400-2	63.53	63.29	0.08	63.21	-
H400-3	63.55	63.31	0.23	63.08	-
T-1	11.99	11.99	0.82	11.17	-
T-2	11.5	11.5	1.12	10.38	-
T-3	9.74	9.75	0.94	8.81	-

Table 8 show the calculations of $Rec_{present}$ based on Fe_{tot*} (Equation 3) and $Rec_{realhem}$ based on Fe_{hem} (Equation 5). The mass used in the calculations are 610 t/h for feed, 95 t/h for H150 and 110 t/h forH400. The numbers are based on the average production at the mineral processing plant at RG (M. K. Tro, personal communication 2018). The $Rec_{realhem}$ is higher than the $Rec_{present}$ for the three series, the largest difference found in series 3 with 2.44 percent points. Figure 5 shows that $Rec_{realhem}$ values are consistently larger than $Rec_{present}$ values.

Table 8: Calculations of $Rec_{present}$ and $Rec_{realhem}$ using Equation 3 and 5, respectively. Based on the values in table 7.

Hematite concentrate	Series	$Rec_{present}$	$Rec_{realhem}$
H150	1	37.83	37.99
	2	33.72	34.49
	3	36.24	37.34
H400	1	47.48	48.88
	2	41.27	42.62
	3	44.33	45.66
H150+H400	1	85.31	86.87
	2	74.99	77.11
	3	80.56	83

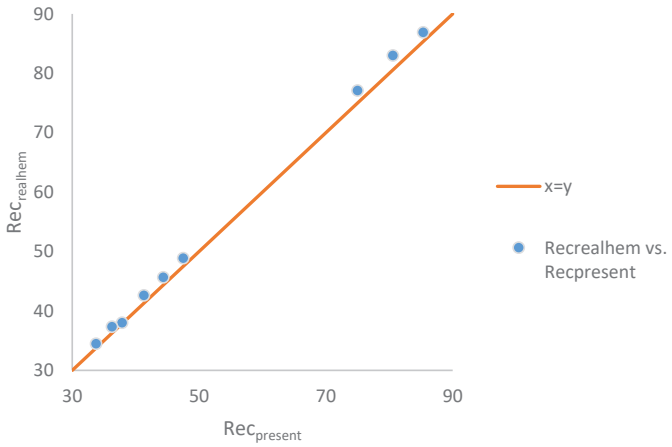

Figure 5: The relationship between $Rec_{realhem}$ and $Rec_{present}$.

5 Discussion

5.1 Element and mineral deportment analyses in the feed, hematite concentrates, and the tailing

Even though all analysed increments are from the Kvannevann deposit, there are still some variations in the Fe_{tot} of the increments in the mill circuit product, hematite concentrate, and tailing samples. The H400-2, H150-3 and H400-3 increments have the highest hematite content, and smaller amounts of non-economic minerals compared to the other hematite concentrates. The variations in Fe_{tot*} and hematite content between the series and between the hematite

concentrates is likely related to differences in ore type distribution in the crude ore or operational differences in the mineral processing plant on the given days the material was processed. The variation in the Fe_{tot*} content (or the Fe_2O_3 content) and the hematite content is related to the amount of Fe_{sil} in the increments. For instance, the H150-1 increments contains 89.94 mass % Fe_2O_3, while the hematite content is 78.9 mass %. This suggests that not all the Fe is located in the hematite. Although some of this difference can be explained by analytical errors in the XRD, the fact that the Fe_{sil} for this increment is 1.90 % clearly indicates that Fe located in non-economic minerals is part of the explanation.

The XRD detected magnetite only in H150-2, however, it was detected in the MCP-2 and H400-2 in the EPMA analyses. In the Rietveld refinement TOPAS software, the quantification will normalise the mineralogy, and depending on overlapping peaks and amount of background, mineral content down to 0.01 % may be detected. However, values < 1% are highly unreliable (Madsen et al, 2001; Scarlet et al., 2002; Hestnes et al., 2013). This can explain why magnetite was not detected by the XRD in MCP-2 and H400-2, and why 0.2 mass % was detected in H150-2. This same effect could also be accountable for the small amounts of amphibole, chlorite and siderite found in T-3 only. Although these minerals would be expected to be in MCP-3, the amounts may have been too small for detection and may have been detected in the tailing 3 because they were enriched in this increment.

The WO_3 content is found only in H150-3, H400-3, and T-3, which derives from the tungsten carbide in the vibratory disc mill used to prepare these increments. The NiO content present in all increments except the three before mentioned, most likely derive from the stainless steel used in preparation of these nine increments.

5.2 Determining the corresponding difference between Fe_{tot*} and Fe_{hem}+ Fe_{mag}

The relationship between Fe_{tot*}, Fe_{hem} and Fe_{sil} follow more or less the same trend in the three series. The largest differences in Fe_{tot*} and Fe_{hem} are found in the mill circuit products and tailings, where Fe_{sil} is around 1 %. The exception is H150-1 where Fe_{sil} is 1.9 %. This high value is caused by the ilmenite content, which contributes 0.9 % Fe, and diopside and epidote with a contribution of 0.76 % Fe. The main non-economic minerals in the hematite concentrates are quartz, epidote, mica, dolomite and garnet. Of these, epidote contributes most to the Fe_{sil} and it is also present in all hematite concentrates (Table 6). Biotite contributes a notable amount of Fe, although it is not present in all hematite concentrates. Quartz contributes with 0.1-0.15 % Fe in the mill circuit products and tailings, due to the large amount of quartz present.

5.3 Estimating the effect of the recovery calculations, and the Fe lost to tailing

The recovery calculations in Table 8 show an increased recovery when calculating the $Rec_{realhem}$ compared to $Rec_{present}$. This corresponds to relatively high Fe_{sil} in the mill circuit products (around 1 %), compared to relatively low Fe_{sil} in the hematite concentrates (0.08 – 0.56 %), apart from H150-1 with 1.9 % Fe_{sil}. The high Fe_{sil} in H150-1 is apparent from the small difference between $Rec_{present}$ H150-1 and $Rec_{realhem}$ H150-1 in Table 8. The results show that more hematite is recovered to the concentrate than could be expected using the $Rec_{present}$ calculation. This indicates an underestimation of hematite recovery with the present estimation method. Based on these results and the findings by Klomstadlien (1984), RG might have a better hematite recovery than they presently are able to calculate. Mineralogical analyses combined with mineral chemistry will enable calculation of the $Rec_{realhem}$, thus preventing unnecessary adjustments of the process.

The increments used in this project are from the Kvannevann deposit which is known to yield good Fe_{tot} grades and -recoveries, with the crude ore containing 28 mass % Fe_{tot*} (average of the increments in the MCP sample). Nevertheless, the differences in $Rec_{present}$ and $Rec_{realhem}$ are relatively large. For other iron ore deposits in the formation, with a different ore type distribution, and where the mineralogy differs from that of the Kvannevann deposit, the difference between $Rec_{present}$ and $Rec_{realhem}$ might be even larger. Non-economic minerals could contribute more of the Fe_{tot*}, thus having a negative effect on the calculated hematite recovery, and the amount of undesirable elements in the hematite concentrate. Increased amounts of biotite, amphibole, pyroxene and feldspar could contribute to more alkalis in the hematite concentrate, while garnet and carbonates could contribute to increased MnO in the hematite concentrate.

Hematite is the largest contributor to Fe in the tailings, constituting 90-93 mass % of the Fe_{tot*} in the tailings. Ideally the Fe in tailings should be only from non-economic minerals. In practice, this is difficult to achieve as there might be unliberated hematite and very fine-grained hematite which the mineral separation techniques will fail to recover. Nonetheless, observations suggest that there are some liberated hematite present in the tailings which should rather have been in the hematite concentrate.

6 Conclusion

There are some mineralogical differences between the increments collected for this paper, despite their origin in one single iron ore deposit. This is an indication of differences in ore type distribution in the crude ore and/or operational differences during production.

The amount of Fe_{sil} is around 1 % in the mill circuit products and tailings, making the amount of recoverable Fe (Fe_{hem}) lower than expected by RG AS (Fe_{tot*}). In the hematite concentrates the Fe_{sil} is lower, with the exception of one increment. These differences in Fe_{tot*}, Fe_{hem} and Fe_{sil} causes the $Rec_{realhem}$ to be higher than $Rec_{present}$.

The results show the importance of distinguishing between Fe_{tot}, Fe_{sil}, Fe_{hem}, and Fe_{mag}. The amount of Fe_{sil} in mill circuit product, hematite concentrates, and tailing will affect the real recovery of hematite, the amount of undesirable elements in the hematite concentrate, and the amount of Fe_{hem} lost to the tailings. By calculating the actual hematite recovery based on Fe_{hem} instead of recovery based on Fe_{tot*}, RG will likely experience an increase in recovery, as the Fe_{tot*} recovery is underestimated compared to the real hematite recovery. Estimating Fe_{hem}, Fe_{mag}, and Fe_{sil} are also important in terms of establishing how much of the Fe resides in non-economic minerals with undesirable elements (MnO, S, and alkalis), as the Fe_{sil} ending up in the hematite concentrate can contribute to higher contents of these elements. The procurement of an XRD with standards specialised for the material produced in RG AS would be advisable, as this would provide the possibility to calculate $Rec_{realhem}$ and $Rec_{realmag}$, and thus gain better quality control of the material through the process.

7 Acknowledgements

This research was funded by the Research Council of Norway (project no. 232428) and RG AS through the Industrial PhD Scheme. Huge thanks to Mari Kristin Tro, Marta Lindberg, Rune Johansen, and Alexander Kühn at RG AS for useful discussions, access to internal reports and other valuable information about production. Thanks also to Torill Sørløkk, Laurentius Tijhuis and Morten Raanes, the operators of XRF, XRD and EPMA, for help with preparation, running and interpretation. Part of the analyses for this paper was conducted by students connected to the course Process mineralogy at NTNU, so thanks to the students who helped with the analyses.

8 References

Bruker (2019) *TOPAS Rietveld analysis software* [online]. Available at: https://www.bruker.com/products/x-ray-diffraction-and-elemental-analysis/x-ray-diffraction/xrd-software/topas/rietveld-analysis-software.html (Accessed: 06.01.2019)

Bugge J.A.W. (1948) 'Rana Gruber: Geologisk beskrivelse av jernmalmfeltene I Dunderlandsdalen', *Norges Geologiske Undersøkelse*, No. 171, pp. 1-149.

Deer, W.A., Howie, R.A., and Zussman, J. (1992) *An introduction to the rock forming minerals*. 2nd edition. Essex, England: Pearson Education Limited.

Hestnes, K.H., Aasly, K., Sandøy, R. and Sørensen, B.E. (2013) 'Occurrence of iron in industrial granitic pegmatite', *Minerals Engineering*, *52*, pp.21-30.

Klomstadlien, (1984) **'**Silikat bundet jern i råmalm, konsentrat og avgang, Rana Gruber AS', Internal report, Norsk Jernverk.

Lotter, N. O., Evans, C. L., & Engstrőm, K. (2018) 'Sampling–A key tool in modern process mineralogy', *Minerals Engineering*, 116, pp. 196-202.

Madsen, I.C., Scarlett, N.V.Y., Cranwick, L.M.D., Lwin, T. (2001) 'Outcomes of the international union of crystallography commission on powder diffraction round robin on quantitative phase analysis: samples 1a to 1h', *Journal of Applied Crystallography*, 34, pp. 409–426.

Melezhik, V.A., Ihlen, P.M., Kuznestov, A.B., Gjelle, S., Solli, A., Gorokhov, I.M., Fallick, A.E., Sandstad, J.S., Bjerkgård, T. (2015) 'Pre-Sturtian (800–730 Ma) depositional age of carbonates in sedimentary sequences hosting stratiform iron ores in the Uppermost Allochthon of the Norwegian Caledonides: A chemostratigraphic approach', *Precambrian Research*, 261, pp. 272−299.

NGU (2017) *Database Norwegian Ores* [online]. Available at: http://geo.ngu.no/kart/mineralressurser_mobil/ (Accessed: 12.03.2018)

Rietveld, H.M. (1967) 'Line profiles of neutron powder-diffraction peaks for structure refinement', *Acta Crystallographica*, 22, pp. 151–152.

Rietveld, H.M. (1969) 'A profile refinement method for nuclear and magnetic structures', *Journal of Applied Crystallography*, 2, pp. 65–71.

Scarlett, N.V.Y., Madsen, I.C., Cranswick, L.M.D., Lwin, T., Groleau, E., Stephenson, G., Aylmore, M., Agron-Olshina, N. (2001) 'Outcomes of the international union of crystallography commission on powder diffraction round robin on quantitative phase analysis: samples 2, 3, 4, synthetic bauxite, natural granodiorite and pharmaceuticals', *Journal of Applied Crystallography*, 35, pp. 383-400.

Søvegjarto, U. (1972) *Berggrunnsgeologiske undersøkelser i Dunderlandsdalen, Nordland*. Post graduate thesis, University of Oslo, 139p.

Søvegjarto, U. (1990) 'Jernmalmer i Rana', In Rui, I.J. (eds). *Deformasjon og remobiliseringav malmer*. Internal technical report no. 76, BVLI-prosjekt, pp. 154 -176.

Tøgersen, M.K., Kleiv, R.A., Ellefmo, S. and Aasly, K. (2018) 'Mineralogy and texture of the Storforshei iron formation, and their effect on grindability', *Minerals Engineering*, *125*, pp. 176-189.

Tøgersen, M.K., Kleiv, R.A., Ellefmo, S., and Aasly, K. (unpublished manuscript) 'Development of a pilot circuit for identifying variations in metallurgical performance for iron ore from Storforshei iron formation'.

Whitney, D.L., Evans, B.W. (2010) 'Abbreviations for names of rock-forming minerals', *American Mineralogist*, 95, pp. 185-187.

Wills, B. A., & Finch, J. (2015) *Wills' mineral processing technology: an introduction to the practical aspects of ore treatment and mineral recovery*. 8th edition. Butterworth Heinemann, Elsevier.

APPENDICES

Appendix A: Chemical analyses not presented in the papers

Chemical analyses of production samples, conducted by the lab at RG

	H150 Chemistry (wt %)				
	Fe_{tot}	Fe-Mag	SiO_2	MnO	S
11 November 2013	62.53	1.72	3.82	0.25	0.016
08 November 2013	63.64	1.18	3.38	0.31	0.017
04 November 2013	64.46	1.31	2.92	0.25	0.017
04 October 2013	63.94	0.56	2.97	0.46	0.015

	H400 Chemistry (wt %)				
	Fe_{tot}	Fe-Mag	SiO_2	MnO	S
11 November 2013	61.35	0.74	5.15	0.21	0.017
08 November 2013	62.75	0.47	4.21	0.34	0.015
04 November 2013	62.46	0.59	4.37	0.26	0.02
04 October 2013	62.58	0.53	3.86	0.35	0.015

XRF and titration analyses compared (XRF analyses conducted at NTNU, titration conducted at RG)

Increments	XRF SiO_2 (wt %)	Titration SiO_2 (wt %)	XRF Fe_{tot} (wt %)	Titration Fe_{tot} (wt %)	XRF MnO (wt %)	Titration MnO (wt %)
1K1 (hematite concentrate)	15.71		50.89	51.67	0.34	
1M1 (middling)	48.61		14.4	14.4	0.66	
1A1 (tailing)	66.7		6.76	7.04	0.35	
1K2 (hematite concentrate)	6.28		62.50	62.26	0.19	
5K1 (hematite concentrate)	12.67		54.76	54.68	0.29	0.31
5M1 (middling)	55.15		12.82	12.93	0.51	
5A1 (tailing)	73.45		5.30	5.39	0.28	0.23
5K2 (hematite concentrate)	5.77	5.56	62.96	62.11	0.21	0.21
5M2 (middling)	29.4		33.14	32.6	0.66	0.69
5A2 (tailing)	49.69		14.76	14.28	0.62	

Appendix B: Modal mineralogy of the pilot circuit outputs

	Mineralogy (wt %)																
Outputs	Ab	Bt	Cal	Chl	Czo	Di	Dol	Ep	Hem	Hbl	Mag	Ms	Phl	Qz	Sd	Ttn	Sp	Total
KV PM	17.2	4.9		2.3			6.6		20.3	2.8	3.4	4.5		38.0	0.04			100.0
KV Mag	6.6	0.7							4.4		79.1	0.4		8.8				100.0
KVK1	7.5	1.8						10.2	55.3	4.4		0.5		20.2				100.0
KVM1	16.9	6.8		1.9			9.1	8.2	9.3	5.2		4.8		37.8				100.0
KVA1	21.2	5.8		1.2			6.2	4.1	3.6	2.7		5.8		49.2	0.1			100.0
KVK2 0,6	3.8	1.3					2.3		86.5	0.6	0.6	0.5		4.4				100.0
KVK2 0,7		0.9					1.5		92.2	0.8		0.5		4.1				100.0
KVK2 0,8		0.4					1.9		91.7	2.0		0.9		3.1				100.0
KVM2 0,6	7.5	3.3		1.3			9.1	12.1	40.6	7.8		1.3		17.0				100.0
KVM2 0,7	7.8	4.4		0.5			10.3	16.3	31.3	8.1		2.9		18.5				100.0
KVM2 0,8	8.1	2.2		3.0			10.7	13.9	37.3	8.3		2.1		14.7				100.0
KVA2 0,6	14.3	5.6		1.7			10.0	13.1	12.1	6.7		2.9		33.6	0.02			100.0
KVA2 0,7	14.4	5.7		3.2			11.1	11.3	10.1	7.0		1.9		35.2	0.06			100.0
KVA2 0,8	15.5	5.4		3.4			8.9	10.1	7.4	5.7		3.5		40.1	0.01			100.0
ST PM	12.8		0.8				6.7	4.0	15.1			5.8	5.2	49.6				100.0
ST Mag		0.4			2.7				5.3		84.5			7.1				100.0
STK1	5.0	1.7						9.5	72.3	0.2				11.3				100.0
STM1	10.7	6.3	0.0	2.0			9.2	11.5	14.1			1.5		44.7				100.0
STA1	13.5	5.3					8.7	3.0	4.3	1.2		2.4		61.6	0.02			100.0
STK2 0,6					1.6				93.8					4.6				100.0
STK2 0,7								2.3	92.9			0.4		4.4				100.0
STK2 0,8		0.4			3.5				92.3					3.8				100.0
STM2 0,6	4.8						1.2	16.0	61.2				3.3	13.6				100.0
STM2 0,7	5.1						6.9	17.4	49.8				4.8	16.0				100.0
STM2 0,8	4.0						7.7	18.8	44.5				8.2	16.7			0.02	100.0
STA2 0,6	8.3	5.5					17.2	15.9	14.6	2.7		1.7		34.2	0.01			100.0
STA 2 0,7	9.4		0.2				13.0	15.6	8.5	2.3			8.9	41.4		0.8		100.0
STA2 0,8	9.4	5.8					17.9	13.1	11.5	2.5		1.3		38.5	0.03			100.0
SØ PM	6.4		2.8	1.2			5.5	3.5	28.0			11.4		41.2				100.0
SØ Mag	4.2	0.9	1.2				2.5		28.8		31.4	4.4		26.6				100.0
SØK1	2.4						3.9		79.9			2.6		11.1				100.0
SØM1	5.7	2.5	3.4				8.2	5.7	18.7			11.8		44.0				100.0
SØA1	8.6	1.7	1.8	2.6			1.8	6.0	10.5			6.4		60.6	0.06			100.0

SØK2 0,6							1.6		89.3		1.8	7.3			100.0
SØK 2 0,7									84.4		3.3	12.3			100.0
SØK2 0,8							0.8		89.6		0.9	8.8			100.0
SØM2 0,6	3.3	0.7	0.8				5.8	7.3	56.5		3.9	21.7			100.0
SØM2 0,7	3.0	2.1	1.4				6.2	7.2	50.1		6.6	23.4			100.0
SØM2 0,8	3.2	0.5	1.8				7.3	8.8	46.1		6.8	25.7			100.0
SØA2 0,6	4.7	2.0	0.6	2.1	10.3		4.3		41.9		4.1	30.0			100.0
SØA 2 0,7	5.5		2.3	1.4	11.3	2.0	8.5		23.3		8.5	37.3			100.0
SØA2 0,8	4.6	0.8	0.5	1.7	10.5		5.3		31.7		5.5	39.6	0.01		100.0

Appendix C: Mineral chemistry

Mineral chemistry (wt %)

SiO_2	Fe_2O_3	Al_2O_3	CaO	Na_2O	K_2O	MgO	TiO_2	P_2O_5	MnO	CuO	Cl	SO_3	V_2O_3	Total
							Magnetite							
0.02	102.14	0.16	0.00	0.02	0.00	0.03	0.00		0.20	0.00		0.00	0.01	102.57
0.00	99.89	0.06	0.00	0.00	0.02	0.01	0.01		0.26	0.03		0.01	0.05	100.33
							Hematite							
0.00	100.70	0.36	0.04	0.04	0.00	0.00	0.02	0.03	0.02		0.02			101.22
0.00	100.82	0.41	0.00	0.00	0.00	0.00	0.03	0.00	0.00		0.01			101.27
0.00	99.69	0.35	0.00	0.00	0.01	0.01	1.43	0.00	0.00		0.02			101.50
0.00	100.29	0.21	0.00	0.03	0.00	0.03	0.00	0.01	0.00		0.00			100.57
0.02	97.71	0.26	0.00	0.00	0.02	0.01	0.08		0.00	0.03		0.00	0.01	98.13
0.22	95.94	0.39	0.00	0.72	0.00	0.03	0.08		0.00	0.05		0.31	0.04	97.77
0.00	97.23	0.26	0.00	0.02	0.00	0.00	0.00		0.03	0.07		0.00	0.01	97.61
0.00	101.85	0.10	0.00	0.03	0.00	0.03	0.00		0.21	0.00		0.03	0.02	102.27
0.00	98.10	0.20	0.00	0.02	0.00	0.00	0.05		0.05	0.00		0.01	0.00	98.43
0.08	93.90	0.12	0.00	0.00	0.00	0.00	4.51		0.19	0.03		0.00	0.09	98.91
0.06	93.21	0.23	0.01	0.00	0.00	0.00	4.57		0.00	0.00		0.00	0.04	98.12
0.18	97.02	0.45	0.09	0.04	0.00	0.00	0.77		0.00	0.04		0.00	0.01	98.60

0.00	97.29	0.32	0.00	0.06	0.00	0.00	0.77	0.05	0.04	0.00	0.01	98.54
0.00	96.07	0.60	0.00	0.04	0.00	0.00	0.19	0.01	0.00	0.00	0.00	96.91
0.00	96.12	0.59	0.00	0.00	0.00	0.04	0.21	0.00	0.01	0.06	0.01	97.03
0.32	98.04	0.42	0.20	0.00	0.02	0.00	0.07	0.05	0.00	0.03	0.04	99.18
0.05	97.34	0.27	0.00	0.00	0.00	0.05	1.12	0.01	0.04	0.05	0.04	98.96
0.05	97.22	0.22	0.00	0.00	0.01	0.01	1.09	0.02	0.06	0.01	0.00	98.68
0.19	95.88	0.07	0.00	0.00	0.00	0.02	2.96	0.08	0.00	0.00	0.05	99.25
0.13	97.24	0.10	0.00	0.00	0.01	0.00	1.46	0.11	0.00	0.00	0.06	99.10
0.04	96.46	0.12	0.00	0.00	0.00	0.00	2.18	0.26	0.02	0.00	0.01	99.09
0.10	97.18	0.04	0.00	0.02	0.00	0.07	0.89	0.15	0.00	0.04	0.00	98.47
0.00	98.45	0.37	0.00	0.00	0.00	0.00	0.45	0.05	0.01	0.00	0.01	99.33
							Ilmenite					
0.03	53.68	0.00	0.00	0.01	0.00	0.31	49.80	1.03	0.07	0.00	0.53	105.45
0.00	58.74	0.00	0.00	0.02	0.01	0.27	43.70	0.91	0.00	0.00	0.52	104.15
							Aegirine-augite					
52.95	18.18	2.30	8.54	7.99	0.08	6.44	0.15	2.31	0.02	0.04	0.00	98.98
53.73	18.38	2.34	8.48	8.53	0.01	6.15	0.12	1.45	0.00	0.03	0.02	99.23
53.43	18.49	1.65	8.11	7.90	0.00	6.52	0.02	3.43	0.04	0.05	0.00	99.63
53.16	22.05	1.92	6.16	9.37	0.02	4.57	0.12	2.50	0.04	0.03	0.00	99.95
53.75	20.20	2.16	7.11	8.88	0.00	5.48	0.05	3.10	0.00	0.02	0.00	100.74
53.75	16.20	1.51	9.95	7.20	0.00	7.77	0.11	3.80	0.02	0.01	0.01	100.33
53.61	17.77	2.10	8.82	7.96	0.01	6.80	0.11	3.34	0.00	0.00	0.06	100.58
53.12	17.83	1.71	8.72	7.74	0.02	6.74	0.15	3.37	0.07	0.01	0.00	99.48
54.23	18.77	2.33	6.95	8.67	0.00	5.72	0.06	3.99	0.02	0.03	0.00	100.77
54.33	19.20	2.38	7.79	8.82	0.01	5.67	0.08	2.96	0.00	0.00	0.03	101.27
54.28	19.40	2.46	7.70	8.83	0.01	5.62	0.11	2.49	0.06	0.00	0.00	100.94
54.19	17.53	2.07	8.89	8.06	0.00	6.75	0.17	3.51	0.07	0.00	0.00	101.25
53.41	17.04	1.67	8.80	7.47	0.03	7.23	0.03	4.27	0.00	0.03	0.01	99.99
							Epidote					
38.23	14.72	21.80	21.44	0.01	0.00	0.06	0.06	0.55	0.01	0.01	0.00	96.88
38.20	14.45	21.78	22.32	0.02	0.00	0.04	0.00	0.26	0.02	0.00	0.02	97.11

38.01	14.79	21.18	21.88	0.02	0.02	0.05	0.05		0.17	0.00		0.00	0.03	96.17
37.98	14.50	22.17	20.90	0.01	0.02	0.03	0.00		0.78	0.00		0.00	0.00	96.40
38.08	14.22	22.43	21.81	0.04	0.00	0.02	0.00		0.70	0.00		0.00	0.01	97.30
37.97	14.05	22.61	22.01	0.00	0.00	0.04	0.09		0.06	0.00		0.00	0.00	96.83
38.34	11.15	24.31	22.84	0.00	0.01	0.01	0.05		0.13	0.00		0.03	0.03	96.91
37.63	15.35	21.86	21.35	0.03	0.02	0.05	0.00		0.49	0.10		0.00	0.00	96.88
37.80	14.41	22.22	21.38	0.00	0.01	0.03	0.01		1.13	0.00		0.00	0.01	97.00
38.30	13.43	22.87	22.10	0.01	0.00	0.02	0.00		0.17	0.00		0.01	0.02	96.93
38.13	14.18	22.46	21.77	0.02	0.00	0.02	0.00		0.98	0.01		0.00	0.01	97.57
37.95	14.96	22.43	21.85	0.00	0.00	0.00	0.00	0.02	0.45		0.02			97.67
38.10	14.04	23.40	22.50	0.00	0.01	0.03	0.05	0.05	0.25		0.02			98.43
38.13	14.14	23.03	22.09	0.03	0.00	0.00	0.02	0.05	0.31		0.03			97.83
38.24	13.43	23.55	22.87	0.03	0.00	0.09	0.00	0.01	0.41		0.01			98.63
39.08	10.20	26.32	23.18	0.01	0.00	0.10	0.11	0.00	0.13		0.00			99.13
37.71	14.81	21.97	21.37	0.00	0.00	0.04	0.00		0.61	0.04		0.00	0.00	96.56
37.54	13.97	22.61	22.29	0.05	0.00	0.02	0.04		0.14	0.00		0.00	0.03	96.68
37.93	14.08	22.72	21.75	0.05	0.01	0.06	0.05		0.57	0.00		0.00	0.00	97.21
37.88	15.36	21.96	21.79	0.02	0.00	0.05	0.01		0.31	0.00		0.00	0.02	97.41
38.11	12.64	23.47	22.12	0.02	0.02	0.03	0.02		0.74	0.00		0.02	0.04	97.20
37.69	13.62	22.41	21.63	0.01	0.01	0.06	0.00		0.64	0.00		0.05	0.00	96.11
37.53	14.46	21.76	20.92	0.00	0.00	0.04	0.00		0.88	0.00		0.00	0.00	95.60
37.51	14.76	22.12	20.96	0.00	0.00	0.12	0.04		0.17	0.00		0.02	0.04	95.74
37.49	13.83	22.46	21.84	0.00	0.00	0.05	0.00		0.74	0.06		0.01	0.01	96.50
37.92	13.99	22.59	21.69	0.00	0.00	0.00	0.01		0.72	0.00		0.00	0.01	96.93
37.80	13.55	22.13	21.76	0.01	0.00	0.02	0.00		0.78	0.00		0.02	0.01	96.08
38.14	12.53	23.46	21.75	0.00	0.00	0.11	0.00		0.76	0.04		0.07	0.00	96.85
37.47	12.82	22.78	21.59	0.00	0.00	0.08	0.05		0.78	0.00		0.03	0.03	95.61
37.97	12.87	23.12	20.90	0.03	0.00	0.09	0.03		1.06	0.12		0.00	0.04	96.22
38.18	13.51	23.19	21.92	0.00	0.00	0.01	0.00		0.29	0.01		0.05	0.01	97.16
38.52	14.56	22.46	22.08	0.00	0.00	0.04	0.00		0.32	0.00		0.00	0.03	98.02
38.38	12.89	23.52	21.82	0.00	0.00	0.09	0.00		0.73	0.00		0.00	0.04	97.46

							Piemonite						
37.36	9.15	20.63	20.16	0.00	0.02	0.04	0.03	7.22	0.03		0.00	0.01	94.65
36.83	11.46	19.83	20.82	0.01	0.03	0.05	0.04	5.83	0.00		0.06	0.02	94.98
							Garnet-1						
37.76	1.90	19.83	4.14	0.01	0.00	0.77	0.16	34.78		0.02			99.37
38.35	1.59	19.72	3.68	0.18	0.02	0.97	0.10	34.43					99.04
37.34	2.38	19.39	4.77	0.03	0.01	0.86	0.16	33.81					98.74
37.31	3.49	19.44	5.79	0.03	0.00	0.79	0.22	32.28	0.08			0.04	99.47
37.90	1.64	19.78	4.38	0.03	0.01	0.66	0.06	35.53					100.00
38.01	2.61	19.26	4.76	0.08	0.00	0.82	0.24	34.17	0.03		0.01		99.99
37.62	2.80	18.84	3.68	0.01	0.00	0.78	0.18	35.30	0.06		0.01		99.26
37.46	2.61	18.50	5.40	0.00	0.01	0.26	0.30	34.49					99.03
37.40	2.06	19.52	4.67	0.00	0.03	0.69	0.10	34.68			0.02	0.01	99.17
37.38	3.04	19.84	4.20	0.05	0.00	1.07	0.15	33.60			0.01		99.34
37.78	1.53	19.77	4.58	0.00	0.00	0.75	0.11	35.40	0.03		0.02	0.01	99.98
37.79	2.28	19.33	4.23	0.09	0.04	0.66	0.15	34.59			0.05	0.02	99.24
37.70	1.67	19.57	6.99	0.05	0.01	0.60	0.25	32.15	0.04		0.01		99.04
37.70	1.88	19.67	4.81	0.00	0.02	0.69	0.05	34.59	0.02				99.42
38.02	2.43	18.83	5.24	0.20	0.00	0.47	0.28	33.50			0.01	0.02	99.00
38.18	1.68	19.50	4.06	0.01	0.00	0.58	0.14	35.35	0.05		0.04	0.01	99.60
							Garnet-2						
38.27	8.01	19.72	4.80	0.07	0.02	1.45	0.09	27.48	0.02		0.00	0.00	99.93
39.07	9.41	19.69	4.06	0.07	0.01	1.78	0.00	26.40	0.05		0.07	0.00	100.61
37.91	11.45	19.63	4.48	0.03	0.00	2.63	0.09	24.00	0.11		0.00	0.01	100.32
37.42	10.14	19.27	4.41	0.04	0.00	1.78	2.11	25.06	0.02		0.01	0.02	100.27
37.83	8.52	19.88	3.96	0.00	0.01	1.30	0.10	29.10	0.00		0.00	0.00	100.70
38.46	12.80	19.79	4.46	0.02	0.03	2.00	0.00	23.24	0.06		0.00	0.00	100.85
38.67	7.94	19.77	4.06	0.01	0.00	1.35	0.08	28.20	0.00		0.03	0.00	100.12
37.94	9.22	19.56	3.31	0.03	0.02	1.65	0.19	28.28	0.04		0.04	0.02	100.30
38.21	6.92	19.43	3.92	0.03	0.03	1.22	0.19	29.71	0.00		0.01	0.00	99.68
37.33	7.18	19.51	3.26	0.02	0.01	1.22	0.04	30.86	0.00		0.00	0.02	99.44

37.50	5.56	19.74	3.74	0.03	0.01	0.90	0.10		31.09	0.00		0.02	0.01	98.69
37.95	7.46	19.83	4.23	0.07	0.01	1.79	0.11		28.39	0.01		0.00	0.01	99.86
							Garnet-3							
37.71	4.96	17.00	4.67	0.00	0.01	0.79	0.15		33.82		0.00	0.00	0.05	99.15
37.20	4.74	18.00	3.68		0.03	0.75	0.11		34.49		0.02			99.01
37.53	4.56	18.44	5.18	0.03		0.77	0.36		32.33					99.19
37.52	5.10	17.03	7.30		0.17	0.93	0.47		29.94	0.01			0.01	98.48
37.22	3.79	18.33	5.53	0.04		0.70	0.13		32.80	0.05			0.01	98.59
37.56	4.12	18.58	4.66			0.50	0.28		34.18	0.04		0.01	0.02	99.94
37.00	4.77	18.81	5.70	0.02		1.38	0.04		30.57					98.27
38.41	4.07	20.01	7.17			1.99	0.06		28.31	0.01		0.01		100.02
37.63	3.28	19.38	5.41	0.08		1.94	0.05		30.98	0.00		0.04		98.79
							Amphibole							
45.41	14.26	10.55	9.96	2.45	0.62	13.11	0.06		0.43	0.05		0.00	0.01	96.89
46.18	13.60	11.74	8.97	2.45	0.19	13.00	0.02		1.05	0.00		0.00	0.00	97.20
45.67	13.83	12.83	9.54	2.53	0.29	12.72	0.01		0.98	0.00		0.00	0.01	98.41
43.11	17.85	12.76	11.13	1.96	0.83	9.78	0.67		0.24	0.03		0.05	0.03	98.45
43.26	17.07	13.85	10.90	1.82	0.73	9.67	0.50		0.27	0.00		0.00	0.03	96.37
							Biotite							
39.48	12.65	17.19	0.00	0.15	9.65	19.21	0.11	0.00	0.26		0.00			98.69
39.40	11.98	17.26	0.00	0.12	9.52	19.13	0.79	0.00	0.16		0.00			98.36
39.52	12.74	17.35	0.00	0.23	8.80	18.63	0.09	0.00	0.17		0.02			97.54
40.38	7.48	16.34	0.00	0.12	9.49	21.57	1.18	0.01	0.63		0.00			97.20
40.15	10.22	17.11	0.08	0.31	8.20	19.71	0.95	0.02	0.22		0.00			96.97
39.69	11.53	17.35	0.00	0.17	9.26	18.85	0.00	0.00	0.43		0.01			97.29
38.64	11.73	16.01	0.03	0.18	9.52	16.95	0.00		0.30	0.01		0.07	0.00	93.42
38.67	11.89	16.47	0.00	0.15	9.53	17.05	0.65		0.15	0.04		0.01	0.06	94.66
38.46	11.76	16.37	0.00	0.12	9.19	16.65	0.68		0.16	0.00		0.04	0.00	93.42
37.32	18.71	16.12	0.00	0.11	9.05	12.28	1.68		0.20	0.00		0.05	0.00	95.53
38.55	15.91	16.09	0.03	0.20	8.91	13.70	1.49		0.15	0.00		0.00	0.02	95.04
39.60	13.64	16.44	0.00	0.09	8.68	16.03	0.76		0.44	0.03		0.00	0.03	95.74

39.36	10.24	15.93	0.04	0.10	9.18	17.49	1.25		0.67	0.04		0.00	0.01	94.30
38.74	12.86	16.47	0.06	0.11	9.24	16.64	0.05		0.22	0.00		0.00	0.02	94.42
37.33	17.72	16.43	0.03	0.18	8.94	13.39	1.33		0.20	0.01		0.04	0.03	95.63
37.40	16.00	16.67	0.11	0.28	8.87	12.81	1.48		0.13	0.06		0.04	0.03	93.87
39.47	13.49	15.92	0.00	0.06	8.76	16.01	0.02		0.62	0.00		0.00	0.04	94.40
38.20	15.93	16.29	0.00	0.09	8.38	13.99	1.54		0.28	0.00		0.02	0.04	94.76
38.10	16.67	17.32	0.04	0.19	8.12	14.29	1.14		0.21	0.00		0.01	0.02	96.09
39.30	11.62	16.97	0.02	0.16	9.50	16.95	0.10		0.28	0.00		0.03	0.01	94.93
39.25	11.51	17.17	0.02	0.22	9.47	17.04	0.02		0.29	0.02		0.02	0.00	95.03
38.31	18.32	17.31	0.00	0.24	9.23	12.52	1.56		0.18	0.02		0.02	0.05	97.76
37.84	18.10	17.51	0.01	0.23	9.34	12.11	1.54		0.18	0.00		0.05	0.05	96.94
38.80	15.72	16.15	0.09	0.22	9.05	14.39	1.94		0.04	0.00		0.05	0.05	96.49
39.43	12.74	16.35	0.00	0.10	9.42	16.51	0.05		0.58	0.00		0.01	0.01	95.20
							Muscovite							
46.57	5.42	25.04	0.01	0.45	8.54	2.63	0.13		0.03	0.00		0.49	0.00	89.30
48.17	6.30	26.33	0.03	0.36	6.67	2.75	0.71		0.10	0.01		0.03	0.06	91.52
47.51	7.47	25.64	0.03	0.33	8.44	2.96	1.01		0.21	0.00		0.05	0.01	93.65
45.93	5.98	28.56	0.18	0.60	8.03	1.78	0.41		0.00	0.04		0.01	0.10	91.62
45.21	5.99	26.69	0.02	1.13	7.65	2.22	0.11		0.02	0.08		0.79	0.02	89.93
47.00	5.99	28.92	0.00	0.54	6.57	1.94	0.39		0.02	0.00		0.00	0.05	91.42
47.19	5.61	27.23	0.00	0.33	10.41	2.97	0.68	0.00	0.05		0.01			94.48
46.72	5.56	29.96	0.00	0.90	8.02	1.90	0.06	0.00	0.04		0.03			93.18
47.37	5.65	28.81	0.00	0.57	7.98	2.38	0.65	0.02	0.05		0.00			93.48
47.23	5.04	29.75	0.00	0.74	8.30	2.14	0.35	0.02	0.04		0.00			93.61
49.00	5.19	26.45	0.00	0.35	8.37	3.51	0.60	0.03	0.07		0.01			93.58
46.99	6.44	27.73	0.01	0.42	8.82	2.54	0.15	0.02	0.07		0.01			93.20
47.15	5.03	27.22	0.00	0.49	9.89	2.25	0.72		0.04	0.01		0.03	0.03	92.86
48.27	4.05	27.76	0.71	0.69	9.28	2.18	0.14		0.00	0.00		0.01	0.00	93.09
47.03	7.51	25.34	0.00	0.27	8.61	2.88	1.09		0.12	0.00		0.02	0.04	92.91
							Quartz							
99.90	0.09	0.00	0.03	0.00	0.00	0.02	0.00	0.03	0.01		0.01			100.09

100.31	0.16	0.00	0.00	0.00	0.03	0.01	0.02	0.01	0.03		0.01		100.58
100.29	0.05	0.02	0.00	0.00	0.00	0.00	0.00	0.00	0.02		0.00		100.38
100.10	0.10	0.02	0.00	0.00	0.01	0.00	0.08	0.00	0.01		0.01		100.32
99.95	0.01	0.01	0.00	0.00	0.00	0.00	0.02	0.03	0.01		0.00		100.03
100.57	0.10	0.16	0.00	0.08	0.00	0.00	0.01	0.00	0.00		0.01		100.92
100.25	0.00	0.01	0.02	0.01	0.01	0.00	0.00	0.00	0.00		0.00		100.29
100.10	0.03	0.00	0.03	0.00	0.00	0.00	0.00	0.01	0.00		0.02		100.20
100.57	0.07	0.01	0.01	0.00	0.00	0.01	0.00	0.06	0.00		0.01		100.74
100.60	0.17	0.04	0.00	0.04	0.03	0.00	0.02	0.02	0.01		0.00		100.93
99.70	0.10	0.00	0.00	0.00	0.00	0.00	0.00	0.01	0.00		0.01		99.82
99.88	0.02	0.00	0.00	0.00	0.00	0.00	0.00	0.08	0.00		0.00		99.97
100.37	0.04	0.00	0.01	0.01	0.02	0.01	0.00	0.00	0.03		0.01		100.49
100.75	0.04	0.00	0.00	0.00	0.01	0.00	0.00	0.02	0.03		0.00		100.85
100.07	0.23	0.00	0.04	0.00	0.00	0.00	0.01		0.06	0.07		0.00	0.00	100.48
99.50	0.21	0.02	0.02	0.01	0.01	0.00	0.00		0.36	0.00		0.02	0.00	100.15
100.02	0.41	0.00	0.00	0.00	0.01	0.02	0.00		0.00	0.00		0.04	0.00	100.50
99.92	0.34	0.00	0.01	0.00	0.01	0.02	0.00		0.00	0.00		0.03	0.00	100.33
99.27	0.57	0.00	0.02	0.00	0.02	0.00	0.04		0.00	0.05		0.04	0.00	100.01
99.96	0.45	0.00	0.02	0.00	0.00	0.00	0.04		0.00	0.09		0.00	0.00	100.56
99.29	0.35	0.10	0.05	0.00	0.00	0.00	0.00		0.00	0.02		0.00	0.01	99.80
98.80	0.85	0.00	0.01	0.00	0.00	0.00	0.01		0.03	0.00		0.00	0.01	99.71
100.05	0.38	0.02	0.04	0.00	0.02	0.00	0.00		0.00	0.00		0.00	0.01	100.52
96.71	0.76	0.53	0.66	0.02	0.01	0.05	0.05		0.00	0.00		0.06	0.00	98.85
98.80	0.55	0.00	0.01	0.18	0.00	0.00	0.01		0.00	0.00		0.23	0.00	99.78
100.13	0.49	0.03	0.09	0.00	0.00	0.04	0.03		0.21	0.04		0.02	0.02	101.08
99.25	1.15	0.00	0.02	0.00	0.01	0.00	0.01		0.01	0.01		0.01	0.01	100.47
100.16	0.74	0.00	0.00	0.00	0.01	0.00	0.03		0.01	0.00		0.00	0.02	100.97
98.93	0.36	0.35	0.11	0.00	0.00	0.03	0.03		1.24	0.00		0.00	0.00	101.04
99.71	2.30	0.02	0.02	0.00	0.02	0.00	0.00		0.00	0.04		0.00	0.00	102.12
99.96	0.35	0.07	0.01	0.00	0.00	0.00	0.04		0.00	0.00		0.00	0.00	100.43
99.62	0.47	0.01	0.02	0.00	0.00	0.00	0.00		0.00	0.00		0.04	0.00	100.15

99.69	0.01	0.00	0.01	0.01	0.02	0.00	0.00		0.06	0.00		0.00	0.00	99.80
98.09	0.89	0.18	0.26	0.02	0.00	0.00	0.00		0.00	0.00		0.19	0.01	99.64
100.76	0.01	0.00	0.01	0.00	0.01	0.00	0.00		0.00	0.00		0.00	0.00	100.79
97.63	0.17	0.19		0.06	0.09	0.04	0.00		0.01				0.00	98.19
							Albite							
68.87	0.60	18.59	0.02	12.25	0.07	0.02	0.92	0.00	0.00		0.00			101.34
69.37	0.17	18.90	0.06	11.95	0.11	0.00	0.08	0.01	0.04		0.01			100.68
68.70	0.52	20.14	0.37	11.69	0.11	0.00	0.00	0.00	0.03		0.00			101.57
69.85	0.14	20.37	0.04	11.91	0.16	0.00	0.01	0.00	0.01		0.01			102.50
69.31	0.23	18.88	0.04	11.59	0.08	0.00	0.00		0.04	0.01		0.02	0.00	100.22
67.97	0.22	19.22	0.47	11.19	0.06	0.00	0.02		0.06	0.01		0.00	0.00	99.22
69.59	0.50	18.95	0.04	11.73	0.11	0.02	0.00		0.34	0.01		0.01	0.02	101.32
							Oligoclase							
66.35	0.06	21.99	2.39	10.66	0.07	0.00	0.00	0.00	0.00		0.00			101.53
64.17	0.19	22.88	3.89	9.67	0.09	0.02	0.00	0.00	0.02		0.00			100.93
66.23	0.09	21.63	2.43	10.43	0.11	0.00	0.00	0.03	0.01		0.00			100.95
64.44	0.11	22.30	3.87	9.72	0.02	0.00	0.04	0.00	0.00		0.00			100.50
65.07	0.18	22.27	3.22	10.14	0.07	0.05	0.00	0.00	0.00		0.00			101.01
65.50	0.31	20.88	2.06	9.27	0.86	0.16	0.00		0.01	0.05		0.00	0.01	99.11
62.16	0.78	23.09	5.07	8.69	0.02	0.00	0.00		0.04	0.02		0.01	0.00	99.88
64.26	0.72	21.59	3.43	9.47	0.06	0.00	0.00		0.00	0.00		0.01	0.01	99.54
							Calcite							
0.00	0.14	0.00	51.36	0.00	0.00	0.00	0.00		0.10	0.00		0.01	0.02	51.61
0.00	0.23	0.11	52.87	0.00	0.00	0.01	0.05		0.17	0.04		0.03	0.00	53.47
0.00	0.06	0.00	53.05	0.00	0.01	0.00	0.01		0.16	0.00		0.01	0.02	53.30
0.00	0.03	0.00	52.25	0.00	0.00	0.02	0.00		0.09	0.00		0.01	0.00	52.39
0.00	3.28	0.02	52.79	0.00	0.03	0.03	0.12		0.08	0.02		0.01	0.02	56.06
							Dolomite-1							
0.00	0.29	0.01	27.94	0.04	0.01	4.40	0.00		22.46	0.01		0.00	0.00	55.14
0.00	0.39	0.03	32.50	0.00	0.00	3.07	0.00		20.59	0.00		0.00	0.00	56.55
0.19	1.11	0.19	31.77	0.05	0.00	2.95	0.01		19.71	0.00		0.00	0.00	55.87

							Dolomite-2							
0.00	1.04	0.00	38.47	0.03	0.01	5.92	0.01	0.00	13.28		0.00			58.76
0.00	0.55	0.03	35.15	0.01	0.01	5.33	0.03	0.02	14.70		0.01			55.84
							Dolomite-3							
0.00	3.24	0.00	28.97	0.01	0.00	12.36	0.00		11.22	0.01		0.00	0.00	55.47
0.00	1.74	0.00	28.25	0.00	0.00	10.35	0.00		18.03	0.03		0.00	0.00	58.24
							Dolomite-4							
0.00	1.10	0.00	32.65	0.01	0.00	22.65	0.05	0.00	1.15		0.01			57.63
							Ankerite-1							
0.00	9.36	0.00	31.13	0.00	0.00	15.05	0.00	0.00	3.08		0.00			58.62
0.00	7.35	0.00	29.58	0.00	0.00	16.87	0.00	0.00	3.97		0.00			57.77
0.00	6.20	0.00	32.31	0.02	0.00	16.64	0.01	0.00	4.19		0.00			59.37
0.00	9.03	0.01	30.10	0.01	0.00	14.89	0.00	0.00	3.76		0.00			57.80
0.00	9.43	0.00	28.38	0.02	0.01	15.09	0.01		1.70	0.10		0.00	0.00	53.79
0.00	5.98	0.03	31.17	0.00	0.00	18.26	0.00		1.67	0.00		0.00	0.00	56.51
0.00	11.19	0.02	31.59	0.04	0.01	15.07	0.00		1.92	0.00		0.06	0.02	58.79
0.05	10.74	0.02	31.55	0.00	0.00	17.73	0.00		2.05	0.01		0.00	0.01	61.08
0.00	15.21	0.01	29.69	0.01	0.00	13.89	0.00		0.75	0.00		0.02	0.01	58.06
0.00	11.48	0.03	29.88		0.00	15.32	0.01		1.61	0.04		0.02	0.00	57.24
0.00	5.91	0.02	30.05	0.00	0.00	16.19	0.00		2.21	0.00		0.00	0.00	53.79
							Ankerite-2							
0.00	2.34	0.02	61.84	0.01	0.04	1.99	0.00	0.04	0.54		0.00			66.80
0.00	2.94	0.01	50.23	0.02	0.00	4.46	0.00	0.00	6.60		0.01			64.26
0.00	2.13	0.01	51.17	0.00	0.02	1.71	0.00		0.70	0.07		0.00	0.04	55.85
0.00	2.91	0.00	55.33	0.06	0.00	3.03	0.08		1.71	0.00		0.03	0.03	63.19
0.00	2.01	0.00	54.04	0.01	0.02	3.09	0.00		3.37	0.00		0.03	0.00	62.57
0.00	1.85	0.02	53.85	0.02	0.00	2.93	0.03		3.97	0.01		0.02	0.00	62.50
0.00	3.61	0.02	55.38	0.06	0.00	3.27	0.00		2.12	0.05		0.05	0.00	64.19
0.00	2.19	0.01	59.72	0.01	0.00	2.55	0.02	0.04	1.35		0.01			65.90
							Ankerite-3							
0.00	4.18	0.01	32.15	0.00	0.01	14.78	0.04	0.04	8.16		0.01			59.37

0.00	4.84	0.03	32.40	0.00	0.00	14.47	0.00	0.00	7.28		0.01			59.03
0.00	7.96	0.00	29.48	0.03	0.00	13.71	0.00		7.53	0.01		0.02	0.03	57.97
0.00	6.57	0.00	30.11	0.04	0.00	14.84	0.00		6.32	0.05		0.00	0.01	57.27
0.00	6.28	0.00	29.15	0.00	0.00	14.60	0.00		4.67	0.00		0.01	0.00	54.08
							Sulphide							
0.18	1.08	0.01	0.05	0.00	0.00	0.00	0.00		0.01	101.46		52.78	0.00	156.52
0.00	71.40	0.00	0.00	0.05	0.00	0.01	0.00		0.00	0.02		137.82	0.04	273.58
0.00	69.66	0.01	0.00	0.00	0.01	0.00	0.00		0.00	0.12		137.30	0.00	269.76
0.00	92.25	0.00	0.00	0.01	0.00	0.00	0.00		0.00	0.02		98.33	0.03	273.65
							Unknown minerals/edge analyses							
26.56	20.69	21.33	0.00	0.01	0.00	19.30	0.06		0.28	0.10		0.05	0.01	88.39
26.60	20.96	21.54	0.00	0.00	0.03	19.08	0.06		0.27	0.00		0.02	0.00	88.56
35.92	11.48	27.57	0.03	2.84	0.01	6.68	0.22		0.06	0.11		0.00	0.01	84.94
36.79	2.44	18.75	3.77	0.02	0.00	2.20	9.08		30.10	0.00		0.01	0.02	103.16
37.35	15.57	19.65	4.55	0.40	0.01	2.06	0.08		19.54	0.00		0.53	0.00	99.75
38.13	20.38	19.91	6.11	0.00	0.01	1.93	0.00	0.00	15.80		0.00			102.27
40.67	5.65	14.73	0.00	0.06	10.01	21.59	1.58	0.02	1.35		0.01			95.67
41.72	4.44	12.31	0.01	0.06	9.81	20.59	1.62		2.33	0.01		0.01	0.07	92.97
47.15	5.03	27.22	0.00	0.49	9.89	2.25	0.72		0.04	0.01		0.03	0.03	92.86
48.27	4.05	27.76	0.71	0.69	9.28	2.18	0.14		0.00	0.00		0.01	0.00	93.09
54.66	17.30	2.34	9.19	7.96	0.00	6.71	0.11		2.41	0.03		0.02	0.00	100.73
55.37	9.07	1.29	2.73	4.17	0.14	16.90	0.02		6.20	0.00		0.00	0.02	95.91

Appendix D: Measurements of surface hardness by Schmidt hammer

Surface hardness values by Schmidt hammer collected from boulders in the Kvannevann, Stensundtjern, and Stortjønna deposits. PF = perpendicular to the foliation, LF = parallel to the foliation, NF = no foliation.

Deposit	Ore type	Sample	Foliation	Surface hardness by Schmidt hammer
Kvannevann	Specular-Hematite	MT-14-51	PF	37
Kvannevann	Specular-Hematite	MT-14-51	PF	36
Kvannevann	Specular-Hematite	MT-14-51	PF	36
Kvannevann	Specular-Hematite	MT-14-51	PF	35
Kvannevann	Specular-Hematite	MT-14-51	PF	35
Kvannevann	Specular-Hematite	MT-14-51	PF	34
Kvannevann	Specular-Hematite	MT-14-51	PF	34
Kvannevann	Specular-Hematite	MT-14-51	PF	29
Kvannevann	Specular-Hematite	MT-14-51	PF	29
Kvannevann	Specular-Hematite	MT-14-51	PF	28
Kvannevann	Specular-Hematite	MT-14-51	LF	49
Kvannevann	Specular-Hematite	MT-14-51	LF	47
Kvannevann	Specular-Hematite	MT-14-51	LF	44
Kvannevann	Specular-Hematite	MT-14-51	LF	42
Kvannevann	Specular-Hematite	MT-14-51	LF	41
Kvannevann	Specular-Hematite	MT-14-51	LF	41
Kvannevann	Specular-Hematite	MT-14-51	LF	40
Kvannevann	Specular-Hematite	MT-14-51	LF	40
Kvannevann	Specular-Hematite	MT-14-51	LF	39
Kvannevann	Specular-Hematite	MT-14-51	LF	38
Kvannevann	Specular-Hematite	MT-14-53	PF	40
Kvannevann	Specular-Hematite	MT-14-53	PF	36
Kvannevann	Specular-Hematite	MT-14-53	PF	34
Kvannevann	Specular-Hematite	MT-14-53	PF	33
Kvannevann	Specular-Hematite	MT-14-53	PF	31
Kvannevann	Specular-Hematite	MT-14-53	PF	31
Kvannevann	Specular-Hematite	MT-14-53	PF	30
Kvannevann	Specular-Hematite	MT-14-53	PF	29
Kvannevann	Specular-Hematite	MT-14-53	PF	29
Kvannevann	Specular-Hematite	MT-14-53	PF	28
Kvannevann	Specular-Hematite	MT-14-53	LF	36
Kvannevann	Specular-Hematite	MT-14-53	LF	35
Kvannevann	Specular-Hematite	MT-14-53	LF	32
Kvannevann	Specular-Hematite	MT-14-53	LF	30
Kvannevann	Specular-Hematite	MT-14-53	LF	30
Kvannevann	Specular-Hematite	MT-14-53	LF	30
Kvannevann	Specular-Hematite	MT-14-53	LF	30
Kvannevann	Specular-Hematite	MT-14-53	LF	29
Kvannevann	Specular-Hematite	MT-14-53	LF	28
Kvannevann	Specular-Hematite	MT-14-53	LF	27

Kvannevann	Specular-Hematite	MT-14-55	PF	47
Kvannevann	Specular-Hematite	MT-14-55	PF	47
Kvannevann	Specular-Hematite	MT-14-55	PF	44
Kvannevann	Specular-Hematite	MT-14-55	PF	44
Kvannevann	Specular-Hematite	MT-14-55	PF	42
Kvannevann	Specular-Hematite	MT-14-55	PF	41
Kvannevann	Specular-Hematite	MT-14-55	PF	40
Kvannevann	Specular-Hematite	MT-14-55	PF	39
Kvannevann	Specular-Hematite	MT-14-55	PF	38
Kvannevann	Specular-Hematite	MT-14-55	PF	38
Kvannevann	Specular-Hematite	MT-14-55	LF	48
Kvannevann	Specular-Hematite	MT-14-55	LF	44
Kvannevann	Specular-Hematite	MT-14-55	LF	42
Kvannevann	Specular-Hematite	MT-14-55	LF	40
Kvannevann	Specular-Hematite	MT-14-55	LF	39
Kvannevann	Specular-Hematite	MT-14-55	LF	37
Kvannevann	Specular-Hematite	MT-14-55	LF	36
Kvannevann	Specular-Hematite	MT-14-55	LF	36
Kvannevann	Specular-Hematite	MT-14-55	LF	35
Kvannevann	Specular-Hematite	MT-14-55	LF	32
Kvannevann	Specular-Hematite	MT-14-12	PF	47
Kvannevann	Specular-Hematite	MT-14-12	PF	42
Kvannevann	Specular-Hematite	MT-14-12	PF	42
Kvannevann	Specular-Hematite	MT-14-12	PF	42
Kvannevann	Specular-Hematite	MT-14-12	PF	41
Kvannevann	Specular-Hematite	MT-14-12	PF	38
Kvannevann	Specular-Hematite	MT-14-12	PF	37
Kvannevann	Specular-Hematite	MT-14-12	PF	36
Kvannevann	Specular-Hematite	MT-14-12	PF	36
Kvannevann	Specular-Hematite	MT-14-12	PF	36
Kvannevann	Specular-Hematite	MT-14-12	LF	43
Kvannevann	Specular-Hematite	MT-14-12	LF	41
Kvannevann	Specular-Hematite	MT-14-12	LF	41
Kvannevann	Specular-Hematite	MT-14-12	LF	41
Kvannevann	Specular-Hematite	MT-14-12	LF	41
Kvannevann	Specular-Hematite	MT-14-12	LF	40
Kvannevann	Specular-Hematite	MT-14-12	LF	40
Kvannevann	Specular-Hematite	MT-14-12	LF	40
Kvannevann	Specular-Hematite	MT-14-12	LF	38
Kvannevann	Specular-Hematite	MT-14-12	LF	38
Kvannevann	Specular-Hematite	MT-14-14	PF	28
Kvannevann	Specular-Hematite	MT-14-14	PF	28
Kvannevann	Specular-Hematite	MT-14-14	PF	28
Kvannevann	Specular-Hematite	MT-14-14	PF	28
Kvannevann	Specular-Hematite	MT-14-14	PF	27
Kvannevann	Specular-Hematite	MT-14-14	PF	26
Kvannevann	Specular-Hematite	MT-14-14	PF	26
Kvannevann	Specular-Hematite	MT-14-14	PF	24

Kvannevann	Specular-Hematite	MT-14-14	PF	22
Kvannevann	Specular-Hematite	MT-14-14	PF	22
Kvannevann	Specular-Hematite	MT-14-14	LF	40
Kvannevann	Specular-Hematite	MT-14-14	LF	36
Kvannevann	Specular-Hematite	MT-14-14	LF	36
Kvannevann	Specular-Hematite	MT-14-14	LF	35
Kvannevann	Specular-Hematite	MT-14-14	LF	34
Kvannevann	Specular-Hematite	MT-14-14	LF	32
Kvannevann	Specular-Hematite	MT-14-14	LF	31
Kvannevann	Specular-Hematite	MT-14-14	LF	27
Kvannevann	Specular-Hematite	MT-14-14	LF	26
Kvannevann	Specular-Hematite	MT-14-14	LF	22
Kvannevann	Specular-Hematite	MT-14-15	PF	42
Kvannevann	Specular-Hematite	MT-14-15	PF	37
Kvannevann	Specular-Hematite	MT-14-15	PF	31
Kvannevann	Specular-Hematite	MT-14-15	PF	27
Kvannevann	Specular-Hematite	MT-14-15	PF	26
Kvannevann	Specular-Hematite	MT-14-15	PF	25
Kvannevann	Specular-Hematite	MT-14-15	PF	24
Kvannevann	Specular-Hematite	MT-14-15	PF	24
Kvannevann	Specular-Hematite	MT-14-15	PF	23
Kvannevann	Specular-Hematite	MT-14-15	PF	21
Kvannevann	Specular-Hematite	MT-14-15	LF	48
Kvannevann	Specular-Hematite	MT-14-15	LF	41
Kvannevann	Specular-Hematite	MT-14-15	LF	40
Kvannevann	Specular-Hematite	MT-14-15	LF	39
Kvannevann	Specular-Hematite	MT-14-15	LF	38
Kvannevann	Specular-Hematite	MT-14-15	LF	36
Kvannevann	Specular-Hematite	MT-14-15	LF	36
Kvannevann	Specular-Hematite	MT-14-15	LF	34
Kvannevann	Specular-Hematite	MT-14-15	LF	33
Kvannevann	Specular-Hematite	MT-14-15	LF	32
Kvannevann	Specular-Hematite	MT-14-19	PF	34
Kvannevann	Specular-Hematite	MT-14-19	PF	33
Kvannevann	Specular-Hematite	MT-14-19	PF	32
Kvannevann	Specular-Hematite	MT-14-19	PF	30
Kvannevann	Specular-Hematite	MT-14-19	PF	30
Kvannevann	Specular-Hematite	MT-14-19	PF	29
Kvannevann	Specular-Hematite	MT-14-19	PF	29
Kvannevann	Specular-Hematite	MT-14-19	PF	27
Kvannevann	Specular-Hematite	MT-14-19	PF	26
Kvannevann	Specular-Hematite	MT-14-19	PF	26
Kvannevann	Specular-Hematite	MT-14-19	LF	33
Kvannevann	Specular-Hematite	MT-14-19	LF	30
Kvannevann	Specular-Hematite	MT-14-19	LF	27
Kvannevann	Specular-Hematite	MT-14-19	LF	25
Kvannevann	Specular-Hematite	MT-14-19	LF	23
Kvannevann	Specular-Hematite	MT-14-19	LF	22

Kvannevann	Specular-Hematite	MT-14-19	LF	21
Kvannevann	Specular-Hematite	MT-14-19	LF	21
Kvannevann	Specular-Hematite	MT-14-19	LF	19
Kvannevann	Specular-Hematite	MT-14-19	LF	17
Kvannevann	Specular-Hematite	MT-14-20	PF	40
Kvannevann	Specular-Hematite	MT-14-20	PF	40
Kvannevann	Specular-Hematite	MT-14-20	PF	39
Kvannevann	Specular-Hematite	MT-14-20	PF	38
Kvannevann	Specular-Hematite	MT-14-20	PF	38
Kvannevann	Specular-Hematite	MT-14-20	PF	37
Kvannevann	Specular-Hematite	MT-14-20	PF	37
Kvannevann	Specular-Hematite	MT-14-20	PF	36
Kvannevann	Specular-Hematite	MT-14-20	PF	36
Kvannevann	Specular-Hematite	MT-14-20	PF	35
Kvannevann	Specular-Hematite	MT-14-20	LF	44
Kvannevann	Specular-Hematite	MT-14-20	LF	44
Kvannevann	Specular-Hematite	MT-14-20	LF	44
Kvannevann	Specular-Hematite	MT-14-20	LF	42
Kvannevann	Specular-Hematite	MT-14-20	LF	41
Kvannevann	Specular-Hematite	MT-14-20	LF	40
Kvannevann	Specular-Hematite	MT-14-20	LF	40
Kvannevann	Specular-Hematite	MT-14-20	LF	39
Kvannevann	Specular-Hematite	MT-14-20	LF	39
Kvannevann	Specular-Hematite	MT-14-20	LF	39
Kvannevann	Specular-Hematite	MT-14-21	PF	34
Kvannevann	Specular-Hematite	MT-14-21	PF	32
Kvannevann	Specular-Hematite	MT-14-21	PF	29
Kvannevann	Specular-Hematite	MT-14-21	PF	28
Kvannevann	Specular-Hematite	MT-14-21	PF	28
Kvannevann	Specular-Hematite	MT-14-21	PF	27
Kvannevann	Specular-Hematite	MT-14-21	PF	27
Kvannevann	Specular-Hematite	MT-14-21	PF	26
Kvannevann	Specular-Hematite	MT-14-21	PF	26
Kvannevann	Specular-Hematite	MT-14-21	PF	26
Kvannevann	Specular-Hematite	MT-14-21	LF	28
Kvannevann	Specular-Hematite	MT-14-21	LF	24
Kvannevann	Specular-Hematite	MT-14-21	LF	24
Kvannevann	Specular-Hematite	MT-14-21	LF	23
Kvannevann	Specular-Hematite	MT-14-21	LF	22
Kvannevann	Specular-Hematite	MT-14-21	LF	20
Kvannevann	Specular-Hematite	MT-14-21	LF	20
Kvannevann	Specular-Hematite	MT-14-21	LF	20
Kvannevann	Specular-Hematite	MT-14-21	LF	20
Kvannevann	Specular-Hematite	MT-14-21	LF	20
Kvannevann	Specular-Hematite	MT-14-24	PF	28
Kvannevann	Specular-Hematite	MT-14-24	PF	28
Kvannevann	Specular-Hematite	MT-14-24	PF	26
Kvannevann	Specular-Hematite	MT-14-24	PF	25

Kvannevann	Specular-Hematite	MT-14-24	PF	24
Kvannevann	Specular-Hematite	MT-14-24	PF	23
Kvannevann	Specular-Hematite	MT-14-24	PF	23
Kvannevann	Specular-Hematite	MT-14-24	PF	21
Kvannevann	Specular-Hematite	MT-14-24	PF	20
Kvannevann	Specular-Hematite	MT-14-24	PF	20
Kvannevann	Specular-Hematite	MT-14-24	LF	39
Kvannevann	Specular-Hematite	MT-14-24	LF	32
Kvannevann	Specular-Hematite	MT-14-24	LF	28
Kvannevann	Specular-Hematite	MT-14-24	LF	27
Kvannevann	Specular-Hematite	MT-14-24	LF	26
Kvannevann	Specular-Hematite	MT-14-24	LF	25
Kvannevann	Specular-Hematite	MT-14-24	LF	22
Kvannevann	Specular-Hematite	MT-14-24	LF	21
Kvannevann	Specular-Hematite	MT-14-24	LF	21
Kvannevann	Specular-Hematite	MT-14-24	LF	20
Kvannevann	Specular-Hematite	MT-14-28	PF	36
Kvannevann	Specular-Hematite	MT-14-28	PF	34
Kvannevann	Specular-Hematite	MT-14-28	PF	33
Kvannevann	Specular-Hematite	MT-14-28	PF	32
Kvannevann	Specular-Hematite	MT-14-28	PF	32
Kvannevann	Specular-Hematite	MT-14-28	PF	31
Kvannevann	Specular-Hematite	MT-14-28	PF	30
Kvannevann	Specular-Hematite	MT-14-28	PF	28
Kvannevann	Specular-Hematite	MT-14-28	PF	28
Kvannevann	Specular-Hematite	MT-14-28	PF	27
Kvannevann	Specular-Hematite	MT-14-28	LF	30
Kvannevann	Specular-Hematite	MT-14-28	LF	30
Kvannevann	Specular-Hematite	MT-14-28	LF	29
Kvannevann	Specular-Hematite	MT-14-28	LF	27
Kvannevann	Specular-Hematite	MT-14-28	LF	26
Kvannevann	Specular-Hematite	MT-14-28	LF	26
Kvannevann	Specular-Hematite	MT-14-28	LF	26
Kvannevann	Specular-Hematite	MT-14-28	LF	26
Kvannevann	Specular-Hematite	MT-14-28	LF	24
Kvannevann	Specular-Hematite	MT-14-28	LF	24
Kvannevann	Specular-Hematite	MT-14-29	PF	38
Kvannevann	Specular-Hematite	MT-14-29	PF	28
Kvannevann	Specular-Hematite	MT-14-29	PF	26
Kvannevann	Specular-Hematite	MT-14-29	PF	24
Kvannevann	Specular-Hematite	MT-14-29	PF	24
Kvannevann	Specular-Hematite	MT-14-29	PF	22
Kvannevann	Specular-Hematite	MT-14-29	PF	22
Kvannevann	Specular-Hematite	MT-14-29	PF	22
Kvannevann	Specular-Hematite	MT-14-29	PF	21
Kvannevann	Specular-Hematite	MT-14-29	PF	20
Kvannevann	Specular-Hematite	MT-14-29	LF	24
Kvannevann	Specular-Hematite	MT-14-29	LF	22

Kvannevann	Specular-Hematite	MT-14-29	LF	22
Kvannevann	Specular-Hematite	MT-14-29	LF	21
Kvannevann	Specular-Hematite	MT-14-29	LF	21
Kvannevann	Specular-Hematite	MT-14-29	LF	20
Kvannevann	Specular-Hematite	MT-14-29	LF	20
Kvannevann	Specular-Hematite	MT-14-29	LF	20
Kvannevann	Specular-Hematite	MT-14-29	LF	19
Kvannevann	Specular-Hematite	MT-14-29	LF	18
Kvannevann	Specular-Hematite	MT-15-102	PF	52
Kvannevann	Specular-Hematite	MT-15-102	PF	50
Kvannevann	Specular-Hematite	MT-15-102	PF	48
Kvannevann	Specular-Hematite	MT-15-102	PF	48
Kvannevann	Specular-Hematite	MT-15-102	PF	47
Kvannevann	Specular-Hematite	MT-15-102	PF	47
Kvannevann	Specular-Hematite	MT-15-102	PF	44
Kvannevann	Specular-Hematite	MT-15-102	PF	44
Kvannevann	Specular-Hematite	MT-15-102	PF	44
Kvannevann	Specular-Hematite	MT-15-102	PF	44
Kvannevann	Specular-Hematite	MT-15-102	LF	48
Kvannevann	Specular-Hematite	MT-15-102	LF	48
Kvannevann	Specular-Hematite	MT-15-102	LF	42
Kvannevann	Specular-Hematite	MT-15-102	LF	40
Kvannevann	Specular-Hematite	MT-15-102	LF	40
Kvannevann	Specular-Hematite	MT-15-102	LF	39
Kvannevann	Specular-Hematite	MT-15-102	LF	39
Kvannevann	Specular-Hematite	MT-15-102	LF	38
Kvannevann	Specular-Hematite	MT-15-102	LF	38
Kvannevann	Specular-Hematite	MT-15-102	LF	38
Kvannevann	Granular-Hematite	MT-14-52	PF	43
Kvannevann	Granular-Hematite	MT-14-52	PF	40
Kvannevann	Granular-Hematite	MT-14-52	PF	39
Kvannevann	Granular-Hematite	MT-14-52	PF	38
Kvannevann	Granular-Hematite	MT-14-52	PF	37
Kvannevann	Granular-Hematite	MT-14-52	PF	34
Kvannevann	Granular-Hematite	MT-14-52	PF	32
Kvannevann	Granular-Hematite	MT-14-52	PF	32
Kvannevann	Granular-Hematite	MT-14-52	PF	32
Kvannevann	Granular-Hematite	MT-14-52	PF	29
Kvannevann	Granular-Hematite	MT-14-52	LF	48
Kvannevann	Granular-Hematite	MT-14-52	LF	43
Kvannevann	Granular-Hematite	MT-14-52	LF	42
Kvannevann	Granular-Hematite	MT-14-52	LF	42
Kvannevann	Granular-Hematite	MT-14-52	LF	42
Kvannevann	Granular-Hematite	MT-14-52	LF	42
Kvannevann	Granular-Hematite	MT-14-52	LF	41
Kvannevann	Granular-Hematite	MT-14-52	LF	39
Kvannevann	Granular-Hematite	MT-14-52	LF	39
Kvannevann	Granular-Hematite	MT-14-52	LF	36

Kvannevann	Granular-Hematite	MT-14-54	PF	50
Kvannevann	Granular-Hematite	MT-14-54	PF	47
Kvannevann	Granular-Hematite	MT-14-54	PF	46
Kvannevann	Granular-Hematite	MT-14-54	PF	46
Kvannevann	Granular-Hematite	MT-14-54	PF	46
Kvannevann	Granular-Hematite	MT-14-54	PF	45
Kvannevann	Granular-Hematite	MT-14-54	PF	44
Kvannevann	Granular-Hematite	MT-14-54	PF	44
Kvannevann	Granular-Hematite	MT-14-54	PF	43
Kvannevann	Granular-Hematite	MT-14-54	PF	42
Kvannevann	Granular-Hematite	MT-14-54	LF	52
Kvannevann	Granular-Hematite	MT-14-54	LF	47
Kvannevann	Granular-Hematite	MT-14-54	LF	46
Kvannevann	Granular-Hematite	MT-14-54	LF	45
Kvannevann	Granular-Hematite	MT-14-54	LF	45
Kvannevann	Granular-Hematite	MT-14-54	LF	44
Kvannevann	Granular-Hematite	MT-14-54	LF	43
Kvannevann	Granular-Hematite	MT-14-54	LF	42
Kvannevann	Granular-Hematite	MT-14-54	LF	41
Kvannevann	Granular-Hematite	MT-14-54	LF	41
Kvannevann	Granular-Hematite	MT-14-06	PF	26
Kvannevann	Granular-Hematite	MT-14-06	PF	26
Kvannevann	Granular-Hematite	MT-14-06	PF	26
Kvannevann	Granular-Hematite	MT-14-06	PF	26
Kvannevann	Granular-Hematite	MT-14-06	PF	25
Kvannevann	Granular-Hematite	MT-14-06	PF	25
Kvannevann	Granular-Hematite	MT-14-06	PF	24
Kvannevann	Granular-Hematite	MT-14-06	PF	24
Kvannevann	Granular-Hematite	MT-14-06	PF	23
Kvannevann	Granular-Hematite	MT-14-06	PF	22
Kvannevann	Granular-Hematite	MT-14-06	LF	45
Kvannevann	Granular-Hematite	MT-14-06	LF	36
Kvannevann	Granular-Hematite	MT-14-06	LF	34
Kvannevann	Granular-Hematite	MT-14-06	LF	33
Kvannevann	Granular-Hematite	MT-14-06	LF	32
Kvannevann	Granular-Hematite	MT-14-06	LF	32
Kvannevann	Granular-Hematite	MT-14-06	LF	32
Kvannevann	Granular-Hematite	MT-14-06	LF	31
Kvannevann	Granular-Hematite	MT-14-06	LF	30
Kvannevann	Granular-Hematite	MT-14-06	LF	29
Kvannevann	Granular-Hematite	MT-14-13	PF	47
Kvannevann	Granular-Hematite	MT-14-13	PF	44
Kvannevann	Granular-Hematite	MT-14-13	PF	43
Kvannevann	Granular-Hematite	MT-14-13	PF	43
Kvannevann	Granular-Hematite	MT-14-13	PF	40
Kvannevann	Granular-Hematite	MT-14-13	PF	40
Kvannevann	Granular-Hematite	MT-14-13	PF	39
Kvannevann	Granular-Hematite	MT-14-13	PF	38

Kvannevann	Granular-Hematite	MT-14-13	PF	38
Kvannevann	Granular-Hematite	MT-14-13	PF	38
Kvannevann	Granular-Hematite	MT-14-13	LF	50
Kvannevann	Granular-Hematite	MT-14-13	LF	47
Kvannevann	Granular-Hematite	MT-14-13	LF	47
Kvannevann	Granular-Hematite	MT-14-13	LF	46
Kvannevann	Granular-Hematite	MT-14-13	LF	46
Kvannevann	Granular-Hematite	MT-14-13	LF	46
Kvannevann	Granular-Hematite	MT-14-13	LF	46
Kvannevann	Granular-Hematite	MT-14-13	LF	44
Kvannevann	Granular-Hematite	MT-14-13	LF	42
Kvannevann	Granular-Hematite	MT-14-13	LF	42
Kvannevann	Granular-Hematite	MT-14-26	PF	33
Kvannevann	Granular-Hematite	MT-14-26	PF	29
Kvannevann	Granular-Hematite	MT-14-26	PF	29
Kvannevann	Granular-Hematite	MT-14-26	PF	28
Kvannevann	Granular-Hematite	MT-14-26	PF	28
Kvannevann	Granular-Hematite	MT-14-26	PF	26
Kvannevann	Granular-Hematite	MT-14-26	PF	24
Kvannevann	Granular-Hematite	MT-14-26	PF	23
Kvannevann	Granular-Hematite	MT-14-26	PF	22
Kvannevann	Granular-Hematite	MT-14-26	PF	22
Kvannevann	Granular-Hematite	MT-14-26	LF	46
Kvannevann	Granular-Hematite	MT-14-26	LF	40
Kvannevann	Granular-Hematite	MT-14-26	LF	38
Kvannevann	Granular-Hematite	MT-14-26	LF	37
Kvannevann	Granular-Hematite	MT-14-26	LF	36
Kvannevann	Granular-Hematite	MT-14-26	LF	32
Kvannevann	Granular-Hematite	MT-14-26	LF	30
Kvannevann	Granular-Hematite	MT-14-26	LF	30
Kvannevann	Granular-Hematite	MT-14-26	LF	28
Kvannevann	Granular-Hematite	MT-14-26	LF	28
Kvannevann	Granular-Hematite	MT-14-27	PF	38
Kvannevann	Granular-Hematite	MT-14-27	PF	34
Kvannevann	Granular-Hematite	MT-14-27	PF	32
Kvannevann	Granular-Hematite	MT-14-27	PF	30
Kvannevann	Granular-Hematite	MT-14-27	PF	30
Kvannevann	Granular-Hematite	MT-14-27	PF	28
Kvannevann	Granular-Hematite	MT-14-27	PF	28
Kvannevann	Granular-Hematite	MT-14-27	PF	27
Kvannevann	Granular-Hematite	MT-14-27	PF	26
Kvannevann	Granular-Hematite	MT-14-27	PF	26
Kvannevann	Granular-Hematite	MT-14-27	LF	36
Kvannevann	Granular-Hematite	MT-14-27	LF	34
Kvannevann	Granular-Hematite	MT-14-27	LF	32
Kvannevann	Granular-Hematite	MT-14-27	LF	30
Kvannevann	Granular-Hematite	MT-14-27	LF	30
Kvannevann	Granular-Hematite	MT-14-27	LF	29

Kvannevann	Granular-Hematite	MT-14-27	LF	29
Kvannevann	Granular-Hematite	MT-14-27	LF	28
Kvannevann	Granular-Hematite	MT-14-27	LF	28
Kvannevann	Granular-Hematite	MT-14-27	LF	26
Kvannevann	Granular-Hematite	Mt-15-101	PF	38
Kvannevann	Granular-Hematite	Mt-15-101	PF	35
Kvannevann	Granular-Hematite	Mt-15-101	PF	34
Kvannevann	Granular-Hematite	Mt-15-101	PF	34
Kvannevann	Granular-Hematite	Mt-15-101	PF	32
Kvannevann	Granular-Hematite	Mt-15-101	PF	32
Kvannevann	Granular-Hematite	Mt-15-101	PF	30
Kvannevann	Granular-Hematite	Mt-15-101	PF	30
Kvannevann	Granular-Hematite	Mt-15-101	PF	30
Kvannevann	Granular-Hematite	Mt-15-101	PF	30
Kvannevann	Granular-Hematite	Mt-15-101	LF	51
Kvannevann	Granular-Hematite	Mt-15-101	LF	44
Kvannevann	Granular-Hematite	Mt-15-101	LF	44
Kvannevann	Granular-Hematite	Mt-15-101	LF	42
Kvannevann	Granular-Hematite	Mt-15-101	LF	40
Kvannevann	Granular-Hematite	Mt-15-101	LF	40
Kvannevann	Granular-Hematite	Mt-15-101	LF	39
Kvannevann	Granular-Hematite	Mt-15-101	LF	38
Kvannevann	Granular-Hematite	Mt-15-101	LF	36
Kvannevann	Granular-Hematite	Mt-15-101	LF	35
Kvannevann	Granular-Hematite	Mt-15-111	PF	56
Kvannevann	Granular-Hematite	Mt-15-111	PF	55
Kvannevann	Granular-Hematite	Mt-15-111	PF	54
Kvannevann	Granular-Hematite	Mt-15-111	PF	54
Kvannevann	Granular-Hematite	Mt-15-111	PF	51
Kvannevann	Granular-Hematite	Mt-15-111	PF	50
Kvannevann	Granular-Hematite	Mt-15-111	PF	50
Kvannevann	Granular-Hematite	Mt-15-111	PF	49
Kvannevann	Granular-Hematite	Mt-15-111	PF	49
Kvannevann	Granular-Hematite	Mt-15-111	PF	49
Kvannevann	Granular-Hematite	Mt-15-111	LF	49
Kvannevann	Granular-Hematite	Mt-15-111	LF	49
Kvannevann	Granular-Hematite	Mt-15-111	LF	48
Kvannevann	Granular-Hematite	Mt-15-111	LF	47
Kvannevann	Granular-Hematite	Mt-15-111	LF	46
Kvannevann	Granular-Hematite	Mt-15-111	LF	44
Kvannevann	Granular-Hematite	Mt-15-111	LF	44
Kvannevann	Granular-Hematite	Mt-15-111	LF	42
Kvannevann	Granular-Hematite	Mt-15-111	LF	42
Kvannevann	Granular-Hematite	Mt-15-111	LF	40
Stensundtjern	Specular-Hematite	MT-14-17	PF	42
Stensundtjern	Specular-Hematite	MT-14-17	PF	38
Stensundtjern	Specular-Hematite	MT-14-17	PF	38
Stensundtjern	Specular-Hematite	MT-14-17	PF	37

Stensundtjern	Specular-Hematite	MT-14-17	PF	36
Stensundtjern	Specular-Hematite	MT-14-17	PF	35
Stensundtjern	Specular-Hematite	MT-14-17	PF	34
Stensundtjern	Specular-Hematite	MT-14-17	PF	31
Stensundtjern	Specular-Hematite	MT-14-17	PF	31
Stensundtjern	Specular-Hematite	MT-14-17	PF	28
Stensundtjern	Specular-Hematite	MT-14-17	LF	47
Stensundtjern	Specular-Hematite	MT-14-17	LF	46
Stensundtjern	Specular-Hematite	MT-14-17	LF	44
Stensundtjern	Specular-Hematite	MT-14-17	LF	43
Stensundtjern	Specular-Hematite	MT-14-17	LF	40
Stensundtjern	Specular-Hematite	MT-14-17	LF	40
Stensundtjern	Specular-Hematite	MT-14-17	LF	34
Stensundtjern	Specular-Hematite	MT-14-17	LF	34
Stensundtjern	Specular-Hematite	MT-14-17	LF	34
Stensundtjern	Specular-Hematite	MT-14-17	LF	31
Stensundtjern	Granular-Hematite	MT-15-114	PF	53
Stensundtjern	Granular-Hematite	MT-15-114	PF	46
Stensundtjern	Granular-Hematite	MT-15-114	PF	46
Stensundtjern	Granular-Hematite	MT-15-114	PF	45
Stensundtjern	Granular-Hematite	MT-15-114	PF	44
Stensundtjern	Granular-Hematite	MT-15-114	PF	44
Stensundtjern	Granular-Hematite	MT-15-114	PF	40
Stensundtjern	Granular-Hematite	MT-15-114	PF	39
Stensundtjern	Granular-Hematite	MT-15-114	PF	39
Stensundtjern	Granular-Hematite	MT-15-114	PF	38
Stensundtjern	Granular-Hematite	MT-15-114	LF	56
Stensundtjern	Granular-Hematite	MT-15-114	LF	56
Stensundtjern	Granular-Hematite	MT-15-114	LF	55
Stensundtjern	Granular-Hematite	MT-15-114	LF	54
Stensundtjern	Granular-Hematite	MT-15-114	LF	53
Stensundtjern	Granular-Hematite	MT-15-114	LF	53
Stensundtjern	Granular-Hematite	MT-15-114	LF	52
Stensundtjern	Granular-Hematite	MT-15-114	LF	50
Stensundtjern	Granular-Hematite	MT-15-114	LF	50
Stensundtjern	Granular-Hematite	MT-15-114	LF	49
Stensundtjern	Specular-Hematite	MT-15-115	PF	39
Stensundtjern	Specular-Hematite	MT-15-115	PF	37
Stensundtjern	Specular-Hematite	MT-15-115	PF	36
Stensundtjern	Specular-Hematite	MT-15-115	PF	36
Stensundtjern	Specular-Hematite	MT-15-115	PF	34
Stensundtjern	Specular-Hematite	MT-15-115	PF	33
Stensundtjern	Specular-Hematite	MT-15-115	PF	33
Stensundtjern	Specular-Hematite	MT-15-115	PF	32
Stensundtjern	Specular-Hematite	MT-15-115	PF	32
Stensundtjern	Specular-Hematite	MT-15-115	PF	31
Stensundtjern	Specular-Hematite	MT-15-115	LF	42
Stensundtjern	Specular-Hematite	MT-15-115	LF	41

Stensundtjern	Specular-Hematite	MT-15-115	LF	40
Stensundtjern	Specular-Hematite	MT-15-115	LF	40
Stensundtjern	Specular-Hematite	MT-15-115	LF	39
Stensundtjern	Specular-Hematite	MT-15-115	LF	38
Stensundtjern	Specular-Hematite	MT-15-115	LF	37
Stensundtjern	Specular-Hematite	MT-15-115	LF	34
Stensundtjern	Specular-Hematite	MT-15-115	LF	34
Stensundtjern	Specular-Hematite	MT-15-115	LF	34
Stensundtjern	Granular-Hematite	MT-15-118	PF	48
Stensundtjern	Granular-Hematite	MT-15-118	PF	46
Stensundtjern	Granular-Hematite	MT-15-118	PF	46
Stensundtjern	Granular-Hematite	MT-15-118	PF	46
Stensundtjern	Granular-Hematite	MT-15-118	PF	46
Stensundtjern	Granular-Hematite	MT-15-118	PF	44
Stensundtjern	Granular-Hematite	MT-15-118	PF	44
Stensundtjern	Granular-Hematite	MT-15-118	PF	44
Stensundtjern	Granular-Hematite	MT-15-118	PF	43
Stensundtjern	Granular-Hematite	MT-15-118	PF	42
Stensundtjern	Granular-Hematite	MT-15-118	LF	52
Stensundtjern	Granular-Hematite	MT-15-118	LF	50
Stensundtjern	Granular-Hematite	MT-15-118	LF	50
Stensundtjern	Granular-Hematite	MT-15-118	LF	48
Stensundtjern	Granular-Hematite	MT-15-118	LF	48
Stensundtjern	Granular-Hematite	MT-15-118	LF	46
Stensundtjern	Granular-Hematite	MT-15-118	LF	45
Stensundtjern	Granular-Hematite	MT-15-118	LF	44
Stensundtjern	Granular-Hematite	MT-15-118	LF	44
Stensundtjern	Granular-Hematite	MT-15-118	LF	43
Stensundtjern	Specular-Hematite	MT-14-18	PF	35
Stensundtjern	Specular-Hematite	MT-14-18	PF	34
Stensundtjern	Specular-Hematite	MT-14-18	PF	33
Stensundtjern	Specular-Hematite	MT-14-18	PF	33
Stensundtjern	Specular-Hematite	MT-14-18	PF	31
Stensundtjern	Specular-Hematite	MT-14-18	PF	30
Stensundtjern	Specular-Hematite	MT-14-18	PF	28
Stensundtjern	Specular-Hematite	MT-14-18	PF	28
Stensundtjern	Specular-Hematite	MT-14-18	PF	28
Stensundtjern	Specular-Hematite	MT-14-18	PF	27
Stensundtjern	Specular-Hematite	MT-14-18	LF	38
Stensundtjern	Specular-Hematite	MT-14-18	LF	36
Stensundtjern	Specular-Hematite	MT-14-18	LF	32
Stensundtjern	Specular-Hematite	MT-14-18	LF	31
Stensundtjern	Specular-Hematite	MT-14-18	LF	30
Stensundtjern	Specular-Hematite	MT-14-18	LF	30
Stensundtjern	Specular-Hematite	MT-14-18	LF	30
Stensundtjern	Specular-Hematite	MT-14-18	LF	28
Stensundtjern	Specular-Hematite	MT-14-18	LF	28
Stensundtjern	Specular-Hematite	MT-14-18	LF	27

Stortjønna	Massive-Hematite	MT-14-02	PF	49.5
Stortjønna	Massive-Hematite	MT-14-02	PF	49
Stortjønna	Massive-Hematite	MT-14-02	PF	48
Stortjønna	Massive-Hematite	MT-14-02	PF	46.5
Stortjønna	Massive-Hematite	MT-14-02	PF	44
Stortjønna	Massive-Hematite	MT-14-02	PF	43
Stortjønna	Massive-Hematite	MT-14-02	PF	42
Stortjønna	Massive-Hematite	MT-14-02	PF	42
Stortjønna	Massive-Hematite	MT-14-02	PF	38
Stortjønna	Massive-Hematite	MT-14-02	PF	37.5
Stortjønna	Massive-Hematite	MT-14-02	LF	58
Stortjønna	Massive-Hematite	MT-14-02	LF	48
Stortjønna	Massive-Hematite	MT-14-02	LF	46.5
Stortjønna	Massive-Hematite	MT-14-02	LF	46
Stortjønna	Massive-Hematite	MT-14-02	LF	44
Stortjønna	Massive-Hematite	MT-14-02	LF	42
Stortjønna	Massive-Hematite	MT-14-02	LF	39
Stortjønna	Massive-Hematite	MT-14-02	LF	37
Stortjønna	Massive-Hematite	MT-14-02	LF	36
Stortjønna	Massive-Hematite	MT-14-02	LF	34
Stortjønna	Massive-Hematite	MT-14-04	PF	53
Stortjønna	Massive-Hematite	MT-14-04	PF	53
Stortjønna	Massive-Hematite	MT-14-04	PF	52
Stortjønna	Massive-Hematite	MT-14-04	PF	52
Stortjønna	Massive-Hematite	MT-14-04	PF	52
Stortjønna	Massive-Hematite	MT-14-04	PF	51
Stortjønna	Massive-Hematite	MT-14-04	PF	48
Stortjønna	Massive-Hematite	MT-14-04	PF	48
Stortjønna	Massive-Hematite	MT-14-04	PF	47
Stortjønna	Massive-Hematite	MT-14-04	PF	47
Stortjønna	Massive-Hematite	MT-14-04	LF	46
Stortjønna	Massive-Hematite	MT-14-04	LF	39
Stortjønna	Massive-Hematite	MT-14-04	LF	38
Stortjønna	Massive-Hematite	MT-14-04	LF	36
Stortjønna	Massive-Hematite	MT-14-04	LF	35
Stortjønna	Massive-Hematite	MT-14-04	LF	34
Stortjønna	Massive-Hematite	MT-14-04	LF	32
Stortjønna	Massive-Hematite	MT-14-04	LF	31
Stortjønna	Massive-Hematite	MT-14-04	LF	29
Stortjønna	Massive-Hematite	MT-14-04	LF	29
Stortjønna	Massive-Hematite	MT-14-25B	PF	45
Stortjønna	Massive-Hematite	MT-14-25B	PF	44
Stortjønna	Massive-Hematite	MT-14-25B	PF	43
Stortjønna	Massive-Hematite	MT-14-25B	PF	42
Stortjønna	Massive-Hematite	MT-14-25B	PF	42
Stortjønna	Massive-Hematite	MT-14-25B	PF	42
Stortjønna	Massive-Hematite	MT-14-25B	PF	40
Stortjønna	Massive-Hematite	MT-14-25B	PF	40

Stortjønna	Massive-Hematite	MT-14-25B	PF	38
Stortjønna	Massive-Hematite	MT-14-25B	PF	38
Stortjønna	Massive-Hematite	MT-14-25B	LF	46
Stortjønna	Massive-Hematite	MT-14-25B	LF	42
Stortjønna	Massive-Hematite	MT-14-25B	LF	40
Stortjønna	Massive-Hematite	MT-14-25B	LF	39
Stortjønna	Massive-Hematite	MT-14-25B	LF	39
Stortjønna	Massive-Hematite	MT-14-25B	LF	38
Stortjønna	Massive-Hematite	MT-14-25B	LF	36
Stortjønna	Massive-Hematite	MT-14-25B	LF	35
Stortjønna	Massive-Hematite	MT-14-25B	LF	32
Stortjønna	Massive-Hematite	MT-14-25B	LF	32
Stortjønna	Massive-Hematite	MT-15-113	PF	62
Stortjønna	Massive-Hematite	MT-15-113	PF	54
Stortjønna	Massive-Hematite	MT-15-113	PF	52
Stortjønna	Massive-Hematite	MT-15-113	PF	52
Stortjønna	Massive-Hematite	MT-15-113	PF	50
Stortjønna	Massive-Hematite	MT-15-113	PF	50
Stortjønna	Massive-Hematite	MT-15-113	PF	48
Stortjønna	Massive-Hematite	MT-15-113	PF	48
Stortjønna	Massive-Hematite	MT-15-113	PF	47
Stortjønna	Massive-Hematite	MT-15-113	PF	46
Stortjønna	Massive-Hematite	MT-15-113	LF	65
Stortjønna	Massive-Hematite	MT-15-113	LF	62
Stortjønna	Massive-Hematite	MT-15-113	LF	56
Stortjønna	Massive-Hematite	MT-15-113	LF	56
Stortjønna	Massive-Hematite	MT-15-113	LF	55
Stortjønna	Massive-Hematite	MT-15-113	LF	54
Stortjønna	Massive-Hematite	MT-15-113	LF	54
Stortjønna	Massive-Hematite	MT-15-113	LF	54
Stortjønna	Massive-Hematite	MT-15-113	LF	52
Stortjønna	Massive-Hematite	MT-15-113	LF	51
Stortjønna	Mylonitic-Hematite	MT-14-03	NF	65
Stortjønna	Mylonitic-Hematite	MT-14-03	NF	63
Stortjønna	Mylonitic-Hematite	MT-14-03	NF	62
Stortjønna	Mylonitic-Hematite	MT-14-03	NF	60
Stortjønna	Mylonitic-Hematite	MT-14-03	NF	60
Stortjønna	Mylonitic-Hematite	MT-14-03	NF	56
Stortjønna	Mylonitic-Hematite	MT-14-03	NF	56
Stortjønna	Mylonitic-Hematite	MT-14-03	NF	54
Stortjønna	Mylonitic-Hematite	MT-14-03	NF	52
Stortjønna	Mylonitic-Hematite	MT-14-03	NF	52
Stortjønna	Mylonitic-Hematite	MT-14-05	NF	49
Stortjønna	Mylonitic-Hematite	MT-14-05	NF	48
Stortjønna	Mylonitic-Hematite	MT-14-05	NF	48
Stortjønna	Mylonitic-Hematite	MT-14-05	NF	48
Stortjønna	Mylonitic-Hematite	MT-14-05	NF	48
Stortjønna	Mylonitic-Hematite	MT-14-05	NF	48

Stortjønna	Mylonitic-Hematite	MT-14-05	NF	47
Stortjønna	Mylonitic-Hematite	MT-14-05	NF	47
Stortjønna	Mylonitic-Hematite	MT-14-05	NF	46
Stortjønna	Mylonitic-Hematite	MT-14-05	NF	46
Stortjønna	Mylonitic-Hematite	Mt-14-25A	PF	48
Stortjønna	Mylonitic-Hematite	Mt-14-25A	PF	48
Stortjønna	Mylonitic-Hematite	Mt-14-25A	PF	48
Stortjønna	Mylonitic-Hematite	Mt-14-25A	PF	48
Stortjønna	Mylonitic-Hematite	Mt-14-25A	PF	47
Stortjønna	Mylonitic-Hematite	Mt-14-25A	PF	47
Stortjønna	Mylonitic-Hematite	Mt-14-25A	PF	46
Stortjønna	Mylonitic-Hematite	Mt-14-25A	PF	46
Stortjønna	Mylonitic-Hematite	Mt-14-25A	PF	46
Stortjønna	Mylonitic-Hematite	Mt-14-25A	PF	46
Stortjønna	Mylonitic-Hematite	Mt-14-25A	LF	50
Stortjønna	Mylonitic-Hematite	Mt-14-25A	LF	45
Stortjønna	Mylonitic-Hematite	Mt-14-25A	LF	43
Stortjønna	Mylonitic-Hematite	Mt-14-25A	LF	41
Stortjønna	Mylonitic-Hematite	Mt-14-25A	LF	40
Stortjønna	Mylonitic-Hematite	Mt-14-25A	LF	37
Stortjønna	Mylonitic-Hematite	Mt-14-25A	LF	37
Stortjønna	Mylonitic-Hematite	Mt-14-25A	LF	35
Stortjønna	Mylonitic-Hematite	Mt-14-25A	LF	35
Stortjønna	Mylonitic-Hematite	Mt-14-25A	LF	34
Stortjønna	Mylonitic-Hematite	MT-15-112	PF	75
Stortjønna	Mylonitic-Hematite	MT-15-112	PF	71
Stortjønna	Mylonitic-Hematite	MT-15-112	PF	69
Stortjønna	Mylonitic-Hematite	MT-15-112	PF	68
Stortjønna	Mylonitic-Hematite	MT-15-112	PF	68
Stortjønna	Mylonitic-Hematite	MT-15-112	PF	67
Stortjønna	Mylonitic-Hematite	MT-15-112	PF	67
Stortjønna	Mylonitic-Hematite	MT-15-112	PF	66
Stortjønna	Mylonitic-Hematite	MT-15-112	PF	66
Stortjønna	Mylonitic-Hematite	MT-15-112	PF	64
Stortjønna	Mylonitic-Hematite	MT-15-112	LF	60
Stortjønna	Mylonitic-Hematite	MT-15-112	LF	59
Stortjønna	Mylonitic-Hematite	MT-15-112	LF	58
Stortjønna	Mylonitic-Hematite	MT-15-112	LF	58
Stortjønna	Mylonitic-Hematite	MT-15-112	LF	51
Stortjønna	Mylonitic-Hematite	MT-15-112	LF	49
Stortjønna	Mylonitic-Hematite	MT-15-112	LF	49
Stortjønna	Mylonitic-Hematite	MT-15-112	LF	48
Stortjønna	Mylonitic-Hematite	MT-15-112	LF	47
Stortjønna	Mylonitic-Hematite	MT-15-112	LF	42

Appendix E: Collars drill cores measured by Equotip and deposit samples

Collars drill cores									
Drill core ID	North	East	Direction	Dip	Heigth	Length	Diameter	Year	Deposit
Bh 66-2011	7367127.1	487188.36	117.59	-47.94	329	334.77	46	2011	Kvannevann
Bh 221-2014	7367385.834	488198.184	339.47	-30	375.91	124	46	2014	Kvannevann east
Bh 222-2014	7367385.821	488198.165	339.12	-15	376.57	124	46	2014	Kvannevann east
Bh 224-2014	7367371.782	488152.159	336.26	-30	378.04	116	46	2014	Kvannevann east
Bh 130-2012	7366784.311	474920.579	360	-35	201.95	102	46	2012	Stensundtjern
Bh 145-2013	7366758.063	473710.473	5.25	-55	267.54	223	46	2013	Stensundtjern
Bh 32-2010	7367486.902	488745.732	155	-45	360.67	41	46	2010	Stortjønna
Bh 33-2010	7367486.238	488746.116	155	-10	361.73	51.70	46	2010	Stortjønna
Bh 89-2011	7367588.623	488549.218	162	-45.9	403.04	265	46	2011	Stortjønna

Collars deposit samples					
Deposit	East	North	Elevation	Zone	Comment
Kvannevann-1	486866.215	7367147.77	156.95	33W	155-33 in map
Kvannevann-2	487204.449	7367199.54	160.95	33W	155-49 in map
Stensundtjern	475144.65	7366755.81	189.04	33W	
Stortjønna	488768.37	7367465.07	338.38	33W	

Appendix F: Drill core sections measured by Equotip

In the core section column, the letters refer to the deposit (KV = Kvannevann, ST = Stensundtjern, and SØ = Stortjønna) from which the drill cores are.

Core section	Drill core	From	To	Length	Comments
KV-1	Bh 221-2014	4.31	6.3	1.99	
KV-2	Bh 221-2014	15.71	15.92	0.21	
KV-3	Bh 221-2014	67.75	70.42	2.67	
KV-4	Bh 221-2014	81.52	97.88	16.36	
KV-5	Bh 224-2014	10.03	10.26	0.23	
KV-6	Bh 224-2014	10.55	13.19	2.64	
KV-7	Bh 224-2014	24.74	28	3.26	
KV-8	Bh 224-2014	28.15	35	6.85	
KV-9	Bh 224-2014	70.63	74.52	3.89	
KV-10	Bh 224-2014	84.58	93.1	8.52	
KV-11	Bh 224-2014	99.66	105.97	6.31	
KV-12	Bh 222-2014	3.8	4.04	0.24	
KV-13	Bh 222-2014	4.53	5.49	0.96	
KV-14	Bh 222-2014	12.6	12.67	0.07	
KV-15	Bh 222-2014	14.23	15.7	1.47	
KV-16	Bh 222-2014	18.44	21.25	2.81	
KV-17	Bh 222-2014	24.25	27.35	3.10	
KV-18	Bh 222-2014	56.85	60.3	3.45	
KV-19	Bh 222-2014	72.93	76.5	3.57	
KV-20	Bh 221-2014	39.4	40.7	1.30	
KV-21	Bh 221-2014	52	54.31	2.31	
KV-22	Bh 224-2014	50.28	50.83	0.55	
KV-23	Bh 224-2014	49	49.94	0.94	
KV-24	Bh 222-2014	36	36.8	0.80	
KV-25	Bh 222-2014	42	44.12	2.12	Garnet mylonite 43.55-43.96 not measured
KV-26	Bh 221-2014	97.88	98	0.12	
KV-27	Bh 224-2014	74.52	81.78	7.26	
KV-28	Bh 224-2014	105.97	106.73	0.76	
KV-29	Bh 222-2014	21.25	24.05	2.80	
KV-30	Bh 222-2014	60.3	62.94	2.64	
KV-31	Bh 221-2014	19.16	21	1.84	
KV-32	Bh 221-2014	21	27.88	6.88	
KV-33	Bh 222-2014	79.98	80.6	0.62	
KV-34	Bh 222-2014	81.02	91	9.98	
KV-35	Bh66-2011	90.67	98.00	7.33	
KV-36	Bh66-2011	133.00	138.00	5.00	
KV-37	Bh66-2011	138.00	144.70	6.70	
KV-38	Bh66-2011	147.00	150.00	3.00	
KV-39	Bh66-2011	268.13	288.14	20.01	
KV-40	Bh66-2011	294.73	296.40	1.67	

ST-1	Bh 130-2012	39.04	41.09	2.05	
ST-2	Bh 130-2012	49.23	49.36	0.13	
ST-3	Bh 130-2012	49.86	52.07	2.21	
ST-4	Bh 145-2013	136	139.09	3.09	
ST-5	Bh 145-2013	156.79	157.08	0.29	
ST-6	Bh 145-2013	204.8	207.35	2.55	
ST-7	Bh 130-2012	21	38.69	17.69	
ST-8	Bh 145-2013	147	150.22	3.22	
ST-9	Bh 145-2013	150.38	152.85	2.47	
ST-10	Bh 145-2013	163.67	179.09	15.42	
ST-11	Bh 145-2013	189	194.09	5.09	
ST-12	Bh 145-2013	139.09	147	7.91	
ST-13	Bh 145-2013	204.21	204.8	0.59	
ST-14	Bh 145-2013	181.39	189	7.61	
ST-15	Bh 145-2013	194.09	196	1.91	
ST-16	Bh 145-2013	196	204.21	8.21	
SØ-1	Bh89-2011	85.05	85.62	0.57	
SØ-2	Bh89-2011	89.11	89.42	0.31	
SØ-3	Bh89-2011	96.15	96.35	0.2	
SØ-4	Bh33-2010	41.7	42	0.3	
SØ-5	Bh33-2010	43.5	43.76	0.26	
SØ-6	Bh33-2010	46.74	48.06	1.32	
SØ-7	Bh33-2010	48.06	48.48	0.42	
SØ-8	Bh33-2010	12.67	21	8.33	
SØ-9	Bh32-2010	7.94	9.58	1.64	
SØ-10	Bh33-2010	39.26	40.36	1.1	
SØ-11	Bh89-2011	94.34	94.8	0.46	
SØ-12	Bh89-2011	94.8	96.15	1.35	
SØ-13	Bh33-2010	42	43	1	
SØ-14	Bh33-2010	43	43.5	0.5	
SØ-15	Bh33-2010	5.49	9.78	4.29	
SØ-16	Bh33-2010	21	28	7	
SØ-17	Bh32-2010	14.9	21.04	6.14	Quartz 19.5-19.6 not measured
SØ-18	Bh32-2010	10.78	10.93	0.15	
SØ-19	Bh32-2010	27.45	28.21	0.76	